From Molecules to Models:
Advances in the 3D Printing of Polymeric Materials
Toward Improved Control, Functionality, and Sustainability

By

Kyle C. H. Chin

A dissertation in partial fulfillment of the requirements for the degree of

Doctor of Philosophy

(Chemical Engineering)

at the

UNIVERSITY OF WISCONSIN-MADISON

2024

Date of final oral examination: 03/13/2024

The dissertation is approved by the following members of the Final Oral Committee:

Andrew J. Boydston, Faculty, Professor, Chemistry

Padma Gopalan, Faculty, Professor, Material Science and Engineering

Reid Van Lehn, Faculty, Associate Professor, Chemical and Biological Engineering

David Lynn, Faculty, Professor, Chemical and Biological Engineering

Acknowledgements

Completing a PhD has been an arduous journey, one that I never anticipated would be as challenging as it turned out to be. Throughout the past five years, my focus has been primarily on the future—completing assignments, teaching lessons, testing hypotheses, conducting experiments, and writing papers. However, in this moment, I feel a deep sense of honor in recognizing the individuals who have imparted valuable lessons, skills, and support that guided me through this thesis and brought me to where I am today.

Foremost, I would like to thank my family. To my parents, Gary Chin and Christine Haug-Chin, I thank you for all the support you have shown me throughout my life and especially over the last five years. It has truly meant the world to me. To my brothers Brent Chin and Cameron Chin, thank you for your unwavering confidence in me in times when I was lacking confidence in myself. I am also fortunate to have an amazing extended family who were always interested in my progress. Thank you to all of you.

Thank you to Dr. Rachel Tritt. I cannot express enough gratitude for the shared journey of the past few years. I have truly appreciated having someone to celebrate the highs and deal with the lows and I am excited to build many new memories with you, Lizzie, and Darcy.

Thank you to my friends. To my day ones, Blake Bronson, Nyles Green, and Matthew Jewell—your friendship has meant a lot over the last 20+ years. Thank you to Dr. Anthony Pyka who always made the effort to call and catch up. I cannot express enough how much those little conversations meant to me. Additionally, I would like to thank Nico Conahan, Lily Gould, Meredith Datena, and Annaliese Laurila. I always looked forward to going home and seeing you all. It truly helped me recharge my batteries. Y'all are the best and I look forward to many more years of friendship.

To my fellow graduate students at the University of Wisconsin-Madison, thank you for sharing this journey with me. Specifically, I would express my appreciation to Dr. Curran Gahan, Dr. Michael Rebarchik, Ryan Cashen, Jack McAlpine, Paul Perkovich, Maya Venkataraman, and Christine Lucky. I look forward to calling everyone doctor soon and seeing all the great things you all will do in the future.

Thank you to Dr. Elliott Gall, who introduced me to the world of research. You have been an incredible mentor to me. I am positive that without the experience I had in your lab and your guidance I would not be where I am today.

Thank you to the members of the Boydston group. I feel very fortunate to have gotten to work with such a fun, supportive, and intelligent group of people who pushed me to be a better scientist, colleague, and mentor. I would specifically like to thank Dr. Chang-Uk Lee, Dr. Cody Schilling, and Dr. Xuejin Yang who were incredible mentors to me. I would also like to thank Dr. Vinnie Rigoglioso who was a great friend and pickleball partner and Meg Tetzloff, Brittany Trinh, Sarah Finnegan, Jerry Miao, and Sean Gitter who were amazing office mates.

I would also like to thank all the collaborators I had the privilege of working with and learning from during graduate school. There are too many of you to thank here but know that I could not have done a fraction of the work contained in this thesis without you. Additionally, I would like to thank the National Science Foundation Graduate Research Fellowship Program under Grant No. DGE-1747503 for funding me for the past three years. Without this support I could not have devoted as much time to my research.

I would also like to thank my thesis committee for their time and consideration over the last five years. Academia can be a tough environment, and I always felt reassured that I had such an understanding and considerate committee to share my research with and gain valuable feedback.

Lasty, I would like to thank my advisor, AJ Boydston. Your mentorship has been invaluable during my time in graduate school. I am thankful for the freedom you gave me to explore my research interests and the inclusive environment you fostered in the group. I truly feel I have been able to develop as an independent scientist and that I am equipped with the knowledge to solve any research problem I may come up against. It has been an honor to be a member of the Boydston group.

Table of Contents

Abstract

Polymers are an important class of materials due to their favorable mechanical properties and chemical resistance. However, traditional manufacturing methods with polymers (e.g. subtractive and formative) limit the structures we can make and thus end uses achievable. Additive manufacturing (AM), commonly called 3D printing (3DP), uses polymers to solve these issues by creating objects directly from computer aided design models with unparalleled geometric freedom. In recent years, polymer 3DP has been increasingly utilized to produce end use products and recognized for its potential to create next generation devices. This has brought a growing demand for the development of polymeric materials that give novel functionality and improved sustainability. Furthermore, the ability to finely control structures provides fundamental research opportunities for developing controlled hierarchical structured materials. To address these diverse challenges and opportunities, a multifaceted approach is needed, combining molecular through macroscale design integrated with 3DP processing.

This dissertation will provide insight into the current state of polymer 3DP and illustrate how we can use bottom-up strategies to engineer solutions to pressing materials challenges. The thesis will be organized into four parts. Part one will showcase the use of bottom-up strategies to investigate materials for 3DP with improved sustainability (Chapter 4), increased toughness (Chapter 5), and stimuli responsiveness (Chapter 6). Part two will discuss use of processing focused strategies using hardware development for accessing novel material functions (Chapter 7 and 8). In part three, we will describe dual wavelength vat photopolymerization (DW-VP), a nascent 3D printing technique, and show how a combination of bottom-up material design and unique processing can be used to design materials with improved control over materials properties (Chapter 9). Lastly, in part four we will explore 3DP as an enabling technology to study unique material architectures for energy absorbing applications (Chapter 10 and 11).

List of Abbreviations

^{1}H NMR — Hydrogen-1 nuclear magnetic resonance spectroscopy

^{13}C NMR — Carbon-13 nuclear magnetic resonance spectroscopy

3DP — 3D printing

4-pG — 4-propylguaiacol

4-pGA — 4-propylguaiacyl acrylate

ABS — acetonitrile butadiene styrene

AM — Additive manufacturing

BAPO or Irg819 — Phenylbis(2,4,6-trimethylbenzoyl)phosphine oxide

BCP — Block copolymer

BG — Bromocresol green

BJT — Binder jetting

CAD — Computer aided design

C_d — Cure depth

CQ — Camphorquinone

CTA — Chain transfer agent

DBU — 1,8-diazabicyclo[5.4.0]undec-7-ene

DCM — Dichloromethane

DED — Directed energy deposition

DEM — Discrete element model

DIC — Digital image correlation

DIW — Direct ink write

DLP — Digital light processing

DMA — Dynamic mechanical analysis

D_p — Penetration depth

DSC — Differential scanning calorimetry

DW-VP — Dual-wavelength vat photopolymerization

EAE — Energy absorption efficiency

E_c — Critical exposure

ECC — 3,4-epoxycyclohexylmethyl-3′,4′-epoxycyclohexane carboxylate

ECMA — 3,4-epoxycyclohexylmethyl acrylate

FEM — Finite element model

FEP — Fluorinate ethylene propylene

FFF — Fused filament fabrication

GMA — Glycidyl methacrylate

GPC — Gel permeation chromatography

HAPPI — Heating at a patterned photothermal interface

HDDA — 1,6-hexandiol diacrylate

HDPE — High density polyethylene

HEA — 2-hydroxyethyl acrylate

IBOA — Isobornyl acrylate

IPA — Isopropyl acrylate

KE — Kinetic energy

LA — Lauryl acrylate

LMA — Lauryl methacrylate

MAM — Methyl methacrylate

MAPDMS — Monomethacryloxypropyl terminated polydimethylsiloxane

MeO-gDCC — Methoxy substituted gem-dicyclopropane

MeO-gDCC-DA — Methoxy substituted gem-dicyclopropane diacrylate

MEX — Material extrusion

MJT — Material jetting

M_n — Molecular weight

MR — Methyl red

PAG — Photoacid generator

PBA — Polybutyl acrylate

PBF — Powder bed fusion

PC — Polycarbonate

PCL — Polycaprolactone

PDMS — Polydimethylsiloxane

PEGDA — Polyethylene glycol diacrylate

PEO — Polyethylene oxide

PET — Polyethylene terephthalate

PGMA — Polyglycidyl methacrylate

PLA — Polylactic acid

PMAPDMS — Polymonomethacryloxypropyl terminated polydimethylsiloxane

PME — Powder material extrusion

PMMA — Polymethyl methacrylate

PS — Polystyrene

PSA — Pressure sensitive adhesive

PTFE — Polytetrafluoroethylene

RAFT — Reversible addition fragmentation chain transfer

RD — Relative density

ROP — Ring opening polymerization

SA — Syringyl acrylate

SEM — Scanning electron microscopy

SEC — Size exclusion chromatography

SHL — Sheet lamination

SLA — Stereolithography

SMA — Syringyl methacrylate

TAS — Triarylsulfonium salts

T_c — Crystallization temperature

T_d — Decomposition temperature

T_g —Glass transition temperature

TGA — Thermogravimetric analysis

T_m — Melt temperature

TPMS — Triply periodic minimal surfaces

TPU — Thermoplastic polyurethane

T_{trans} — Transition temperature

UV — Ultra violet

VP — Vat photopolymerization

List of Tables

List of Figures

Chapter 1: 3D Printing: A Brief Introduction to a Disruptive Technology

Manufacturing and 3D Printing's Role

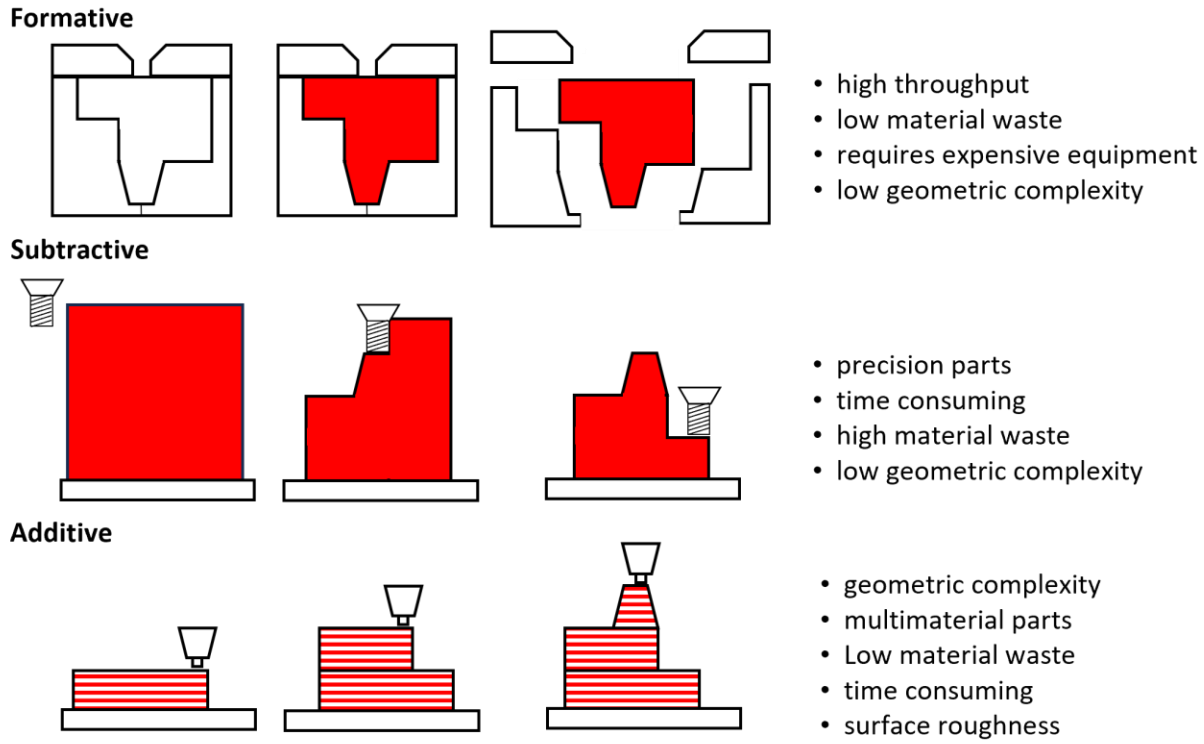

Figure 1.1. *Comparison of formative, subtractive, and additive manufacturing along with some advantages and disadvantages to each manufacturing method.*[1]

Manufacturing processes can be categorized into formative, subtractive, and additive methods, each exhibiting distinct advantages and disadvantages(Figure 1.1).[2] Formative manufacturing, exemplified by techniques like injection molding and forging, involves shaping materials into their final form often utilizing molds. This approach is high throughput but requires additional equipment such as molds, extruders, and furnaces, all of which have finite lifespans and can incur substantial replacement or manufacturing costs. In subtractive manufacturing, material is removed from a bulk slab until the final desired geometry is obtained. Although this method yields high precision parts and utilizes more cost-effective tooling, it is time-intensive and results in significant material waste. Both formative and subtractive manufacturing face constraints in dealing with intricate part geometries and difficulties in creating precise multimaterial architectures.

Contrastingly, additive manufacturing (AM) methods enable precise materials placement through a digital workflow, minimizing materials waste and facilitating the fabrication of complex geometries. Additionally, because material placement is programmed into the process, several AM methods accommodate simultaneous printing of multiple materials enhancing versatility. Also, AM has been touted for its elimination of supply chain management, reduced material waste, and low carbon footprint.[3] Nevertheless, these benefits come at the expense of lengthy manufacturing times, due to the layer-by-layer object construction, and inherent tradeoffs between surface roughness, defects, and productivity.[3] Despite these drawbacks, the unparalleled geometric freedom and digital workflow positions AM to be a revolutionary technology poised to disrupt the current manufacturing paradigm.[4]

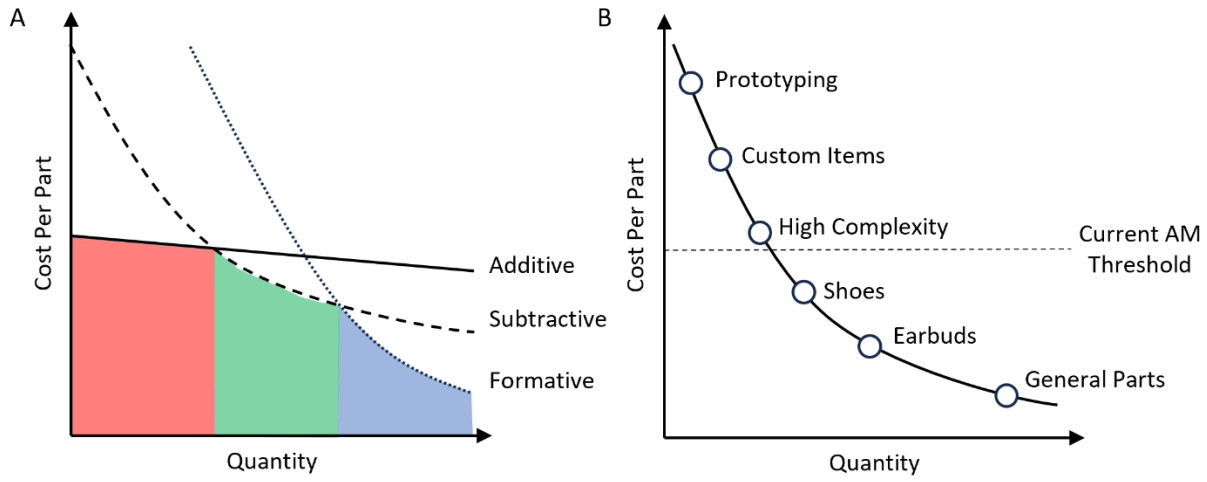

Figure 1.2. *A) Cost per part v quantity comparison illustrating general trends of formative, subtractive, and additive manufacturing.[5] B) Cost per part v quantity comparison showing the current threshold for AM technologies.[6]*

The initial impact of AM was first evident in its ability to dramatically expedite prototyping by generating custom parts directly from computer aided design models.[7] This departure from traditional manufacturing methods, such as formative and subtractive, allowed the creation of test parts in a matter of hours rather than days. Additional advancements in hardware and materials have expanded the applications beyond rapid prototyping and now facilitate production of end use parts.

While AM is situated for end use parts production, its widespread adoption into bulk manufacturing encounters economy of scale challenges, particularly evident in the relationship between cost per part and the required quantity of the part.[8] AM excels in areas with low production volume and high value per item due to the lower entry level equipment costs compared to formative or subtractive methods. Alternatively, at medium and high production volumes, subtractive and formative, respectively, are superior (Figure 1.2A). However, as the demand for customized products grows (e.g. prosthetics, hearing aids, and dental aligners), AM prices drop, and greater throughputs are achieved, AM technologies will become more practical for lower-cost and higher-volume items (Figure 1.2B). However, it is in the niche areas of complexity, mass customization, and low production volume that AM currently thrives.

Although still predominately in niche applications, AM is gradually gaining mainstream recognition as a technology positioned to bridge the third industrial revolution,[9] defined by automation, and the fourth industrial revolution,[10] defined by digitizing processes. Former President Barack Obama, in his 2013 State of the Union address, described AM as a technology "that has the potential to revolutionize the way we make almost everything".[11] In 2022, AM gained further recognition when it was included in the White House's list of critical and emerging technologies.[12] The global AM market size was evaluated at $15 billion (USD) in 2022 and is projected to grow at a compound annual growth rate of ~20% in the next decade.[13] However, sustained growth will require advancements in hardware, software, materials, and AM services.

Introduction to 3D Printing Processes

AM, often referred to as 3D printing (3DP), is the process of joining material to make parts from a 3-dimensional digital model. Its definition is necessarily broad as the set of techniques for the formation of objects are diverse and constantly evolving. This evolution can be traced to the wide array of end use applications and materials (e.g. metals, polymers, and ceramics) that require tailored consideration in their processing. Today, there are seven ISO/ASTM recognized processing categories: binder jetting (BJT), directed energy deposition (DED), material extrusion (MEX), material jetting (MJT), powder bed fusion (PBF), sheet lamination (SHL), and vat photopolymerization (VP).[14] Multiple variations and

subclassifications of these techniques exist and additional terminology for these techniques has also been described. A simplified image of these processing techniques can be found in Figure 1.3.

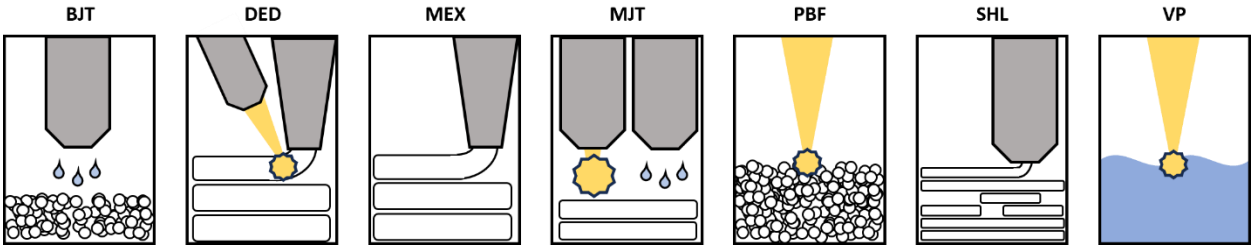

Figure 1.3. *Simple visual representation of the seven 3DP processing types.*

BJT: A liquid binding agent is selectively deposited to join powder material.

DED: Focused thermal energy is used to fuse materials by melting them as they are deposited.

MEX: Material is dispensed through a nozzle or orifice.

MJT: Droplets of feedstock are selectively deposited.

PBF: Thermal energy selectively fuses regions of a powder bed.

SHL: Sheets of material are bonded together.

VP: Liquid photopolymer in a vat is cured by light activated polymerization.

While the techniques for AM differ substantially, the general workflow for 3DP shares four main steps (Figure 1.4): (1) preparing the model, (2) slicing the model, (3) printing the model, and (4) post processing.

In the first step, a 3D file is generated using a computer aided design (CAD) application. While this step can be as simple as joining shapes together into a final construct, more complex methods can also be employed leveraging the geometric freedom that an additive approach to manufacturing affords. For example, to reduce weight while maintaining the strength of a part, topological optimization can be utilized removing material from areas that will experience low internal stresses in the end use applications, while more material can be used to reinforce areas that may experience high internal stresses.[15] The final design file can be exported into a variety of formats suitable for 3DP. These formats (e.g. STL, OBJ, 3MF, STEP)

often involve dissecting the object into a triangular mesh where the faces and vertices are saved for future recreation in a slicing program.

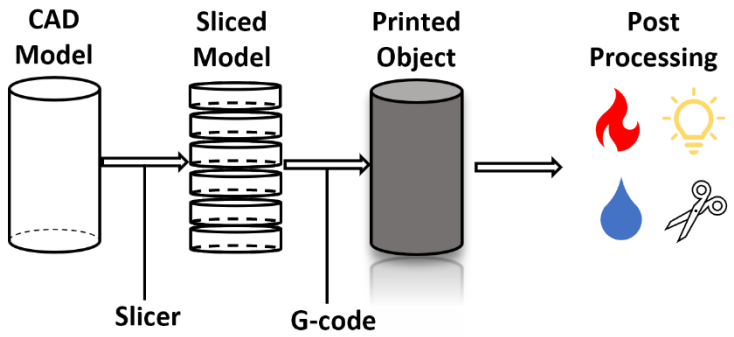

Figure 1.4. *Diagram showing the general workflow for 3DP objects.*

In the second step, the 3D design is loaded into a slicing program used to prepare the set of printing instructions for your given 3DP method. In this program, the design will need to be oriented, support structures added, and material specific settings accounted for which usually occurs in a virtual environment so that settings can be visualized. The defined settings will be distinct and depend on the 3DP process used. Once all settings are to the user's specifications, the design can be sliced and printing instructions compiled, often in the form of G-code, and packaged into a format suitable for the printer to understand.

In the third step, the sliced file can be loaded onto the printer and material added. The printer may need to be calibrated in some way prior to printing (e.g. leveling the build plate). Once the printer is prepared, the print can be started and requires minimal to no intervention. The printing process can often be time consuming and the initial settings for a given design fine-tuned to produce the best outcome. This is often done iteratively and through trial and error, although more complex approaches are being developed that integrate machine learning and real-time print monitoring.

In the fourth and final step, the now printed object is removed from the build area. The printed object may be ready for use or may require further post processing steps that aid in either cleaning up any inconsistencies that may have occurred during a print or setting in the final properties of materials. Common cleaning procedures include removal of supports, washing the exterior of the part, or sanding the surface.

Examples of post processing steps for setting final materials properties include removing binder through a solvent wash or thermal treatment, thermal or UV induced curing, or thermal sintering.

Brief Historical Account

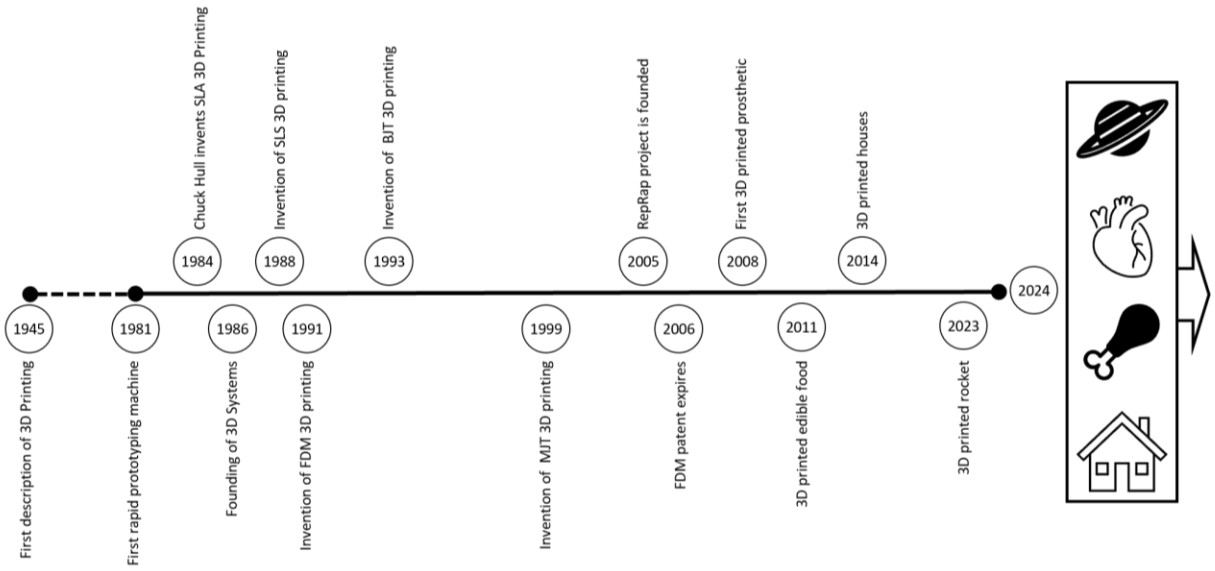

Figure 1.5. *Timeline of important events and future perspective*

3DP has rapidly progressed in the last ~40 years since its initial creation. While a comprehensive account of all significant contributions during this period is beyond the scope of this document, key milestones provide a glimpse into the beginnings, the current state of 3DP, and the potential of the technology. A timeline showing some of these milestones is shown in Figure 1.5 and reveals key events that have transformed a technology originally described in science fiction into reality.

The general concept for 3DP as we know it today can be traced back to a science fiction short story by Murray Leinster called *Things Pass By*. In the story, Murray describes a machine termed a "plastic constructor" writing,

> Ordinarily, you make a specialized machine-tool to turn out one particular part, and it will produce that part cheaper than any other method can do. But if you try to change the product, the machine is useless. You get efficiency at the cost of flexibility. For that reason, there aren't any mass-production machines for big objects like ships and so on. It's cheaper to be inefficient and flexible.

> But this constructor is both efficient and flexible. I feed magnetronic plastics — the stuff they make houses and ships of nowadays — into this moving arm. It makes drawings in the air following drawings it scans with photo-cells. But plastic comes out of the end of the drawing arm and hardens as it comes. This thing will start at one end of a ship or a house and build it complete to the other end, following drawings only.[16]

Remarkably, this description almost perfectly describes the motivation behind 3DP's eventual realization and closely resembles one of the first 3DP processes. The actual realization of a device capable of turning a drawing into a part, termed rapid prototyping, was first realized 36 years later in 1981 by Japanese inventor Dr. Hideo Kodama.[17] Shortly after, in 1984, Charles "Chuck" Hull invented stereolithography (SLA), a subset technique of what is now called VP, capable of converting liquid photoresins into solid parts using a UV laser.[18] He later went on to found 3D Systems, the world's first 3DP company in 1986, developed the STL file format, and the first commercially available 3D printer in 1988.[17] Hull is often regarded as the father of 3DP.

While SLA was the first 3DP method developed, several others were quick to follow including selective laser sintering (SLS)[20] by Carl Deckard and fused deposition modelling (FDM)[21] by Scott Crump in 1990. FDM, most closely resembling the "plastic constructor", would become the most popular method of 3DP on the market and would lead to the founding of Stratysis. Throughout the 90s, the technology would continue to expand and even more methods (e.g. BJT in 1993[22] and MJT in 1999[23]) and companies (e.g. Z Corporation and Objet Geometries) appeared. However, the 3D printers being developed at this point were costly and inaccessible to most people.

This all began to change in 2005 when Adrian Bower began an open-source initiative called the RepRap project.[17] This was aided by the expiration of many of the original 3DP technology patents. Both events catalyzed a surge in the prevalence of FDM 3D printers, dramatically increasing their availability and lowering their cost. Companies such as MakerBot (2008) and Prusa (2010) began to release entry level desktop printers for the masses, bringing this once costly technology to the average hobbyist and tinkerer.

However, the 3D printers were not the only innovations occurring as people began to push the boundaries of how 3DP could be used and what could be fabricated using 3DP. Some examples of these innovations include 3DP of implantable artificial organs,[24,25] prosthesis,[26] meat,[27] and rockets.[28]

3DP technology has now found a variety of commercial applications across many industries including automotive, aerospace, fashion, and health.[7] While remarkable applications of the technology have been possible, the true adoption of 3DP into many industries is hampered by the technology being unreliable, defect-prone, limited in material scope, and having low throughput among other challenges.[3,8] If the challenges can be overcome, AM is poised to make a large impact on manufacturing and many aspects of daily life.

References

1. Redwood, B., Schöffer, F. & Garret, B. *The 3D Printing Handbook: Technologies, Design and Applications*. (3D Hubs B.V., 2017).

2. Pereira, T., Kennedy, J. V. & Potgieter, J. A comparison of traditional manufacturing vs additive manufacturing, the best method for the job. *Procedia Manuf.* **30**, 11–18 (2019).

3. Srivastava, M., Rathee, S., Patel, V., Kumar, A. & Koppad, P. G. A review of various materials for additive manufacturing: Recent trends and processing issues. *J. Mater. Res. Technol.* **21**, 2612–2641 (2022).

4. Berman, B. 3-D printing: The new industrial revolution. *Bus. Horiz.* **55**, 155–162 (2012).

5. What is 3D printing? How does 3D printing work? | Protolabs Network. https://www.hubs.com/guides/3d-printing/.

6. Additive Manufacturing: Industry Trends and Outlook | Formlabs. https://formlabs.com/blog/additive-manufacturing/.

7. Srivastava, M. & Rathee, S. Additive manufacturing: recent trends, applications and future outlooks. *Prog. Addit. Manuf. 2021 72* **7**, 261–287 (2021).

8. Thomas, D. S. & Gilbert, S. W. Costs and Cost Effectiveness of Additive Manufacturing A Literature Review and Discussion. doi:10.6028/NIST.SP.1176.

9. A third industrial revolution | The Economist.

10. The Fourth Industrial Revolution: what it means and how to respond | World Economic Forum. https://www.weforum.org/agenda/2016/01/the-fourth-industrial-revolution-what-it-means-and-how-to-respond/.

11. Remarks by the President in the State of the Union Address | whitehouse.gov. https://obamawhitehouse.archives.gov/the-press-office/2013/02/12/remarks-president-state-union-address.

12. Technologies for American Innovation and National Security | OSTP | The White House. https://www.whitehouse.gov/ostp/news-updates/2022/02/07/technologies-for-american-innovation-and-national-security/.

13. Additive Manufacturing Market Size, Trends, Report By 2032. https://www.precedenceresearch.com/additive-manufacturing-market (2023).

14. ASTM 52900. Additive Manufacturing - General Principles - Terminology. *ASTM Int.* **2021**, 1–14 (2021).

15. Zhu, J. *et al.* A review of topology optimization for additive manufacturing: Status and challenges. *Chinese J. Aeronaut.* **34**, 91–110 (2021).

16. Leinster, M. Things Pass By. in *Ace Books* 25 (Standard Magazines Inc., 1945).

17. History of 3D Printing: When Was 3D Printing Invented? | All3DP. https://all3dp.com/2/history-of-3d-printing-when-was-3d-printing-invented/.

18. Hull, C. W. & Arcadia, C. Apparatus for production of three-dimensional objects by stereolithography. (1984).

19. Chuck Hull and Stereolithography. https://spie.org/news/spie-professional-magazine-archive/2013-

january/chuck-hull#_=_.

20. Deckard, C. R. Method for selective laser sintering with layerwise cross-scanning. **142**, 104 (1990).

21. Crump, S. Apparatus and method for creating three-dimensional objects. (1989).

22. Sachs, E. M., Haggerty, J. S., Cima, M. J. & Williams, P. A. Three-dimensional printing techniques. 10 (1989).

23. Gothait, H. Apparatus and method for three dimensional model printing. (1999).

24. Murphy, S. V. & Atala, A. 3D bioprinting of tissues and organs. *Nat. Biotechnol.* **32**, 773–785 (2014).

25. Dey, M. & Ozbolat, I. T. 3D bioprinting of cells, tissues and organs. *Sci. Reports 2020 101* **10**, 1–3 (2020).

26. Manero, A. *et al.* Implementation of 3D Printing Technology in the Field of Prosthetics: Past, Present, and Future. *Int. J. Environ. Res. Public Health* **16**, (2019).

27. Kang, D. H. *et al.* Engineered whole cut meat-like tissue by the assembly of cell fibers using tendon-gel integrated bioprinting. *Nat. Commun. 2021 121* **12**, 1–12 (2021).

28. Amos, J. 3D printed rocket takes to the sky over Florida - BBC News. *BBC* https://www.bbc.com/news/science-environment-64893578 (2023).

Chapter 2: Introduction to Polymers and 3D Printing of Polymeric Material

Introducing Polymers

The development of materials is a cross disciplinary endeavor bringing together engineers and scientists from many fields. This collision of ideas and expertise creates enormous opportunity for the development of society altering materials via innovations in ideas, design, and technology. Historically, the discovery of certain materials and their properties has brought about unprecedented advancements warranting entire eras being described by their defining material. For example, the Metal Age (3200-1 BCE), divided into the Copper Age, Bronze Age, and Iron Age, brought unprecedented changes to settlement organization, ritual life, technology, and human interactions.[1,2]

Transporting to the present and a new class of material is ubiquitous with the 20th and 21st century—plastics. Plastics, more broadly called polymers (composition of the Greek words *poly* and *meros* meaning many parts), were originally correctly described by Hermann Staudinger in 1920 as large macromolecules made up of covalently bound repeat units termed monomers.[3] Their macromolecular nature and ability to be synthetically produced imparts desirable and unique material properties such as high chemical resistance, durability, and low weight as well as economic benefits driving their use in virtually all areas of industry. This ranges from everyday items such as plastic bags, bottles, and clothing, to adhesives, electronics, and medicine.[4,5] These attributes, while beneficial from a material standpoint, have caused the world to be overrun with plastics.[6–9] While natural polymers such as DNA, cellulose, proteins, and natural rubbers exist, the current state of the planet necessitates synthetic polymers. Calculations show if all the polyester and nylon in use today were replaced by cotton and wool, there would not be enough arable land left to feed the populace.[5] Needless to say, polymers have gained large interest in the scientific community for many reasons and there is ample opportunity to design new polymers with novel functionality and sustainability criterium.

3D Printing of Polymers

Polymers are the most widely used materials for 3DP due to their many useful properties and their processability. Currently, there is a diverse range of polymer materials that have been used in 3DP including thermoplastics, thermosets, elastomers, hydrogels, functional polymers, polymer blends, polymer composites, and biological polymers.[10] There are also a variety of 3DP methods used to print the diverse range of polymer materials, but the most encountered methods are PBF, MEX, MJT, and VP.[11] These four processes vary dramatically in chemical feedstock, energy source, and chemistry. One way the processes can be categorized is if there is a physical or chemical change. For example, PBF and MEX typically use prebuilt polymers that undergo processing-induced physical changes to form their 3D structure, while MJT and VP use a chemical reaction during 3DP to set the object's final geometry. A brief description of these methods is below.

PBF, also commonly known as selective laser sintering, converts powdered polymer material (<1 mm) into a 3D object through a layer-by-layer thermal approach (Figure 2.4A).[10] In this process, a thin layer of thermoplastic powder is evenly dispersed onto the build platform. A focused laser then scans the surface of the powder dictated by the given CAD model. During this scan, the laser radiation is absorbed by the affected polymer powder causing it to soften and fuse with the neighboring particles within the affected zone. The build plate then lowers, and a fresh layer of polymer powder is moved on top of the previous layer. The unaffected polymer powder remains as support material for the next layers and can be recycled into future prints. This process is repeated until the entire object is constructed. Due to the high temperatures that can be reached in PBF, engineering and high-performance thermoplastics are the preferred build materials. There are many considerations in this printing method including the polymer powder's thermal, rheological, chemical, and morphological properties and printing parameters such as laser raster speed, atmosphere, and environmental temperature which can strongly dictate the resolution, density, mechanical properties, and porosity of the final part.[10]

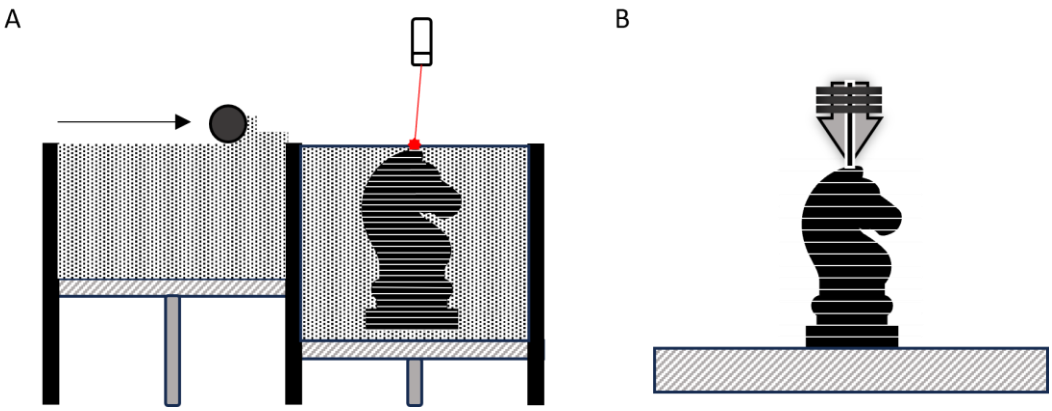

Figure 2.4. *A) Schematic of the PBF process B) Schematic of a generic MEX process.*

The other 3DP method that uses a softening approach is MEX. MEX methods are the most common method of 3DP. In MEX, material is extruded onto a build platform from a nozzle or orifice that acts as the print head (Figure 2.4 B). The print head or build plate, dependent on print mechanical mechanism, is then moved to facilitate the extrusion of material on top of the previous layer[10]. MEX methods can be quite diverse, as the stimuli that enables softening can vary dramatically depending on the build material. Comon stimuli are temperature or pressure. Build materials for this type of 3DP are commonly thermoplastics, colloids, or suspensions. A more in-depth look into two types of 3DP used in this thesis, fused filament fabrication (FFF) and direct ink write (DIW), will be examined in the next section of this chapter.

Forming the final polymer material in an in-situ 3DP process is also a common approach. To do this, a liquid precursor mixture is formed that reacts with a stimulus to evoke a phase change in the material. This change is usually driven by photopolymerization. In MJT, this liquid precursor material, or ink, is jetted onto the build surface (Figure 2.5A). This is often accomplished using piezoelectric actuators to rapidly dispense the microdroplets of ink onto the build surface.[10] This requires the ink be a low viscosity liquid (<20 cP) and have suitable surface tension so that it can keep its shape after jetting.[10] Upon dispensing, a UV light sweeps over the build surface, curing the material and locking it into place. Typically, the solidification process is aided by kinetics and solidification induced by forming a crosslinked thermoset network. The build plate then lowers making room for the next layer to be built on top of the previous one.

Unfortunately, the stringent material requirements hinder the performance of the material currently available using this technique. Despite this, MJT currently enables the highest level of multimaterial control of any 3DP method.

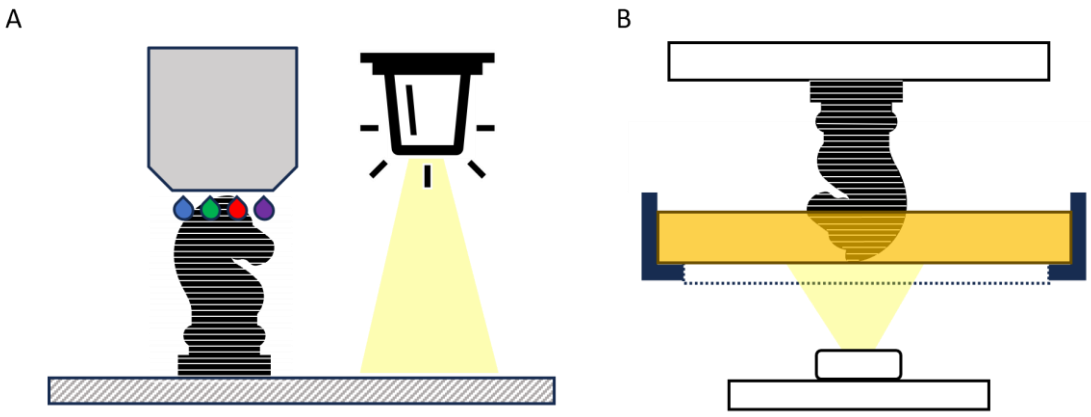

Figure 2.5. *A) Schematic of the MJT process B) Schematic of the DLP VP process.*

VP also uses a liquid precursor material, commonly referred to as photoresins, and stimuli induced phase change to form the final part. In this case, light is used as the stimulus to pattern a vat of liquid photoresin into a solid part.[12] While there are now volumetric approaches, allowing entire objects to be materialized simultaneously,[13,14] we will focus on digital light processing (DLP) VP which is a layer-by-layer process. In this process, patterned light from a projector travels through a transparent window into a vat of photosensitive resin (Figure 2.5B). Upon light exposure, the resin polymerizes causing a transition from liquid to solid and confined to regions exposed to light. The build platform is then moved an incremental amount allowing fresh resin to be polymerized forming the next layer of solid material joined to the previously solidified layer. Typical resins are composed of acrylate or epoxy monomers, crosslinking species, and a photoinitiator. While the chemistry is similar to MJT, the viscosity constraints are less stringent with up to ~5000 cP achievable. Additionally, the resolution and feature sizes can be extremely small with VP methods such as two photon polymerization approaching sub-micron features.[10,12] This opens a larger design space which can result in functional materials. Additionally, this technique yields high complexity with minimal support.

Deeper Dive into Material Extrusion

FFF and DIW are the two types of MEX 3DP methods used throughout this work. While both methods involve the extrusion of material out of a nozzle, the mechanisms, and physical phenomena behind each are distinct.

In FFF, thermoplastic polymers that have been formed into long filaments are fed into the print head, softened by application of heat, and extruded from the print head. This leverages the two thermal transitions seen in semicrystalline thermoplastic polymer materials: the glass transition temperature (T_g) and the melt temperature (T_m). The T_g is often considered a second order phase transition associated with molecular mobility and the glassy/ amorphous state. The T_g is not a thermodynamic property but kinetic in nature and can showcase a range of values depending on many molecular and processing factors.[15] Importantly, above this temperature, the polymer exhibits a softening associated with faster timescales of relaxation. The T_m is a first order phase transition and thermodynamic parameter associated with the crystalline domains of a polymer. A polymer's ability to crystallize is dependent on the packability of the polymer chains related to its microstructure (e.g. tacticity). Not all polymers can form crystalline domains, but those that do will showcase a T_m and transition from a viscoelastic solid to a viscoelastic liquid with heating which comes with a substantial drop in viscosity. Importantly, both thermal transitions are reversible with temperature. A common technique for determining these transitions is differential scanning calorimetry (DSC) which is a thermoanalytic technique for measuring the amount of energy to raise or lower the temperature of a material. During phase transitions, excess energy is either required or released, resulting in clear indicators in the DSC curve (Figure 2.6A). Notably both T_g and T_m are endothermic transitions with distinct indicators enabling us to identify these transitions. Dynamic mechanical analysis (DMA) can also be used to determine the phase transition temperatures by monitoring changes in mechanical properties with increasing temperature (Figure 2.6B).

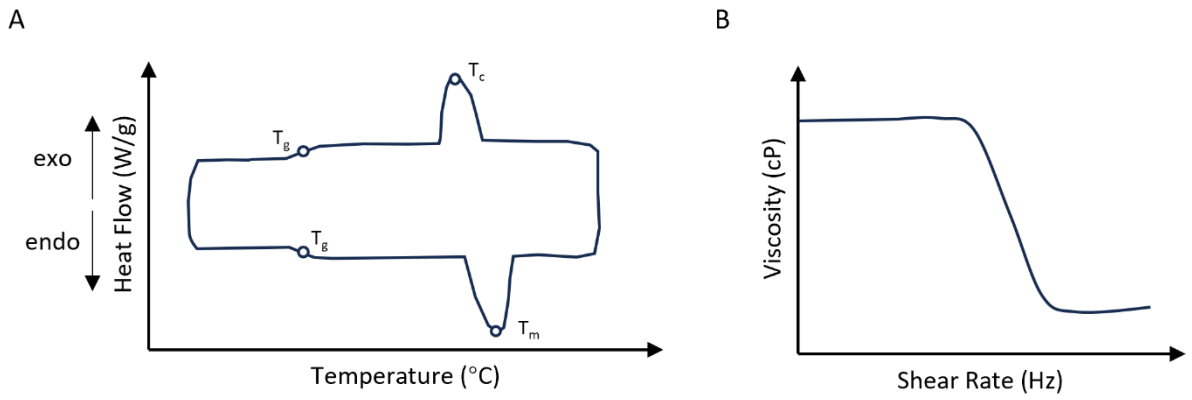

Figure 2.6. *A) Example of a standard DSC trace for a semicrystalline materials with different phase transitions labeled including the T_g, T_m, and crystallization temperature (Tc). B) Example rheology measurement for a shear thinning fluid where a sharp decrease in viscosity occurs at a given shear rate.*

In FFF, the thermoplastic build material must be brought above its T_g for entirely amorphous thermoplastics or T_m for semicrystalline thermoplastics. Besides these thermal transition considerations, the temperature chosen will dictate the degree to which a polymer will flow and the success in being extruded from the nozzle. For this reason, many high-performance polymers and engineering plastics have high melt viscosities and are challenging to print in MEX.[16] To facilitate the heating of the polymer the hot end print head is designed to have a hot zone, a transition zone, and a cool zone which facilitates controlled softening and dispensing. The location of the print head is dictated during extrusion which can impart anisotropic properties and functionality through the shear induced alignment of polymers or additives within the thermoplastic materials.[17] Upon extrusion, the thermoplastic rapidly cools to the ambient environmental temperature and solidifies. This allows the next layer of material to then be dispensed on top of it where it can fuse to the previous layer. Adhesion between layers can significantly affect the performance of the final part.[10] The resulting resolution of this technique is dictated by nozzle size which can be limited to factors such as additive size or viscosity of the softened thermoplastic build material which will dictate the pressure required for extrusion. However, this is typically in the range of 100s of μm.

In DIW, pressure is used to induce extrusion of carefully designed inks. The inks are typically polymer melts, colloids, or stable suspensions designed to exhibit non-Newtonian rheological properties.[18,19] Shear

thinning, also called a Bingham plastic, is typically the most desirable material behavior. This can be expressed through a power law model relating the shear rate to the viscosity of the complex fluid (Eq 2.1),

$$\eta(\dot{\gamma}) = K\dot{\gamma}^{n-1} \quad \text{Eq 2.1}$$

where $\eta(\dot{\gamma})$ is the shear rate dependent viscosity, $\dot{\gamma}$ is the shear rate, K is the consistency index, and n is the power index. K and n can be obtained through fitting experimental data. Typically, shear thinning behavior is required where increases in shear rate leads to decreases in the viscosity of the material ($0 < n < 1$). This enables the fluid to readily flow with applied shear stress from the nozzle and regain its solid like behavior when shear is removed[18]. The fluid must also be able to structurally support layers built on top of it. This is typically aided by either the addition of yield stress behavior (whereby the fluid behaves as a solid up until a certain shear rate) or is locked into place via an additional stimulus.[19] This is often done through heating, evaporation, or gelation to induce phase change.

The resolution of DIW is also dictated by nozzle size which is chosen based on the rheology of the ink and the required pressures to induce flow. A model that describes the extrusion of a power law fluid out of a cylindrical nozzle is shown in Eq 2.2.[20]

$$\Delta P = 2KL_1R_1^{-(3n+1)}\left(Q\frac{3n+1}{\pi n}\right)^n \quad \text{Eq 2.2}$$

In this equation, ΔP is the pressure drop required to extrude a power law fluid described by K and n through a cylindrical nozzle of a given length (L_1) and radius (R_1) at a certain flow rate (Q). In this relationship, the pressure drop required to extrude at a given flow rate is related to the nozzle length, radius, and processing flow rate which limit the size of nozzle and extrusion rates possible for a given ink based on the pressures attainable by the printing system.

Deeper Dive into Vat Photopolymerization

VP is accomplished through light induced curing driven by photopolymerization. Understanding this reaction is key to understanding the VP process. Central to this reaction is light which becomes an important

aspect of this thesis. Light is a form of electromagnetic radiation that exhibits both particle and wave like behavior (Figure 2.7). Our ability to tune these properties makes light an excellent stimulus. For example, light can be spatially controlled via projectors or lasers allowing fine control over features. Additionally, the energy of light can be tuned by varying the wavelength (or frequency) of the radiation. Furthermore, the intensity of light can be controlled through focusing or increasing the power of the light source. Importantly, light can be used to mediate wavelength selective chemical transformations.[21,22]

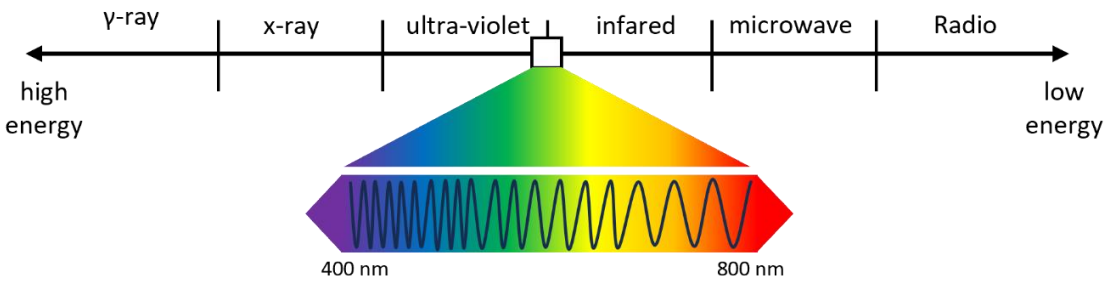

Figure 2.7. *Diagram showing the full spectrum of light including the small portion visible to humans.*

VP most commonly utilizes free-radical mediated photopolymerizations of acrylates to form 3D structures.[12] This is a chain growth polymerization and as such follows the three main polymerization steps (Scheme 2.1). First, irradiation with light results in the generation of a radical species from a photoinitiator. These photoinitiators are classified as Norrish Type I or Norrish Type II.[12,23] Type I photoinitiators cleave when irradiated with an appropriate wavelength of light to directly form radical species. Type II photoinitiators are multicomponent systems consisting of a light absorbing molecule (typically a dye or sensitizer) and a co-initiator (typically a tertiary amine). Upon irradiation, the light absorbing molecule transitions into an excited state where they can undergo hydrogen abstraction or energy transfer with the initiator to form the active radical toward polymerization. Developing novel photoinitiators with lower toxicity and higher absorption wavelength is an active area of research.[12] The active radicals from type I or II processes can react with acrylate monomers in the propagation step to form the resulting polymers before being terminated either from disproportionation, combination, or by oxygen inhibition.

Scheme 1. *Initiation, propagation, and termination mechanisms for the free radical polymerization of acrylate. Both a Norrish Type I and Type II mechanism are shown in addition to the three common termination mechanisms.*

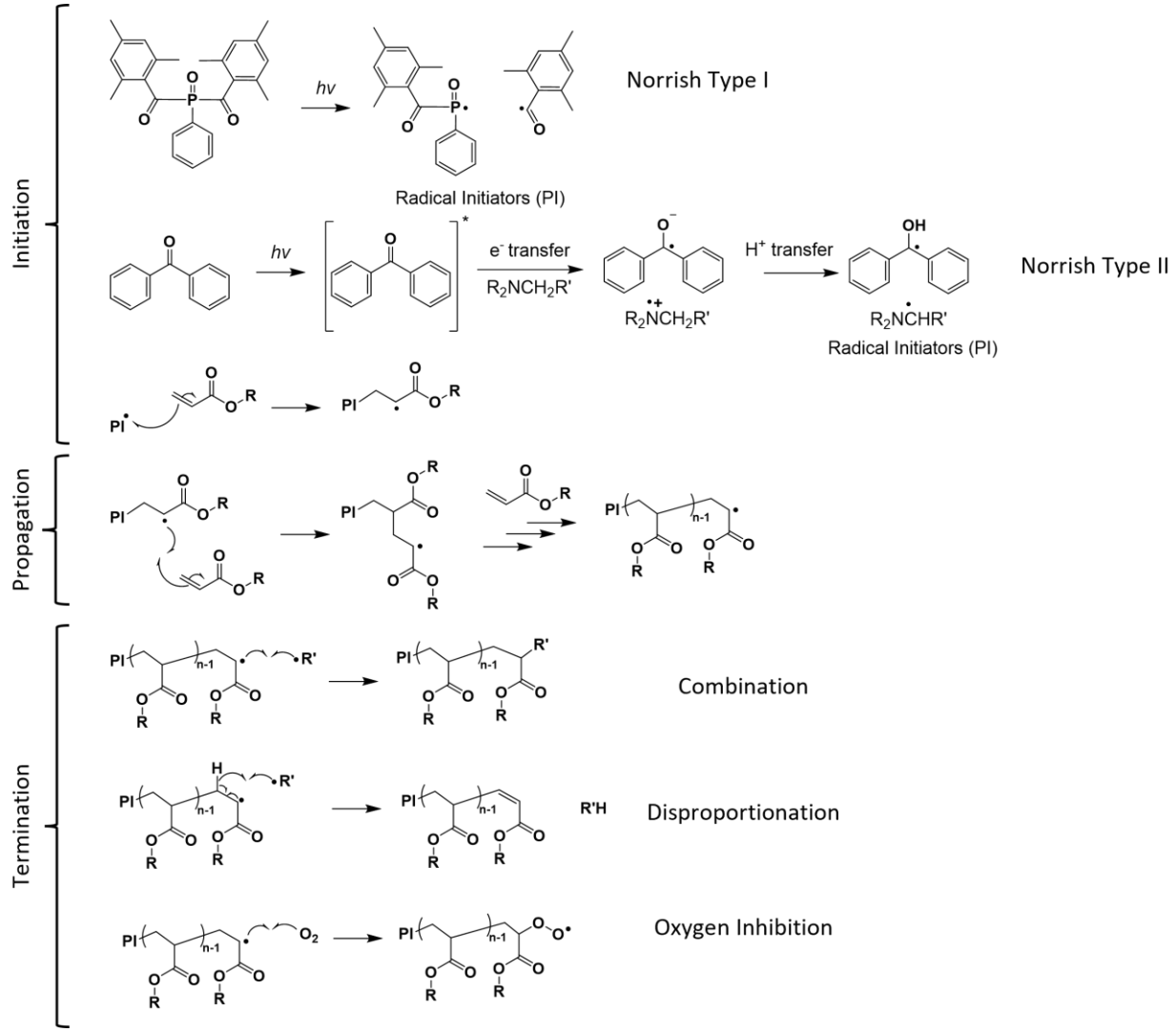

Cationic photopolymerizations are also used in VP processes and are commonly implemented to make materials from the ring-opening polymerization (ROP) of epoxides.[10,12] This is valuable as epoxide monomers have low volumetric shrinkage compared to acrylate monomers and can make materials with good chemical resistance and mechanical properties. Cationic photopolymerization also follows a chain growth mechanism whereby the active species is now a cation (Scheme 2.2). This requires a new initiation method using acid as the initiating species. To make cationic ROP of epoxides suitable for VP, photoacid generators (PAGs) are employed as the photoinitiators to enable the reaction to be light activated. Common

PAGs are onium salts such as iodonium and sulfonium cations with bulky non nucleophilic anions such as hexafluoroantimonate, hexafluorophosphate, tetrafluoroborate.[24] The cations play the role of the light active species while the anions dictate the acid strength. Under the appropriate UV irradiation, onium salts undergo photolysis resulting in the creation of a Brønsted acid. In the case of epoxides, this acid associates with the oxygen contained within the ring and forms an oxonium ion. The oxonium ion is a better leaving group and so upon nucleophilic attack of another epoxide to a carbon adjacent to the oxonium ion the ring opens, leaving an activated chain end ready to propagate with other monomers in solution.[25] Notably, epoxide polymerizations are typically slower than acrylate polymerizations due to their living characteristics, limiting their use in VP.[10] For this reason, hybrid resins consisting of epoxides and acrylates can be advantageous, combining the fast cure times exhibited by acrylates and the low volumetric shrinkage exhibited from epoxides.

Scheme 2.2. *Cationic ROP of epoxides is shown with mechanisms for iodonium and sulfonium salt PAGs.*

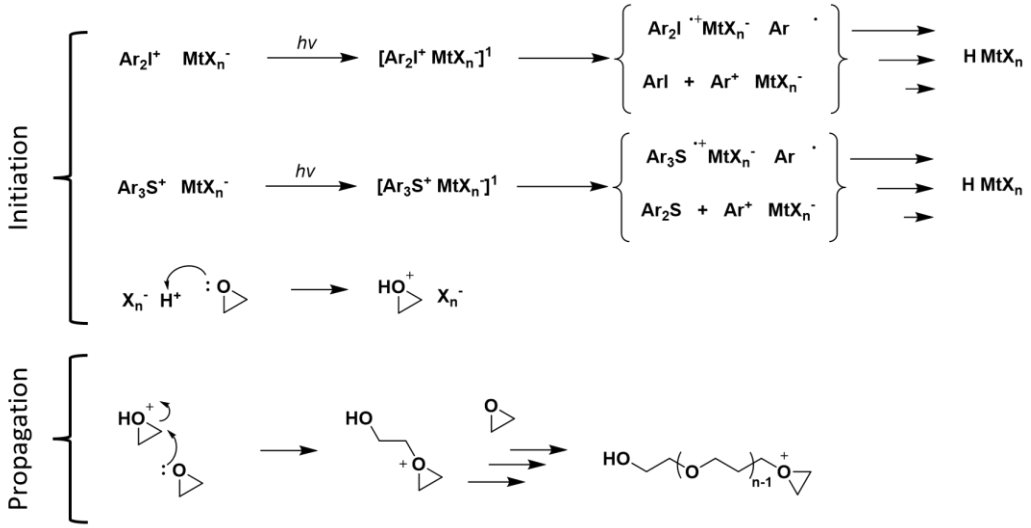

VP photoresins typically consist of a mixture of monomer diluent, oligomer, crosslinker, and photoinitiator. However, other components can also be added to instill desired properties and improve resolutions. Generally, the monomer diluent mixture ensures that the resin remains a suitable viscosity while also contributing, along with the oligomers, to the final properties of the printed materials. Crosslinker is typically added to aid in the curing of a material by facilitating rapid transition from liquid to robust solid.

This is important as rapid solidification is needed to ensure short print times and to limit diffusion of reactive groups away from the intended cure area. This typically means that materials printed with VP will be thermosets. Excessive crosslinking can lead to brittle materials and so a balancing crosslinker and other components is important to maintain ability to be printed and final properties. Lastly, the photoinitiator is needed to make the mixture react with spatial control. Choice of photoinitiator will dictate the wavelength of light needed for printing and the amount can also contribute to curing kinetics due to creating more active chains.

Notably, light absorption, curing kinetics, and gelling all play significant roles in a photoresin's ability to be printed in VP. These are all transient processes throughout curing and their interplay can be quite complex. However, a simplified method was developed for determining a resin's printing characteristics called a working curve where a critical exposure (E_c) and a penetration depth (D_p) is determined.[26] To construct a working curve, resin is cured with the printing light source for incremental amounts of time and the thickness of the cured material, the cure depth (C_d), measured. Eq 2.3 is used to relate the exposure (E_{max}) to the C_d which is linear on a log scale.

$$C_d = D_p \ln \frac{E_{max}}{E_c} \qquad \text{Eq 2.3}$$

The x-intercept and the slope of the line yields E_c and D_p, respectively. E_c represents the critical dose of light needed to reach gelation while D_p relates thickness of a given layer for a given exposure. Low E_c values indicate the resin can print rapidly while a low D_p indicates thin layers can be printed. This simple test reveals important characteristics of the photoresin including optimal exposure times for a given layer thickness and is often used to determine optimal print settings.

References

1. History of Europe - Prestige and status | Britannica. https://www.britannica.com/topic/history-of-Europe/Prestige-and-status.
2. Materials that Changed History | School of Materials Science and Engineering. http://www.materials.unsw.edu.au/materials-changed-history.
3. Staudinger, H. Über Polymerisation. *Berichte der Dtsch. Chem. Gesellschaft (A B Ser.* **53**, 1073–1085 (1920).
4. Namazi, H. Polymers in our daily life. *BioImpacts* vol. 7 73–74 (2017).
5. Fundamental Principles of Polymeric Materials, 3rd Edition | Wiley. https://www.wiley.com/en-us/Fundamental+Principles+of+Polymeric+Materials%2C+3rd+Edition-p-9780470505427.
6. Rhodes, C. J. Plastic pollution and potential solutions. *Science progress* vol. 101 207–260 (2018).
7. Law, K. L. Plastics in the Marine Environment. *Annual Review of Marine Science* vol. 9 205–229 (2017).
8. Plastic Pollution - Our World in Data. https://ourworldindata.org/plastic-pollution?utm_source=newsletter.
9. Cressey, D. Bottles, bags, ropes and toothbrushes: The struggle to track ocean plastics. *Nature* **536**, 263–265 (2016).
10. Ligon, S. C., Liska, R., Stampfl, J., Gurr, M. & Mülhaupt, R. Polymers for 3D Printing and Customized Additive Manufacturing. *Chem. Rev.* **117**, 10212–10290 (2017).
11. Ngo, T. D., Kashani, A., Imbalzano, G., Nguyen, K. T. Q. & Hui, D. Additive manufacturing (3D printing): A review of materials, methods, applications and challenges. *Compos. Part B Eng.* **143**, 172–196 (2018).
12. Bagheri, A. & Jin, J. Photopolymerization in 3D Printing. (2019) doi:10.1021/acsapm.8b00165.
13. Kelly, B. *et al.* Computed Axial Lithography (CAL): Toward Single Step 3D Printing of Arbitrary Geometries. (2017).
14. Regehly, M. *et al.* Xolography for linear volumetric 3D printing. *Nature* **588**, 620–624 (2020).
15. Hiemenz, P. C. & Lodge, T. Polymer chemistry (2nd edition). 587 (2007).
16. Das, A. *et al.* Current understanding and challenges in high temperature additive manufacturing of engineering thermoplastic polymers. *Addit. Manuf.* **34**, 101218 (2020).
17. Parandoush, P. & Lin, D. A review on additive manufacturing of polymer-fiber composites. *Compos. Struct.* **182**, 36–53 (2017).
18. Lewis, J. A. Direct Ink Writing of 3D Functional Materials**. (2006) doi:10.1002/adfm.200600434.
19. Rau, D. A., Bortner, M. J. & Williams, C. B. A rheology roadmap for evaluating the printability of material extrusion inks. *Addit. Manuf.* **75**, 103745 (2023).
20. Lenk, R. S. Rheology and Die Design. *Dev. Plast. Technol.* 229–279 (1982) doi:10.1007/978-94-009-6622-2_6.
21. Ehrmann, K. & Barner-Kowollik, C. Colorful 3D Printing: A Critical Feasibility Analysis of Multi-

Wavelength Additive Manufacturing. *J. Am. Chem. Soc.* **145**, 46 (2023).

22. Lu, P. *et al.* Wavelength-selective light-matter interactions in polymer science. *Matter* **4**, 2172–2229 (2021).

23. Ahn, D., Stevens, L. M., Zhou, K. & Page, Z. A. Rapid High-Resolution Visible Light 3D Printing. doi:10.1021/acscentsci.0c00929.

24. Crivello, J. V. The Discovery and Development of Onium Salt Cationic Photoinitiators. *J Polym Sci A Polym Chem* **37**, 4241–4254 (1999).

25. Herzberger, J. *et al.* Polymerization of ethylene oxide, propylene oxide, and other alkylene oxides: Synthesis, novel polymer architectures, and bioconjugation. *Chem. Rev.* **116**, 2170–2243 (2016).

26. Jacobs, P. F., Reid, D. T., Computer & of SME., A. S. A. *Rapid Prototyping \& Manufacturing: Fundamentals of Stereolithography*. (Society of Manufacturing Engineers, 1992).

Chapter 3: A Research Perspective on Polymer 3D Printing

Designing novel functional materials is a difficult task requiring an understanding of the intricate interplay between structure, property, and processing on material performance (Figure 3.1A).[1] Material scientists seek to control the structure of a material across length scales using fundamental understanding of phenomena from many fields to develop innovative materials for future technologies. Many material scientists have turned to 3DP as a pivotal technology to provide the fine control needed to create next generation technologies due to its ability to tailor molecular to macro scale order within a material through a bottom-up approach to material design.[2–5] While there have been significant strides in 3DP of functional materials[4] and complex architectures[6,7] there are still significant contributions to be made in expanding the utility of 3DP. This thesis will explore 3DP as a manufacturing technique focusing on enhancing specific properties of polymeric materials for 3DP.

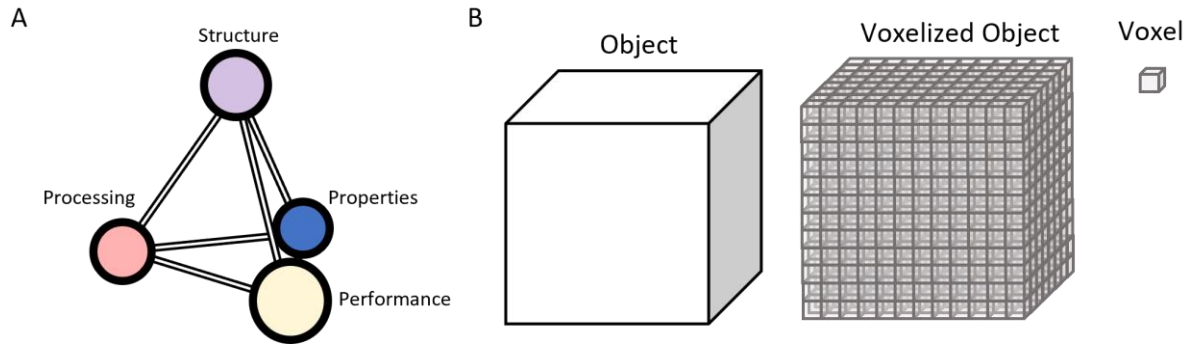

Figure 3.1. *A) Schematic showing the tenants of material science and their interconnections B) Diagram of the deconstruction of an object into individual voxels*

This chapter will provide a research perspective on some of the existing material challenges in 3DP of polymeric materials. Specifically, it will introduce a bigger picture of existing challenges in using polymeric materials for 3DP. A description of some of the desirable properties found in nature will serve to demonstrate how control over multiple length scales can be valuable. I will then discuss instilling properties not readily seen in nature through precise structural control of objects.

3DP provides placement of molecular level building blocks into precise locations. By designing the chemistry of each material discrete volumes, called a voxel, can be manipulated with high levels of control

(Figure 3.1B). By prescribing micro and mesoscale order through processing, kinetic, or thermodynamic driven assembly, and controlling macroscopic material placement using 3DP, materials can be designed from the bottom-up (Figure 3.2A). This provides opportunities for unparalleled geometric complexity and precise chemical control, enabling the formation of materials previously unattainable by traditional manufacturing approaches.

Nature has undergone billions of years of refinement to develop remarkable materials with advantageous traits.[2,8] By understanding the mechanism behind these remarkable materials we can better replicate their arrangement and ultimately their function. The synthesis of many biomaterials occurs over long-time scales and requires a bottom-up process which makes replication difficult using traditional subtractive and formative manufacturing methods. However, the layered methodology introduced by 3DP provides a promising method to emulate and accelerate the bottom-up process.

Materials like butterfly wings,[9] peacock feathers,[10] and chameleon skin[11] use nanostructures to create their unique colors. Additionally, natural structural materials such as wood, bone, and nacre have mechanical properties that can rival those of the best currently available synthetic materials.[8,12] Importantly, many of these materials are comprised of simple chemical compounds arranged in hierarchical structures that yield their remarkable properties such as photonics, strength, durability, and stimuli responsiveness.[12]

Bone is a material that has many characteristics we hope to replicate such as excellent mechanical properties[8] and the ability to self-reinforce and heal itself.[13] Bone is an example of a material with a complex hierarchical structure that uses multiple mechanisms to mitigate fracture and transport compounds throughout its matrix.[8]

At the molecular level, bone is primarily made up of two major components that make up 95% of the dry weight of bone: collagen (an organic polymer) and hydroxyapatite nanocrystals (an inorganic component). The collagen molecules are comprised of amino acid sequences that preferentially form a triple helix. The hydroxyapatite nanocrystals are periodically distributed along the oriented collagen making mineralized

fibers. These mineralized fibers arrange themselves into collagen fibrils which form into lamellar structure, called osteons, that surround blood vessels (important for maintaining transport throughout the body). All these features contribute to the macroscopic structure of bone which has a compact layer near the surface and a porous marrow filled layer in the interior. As seen in Figure 3.2B, the ordering of the structural components span molecular through macroscopic regimes and provide insight into valuable material motifs such as gradient porosity, precision multimaterial objects, and complex structuring which ultimately enable the unique properties of bone.

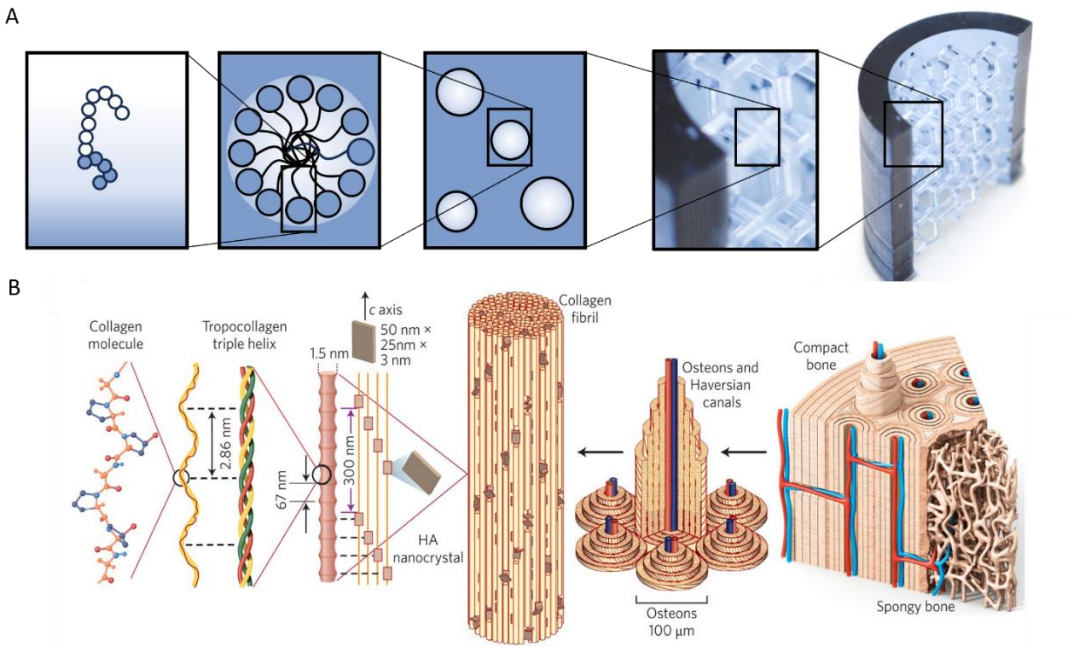

Figure 3.2. *A) Breakdown of 3D printing's potential to design materials from the bottom-up starting at the molecular level through the macroscopic. B) Structure of bone showing hierarchical structure starting at the molecular level (Reprinted with permission from ref 8).*

This hierarchical ordering in bone illustrates the complexity and fine control desired within 3D printed architectures. However, achieving this is quite challenging even with 3DP's precision since the length scales involved go beyond the resolution of current 3DP technology. To accomplish this, innovation in 3DP hardware to accommodate multimaterial structures and chemistry to garner unique reactivity and control over molecular, nano, and meso scale will be required. Throughout this thesis, better control over these

aspects will be presented using novel chemical means, through hardware, or a synergetic combination of both.

We can also induce properties not readily observed. To do this, researchers must think beyond the chemistry of a material and toward object geometry.[7,14,15] A simple example of this is changes in aspect ratio which can make a stiff material flexible and vice versa (a result of the scaling relationship between bending v compressive energy contributions).[16] Metamaterials are one way geometry is leveraged.[17] Metamaterials are materials that exhibit properties not seen in natural materials such as negative Poisson ratio, negative coefficients of thermal expansion, and waveguiding phenomena.[15,18] Often, their unique properties are derived from the structure of a material in combination with the intrinsic chemistry of its matrix but can also be material ambivalent. These remarkable materials are being studied more and more as their ability to be created has expanded in part due to 3DP. Discussions of specific geometry induced properties are contained in chapters 10 and 11.

Throughout this thesis, I will give many examples of how we are using 3D printing to enable emerging properties that can someday get us closer to the fine control provided in nature as well as instill useful properties not observed in nature. The thesis will be arranged in four parts. Each part will focus on a grouping of projects. Part one will describe three investigations where materials were designed from the bottom-up to achieve improved sustainability, toughness, and stimuli responsiveness. Part two will highlight creating two novel 3DP techniques for enhanced chemical control over polymeric build materials. Part three will explain efforts at expanding the chemistry behind dual wavelength vat photopolymerization (DW-VP) to gain control over novel material properties. Lastly, part four will describe using 3DP for fine geometric control toward bistable mechanical metamaterials and graded lattices for energy absorption applications. Hopefully by the end of the thesis, a better understanding of the challenges that exist when trying to achieve such structural control and will be evident as well as my contribution to this effort.

References

1. Callister, W. D. & Rethwisch, D. G. *Materials Science and Engineering: An Introduction*. (Wiley, 2013).

2. Du Plessis, A. *et al.* Beautiful and Functional: A Review of Biomimetic Design in Additive Manufacturing. (2019) doi:10.1016/j.addma.2019.03.033.

3. Saroia, J. *et al.* A review on 3D printed matrix polymer composites: its potential and future challenges. *Int. J. Adv. Manuf. Technol.* **106**, 1695–1721 (2020).

4. Valino, A. D. *et al.* Advances in 3D printing of thermoplastic polymer composites and nanocomposites. *Prog. Polym. Sci.* **98**, 101162 (2019).

5. Ngo, T. D., Kashani, A., Imbalzano, G., Nguyen, K. T. Q. & Hui, D. Additive manufacturing (3D printing): A review of materials, methods, applications and challenges. *Composites Part B: Engineering* vol. 143 172–196 (2018).

6. Schaedler, T. A. & Carter, W. B. Architected cellular materials. *Annu Rev Mater Res* **46**, 187–210 (2016).

7. Feng, J., Fu, J., Lin, Z., Shang, C. & Li, B. A review of the design methods of complex topology structures for 3D printing. *Vis. Comput. Ind. Biomed. Art* **1**, 1–16 (2018).

8. Wegst, U. G. K., Bai, H., Saiz, E., Tomsia, A. P. & Ritchie, R. O. Bioinspired structural materials. *Nat. Mater.* **14**, 23–36 (2015).

9. Wilts, B. D., Matsushita, A., Arikawa, K. & Stavenga, D. G. Spectrally tuned structural and pigmentary coloration of birdwing butterfly wing scales. *J. R. Soc. Interface* **12**, (2015).

10. Zi, J. *et al.* Coloration strategies in peacock feathers. *Proc. Natl. Acad. Sci. U. S. A.* **100**, 12576–12578 (2003).

11. Teyssier, J., Saenko, S. V., Van Der Marel, D. & Milinkovitch, M. C. Photonic crystals cause active colour change in chameleons. *Nat. Commun. 2015 61* **6**, 1–7 (2015).

12. Nepal, D. *et al.* Hierarchically structured bioinspired nanocomposites. *Nat. Mater. 2022 221* **22**, 18–35 (2022).

13. Bigham-Sadegh, A. & Oryan, A. Basic concepts regarding fracture healing and the current options and future directions in managing bone fractures. *Int. Wound J.* **12**, 238 (2015).

14. Sharon, E. & Efrati, E. The mechanics of non-Euclidean plates. *Soft Matter* **6**, 5693–5704 (2010).

15. Jiao, P., Mueller, J., Raney, J. R., Zheng, X. (Rayne) & Alavi, A. H. Mechanical metamaterials and beyond. *Nat. Commun. 2023 141* **14**, 1–17 (2023).

16. van Manen, T., Janbaz, S. & Zadpoor, A. A. Programming the shape-shifting of flat soft matter. *Mater. Today* **21**, 144–163 (2018).

17. Kadic, M., Milton, G. W., van Hecke, M. & Wegener, M. 3D metamaterials. *Nature Reviews Physics* vol. 1 198–210 (2019).

18. Liu, R., Ji, C., Zhao, Z. & Zhou, T. Metamaterials: Reshape and Rethink. *Engineering* **1**, 179–184 (2015).

Part One

Designing Materials from the Bottom-Up

Chapter 4: Vat 3D Printing of Bioderivable Photoresins − Toward Sustainable and Robust Thermoplastic Parts

Reprinted (adapted) with permission from:

Chin, K. C. H., Cui, J., O'Dea, R. M., Epps, T. H. & Boydston, A. J. Vat 3D Printing of Bioderivable Photoresins – Toward Sustainable and Robust Thermoplastic Parts. *ACS Sustain. Chem. Eng.* **11**, 1867–1874 (2023).

Abstract

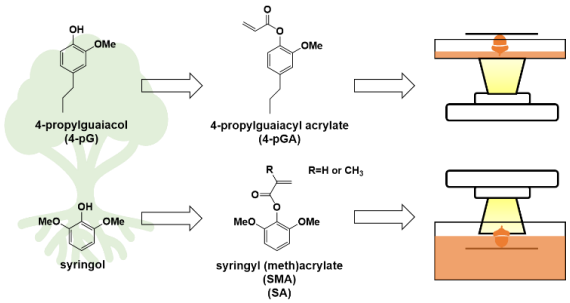

Vat photopolymerization 3D printing (3DP) of thermoplastic materials is exceedingly difficult due to the typical reliance on cross-linking to form well-defined, solid objects on timescales relevant to 3DP. Additionally, photoresin build materials overwhelmingly rely upon nonrenewable feedstocks. To address these challenges, we report the vat 3DP of bioderivable photoresins that produced thermoplastic parts with highly tunable thermal and mechanical properties. The photoresins were formulated from two monomers that are easily obtainable from lignin deconstruction: 4- propylguaiacyl acrylate (4-pGA) and syringyl methacrylate (SMA). These bioderivable materials generated printed parts that ranged from soft elastomers to rigid plastics. For example, for 4-pGA-based materials, the breaking stresses varied from 0.20 to 20 MPa and breaking strains could be tuned from 4.7% up to 1700%, whereas 3D-printed SMA-based materials resulted in higher breaking stresses (~30 MPa) and T_gs (~132 °C). Notably, parts printed from these bioderivable formulations exhibited thermoplastic behavior and were largely soluble in common organic solvents—expanding the application and repurposing of the 3D-printed parts. We highlight this feature by reusing a 3DP part via solvent casting. Overall, the tunable properties and thermoplastic behavior of the lignin-derivable photoresins showcase renewable lignin resources as promising biofeedstocks for sustainable 3DP.

Introduction

Using 3D printing (3DP) technologies, objects can be efficiently constructed from digital models, affording increased flexibility in design and functionality. 3DP has found broad application in medical devices,[1,2] transportation,[3] electronics,[4] robotics,[5–7] and other fields.[8,9] Among the different 3DP techniques, vat photopolymerization builds solid 3D objects through patterned layer-by-layer curing of a liquid photoresin.[10] These patterns are created from light delivered *via* either 2D projections or rastering lasers.[10] Objects also can be constructed volumetrically by projecting a directed light dosage into the resin.[11,12] The advantages of vat photopolymerization include high feature resolution, comparatively fast print times, and direct access to overhangs and hollow voids without supports.[10]

Vat photopolymerization resins typically consists of a monofunctional monomer, a multifunctional monomer, and a photoinitiation system.[10,13–15] Although these are the base components, more complex resins can include fillers, additives, and dyes that enhance the properties or resolution of the printed parts.[10] Because the macromolecular scaffold is created from precursor monomer during the photocuring process, the resin components must have high polymerization rates, and often, crosslinking is required to reach rapid gelation at low conversions. Hence, the vast majority of photoresin monomers comprise acrylate and methacrylate functionalities because their rapid cure times reduce the amount of crosslinker needed to produce quality parts. Additionally, the need for low viscosity resins precludes the use of viscous components, such as oligomers, that could aid in forming fixity and improve the final properties of printed parts.[10] The above constraints typically result in networks that exhibit inferior mechanical and thermal properties in comparison to commodity and high-performance plastics polymerized *via* conventional techniques (*e.g.*, bulk or solution free-radical, controlled-radical, or ionic polymerization).[10,16] Thus, photoresin systems that can produce parts using 3DP techniques without compromising the thermal and mechanical properties of the materials are highly desirable.

Sustainability also is a key metric for printable resin formulations; however, most commercial monomers for vat photopolymerization 3DP are obtained from finite and non-renewable, petroleum-based chemicals.

Renewable alternatives could enhance materials sustainability.[17] One promising strategy for more environmentally friendly monomer sourcing is the deconstruction of lignocellulosic biomass, especially lignin.[18–22] Lignin is the second most abundant biopolymer behind cellulose and is reported to account for about 30% of the organic carbon in the biosphere,[23] making it an ideal candidate to replace petrochemical sources.

The molecular structure of lignin results in a highly crosslinked and amorphous aromatic network; however, despite its recalcitrant nature, lignin can be deconstructed to produce a variety of small molecule aromatic compounds that are useful as building blocks for new value-added chemicals, pharmaceuticals, fuels, and polymers.[18,24–26] Macromolecular products based on lignin-derived starting materials have already demonstrated performance-advantaged characteristics in various areas, such as the production of elastomers,[26,27] commodity plastics,[17] epoxy resins,[25,28,29] high-T_g (glass transition temperature) materials,[30,31] and pressure-sensitive adhesives (PSAs).[32]

Herein, we investigated the 3DP of lignin-derivable photoresin formulations using vat photopolymerization. Our monomer pool was selected from recent reports that highlighted acrylate-based monomers produced from feedstocks accessible through lignin deconstruction.[31,32] For example, the above-mentioned, high-performance PSAs were generated using 4-propylguiaicyl acrylate (4-pGA) as a key component, illustrating their potential use as robust elastomers.[32] As another example, attractive features of polymers synthesized from bio-derivable syringyl methacrylate (SMA) include high T_gs (205 °C) that exceed those typically achievable with vat photopolymerization 3DP.[31] We therefore aimed to determine the extent to which vat photopolymerization 3DP could capture the attractive features offered by lignin-derived monomers.

Results and Discussion

3D printing of 4-pGA- and SMA-based resins

Motivated by previous work on lignin-derived (meth)acrylates, we selected 4-propylguaiacol (4-pG) and syringol as starting materials for our development of biobased 3DP resins.[31,32] We employed standard

synthetic manipulations to convert 4-pG to 4-pGA and syringol to SMA (Figure 1).[32] Our studies also made use of syringyl acrylate (SA), lauryl acrylate (LA), lauryl methacrylate (LMA), and Irgacure 819 (Irg 819) as depicted in Figure 4.1.

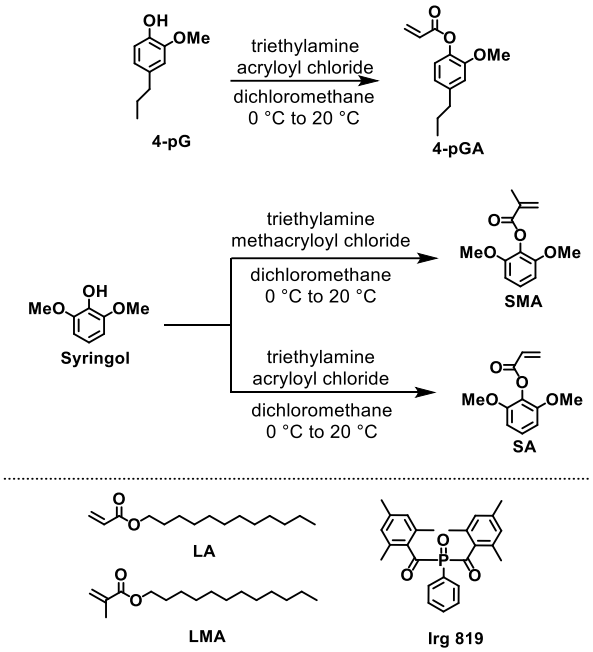

Figure 4.1. *Top) Route for conversion of 4-pG and syringol into 4-pGA, SMA, and SA monomers for 3DP. Bottom) Illustration of LA, LMA, and Irg 819 molecules, which are additional species used in this investigation.*

To gauge the general characteristics of the 4-pGA and SMA resins, we performed bulk curing screens of each monomer using Irg 819 as the photoinitiator. Each resin system yielded optically transparent materials (Figure 4.2, top). We found that homopolymerization of 4-pGA resulted in qualitatively stiff, brittle specimens. Thus, LA was incorporated as a comonomer to reduce brittleness, resulting in slightly tacky samples that could be stretched to high strains without breaking (Figure 4.2, middle). Post stretch, the samples took ~1 h to relax back to their original shape. In addition to imparting high flexibility to the printed parts, LA offers low volatility, and it can be produced from sustainable sources.[33,34] Homopolymerization of SMA also resulted in stiff, brittle specimens but had the benefit of producing high T_g samples (Figure 4.2, bottom).[31]

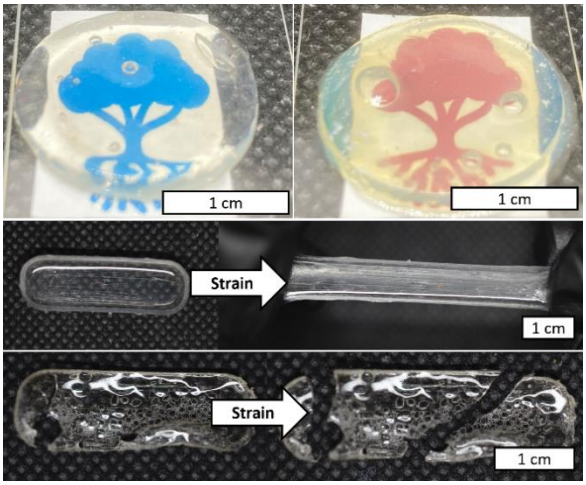

Figure 4.2. *Top) Cured drops of 4-pGA-3(left) and SMA-1 (right) resin. Middle) 4-pGA-3 resin cured into a rectangle and stretched to large strains. Bottom) SMA-1 resin cured into a rectangle. Sample broke upon stretching showing its stiff and brittle nature.*

Following the bulk curing experiments, we transitioned to vat photopolymerization 3DP. Photoresins with 4-pGA as the primary component were printed using a bottom-up printing setup (Figure A1). We found that the addition of 4-pG as an inhibitor was effective at suppressing overgrowth during printing, which offered a practical solution given that 4-pG was already part of the sustainable resin sourcing. Although SMA is a solid at room temperature, it has a melting point of 40 °C. Thus, we implemented a top-down printer configuration (images were projected from above the vat) that enabled heating of the resin vat in a water bath that was set to 40 °C (Figure A2). For prints using SMA as the main component, we again employed 4-pG as an inhibitor. Layer cure times for each resin were systematically determined by illuminating photoresins with sequentially longer light exposures until solid material remained after washing away any uncured material with isopropyl alcohol (Figure A3, Table A1). Using this approach, parts could be printed with good resolution (*i.e.*, small feature sizes) and complex geometries, such as voids and overhangs (Figure 4.3, Figure A4). While resolution varied depending on resin, in general, dimensional accuracy of 400 µm was achieved and features sizes as small as 500 µm were achieved (Figure A5).

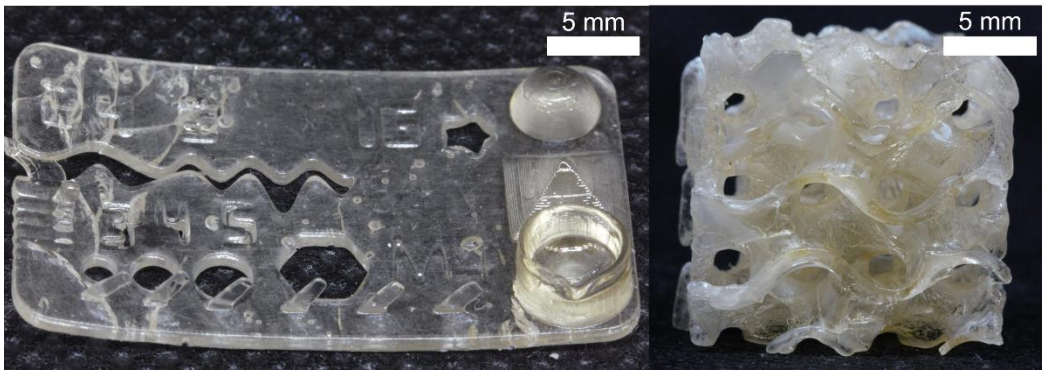

Figure 4.3. *Printed objects from SMA-3 resin. The left object illustrates the ability to achieve good resolution with small features. The right object is a complex lattice architecture that would be difficult to produce with non-additive techniques.*

Thermal and mechanical properties of parts produced from 4-pGA-based resins

Table 4.1. *Summarized compositions and thermal and mechanical properties for 4-pGA resins. The data shown for mechanical testing are the mean and standard deviation for five replicate experiments. Note: Of the five samples tested for 4-pGA-4, two broke, whereas the other three hit the maximum strain of the instrument (~2000%). In this case, the maximum strain and corresponding stress were used for calculations.*

Resin	4-pGA (wt %)[a]	LA (wt %)[a]	SA (wt %)[a]	Breaking strain (%)	Breaking stress (MPa)	Yield stress (MPa)	T_g (°C)	$T_{g,theo}$ (°C)[b]
4-pGA-1	91	9	0	220 ± 30	7.1 ± 0.6	10.1 ± 0.5	18	27
4-pGA-2	83	17	0	298 ± 9	4.4 ± 0.5	2.70	12	17
4-pGA-3	66	34	0	680 ± 30	1.53 ± 0.06	--	1	-1
4-pGA-4	50	50	0	1700 ± 100	0.20 ± 0.06	--	-15	-17
4-pGA-5	25	50	25	600 ± 30	1.4 ± 0.2	--	1	-6
4-pGA-6	60	10	30	4.7 ± 0.9	20± 2	--	38	43

[a]Weight percent of monomer component [*]All resins contained 0.04 wt % 4-pG as inhibitor and 0.2 wt % Irg 819 as photoinitiator relative to the total monomer weight. [b]Theoretical T_gs ($T_{g,theo}$) were determined from the Fox equation (Equation S1)with experimentally determined T_gs for 4-pGA and SA (38 and 113 °C, respectively) and the literature value of T_g for LA (-55 °C).

With printability confirmed, we focused on understanding the mechanical properties of the printed parts. We determined that the tensile mechanical properties can be tuned dramatically by changing the feed ratio of 4-pGA and LA (Figure 4.4A, Table 4.1). For example, 4-pGA-1 printed samples were rigid, yielded under tension, showed large plastic deformation (220%), and displayed strain hardening beyond the yield point. As the fraction of LA was systematically increased (cf. 4-pGA-1 through 4-pGA-4), the printed

specimens became more ductile, likely due to the long aliphatic sidechain of LA increasing chain mobility and free volume. The yield stress decreased across this series with concomitant increases in breaking strain. At higher loadings of LA (4-pGA-3 and 4-pGA-4), the stress-strain curves exhibited characteristics of a soft elastomer, with breaking strains reaching as high as 677% and 1700%, respectively. We also briefly investigated the influence of SA in the photoresin formulation. Adding SA offered an opportunity for fine-tuning of mechanical properties (Figure 4.4A, Table 4.2). In the case of soft elastomers (4-pGA-4), partial displacement of 4-pGA with SA (4-pGA-5) resulted in stiffer products with lower breaking strain. In the case of rigid materials (4-pGA-1), the addition of SA increased the breaking stress, albeit at the expense of ductility (4-pGA-6).

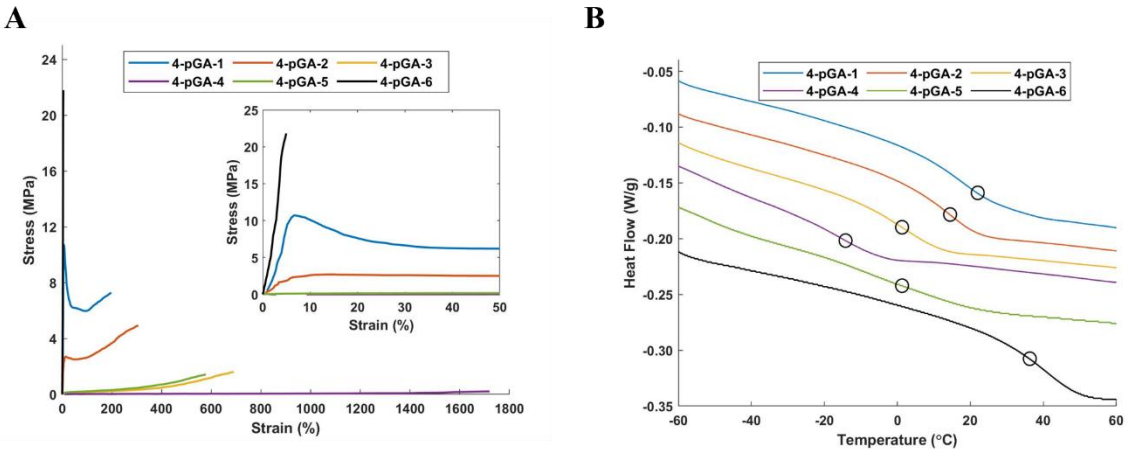

Figure 4.4 *A) Representative stress-strain curves of parts produced from 4-pGA-based resin formulations. Inset plot shows a zoomed-in section from 0 to 50 % strain. B) Representative differential scanning calorimetry (DSC) traces of the second heating cycle to illustrate the shift in T_g of parts produced from 4-pGA-based resins. T_g of each sample is circled. Curves are shifted vertically for clarity in panel B.*

The thermal properties of the printed 4-pGA-based parts were assessed by differential scanning calorimetry (DSC) (Figure 4.4B, Table 4.2). Monomers 4-pGA and SA were each homopolymerized *via* uncontrolled radical polymerization; the resulting polymers exhibited T_gs of 38 and 113 °C, respectively (Figure A6). Homopolymerization of LA produced a free-flowing polymer melt, indicating it would not be suitable for 3DP as a homopolymer. Poly(lauryl acrylate) has a reported T_g of -55 °C. [35] In general, the T_g of printed parts decreased with increasing amounts of LA with a range of -15 to 38 °C. In each case, we noted a single T_g, consistent with a homogenous, statistical distribution of comonomers (as opposed to block-like

microstructures). Additionally, the inclusion of SA at the expense of 4-pGA in the formulation increased the T_g (*e.g.*, 4-pGA-1 versus 4-pGA-6, 4-pGA-4 versus 4-pGA-5). These trends align with theoretical predictions of T_g for each resin compositions determined using the Fox equation (Table 4.1, Equation S1).[36] 4-pGA-1 and 4-pGA-6 were also characterized by dynamic mechanical analysis (DMA) to assess their thermomechanical properties (Figure A7**)**. No obvious rubbery plateaus were present in the temperature range measured (23 – 100 °C). For 4-pGA-1, the storage modulus began decreasing around the T_g, 18 °C, with a more extreme drop at approximately 40 °C. Replacing some 4-pGA with SA (4-pGA-6) shifted the corresponding transitions to 38 and 50 °C, respectively. The values measured by DMA were consistent with the T_g trends determined by DSC.

Thermal and mechanical properties of parts produced from SMA-based resins

Table 4.2. *Summary of mechanical properties under tension (SMA-1 post-cure 40 °C and SMA-2) and compression (SMA-1 post-cure 140 °C and SMA-3) along with thermal data determined by DSC. The data shown for mechanical testing are the mean and standard deviation for five replicate experiments.*

Resin[a]	SMA (wt %)[b]	LMA (wt %)[b]	Irg 819 (wt %)[c]	Post-cure temperature (°C)	Breaking strain (%)	Breaking stress (MPa)	T_g (°C)
SMA-1^T	100	0	0.2	40	1.7 ± 0.4	7 ± 1	166[d]
SMA-1^C	100	0	0.2	140	2.4 ±0.4	30 ± 9	122
SMA-2^T	50	50	0.2	40	3 ± 1	1.9 ± 0.6	--[e]
SMA-3^C	100	0	1	140	1.9 ± 0.3	30 ± 8	132

[a]Superscript T = analysis done under uniaxial tension; superscript C = analysis done under uniaxial compression. [b]Weight percent of monomer component. [c]Weight percent with respect to total monomer components. [d]DSC measurement obtained from a sample after purification by precipitation. [e]No definable T_g from DSC traces likely due to undercuring.

We also printed a series of specimens for uniaxial tensile testing of SMA-based samples. We chose to focus on SMA over SA given that homopolymers of SMA led to parts with higher T_gs, and therefore SMA provides an upper bound on thermal properties in our studies. The parts produced from SMA-1 with a post-cure at 40 °C for 1 h were very brittle (breaking strain of only 2%) and weak (breaking stress of only 7 MPa) (Figure A8, Table 4.2), and they did not show any plastic deformation before break. Attempts to

toughen the materials by adding LMA to the formulation (SMA-2) were unsuccessful, as the breaking strain and stress were still low (breaking strain of only 3% and breaking stress of only 2 MPa) (Figure A8, Table 4.2).

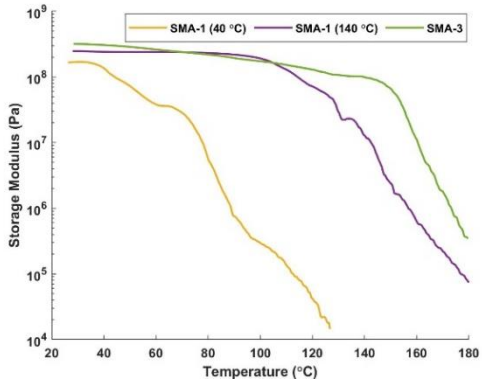

Figure 4.5. *DMA data showing the storage modulus versus temperature for relevant printed SMA-based resins.*

For samples printed using SMA-1 postcured at 40 °C, multiple glass transitions were detected by DSC, which is indicative of under-curing and plasticization, presumably by remaining monomer and oligomers (Figure A9). After dissolving these SMA-1 printed parts in dichloromethane and precipitating the polymer by adding the solution dropwise into excess methanol, a T_g of 166 °C was observed (Table 4.2, Figure A9). To improve the degree of curing in printed parts, SMA-1 samples were post-cured at 140 °C, instead of 40 °C. After this adjustment, the printed part only exhibited a single T_g of 122 °C (Table 4.2, Figure A9). Extending the 140 °C post-curing time beyond 1 h resulted in only small increases in T_g (Figure A10). Further adjustment of the formulation (SMA-3) by adding additional photoinitiator gave parts with a T_g of 132 °C (Figure A11). After post-curing at 140 °C, SMA specimens became more brittle, likely due to reduced plasticization, making the thin tensile testing samples unsuitable for analysis. Thus, printed cylinders were assessed under uniaxial compression. SMA-1 with 140 °C post-cure and SMA-3 gave similar results, with compressive breaking strains of 2% and compressive strengths of 30 MPa (Figure A12, Table 4.2).

DMA was used to evaluate the thermomechanical performance of SMA-1 and SMA-3 printed parts. The SMA specimens exhibited stable storage moduli at high temperature consistent with their high T_g values (Figure 4.5). A drop in storage modulus occurred above 100 °C for SMA-1 postcured at 140 °C. Increasing the percentage of photoinitiator (SMA-3) further increased the storage modulus and pushed the drop in storage modulus up to 140 °C. The impact of post-cure is evident in the DMA results for these two resins with the SMA-1 sample postcured at 140 °C retaining its storage modulus up to much higher temperatures than samples postcured at 40 °C (Figure 4.5). The DMA results demonstrate that parts printed with SMA can retain their mechanical properties at temperatures significantly above 100 °C.

Reprocessability of 4-pGA and SMA thermoplastics

Table 4.3. *SEC results from printed samples dissolved in chloroform using polystyrene standards.*

Formulation	M_n (kDa)	M_w (kDa)	$Đ$
4-pGA-1	487	1,390	2.9
4-pGA-2	421	1,320	3.1
4-pGA-3	257	1,010	3.9
4-pGA-4	304	877	2.9
4-pGA-5	350	1,030	2.9
4-pGA-6[a]	111	626	5.6
SMA-1	193	449	2.3
SMA-2	85.3	312	3.7
SMA-3	58.8	303	5.2

[a] *Solubility was obtained by using higher purity LA*

Although each of the aforementioned resin systems were printed without the use of crosslinkers, we still found good fixity of solid layers during printing. Most commonly, vat photopolymerization 3DP overwhelmingly produces thermoset parts due to the deliberate incorporation of crosslinkers, which give part fixity at low monomer conversion. Notably, vat photopolymerization 3DP of thermoplastics is rare because it requires striking a difficult balance between polymerization and polymer solubility.[37] The gelation during polymerization of monofunctional acrylates has been reported in bulk polymerization, but it is usually attributed to a reaction that is specific to the side chain of the acrylate or an alternative crosslinking mechanism such as branching and chain combination.[38,39] In our case, the creation of a

thermoset was not necessary, and when the samples made with SMA-3 or 4-pGA-3 were placed in dichloromethane, they appeared to fully dissolve within 1 and 24 h, respectively (Figure A13).

To further investigate the nature of the thermoplastics, samples were printed from each resin, and molecular weight distributions were measured using size exclusion chromatography (SEC) with a chloroform mobile phase, a refractive index detector, and calibration against polystyrene standards. All of the printed samples exhibited relatively high molecular weights and broad dispersities—consistent with uncontrolled photoinitiated radical polymerizations (Table 4.3, Figure A14).[40] The two families of resin formulations led to considerably different solubilities of their respective printed parts, in agreement with previous literature reports (Table A2).[41] For instance, SMA-3 gave products that were soluble in dichloromethane and chloroform but insoluble in the other solvents that we tested. In contrast, products from 4-pGA-3 were found to be soluble in a range of organic solvents, including chlorinated solvents, ethers, hydrocarbons, and terpenes. The solubility in food-grade terpenes presents an opportunity for hazard reduction associated with parts clean-up and post-print treatments.

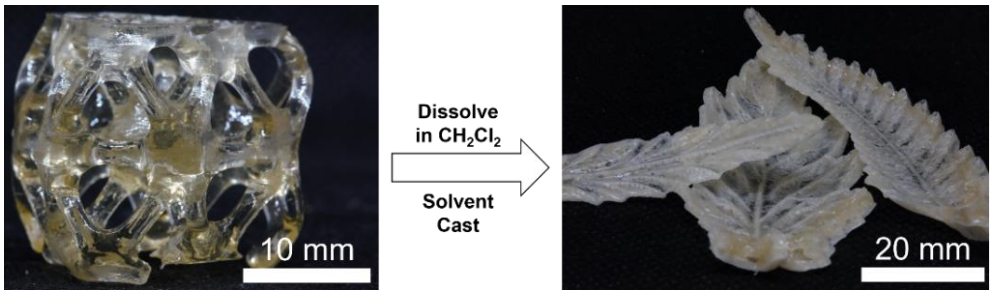

Figure 4.6. *Illustration of the ability to solvent cast printed parts. A 3D-printed lattice from SMA-3 was dissolved in dichloromethane. The dissolved polymer could then be poured into a leaf mold, and the solvent evaporated away.*

The ability to print thermoplastic polymers in vat photopolymerization is rare and offers multiple advantages in sustainability and application. For example, the recycling options for printed thermoset objects are limited. However, parts prepared from 4-pGA- and SMA-based resins can be dissolved and repurposed using simple reprocessing steps such as solvent casting. To illustrate the potential recyclability of biobased prints, the parts were dissolved in dichloromethane and solvent casted into leaf molds (Figure

4.6). More broadly, one can envision using vat photopolymerization 3DP of thermoplastics to create sacrificial molds or for investment casting. Both of these important manufacturing methods can be made more accessible with 3DP, streamlining the fabrication of parts.[37,42–44]

Conclusion

The 3D printing of a series of photoresin formulations using lignin-derivable monomers was reported. The thermomechanical properties of the resulting materials were characterized, and straightforward adjustments to monomer composition were leveraged to generate materials ranging from rigid plastics to soft and stretchable elastomers. Notably, each series of resins was printed without the use of crosslinker and resulted in thermoplastic parts. The thermoplastic properties enabled reprocessing of printed parts by solvent casting and broadened the applicability of vat photopolymerization 3DP. The reprocessability also provides an opportunity for recycling *via* solvent means. Overall, this work demonstrates several unique advantages of lignin-derived monomers in the development of more sustainable 3DP photoresins for high-performance additive manufacturing.

Experimental Section

Materials: Triethylamine (≥99.5%), 4-pG, syringol, methacryloyl chloride (97%), acryloyl chloride (97%), Irg 819 (97%), LMA (96%), LA (90%), nile red, dichloromethane (≥99.8%), tetrahydrofuran (≥99.9%), and L-fenchone (≥98%) were all purchased from Sigma Aldrich. Higher purity lauryl acrylate (>98%) and (+/-)limonene (>95%) were purchased from TCI. Chloroform (99.9%), toluene (99.9%), isopropyl alcohol (>99.9%), and *p*-xylene (99.9%) were purchased from Fisher Chemicals. Krytox® GPL103 was purchased from Amazon. All materials were used as received.

Synthesis of monomers: 4-pGA, SMA, and SA were synthesized following a procedure reported in literature.[32] In brief, the respective aromatic monomers and triethylamine (1.2 mol eq) were dissolved in dry dichloromethane in a round-bottom flask. The solution was immersed in an ice-water bath and cooled to 0 °C before (meth)acryloyl chloride (1.4 mol eq) was added drop wise. The cooling bath was then removed, and the solution was stirred unmonitored for 12 h. After the reaction, a white precipitant was filtered out and rinsed with dichloromethane. The organic phase was washed with aqueous solutions of sodium bicarbonate (saturated), 1.0 M NaOH, and 1.0 M HCl. The products were further purified by running through a basic alumina plug and concentrated by rotary evaporation.

3D printing setups: All photoresins were printed on a home-built digital light processing (DLP) 3D printer. For the bottom-up printer, images were projected from an Acer X152H projector. The position of the lens was adjusted so that image could be focused on the bottom of vat, which was about 10 cm away from the lens. For the top-down printer, images were projected from a ViewSonic Projector (PA503S). An extra lens was used to focus the image to the top surface of the photoresin, which was about 15 cm away from the lens. Krytox® GPL103 oil was used to support the photoresin (Figure A1, Figure A2). Creation Workshop was used to slice STL files and control each printer setup. All print files are linked in the Supporting Information.

Top-Down 3D printing of SMA resins: Photoresins were floated on a layer of fluorinated oil (~20 mm thick) and brought to 40 °C using a heated water bath. Print settings included a layer thickness of 0.1 mm and

layer cure times of 5 - 35 s. Irgacure 819 was used as the photoinitiator, 4-pG was the inhibitor, and lauryl methacrylate (LMA) was a property modifier. After printing, each test specimen was postcured for 1 h using 405-nm light, followed by thermal curing in an oven for 1 h unless otherwise specified. When printing SMA-2, the incorporation of LMA was assessed by ^{1}H NMR spectroscopy analysis of the uncured photoresin before and after printing, which confirmed equal consumption of SMA and LMA during printing (Figure A13).

Bottom-up 3D printing of 4-pGA resins: Printing involved a bottom-up printer design (images projected from below the resin vat) with a bottom layer of fluorinated oil about 1-mm thick in the vat, layer thicknesses of 0.1 mm, and layer cure times of 10 – 35 s. After printing, each test specimen was postcured at ~20 °C for 1 h using 405-nm light. Analysis of the residual photoresin's composition by ^{1}H NMR spectroscopy confirmed that the composition did not change after printing indicating consistent incorporation of the monomers throughout the printed part (Figure A13).

Mechanical tests: Tensile and compressive tests were conducted on a MTS Criterion® Electromechanical Testing System. For the tensile tests, an ASTM D638 type V specimen was printed. The strain rate was set to 10 mm/min for more rigid plastics (parts produced from SMA-based photoresins, 4-pGA-1, 4-pGA-2, 4-pGA-6) and 50 mm/min for elastomers (4-pGA-3, 4-pGA-4, and 4-pGA-5). Tensile strain was measured through video analysis by measuring the distance between series of lines that were drawn on the dogbones in the gauge region prior to testing. Strain was calculated based on the change in distance between the lines on the dogbones. Stress-strain curves were obtained by correlating stress and strain values. For the compressive tests, a pillar with a diameter of 5 mm and a height of 10 mm was printed. The compressive rate was set to 1 mm/min.

Nuclear Magnetic Resonance (NMR) spectroscopy: ^{1}H and ^{13}C NMR spectra were obtained using Bruker Avance III 400 or 500 MHz spectrometers. ^{1}H NMR spectra of combined resins were taken using the Bruker Avance III 400 MHz spectrometer, while ^{1}H and ^{13}C NMR spectra were obtained using the Bruker Avance III 500 MHz spectrometer. Chemical shifts are reported in delta (δ) units, expressed in parts per million

(ppm) downfield from tetramethylsilane using residual protio-solvent as an internal standard ($CDCl_3$, δH = 7.26 ppm for ^{1}H NMR, δC = 77.16 ppm for ^{13}C NMR) (Figure A13, Figure A14, Figure A15).

Thermogravimetric Analysis (TGA), DSC, and DMA: TGA was conducted on a TA TGA Q50 under nitrogen from room temperature to 600 °C at a rate of 10 °C/min (Figure A16). DSC tests were conducted on a TA DSC Q200 calorimeter under air. Samples were sealed in a Tzero aluminum pan and lid. A heat-cool-heat profile was conducted at a 10 °C/min heating and cooling rate. The temperature range depended on the decomposition temperature determined using TGA and varied between samples. The second heating cycle was used to measure T_g. DMA tests were done on a PerkinElmer DMA 8000. Sinusoidal forces were applied to rectangular samples. The strain was 0.03, frequency was 1 Hz, and heating rate was 3 °C/min.

Gas Chromatography-Mass Spectrometry (GC-MS): GC-MS was conducted on a Shimadzu QP-2020 NX (Shimadzu Corporation) equipped with a MS detector, a flame ionization detector, an AOC-20i autosampler, and a Rtx-5MS column. Samples were dissolved in methanol prior to analysis. The injector temperature was set to 300 °C with a split ratio of 40:1, and the initial oven temperature was set to 50 °C. The oven temperature was held at 50 °C for 1 min before ramping to 315 °C at a rate of 15 °C/min. The MS interface temperature was set to 250 °C with an ion source temperature of 230 °C. GC-MS chromatograms were analyzed using Shimadzu GCMSsolution software (Figure A17).

SEC: Gel-permeation chromatography was conducted on a Tosoh EcoSEC 8320 (Tosoh Bioscience) equipped with a refractive index detector, a TSKgel HHR-H guard column, and two TSKgel GMHHR-N columns in series. The mobile phase was chloroform. The flow rate was 1.00 mL/min, and the temperature was 40 °C. Samples were dissolved in chloroform at a concentration of 1.0 mg/mL for at least 12 h and filtered through 0.1 μm poly(tetrafluoroethylene) syringe filters prior to analysis. A cubic calibration curve of $\log_{10}$(M) vs. retention time was made using a series of 9 polystyrene standards ranging from 589 g/mol to 2,110,000 g/mol (Figure A14) (PStQuick C and PstQuick D, Tosoh Bioscience). All reported molecular weights are polystyrene equivalent molecular weights.

Solvent Casting: Printed parts were first dissolved in dichloromethane. Once fully dissolved, the mixture was poured into silicon molds and left until fully solidified. The parts were then carefully removed from the mold revealing solvent casted pieces.

References

1. Javaid, M. & Haleem, A. Additive manufacturing applications in medical cases: A literature based review. *Alexandria J. Med.* **54**, 411–422 (2018).

2. Datta, P., Ayan, B. & Ozbolat, I. T. Bioprinting for vascular and vascularized tissue biofabrication. *Acta Biomater.* **51**, 1–20 (2017).

3. Leal, R. *et al.* Additive manufacturing tooling for the automotive industry. *Int. J. Adv. Manuf. Technol.* **92**, 1671–1676 (2017).

4. Adams, J. J. *et al.* Conformal printing of electrically small antennas on three-dimensional surfaces. *Adv. Mater.* **23**, 1335–1340 (2011).

5. Kim, Y., Yuk, H., Zhao, R., Chester, S. A. & Zhao, X. Printing ferromagnetic domains for untethered fast-transforming soft materials. *Nature* **558**, 274–279 (2018).

6. Sachyani Keneth, E., Kamyshny, A., Totaro, M., Beccai, L. & Magdassi, S. 3D Printing Materials for Soft Robotics. *Adv. Mater.* **33**, 2003387 (2021).

7. Wallin, T. J., Pikul, J. & Shepherd, R. F. 3D printing of soft robotic systems. *Nat. Rev. Mater.* **3**, 84–100 (2018).

8. Lei, M. *et al.* 3D Printing of Auxetic Metamaterials with Digitally Reprogrammable Shape. *ACS Appl. Mater. Interfaces* **11**, 22768–22776 (2019).

9. Tofail, S. A. M. *et al.* Additive manufacturing: scientific and technological challenges, market uptake and opportunities. *Mater. Today* **21**, 22–37 (2018).

10. Appuhamillage, G. A. *et al.* 110th Anniversary: Vat Photopolymerization-Based Additive Manufacturing: Current Trends and Future Directions in Materials Design. *Ind. Eng. Chem. Res.* **58**, 15109–15118 (2019).

11. Kelly, B. E. *et al.* Volumetric additive manufacturing via tomographic reconstruction. *Science* **363**, 1075–1079 (2019).

12. Shusteff, M. *et al.* One-step volumetric additive manufacturing of complex polymer structures. *Sci. Adv.* **3**, eaao5496 (2017).

13. Zhang, J., Hu, Q., Wang, S., Tao, J. & Gou, M. Digital light processing based three-dimensional printing for medical applications. *Int. J. Bioprinting* **6**, 12–27 (2020).

14. Phillips, R. Photopolymerization. *J. Photochem.* **25**, 79–82 (1984).

15. Crivello, J. V. & Reichmanis, E. Photopolymer materials and processes for advanced technologies. *Chem. Mater.* **26**, 533–548 (2014).

16. Boydston, A. J., Cui, J., Lee, C. U., Lynde, B. E. & Schilling, C. A. 100th Anniversary of Macromolecular Science Viewpoint: Integrating Chemistry and Engineering to Enable Additive Manufacturing with High-Performance Polymers. *ACS Macro Lett.* **9**, 1119–1129 (2020).

17. Mathers, R. T. How well can renewable resources mimic commodity monomers and polymers? *J. Polym. Sci. Part A Polym. Chem.* **50**, 1–15 (2012).

18. Upton, B. M. & Kasko, A. M. Strategies for the conversion of lignin to high-value polymeric materials: Review and perspective. *Chem. Rev.* **116**, 2275–2306 (2016).

19. Wang, H., Pu, Y., Ragauskas, A. & Yang, B. From lignin to valuable products–strategies,

challenges, and prospects. *Bioresour. Technol.* **271**, 449–461 (2019).

20. Ragauskas, A. J. *et al.* Lignin valorization: improving lignin processing in the biorefinery. *Science* **344**, 1246843 (2014).

21. O'Dea, R. M., Willie, J. A. & Epps, III, T. H. 100th Anniversary of Macromolecular Science Viewpoint: Polymers from Lignocellulosic Biomass. Current Challenges and Future Opportunities. *ACS Macro Lett.* **9**, 476–493 (2020).

22. Mahajan, J. S., O'Dea, R. M., Norris, J. B., Korley, L. T. J. & Epps, III, T. H. Aromatics from Lignocellulosic Biomass: A Platform for High-Performance Thermosets. *ACS Sustain. Chem. Eng.* **8**, 15072–15096 (2020).

23. Boerjan, W., Ralph, J. & Baucher, M. Lignin Biosynthesis. *Annu. Rev. Plant Biol.* **54**, 519–546 (2003).

24. O'Dea, R. M. *et al.* Ambient-pressure lignin valorization to high-performance polymers by intensified reductive catalytic deconstruction. *Sci. Adv.* **8**, eabj7523 (2022).

25. Bassett, A. W. *et al.* Dual-functional, aromatic, epoxy-methacrylate monomers from bio-based feedstocks and their respective epoxy-functional thermoplastics. *J. Polym. Sci.* **58**, 673–682 (2020).

26. Li, H. *et al.* High Modulus, Strength, and Toughness Polyurethane Elastomer Based on Unmodified Lignin. *ACS Sustain. Chem. Eng.* **5**, 7942–7949 (2017).

27. Liu, W., Fang, C., Wang, S., Huang, J. & Qiu, X. High-Performance Lignin-Containing Polyurethane Elastomers with Dynamic Covalent Polymer Networks. *Macromolecules* **52**, 6474–6484 (2019).

28. Hernandez, E. D., Bassett, A. W., Sadler, J. M., La Scala, J. J. & Stanzione, J. F. Synthesis and Characterization of Bio-based Epoxy Resins Derived from Vanillyl Alcohol. *ACS Sustain. Chem. Eng.* **4**, 4328–4339 (2016).

29. Nicastro, K. H., Kloxin, C. J. & Epps, III, T. H. Potential Lignin-Derived Alternatives to Bisphenol A in Diamine-Hardened Epoxy Resins. *ACS Sustain. Chem. Eng.* **6**, 14812–14819 (2018).

30. Zhou, J., Zhang, H., Deng, J. & Wu, Y. High Glass-Transition Temperature Acrylate Polymers Derived from Biomasses, Syringaldehyde, and Vanillin. *Macromol. Chem. Phys.* **217**, 2402–2408 (2016).

31. Holmberg, A. L., Reno, K. H., Nguyen, N. A., Wool, R. P. & Epps, III, T. H. Syringyl Methacrylate, a Hardwood Lignin-Based Monomer for High-Tg Polymeric Materials. *ACS Macro Lett.* **5**, 574–578 (2016).

32. Wang, S., Shuai, L., Saha, B., Vlachos, D. G. & Epps, III, T. H. From Tree to Tape: Direct Synthesis of Pressure Sensitive Adhesives from Depolymerized Raw Lignocellulosic Biomass. *ACS Cent. Sci.* **4**, 701–708 (2018).

33. Çayli, G. & Meier, M. A. R. Polymers from renewable resources: Bulk ATRP of fatty alcohol-derived methacrylates. *Eur. J. Lipid Sci. Technol.* **110**, 853–859 (2008).

34. Meier, M. A. R., Metzger, J. O. & Schubert, U. S. Plant oil renewable resources as green alternatives in polymer science. *Chem. Soc. Rev.* **36**, 1788–1802 (2007).

35. Coelho, J. F. J. *et al.* Synthesis of Poly(lauryl acrylate) by Single-Electron Transfer/Degenerative Chain Transfer Living Radical Polymerization Catalyzed by Na2S2O4 in Water. *Macromol. Chem. Phys.* **208**, 1218–1227 (2007).

36. Hiemenz, P. C. & Lodge, T. Polymer chemistry (2nd edition). 587 (2007).

37. Deng, S., Wu, J., Dickey, M. D., Zhao, Q. & Xie, T. Rapid Open-Air Digital Light 3D Printing of Thermoplastic Polymer. *Adv. Mater.* **31**, 1903970 (2019).

38. Zhu, S. & Hamielec, A. E. Gel formation in free radical polymerization via chain transfer and terminal branching. *J. Polym. Sci. Part B Polym. Phys.* **32**, 929–943 (1994).

39. Fox, T. G. & Gratch, S. Crosslinking in Monovinyl Monomers (I). By Chain Transfer With the Polymer Chain. *Ann. N. Y. Acad. Sci.* **57**, 367–383 (1953).

40. Miller-Chou, B. A. & Koenig, J. L. A review of polymer dissolution. *Prog. Polym. Sci.* **28**, 1223–1270 (2003).

41. Emerson, J. A., Garabedian, N. T., Burris, D. L., Furst, E. M. & Epps, III, T. H. Exploiting Feedstock Diversity to Tune the Chemical and Tribological Properties of Lignin-Inspired Polymer Coatings. *ACS Sustain. Chem. Eng.* **6**, 6856–6866 (2018).

42. Post, B. K. *et al.* Big area additive manufacturing application in wind turbine molds. *Solid Free. Fabr. 2017 Proc. 28th Annu. Int. Solid Free. Fabr. Symp. - An Addit. Manuf. Conf. SFF 2017* 2430–2446 (2020).

43. Le Néel, T. A., Mognol, P. & Hascoët, J. Y. A review on additive manufacturing of sand molds by binder jetting and selective laser sintering. *Rapid Prototyp. J.* **24**, 1325–1336 (2018).

44. Wang, J., Sama, S. R., Lynch, P. C. & Manogharan, G. Design and topology optimization of 3D-printed wax patterns for rapid investment casting. *Procedia Manuf.* **34**, 683–694 (2019).

Chapter 5: Block copolymer additives for toughening 3D printable epoxy resin

Reprinted (adapted) with permission from:

Chen, R.; Cai, J.; **Chin, K. C. H.**; Wang, S.; Boydston, A. J.; Thevamaran, R.; Gopalan, P. Block Copolymer Additives for Toughening 3D Printable Epoxy Resin. *Giant* **2024**, *17*, 100204.

Abstract

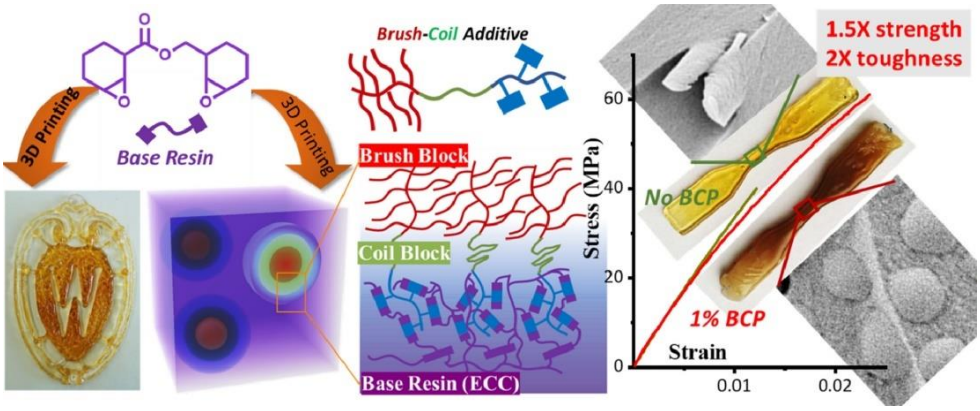

We explore the potential for using a brush-coil triblock copolymer to enhance the mechanical properties of epoxy resin for 3D printing applications. Epoxy resins are widely used in structural material and adhesive and have great potential for 3D printing. However, the highly brittle nature of epoxy resins requires the use of large concentrations of toughening agents that pose significant challenges in meeting rheological requirements of 3D printing. We report a reactive brush-coil block copolymer with three distinct blocks that can phase separate and chemically crosslink with the base epoxy resin to form spherical aggregates. Detailed scanning electron microscopy imaging shows that these aggregates can arrest and deflect cracks during propagation and can synergistically strengthen (~ 1.5×) and toughen (~ 2×) the epoxy resin with even 1 wt% of the BCP additive to the base resin. Importantly, both the modulus and the glass transition temperatures are preserved. Direct ink writing (DIW) and digital light processing (DLP) 3D printing of the modified resins also shows the same strengthening and toughening effects seen in mold-cast samples, demonstrating its compatibility with 3D printing processes. These findings suggest that brush-coil triblock copolymers additives at very low concentrations can synergistically improve the mechanical properties of epoxy resin for 3D printed parts.

Introduction

Research in 3D printing (also known as additive manufacturing) has accelerated over the last decade due to its ability to custom design complex shapes. Potential applications of these custom printed components are already showing great potential in soft-robots [1,2] microfluidics [3] and tissue engineering [4]. Based on the nature of the process, printing can be broadly categorized into those that undergo a physical change such as melting or softening and those that require a chemical change such as chemical crosslinking [5]. The methods based on chemical crosslinking are particularly attractive as the process can be expanded to thermosetting resins that are typically hard to print [6,7]. Prime among them is epoxy resin chemistry.

Epoxy resins have high modulus, good thermomechanical properties, and good chemical resistance leading to a wide range of applications in composites, adhesives and coatings [8]. However, the highly crosslinked nature of the resin makes them brittle and unsuitable for many applications without further modifications. Some of the common approaches used to toughen commercial epoxy resins add soft, rubbery fillers in the form of liquid rubber or rubber micro spheres [9]. The resulting soft spherical aggregates in the epoxy resin improve the toughness of the resin by arresting and deflecting crack propagation [8]. As a trade-off, increase in material toughness is often accompanied by the inevitable decrease of modulus, strength, and thermal properties such as glass transition temperature (T_g)[10] of the matrix polymer. These properties are closely tied to lack of interfacial adhesion of the additives to the matrix, which is well documented in multiphase material formulations [11]. In many of these studies the added rubber particles are dispersed in the epoxy but do not have significant adhesion to the base resin, thereby leading to deterioration of mechanical properties including the toughness. From a morphological perspective, both reactive and non-reactive block copolymer additives where one block is compatible/ reactive with base epoxy resin, and the other is often rubbery incompatible block, have been studied. In most of these studies the base epoxy resin is aromatic diglycidyl ether of bisphenol A (DGEBA) based, and the block copolymer (BCP) additive is a linear di- or triblock, where under high BCP concentrations self-assembled structures [10,[12], [13], [14]] are observed. Often the choice of the rubbery blocks in these BCPs includes

known elastomers such as poly (butyl acrylates), poly (butadiene), or poly(butadiene-acrylonitrile) blocks, but the coil blocks vary widely to be compatible with epoxy resin, such as PEO, PMMA, PS or polycaprolactone. For example, the addition of 5–20 wt% of a non-reactive triblock copolymer poly(methyl methacrylate)-b-poly(butyl acrylate)-b-poly(methyl methacrylate) (MAM) to a Bisphenol A epoxy resin (E51) resulted in increased toughness but a decrease in tensile strength[15]. A reactive version of the same triblock resulted in further improvements in the toughness, but the strength and modulus values still decreased [16]. A recent report used just 1 wt% of a reactive core-shell bottlebrush copolymer with a rubbery block of PBA as core and an epoxy reactive block of polyglycidyl methacrylate (PGMA) as the shell, that resulted in increase in toughness while maintaining the elastic modulus, but the yield strength decreased by 10 %[17]. There are numerous other studies that measure fracture toughness of a BCP/epoxy blend, but do not report the tensile strength or the modulus [18].

Using these toughened resins in 3D printing poses other challenges, as the high BCP concentrations adversely affects the rheological properties by increasing the viscosity of the uncured resin [19,20]. The required viscosity for digital light processing (DLP) printing is quite low (< 10 Pa·s) [20], whereas for methods such as direct ink writing (DIW) is relatively high (0.01–100 Pa·s at ~0.1 s-1) with an added requirement of shear thinning behavior for extrudability, and yield stress characteristics for retention of shape upon extrusion. [7,21]. In addition, for thermoset resins, the cure kinetics during these processes is also critically important to have well defined printed parts. It is well known that polymer architectures have a profound influence on the rheological and self-assembly behavior [22]. Among them, bottlebrush copolymers have low viscosity in melt and in solution due to low interchain entanglements [23], and can self-assemble more easily due to favorable kinetics from low entanglements [24]. Both viscosity and morphology are important when using these BCPs as additives in 3D printing.

Simplification of the formulation with the least amount of additives can offer a generalizable resin platform, reduce cost to manufacture, and minimize processing variables that must be considered. In this work we explore an alternative BCP architecture that requires at most 1 wt% BCP concentration, hence largely

preserving the rheological properties of the base resin. This gives flexibility to precure the resin to use in either DIW or DLP, if the cure kinetics can be accelerated. We demonstrate the design of a brush-coil BCP that can synergistically strengthen and toughen a commonly used cycloaliphatic epoxy base resin with low BCP concentration and is compatible with 3D printing (Fig. 5.1). A soft, epoxy-phobic poly [monomethacryloxypropyl terminated polydimethylsiloxane (MAPDMS)] (PMAPDMS) block is selected for the core-forming brush block. For the epoxy-philic coil block, polystyrene (PS) chain is selected for its solubility in the resin. The flexible coil nature of the second block also allows for the formation of high curvature spherical aggregates [25,26]. A short, cross-linkable poly (glycidyl methacrylate) (PGMA) block is attached to the PS chain end to improve the interfacial adhesion by crosslinking with the base epoxy resin. We study the effect of increased BCP concentrations from 1 to 10 wt% in the base 3,4-epoxycyclohexylmethyl-3′,4′-epoxycyclohexane carboxylate (ECC) resin, on its rheological, crosslinking, morphological, and mechanical properties. We demonstrate that with just 1 wt% BCP concentration, ∼1.5 times improvement in strength and ∼2 times improvement in toughness is achievable and more importantly we demonstrate the DIW from these modified resins. We further show that these BCPs can be incorporated into an ECC/acrylate blend and used for DLP process, with similar improvements in mechanical properties.

Results and Discussion

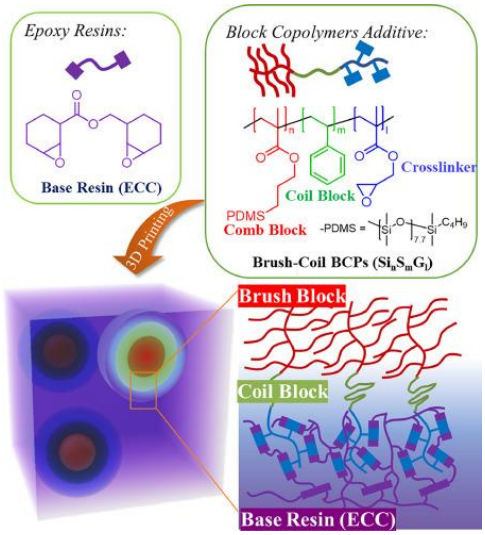

***Figure* 5.1.** *Structure of base resin, the custom designed brush-coil BCPs and the schematic of the expected morphology in the blend is depicted.*

Design and synthesis of bottlebrush

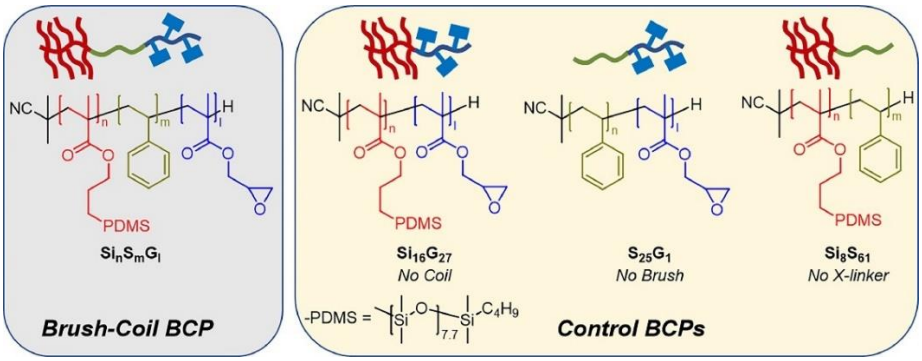

Figure 5.2. *Structures of the brush-coil BCPs and controls studied.*

The brush-coil BCPs were synthesized via three steps of sequential reversible addition fragmentation (RAFT) polymerization of monomethacryloxypropyl terminated polydimethylsiloxane (MAPDMS), styrene (S) and glycidyl methacrylate (GMA). The chain-end RAFT chain transfer agent (CTA) was substituted with a proton to avoid side reactions (see Supplementary Information for synthetic procedure and characterizations). The PMAPDMS provides the rubbery (T_g = −120 °C) [27] block, and the brush architecture as the PDMS chains are grafted on to the polymerizable methacrylate backbone. The bottle brush architecture offers two advantages: 1) lower viscosity compared to its linear counterpart, and 2) elastomeric characteristic at lower weight% loading. The other two blocks are composed of PS and PGMA. The PS chain is the epoxyphilic corona that also provides the glassy (T_g = 100 °C) [28] component to retain mechanical properties. The T_g of the microphase segregated PS in epoxy resin is known to be lower than a bulk sample [29]. The terminal PGMA units provide the critical covalent anchoring to the epoxy base resin. To study the effect of composition of the BCP additive on the toughness of the base epoxy resin, three different PS block lengths were synthesized. To understand the role of each block, three additional control samples with one of the three blocks missing were also synthesized (Fig. 5.2, Table 5.1).

Table 5.1. *Composition of the Controls (in yellow) and the brush-coil BCPs (gray) in Figure 5.1.*

Sample name [a]	M_n[g/mol] [b]	f_{st}[%] [a]	Appearance
$Si_{16}G_{27}$	5764	0	Colorless, viscous liquid
$S_{25}G_1$	6312	0.93	White, solid powder
Si_8S_{61}	10,954	0.55	White, solid powder
$Si_{11}S_{24}G_6$	7638	0.19	White, viscous liquid
$Si_{11}S_{80}G_{12}$	7308	0.45	White, rubbery solid
$Si_{11}S_{149}G_5$	9966	0.58	White, solid powder

a) S stands for Styrene, G for GMA and Si for PMAPDMS. The subscript in the sample name corresponds to the degree of polymerization of each monomer in the final copolymer as determined by 1H NMR. b) Mn determined by GPC.

The thermal properties of the BCP additives were studied by DSC (Fig. 5.3). In the first heating cycle, distinct T_gs corresponding to PGMA (T_g = 70 °C [30]) and PS (T_g = 100 °C), as well as an exothermic peak (140.5 °C) corresponding to the crosslinking of PGMA was observed. This indicates that most likely the PS and PMAPDMS are phase segregating and PGMA undergoes effective self- crosslinking. The crosslinking of PGMA was further confirmed by the disappearance of the T_g peak for PGMA in the second heating cycle. For $Si_{11}S_{24}G_6$, the thermal transitions were difficult to observe likely due to the short PS segment leading to disordered morphology. For control BCPs (Fig. B7) Si_8S_{61} and $S_{25}G_1$, single T_g for PS was detected. However, the T_g for PGMA was not observed likely due to short PGMA segment.

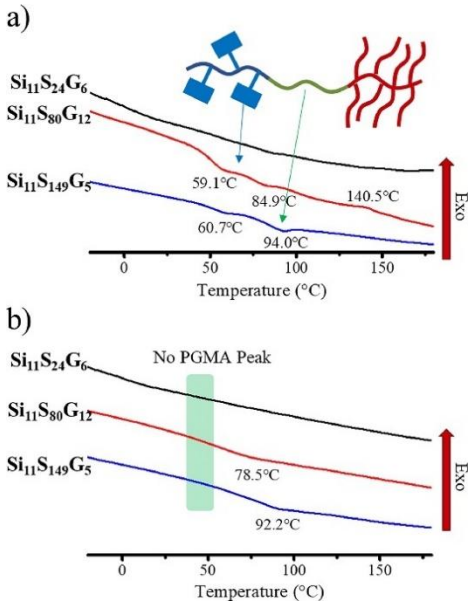

Figure 5.3. *Differential scanning calorimetry (DSC) measurement of BCPs a) first heating cycle and b) second heating cycle. Exothermic points up.*

Block copolymer toughened resin curing

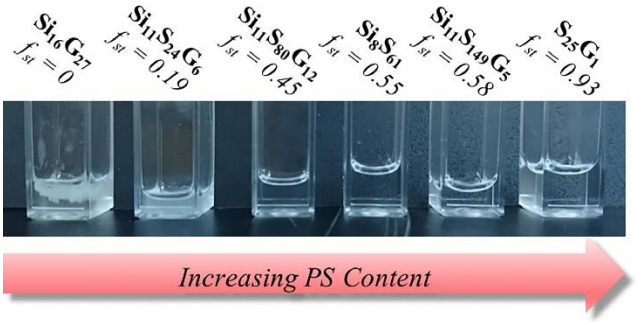

Figure 5.4. *The solution turbidity indicates the improved solubility of BCPs (1 wt%) with increasing polystyrene content in the base ECC resin.*

To test if these BCP additives will toughen the base resin, we first examined their solubility in the resin (Fig. 5.4). We chose the cycloaliphatic resin, 3,4-epoxycyclohexylmethyl-3′,4′-epoxycyclohexane carboxylate (ECC) as our base resin due to its widespread application in 3D printing [31]. The BCP (1 wt%) was dissolved in 2 mL of dichloromethane (DCM) and then mixed with ECC resin and dried under air flow with stirring. Upon drying, the control sample, without a PS block ($Si_{16}G_{27}$), crashes out of the solution due to insolubility in the base resin, hence the epoxyphilic block is critical for its compatibility with ECC. Uniform dispersion was achieved with the BCPs with PS content equal or higher than in $Si_{11}S_{80}G_{12}$ resulting in a clear solution. Turbidity test (Figure B8) also confirms this observation.

Mold-cast dog-bone samples were prepared from these blends to evaluate the mechanical properties in uniaxial tension (Fig. 5.5). We first tested the control BCPs without core-forming PMAPDMS block ($S_{25}G_1$) or crosslinking PGMA block (Si_8S_{61}) and one brush-coil BCP ($Si_{11}S_{80}G_{12}$) against pure ECC resin. The ECC resin was mixed with a photoacid generator (triarylsulfonium hexafluoroantimonate salts, TAS) to initiate crosslinking and cured under UV light. These conditions are comparable to those in the actual 3D printing (See Supplementary Information for experimental details). We observed over 1.7 times increase in the toughness in $Si_{11}S_{80}G_{12}$ blends and an over 44 % increase in the failure strength compared to the base ECC resin. For the control $S_{25}G_1$ blends, no further toughening compared to ECC resin was observed, as it does not contain the core forming PMAPDMS block. When the BCP additive is not crosslinked to the base

resin, for example with the control blend of Si_8S_{61} with ECC, a smaller (0.44×) enhancement in toughness was observed. Hence the presence of low T_g elastomeric PMAPDMS as well as covalent crosslinking of the additive with ECC via GMA units are important to enhance the toughness. Importantly, in all the BCP/ECC blends, we did not observe a statistically significant decrease in the modulus. In fact, the T_g of the crosslinked blends measured by DSC (137 °C and 143 °C) show the least changes compared to the base resin (140 °C) (Fig. 5.5(d)), hence the thermal characteristics are largely preserved.

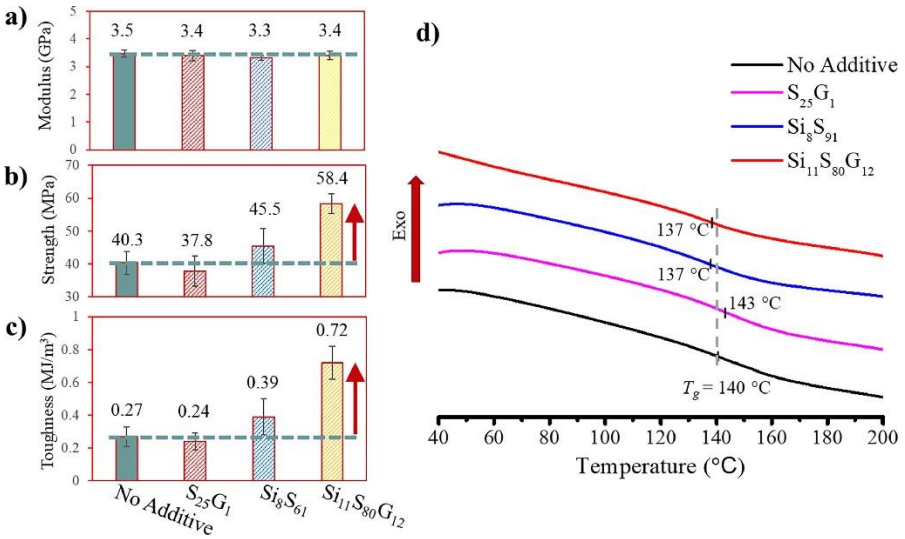

Figure 5.5. *The BCP (1 wt%)/ECC blend was photo cross-linked in a mold to form dog-bone samples and the a) modulus b) failure strength and c) toughness was measured as a function of the composition of the BCP. The arrows indicate the increase of toughness and strength for BCP/ECC blends. d) DSC curves of the cured samples show T_g (dotted line) comparable for all 4 samples tested.*

To understand the toughening mechanism of the BCP additive, we examined the fracture surface of the tensile tested samples by scanning electron microscopy (SEM) (Fig. 5.6). The pure ECC fracture surface was a smooth, mostly featureless surface that is characteristic of a brittle failure with low intrinsic toughness. In contrast, the fracture surface of the ECC with BCP additive ($Si_{11}S_{149}G_5$) show a large number of smooth spherical structures of variable sizes uniformly distributed within the matrix, that are fused with the base resin (Figure B9). The spherical aggregates are most likely composed of the BCP bonded to the resin, and the presence of the cracks also agrees with similar observations of crack arrest and deflection in DGEBA/non-reactive triblock copolymer blends [32]. While some of such features are also present in the control blends of ECC/Si_8S_{61}, their shape is more spherical in appearance. The lower toughness in the

ECC/Si_8S_{61} blend is attributable to the reduced interfacial adhesion from the lack of covalent bonding leading to lower stress transfer. The fracture surface of ECC/$S_{25}G_1$ is similar to pure ECC resin, as it consists of epoxyphilic PS and PGMA. Hence the presence of elastomeric PMAPDMS is essential for the formation of the spherical aggregates and the resulting intrinsic toughening of the material as the crack develops and progresses.

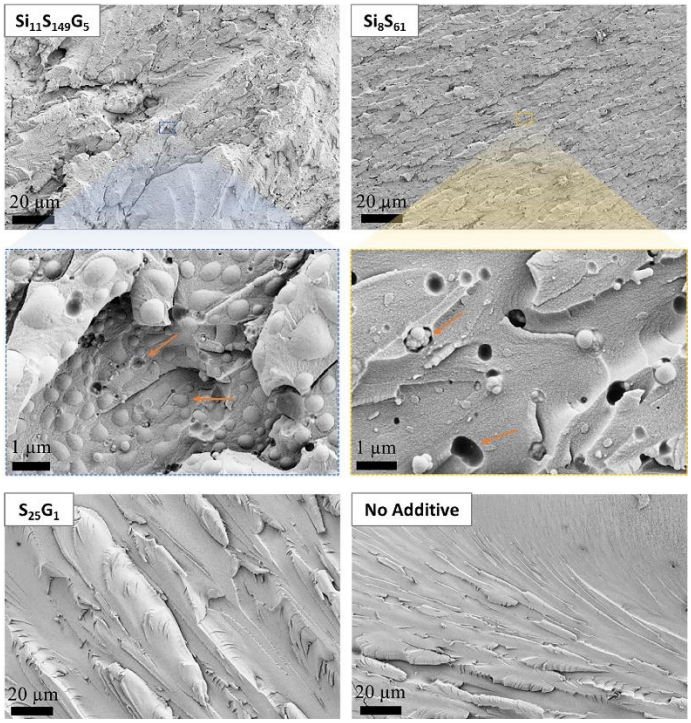

Figure 5.6. *Top-Down SEM images of the fracture surfaces for BCP/ECC blends with insets showing zoom-in view. Orange arrows indicate the spherical aggregates formed by BCP.*

An increase in the BCP additive $Si_{11}S_{80}G_{12}$ from 1 to 5 to 10 wt% in the base ECC resin resulted in deterioration of toughness, tensile modulus as well as the tensile strength (Fig. 5.7). The optical transparency of the samples also deteriorates leading to opaque cured samples at 10 wt% BCP concentration (Figure 5.7(a)). The loss of optical transparency indicates the presence of much larger aggregates in the crosslinked blend [33,34]. These larger aggregates serve as macroscale defects leading to the loss of mechanical properties and premature failure. The T_g measured by DSC shows an increase of 11 °C for the 10 wt% BCP concentration (Fig. B10). One possible explanation for this increase is due to the increased crosslink density in the cured resin. It should be noted that tensile strength and toughness of the

5 wt% concentration sample are still higher than the base ECC resin though lower than the 1 wt% concentration samples.

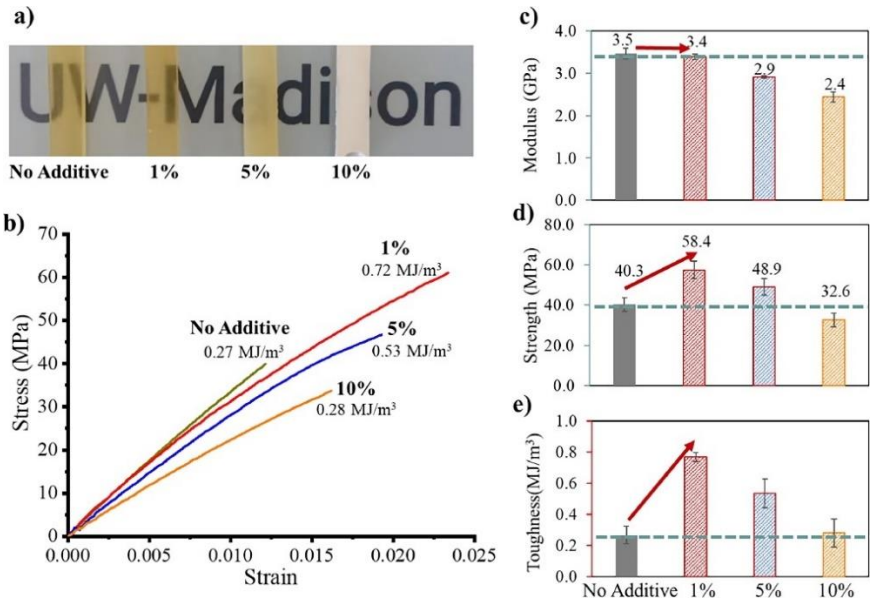

Figure 5.7. *Increased concentration of $Si_{11}S_{80}G_{12}$ additive to ECC affects the a) optical transparency, b) stress-strain-stress response, c) modulus, d) strength, and e) toughness of the cured blends.*

Analysis of the fracture surface of the tensile tested samples using SEM and white light interferometry (Fig. 5.8) show a more complex out-of-plane fracture topography (see the height profile measured normal to the fractured surface in Fig. 5.8(b)) with increase in density of micro fissures and number of aggregates (Fig. 5.8(c)) with increased concentration of $Si_{11}S_{80}G_{12}$ in ECC. The smooth spherical aggregates in the 1 wt% blends (Figure 5.8(c)) most likely consist of PMAPDMS core with PS and PGMA blocks extending into the ECC resin (Fig. 5.1). The PGMA block by design crosslinks with the epoxy groups in ECC leading to a gradient in crosslinking from low to high as we go into the bulk crosslinked ECC resin. The point at which these aggregates detach from the bulk ECC during tensile testing likely represents the transition into more brittle ECC resin. Upon closer inspection of, for example 5 wt% concentration sample (Fig. 5.8(c)), a large number of craters in addition to spherical aggregates can be observed, which is quite distinct from the 1 wt% sample. As the number of nucleation sites for the formation of these aggregates increases with the increasing concentration of the BCP additive, there exists a tradeoff where the modulus is no longer preserved but the toughness is still higher than the base resin. At

the highest concentration of 10 wt%, we no longer observe a continuous matrix but more flake-like features, and numerous microcracks, which correlates with the increased T_g, due to more crosslinks discussed above. In contrast for the pristine samples (before tensile testing) prepared by microtome (Fig. B11), no micro-fissures were observed but the spherical aggregates are seen, confirming that the micro-fissures only form during loading and lead to larger cracks, and eventual brittle failure.

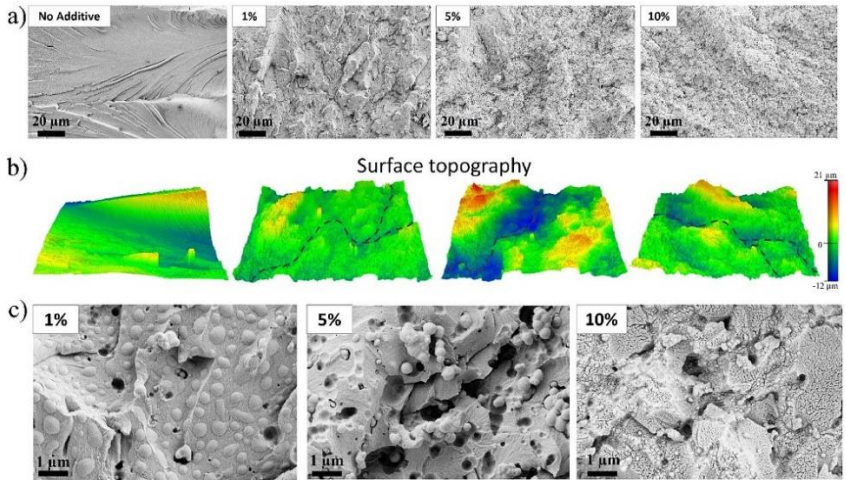

Figure 5.8. *Fracture surface of samples with increasing BCP additive of 0–10 wt% by a) top-down SEM images of the and b) optical profilometer shows roughness of the surface, with the dashed line indicating the possible crack propagation path across the fracture surface. Zoom-in view c) on the fracture surface BCP/ECC blend shows spherical aggregates and microfissures.*

We also studied the effect of select changes in the composition of the brush-coil BCP by mainly increasing the polystyrene block length from 24 to 149 repeat units. In fact, the toughness of all the resulting cured blends is 1.3 to 2 times higher than that of the base ECC resin (Fig. 5.9(a), (b)). Increase in the toughness with increase in the PS block length may be attributed to the increased phase segregation tendencies. The T_g of the crosslinked blends (Fig. 5.9(c)) stays constant at ~ 140 °C and does not change with the PS length.

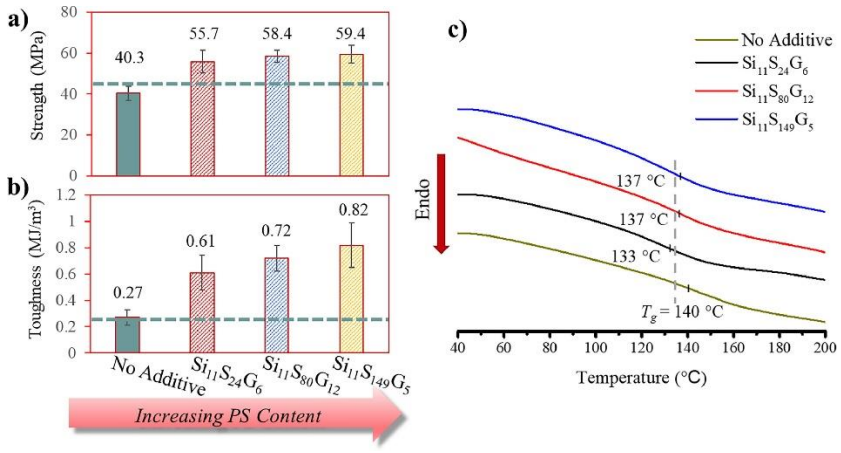

Figure 5.9. *Effect of increasing in the PS block length in the brush-coil BCP additive (1 wt%) in ECC resin was studied for changes to a) Tensile strength, b) Toughness, and c) T_g by DSC.*

DIW printing of ECC resin containing brush-coil BCP additive

We chose direct ink write (DIW) to demonstrate the printability of the ECC blends. DIW of epoxy resins is quite challenging due to the slow curing kinetics and Newtonian rheological properties [35]. To overcome these issues, chemical modification either through forming hybrid resins (i.e. acrylate-epoxy) [36], added rheological modifiers [37], or a combination of both [38], [39], [40] have been explored. Only 2D printing is known for epoxy resin without such additives [41]. Our approach is to lightly precure the resin to create a DIW ink with ideal rheological properties, without any additional additives, which is beneficial for scalability, processing and cost. The pure epoxy resin was thermally precured at 120 C for increasing amounts of time and the rheological properties characterized (Fig. 5.10(a)). When precured for 20 min the viscosity increases to 9 Pa·s compared to 0.4 Pa·s for as received ECC. However, the behavior remains Newtonian. After 22 min of precuring the prepolymer viscosity increases to 65 Pa·s and exhibits the desired shear thinning behavior for DIW printing. Precuring for longer than 25 min resulted in a prepolymer that was too viscous to extrude from an 18-gauge needle used in our custom DIW printer.

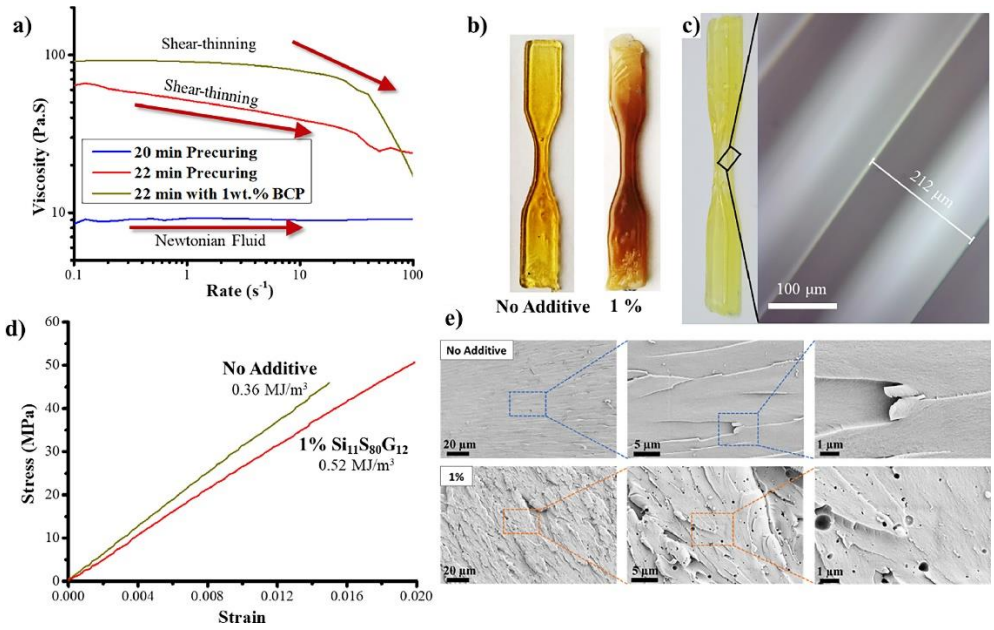

Figure 5.10. *a) ECC resin and its blends with the BCP (1 wt%) were studied for changes to viscosity as a function of shear rate, which clearly show the desired shear thinning behavior of precured prepolymer. b) DIW printed dog bone samples of the ECC and ECC/BCP blends after thermal annealing (b) are shown, along with the c) optical microscopy side view image of the DIW printed ECC sample before thermal annealing showing each printed layer line and the layer thickness. d) The stress-strain responses of the printed tensile bars, along with the fracture surface SEM image e).*

Typically, shape fidelity can be achieved with yield stress fluids (they become solid like with the absence of shear) or an external stimulus can be used (such as photocuring). We chose the latter to preserve the shape. DIW printing was performed using a UV-assisted printing setup whereby layers were extruded onto a build platform, photocured to prevent further deformation, and followed by the extrusion of the next layer onto the previously cured layer (Fig. 5.10(b), Fig. B12). This approach allows for slight under curing enabling further covalent bonding to form between layers creating good layer adhesion. With this process, we were able to print simple multi-layered objects with well-controlled layer height (Fig. 5.10(c), Table B1). Next, we explore if the toughness still increases in the test samples prepared via DIW printing. Two inks were prepared either containing precured pure ECC or pre-cured ECC/BCP (1 wt% $Si_{11}S_{80}G_{12}$) blend. After conducting a tensile test (Fig. 5.10(d)), we observed that the 3D printed pure ECC resin sample exhibited comparable mechanical performance to the mold-cast sample. The modulus, failure strength, and toughness were almost identical, indicating that our established 3D printing protocol did not negatively impact the cured ECC resin's performance. With the BCP additive in ECC, as expected higher toughness

(0.52 MJ/m3), and tensile strength (50.7 MPa), compared to pure ECC (toughness: 0.36 MJ/m3, tensile strength: 45.9 MPa), was observed. However, unlike the cast samples the DIW samples showed a decrease in modulus from 3.4 MPa (for pure ECC) to 2.7 MPa with 1 wt% additive. The fracture surface examined with SEM shows the emergence of a complex topography in BCP added sample (Fig. 5.10(e)) compared to the controlled ECC resin, similar to the intrinsic toughening mechanisms seen in the mold-cast samples (Fig. 5.8).

These results are encouraging as these are to the best of our knowledge, the first examples of DIW of chemically unmodified ECC resin with BCP additives. The reduction in modulus from the cast to the DIW printed samples highlights the challenges of translating bulk properties into printed parts for thermosets such as ECC. These differences we believe are attributable to the pre-curing processes necessary for the DIW process which may alter the overall miscibility of the BCP additive with the base resin. The photocuring process used in the mold-cast samples is very rapid (< 3 min), whereas the thermal precuring process is over a larger time frame of ∼22 min. These differences in the cure kinetics may also play a role in the miscibility of the BCP additive in the base resin. Further optimization of the precuring process/composition of the BCP additive may be necessary to preserve the modulus of the DIW samples.

DLP printing of ECC/Acrylate mixed resin with BCP additive

With the success from DIW printing, we examined the use of brush-coil BCP additive in digital light processing (DLP). DLP is a 3D printing technique that utilizes the fast curing of resin by patterned light to achieve the desired shape. Its fast-printing speed, good scalability and mild working condition [6], are all highly desirable. One drawback of DLP is the limited available resin chemistries. This is partially a result of the fast (∼10 s) photocuring kinetics required for the printing process [42]. This limits the performance of the printed part. In order to expand the application scope of the DLP printing, various approaches have been taken, including the development of new chemistries/photopolymers introducing desired properties [43,44], new processing techniques [45] and additives [42]. Among them, additives stand out as requiring least modification to the existing DLP technology. BCPs are one of the promising candidates for the

toughening of printed objects. To test the application of our brush-coil BCP's in DLP printing, we demonstrated the printing of a mixed ECC/isobornyl acrylate (IBOA) resin with BCP additive.

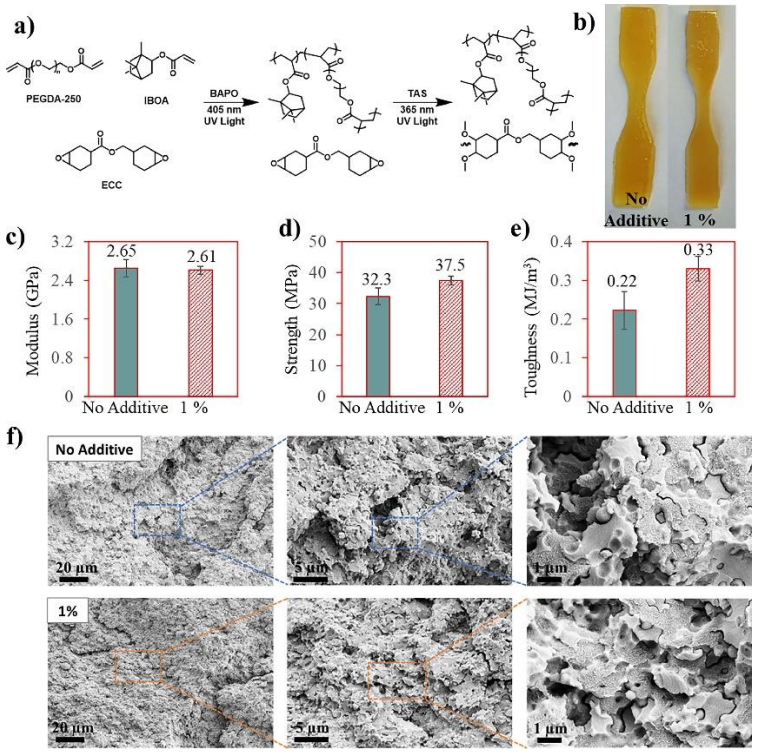

Figure 5.11. *ECC/IBOA 60:40 wt./wt. mixed resin and its blends with the BCP (1 wt%) were studied for a) DLP printing based on the fasting curing kinetic of IBOA and subsequent curing of ECC resin. (b) DLP printed dog bone samples of the ECC/IBOA mixed resin and its blend with BCP (b) are shown, along with the (c) modulus, (d) failure strength and (e) toughness of the cured samples (p value is 0.033). Fracture surface after tensile testing for blends with or without BCP additive were imaged by SEM (f).*

We chose to use an ECC/IBOA 60:40 wt./wt. mixed resin because the pure ECC cures relatively slowly under UV light (~3 min required [46]) and does not meet the requirements for DLP printing. ECC/IBOA mixed resin, on the other hand, solidifies under 30 s and is known to print using the DLP technique [31,[47], [48], [49]]. We printed the resin using a commercial DLP printer that cures the acrylate monomers with 405 nm UV light to form soft acrylate matrix highly swollen in ECC monomer. When postcured with 365 nm UV light, the remaining ECC completely cures to form an interpenetrating acrylate epoxy network that transforms the part into a rigid material (Fig. B13). This process gives well defined shape (Fig. 5.11(b), Fig. B14). Using this process, we printed dog bone samples and performed tensile tests to explore whether there is an improvement in the mechanical performance of the BCP blends

(Fig. 5.11(c)–(e)). When compared with the resin without additive, cured BCP blends show comparable modulus, yet the failure strength and toughness both increased. A 16 % increase in failure strength and 50 % increase in toughness is observed. The fracture topography (Fig. 5.11(f)) interestingly is much more complex for both control and BCP samples than what is observed in DIW printed samples (Fig. 5.10). In fact, the interpenetrating network is clearly visible in the SEM with the smoother surface from ECC intermixed with domains of rougher acrylate resin. The specific effect of BCP additive in DIW is not discernable in the SEM images of the fracture surface, however, is evident in the improved mechanical properties (Fig. 5.11(d)-(e)). The PGMA and PS block of the BCP are compatible with both the ECC and the acrylate resins, hence the BCP domains can form aggregates in both acrylate and epoxy domains. It is also likely that the BCP may be acting as a compatibilizer between the acrylate and the epoxy domains leading to improved toughness.

Conclusion

In summary, BCP poly (MAPDMS-b-S-b-GMA) with a brush-coil architecture has been studied as an additive for the toughening of 3D printable cycloaliphatic epoxy resin. The brush-coil architecture was chosen to impart favorable rheological properties and enhanced phase separation characteristics over their linear counterparts. In cast samples that are rapidly photocured, the toughness of ECC improved 2× with only 1 wt% of BCP additive. Analysis of the tested samples indicates that aggregation induced by the BCP additive leads to intrinsic toughening mechanisms, including microfissure formation and crack arrest and deflection, which may explain the observed synergistic strengthening and toughening. This BCP additive was also compatible with 3D printing process. The BCP/ECC blends as well as BCP-ECC/Acrylate blends were successfully printed using DIW and DLP respectively, and showed improved toughness and strength compared to the base resin. The use of only 1 wt% brush-coil BCP additive compared to the > 10 wt% typically required for linear BCPs, minimizes changes in the viscosity of the resin and therefore enhances the compatibility of this additive with the 3D printing process, by keeping the formulation simple and cost effective. This study offers a route to incorporate reactive BCPs to a 3D printable thermosetting resin.

Careful attention to the cure kinetics, and the induced morphological changes are critical to simultaneously enhance the toughness without compromising on the modulus.

Experimental

Materials: Monomethacryloxypropyl terminated polydimethylsiloxane (MAPDMS) is purchased from Gelest. All other chemicals used in this work are purchased from Sigma-Aldrich. Methyl methacrylate (MMA), glycidyl methacrylate (GMA) and MAPDMS were filtered through a silica gel plug prior to use. Other chemicals were used as received.

Gel Permeation Chromatography (GPC): GPC was done on a Waters GPC using tetrahydrofuran (THF) as mobile phase. The system was running at a flow rate of 1.0 mL/min and column temperature was 40°C. Samples ware dissolved in THF and filtered with 0.2 μm syringe filter (13mm PTFE filter, GE Healthcare). GPC system was calibrated with polystyrene standard.

Nuclear Magnetic Resonance (NMR): NMR spectra were taken on Bruker Avance-400 400MHz spectrometer. Deuterated chloroform (CDCl3) was purchased from Sigma-Aldrich.

Differential Scanning Calorimetry (DSC): DSC was performed on a TA Instruments Q100 in Hermatic Aluminum pan at 10 K/min heating rate. Thermogravimetric analysis was performed on a TA Instruments Q500 under nitrogen atmosphere at 10 K/min heating rate.

Rheology: Rheology was measured on a TA Instruments ARES using 25 mm cone-plate geometry. The measurements were conducted under room temperature and shear rate scanned was 0.01 to 500 s-1 .

Scanning Electron Microscopy (SEM): SEM was performed on a Zeiss LEO 1550VP using in-lens detector. Sample is sputter coated with 5 nm Au conducting layer prior to experiment using a Leica EM ACE600 sputter coater.

Synthesis of Reactive Comb-Coil Copolymer: Triblock reactive comb-coil copolymers are synthesized via a sequential reversible addition-fragmentation polymerization (RAFT) approach.

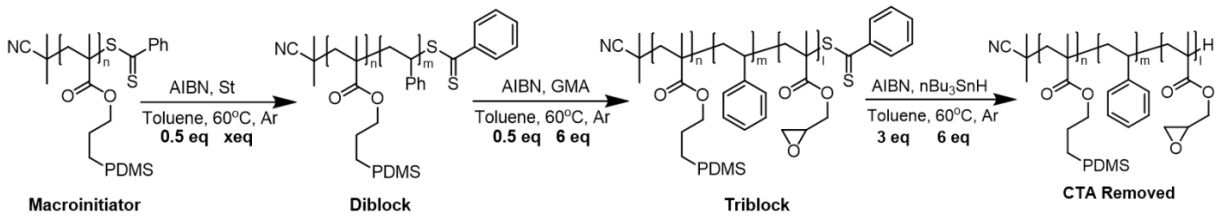

Synthesis of PMAPDMS Macroinitiator: 13.4 mmol of MAPDMS (10.94 g), 1.34 mmol of azobisisobutyronitrile (AIBN, 220.4 mg) and 2.68 mmol of 2-cyano-2-propyl benzodithioate (594.2 mg) and 20 mL of anisole were added to a round bottom flask. Then, the reaction mixture was purged with Ar for 45 minutes. After purging, the reaction is allowed to proceed at 60℃ for 18 hours. The resulting mixture was precipitated in methanol 3 times and dried under vacuum overnight. We achieved pure polymer as a red, viscous liquid. The yield is 8.7840 g (74%). Mn and Đ are determined by GPC to be 6371 g/mol and 1.18.

Synthesis of P(MAPDMS-b-St): 1.5 g PMAPDMS (0.24 mmol) 1.432 g styrene (13.7 mmol, 1.575 mL), 19.9 mg AIBN (0.12 mmol) and 5 mL anisole were added to a Schlenk flask. The reaction mixture is purged with Ar for 30 minutes and heated to 60 ºC for 18 hours. The resulting mixture was precipitated in methanol for 3 times and dried under vacuum overnight. The resulting polymer is a red, soft and tacky solid and yield is 1.6290 g (56%). Mn and Đ are determined by GPC to be 8681 g/mol and 1.16.

Synthesis of P(MAPDMS-b-St-b-GMA): 1.6290 g P(MAPDMS-b-St) (0.19 mmol) 0.204 g GMA (1.43 mmol, 0.191 mL), 19.9 mg AIBN (0.12 mmol) and 5 mL anisole were added to a Schlenk flask. The reaction mixture is purged with Ar for 30 minutes and heated to 60 ºC for 18 hours. The resulting mixture was precipitated in methanol for 3 times and dried under vacuum overnight. The resulting polymer is a red, soft and tacky solid and yield is 1.5448 g (84%). Mn and Đ are determined by GPC to be 8102 g/mol and 1.26.

$Si_{11}S_{80}G_{12}$: Increase the loading of styrene in 2nd step to 2.46 g (98.5 eq.). The resulting polymer is a white, rubbery solid. Mn and Đ are determined by GPC to be 7706 g/mol and 1.38 (Fig B2).

$Si_{11}S_{149}G_5$: Increase the loading of styrene in 2nd step to 3.83 g(153.3 eq.). The resulting polymer is a white, rubbery solid. Yield is . Mn and Đ are determined by GPC to be 9966 g/mol and 1.33 (Fig B3).

$Si_{16}G_{27}$: Skiped the 2nd step. The resulting polymer is a colorless liquid. Mn and Đ are determined by GPC to be 5764 g/mol and 1.10 (Fig B4).

$S_{25}G_1$: Skiped the 1st step. The resulting polymer is a white solid. Mn and Đ are determined by GPC to be 6312 g/mol and 1.12 (Fig B5).

Si_8S_{61}: Skipped the 3rd step. The resulting polymer is a white solid. Mn and Đ are determined by GPC to be 10954 g/mol and 1.26 (Fig B6)

Chain-end substitution of P(MAPDMS-b-St-b-GMA): 1.5448 g P(MAPDMS-b-St) 200 μL tributyltin hydride, 20 mg AIBN and 5 mL anisole were added to a Schlenk flask. The reaction mixture is purged with Ar for 30 minutes and heated to 60 ºC for 18 hours. The resulting mixture was precipitated in methanol for 3 times and dried under vacuum overnight. The resulting polymer is a colorless, soft and tacky solid and yield is 1.4054 g (91%). Mn and Đ are determined by GPC to be 7638 g/mol and 1.22 (Fig B1).

Mold Cast Sample Preparation: The ECC resin, 6 % wt. of 50% wt. TAS solution in propylene carbonate (3% wt. loading of TAS) and a solution of BCP additive in DCM when blending is required was mixed thoroughly and dried under air under constant stirring for 2 hours. The mixed resin was further dried under vacuum overnight. After the drying process was finished, the mixed resin was then carefully poured into a mold made with crosslinked PDMS sheet as side wall and glass slides as top and bottom face. The glass slides were covered with a thin layer of vacuum grease as a releasing agent. The resin in the mold was then cured in SpectroUV XL-1500 Spectrolinker 365 nm UV crosslinking chamber for 5 minutes. The sample after UV curing was then thermally post-cured at 110 °C for 1 hour and 160 °C for 2 hours. After postcuring, the cured parts were carefully removed using an Exacto knife and soaked in hexane and acetone respectively for 30 minutes. The hexane and acetone soaking step is to remove the grease used as mold releasing agent

and epoxy resin monomers and oligomers, respectively. After that, the cured parts are dried under vacuum overnight.

Tensile Test: The quasi-static tensile tests were carried out using an Instron ElectroPulse E3000 universal testing system with a 5 kN loadcell. Elongation of the sample was recorded by taking videos, and the tensile strain was calculated by digital image correlation (DIC) analysis. Three samples of each sample were tested with the tensile strain rate of 10^{-2} s^{-1} . The topography of fracture surface was examined by scanning electron microscopy (SEM) and Zygo white light optical profilometer (spatial resolution: 0.43 μm in lateral and up to 0.1 nm in depth directions

Determination of Diameter of Spherical Aggregates: We analyzed the diameter distributions of the spherical aggregates, from over 100 measurements from the SEM images for the 1% and 5% loaded ECC blends. The average diameter of 1% and 5 % BCP aggregates are 564±98 nm and 502±157 nm, respectively (Fig.B9). Since the spherical aggregates are composed of the BCP bonded to the matrix resin, the measured size does not represent the actual size of aggregates from pure BCP.

Turbidity: The turbidity of ECC-BCP mixture was characterized by measuring the absorption at 500 nm wavelength by UV-Vis spectrometer (Varian Cary 50). The absorption is reported here as the turbidity of the solution.

Direct Ink Write Resin Preparation: The mixed resin was placed in an aluminum weighing pan over a hotplate that was set to 140 °C. It was then heated under vigorous stirring and constantly monitored by removing from the hotplate and cooling down to room temperature and checking the viscosity of the resin. A resin that shows rod-climbing behavior at room temperature is considered ready for print and rheological measurement shows a viscosity between 40-120 Pa·s. The process usually takes 25 minutes on the hotplate

Direct Ink Write Printing: Direct ink write printing was accomplished using a modified Ender 3 by Creality printer (Figure B12). In short, the Ender 3 print head was removed and extruder unplugged from the mother board. A stepper motor driven syringe pump replaced the print head and was plugged into the now vacant

extruder pins on the mother board. A 370 nm Kessil lamp was positioned to illuminate the object after every layer. To accomplish this, the Kessil lamp was plugged into a relay operated through the fan pins on the motherboard and the M106 and M107 Gcode commands were used to toggle the light on and off. To illuminate each layer, postprocessing settings were set to include a timelapse followed by the insert at layer change command. Timelapse settings were set with the M106 command (fan on), 30,000 msec delay, parking of print head such that the object moves under the Kessil lamp, and 5 mm of extra retraction. The insert at layer change worked to turn the Kessil lamp off before the start of the next layer using the M107 command (fan off). Gcode files were loaded onto the printer via Octoprint.

Digital Light Processing Resin Formulating: Resins were formulated using the compositions described in Table B2. To prepare resins, all components were mixed and stored in the dark for 24 hours to allow solid components to dissolve completely. For R2, the addition of the BCP was accomplished by first dissolving the desired amount of BCP in dichloromethane (DCM). The dissolved solution was added to the other resin components and allowed to stir in the dark for 30 minutes with a low stream of dry air flowing over the top of the solution to remove bubbles that may have formed. The mixed solution was then placed under vacuum for 1 hour to remove any remaining DCM. All components in the formulations were used as received and without any additional purification.

Digital Light Processing Printing: DLP printing was done using a commercial Elegoo Mars 3 printer that has a 405 nm light source. Print files were either obtained from Thingiverse or prepared using Autodesk Fusion 360. To print, STL files were uploaded to LycheeSlicer and arranged in the build area. Print parameters for the resins were determined iteratively and are shown in Table B3. Resin R1 and R2 used the same print parameters. After printing, the exterior of parts were washed with isopropyl alcohol and allowed to dry for 30 minutes. The printed parts are then post-cured and thermally annealed following the same protocol used in mold-casted samples.

References

1. N.W. Bartlett, M.T. Tolley, J.T.B. Overvelde, J.C. Weaver, B. Mosadegh, K. Bertoldi, G.M. Whitesides, R.J. Wood, A 3D-printed, functionally graded soft robot powered by combustion, Science (80-.) 349 (2015) 161–165, doi:10.1126/science. aab0129.

2. M. Wehner, R.L. Truby, D.J. Fitzgerald, B. Mosadegh, G.M. Whitesides, J.A. Lewis, R.J. Wood, An integrated design and fabrication strategy for entirely soft, autonomous robots, Nature 536 (2016) 451–455, doi:10.1038/nature19100.

3. A.K. Au, W. Huynh, L.F. Horowitz, A. Folch, 3D-printed microfluidics, Angew. Chemie - Int. Ed. 55 (2016) 3862–3881, doi:10.1002/anie.201504382.

4. F.P.W. Melchels, M.A.N. Domingos, T.J. Klein, J. Malda, P.J. Bartolo, D.W. Hutmacher, Additive manufacturing of tissues and organs, Prog. Polym. Sci. 37 (2012) 1079–1104, doi:10.1016/j.progpolymsci.2011.11.007.

5. A.J. Boydston, B. Cao, A. Nelson, R.J. Ono, A. Saha, J.J. Schwartz, C.J. Thrasher, Additive manufacturing with stimuli-responsive materials, J. Mater. Chem. A. 6 (2018) 20621–20645, doi:10.1039/C8TA07716A.

6. Z. Zhao, X. Tian, X. Song, Engineering materials with light: recent progress in digital light processing based 3D printing, J. Mater. Chem. C. 8 (2020) 13896– 13917, doi:10.1039/d0tc03548c

7. M.A.S.R. Saadi, A. Maguire, N.T. Pottackal, M.S.H. Thakur, M.M. Ikram, A.J. Hart, P.M. Ajayan, M.M. Rahman, Direct ink writing: a 3D printing technology for diverse materials, Adv. Mater. 34 (2022) 1–57, doi:10.1002/adma. 202108855.

8. A.C. Garg, Y.W. Mai, Failure mechanisms in toughened epoxy resins-a review, Compos. Sci. Technol. 31 (1988) 179–223, doi:10.1016/0266-3538(88)90009-7.

9. R. Bagheri, B.T. Marouf, R.A. Pearson, Rubber-toughened epoxies: a critical review, Polym. Rev. 49 (2009) 201–225, doi:10.1080/15583720903048227.

10. L. Ruiz-Pérez, G.J. Royston, J.P.A. Fairclough, A.J. Ryan, Toughening by nanostructure, Polymer (Guildf) 49 (2008) 4475–4488, doi:10.1016/j.polymer. 2008.07.048.

11. D.A. Norman, R.E. Robertson, Rigid-particle toughening of glassy polymers, Polymer (Guildf) 44 (2003) 2351–2362, doi:10.1016/S0032-3861(03)00084-3.

12. Q. Guo, J.M. Dean, R.B. Grubbs, F.S. Bates, Block copolymer modified novolac epoxy resin, J. Polym. Sci. Part B Polym. Phys. 41 (2003) 1994–2003, doi:10.1002/ polb.10554.

13. R.B. Grubbs, J.M. Dean, M.E. Broz, F.S. Bates, Reactive block copolymers for modification of thermosetting epoxy, Macromolecules 33 (2000) 9522–9534, doi:10.1021/ma001414f.

14. S. Ritzenthaler, F. Court, E. Girard-Reydet, L. Leibler, J.P. Pascault, ABC triblock copolymers/epoxy-diamine blends. 2. Parameters controlling the morphologies and properties, Macromolecules 36 (2003) 118–126, doi:10.1021/ma0211075.

15. L. Tao, Z. Sun, W. Min, H. Ou, L. Qi, M. Yu, Improving the toughness of thermosetting epoxy resins: via blending triblock copolymers, RSC Adv 10 (2020) 1603–1612, doi:10.1039/c9ra09183a.

16. F. Nian, J. Ou, Q. Yong, Y. Zhao, H. Pang, B. Liao, Reactive block copolymers for the toughening of epoxies: effect of nanostructured morphology and reactivity, J. Macromol. Sci. Part A Pure Appl. Chem. 55 (2018) 533–543, doi:10.1080/ 10601325.2018.1476826.

17. J. Moon, Y. Huh, S. Kim, Y. Choe, J. Bang, Reactive core-shell bottlebrush copolymer as highly effective additive for epoxy toughening, Chinese J. Polym. Sci. 39 (2021) 1626–1633, doi:10.1007/s10118-021-2614-z.

18. L.C. Jheng, I.H. Wang, T.H. Hsieh, C.T. Fan, C.H. Hsiao, C.P. Wu, M.T. Leu, T.Y. Chang, Toughening of epoxy thermosets with nano-sized or micronsized domains of poly(ethylene oxide)-b-poly(butadiene-co-acrylonitrile)-bpoly(ethylene oxide) triblock copolymers synthesized using room temperature ester coupling reaction, J. Appl. Polym. Sci. 138 (2021) 1–12, doi:10.1002/app. 50096.

19. H.M. Chong, A.C. Taylor, The microstructure and fracture performance of styrene-butadiene-methylmethacrylate block copolymer-modified epoxy polymers, J. Mater. Sci. 48 (2013) 6762–6777, doi:10.1007/s10853-013-7481-8.

20. B. Narupai, A. Nelson, 100th anniversary of macromolecular science viewpoint: macromolecular materials for additive manufacturing, ACS Macro Lett 9 (2020) 627–638, doi:10.1021/acsmacrolett.0c00200.

21. D.A. Rau, M.J. Bortner, C.B. Williams, A rheology roadmap for evaluating the printability of material extrusion inks, Addit. Manuf. 75 (2023) 103745, doi:10. 1016/j.addma.2023.103745.

22. R. d'Arcy, J. Burke, N. Tirelli, Branched polyesters: preparative strategies and applications, Adv. Drug Deliv. Rev. 107 (2016) 60–81, doi:10.1016/j.addr.2016. 05.005.

23. Z. Li, M. Tang, S. Liang, M. Zhang, G.M. Biesold, Y. He, S.M. Hao, W. Choi, Y. Liu, J. Peng, Z. Lin, Bottlebrush polymers: from controlled synthesis, self-assembly, properties to applications, Prog. Polym. Sci. 116 (2021) 101387, doi:10.1016/j. progpolymsci.2021.101387.

24. G. Xie, M.R. Martinez, M. Olszewski, S.S. Sheiko, K. Matyjaszewski, Molecular bottlebrushes as novel materials, Biomacromolecules 20 (2019) 27–54, doi:10. 1021/acs.biomac.8b01171.

25. J. Huang, A. Hall, I. Jayapurna, S. Algharbi, V. Ginzburg, T. Xu, Nanocomposites based on coil-comb diblock copolymers, Macromolecules 54 (2) (2021) 1006– 1016, doi:10.1021/acs.macromol.0c02441.

26. J. Rzayev, Molecular bottlebrushes: new opportunities in nanomaterials fabrication, ACS Macro Lett. 1 (2012) 1146–1149, doi:10.1021/mz300402x.

27. D. Neugebauer, Y. Zhang, T. Pakula, K. Matyjaszewski, PDMS-PEO densely grafted copolymers, Macromolecules 38 (2005) 8687–8693, doi:10.1021/ma0514828.

28. J. Rieger, The glass transition temperature of polystyrene, J. Therm. Anal. 46 (1996) 965–972, doi:10.1007/bf01983614.

29. W. Fan, L. Wang, S. Zheng, Nanostructures in thermosetting blends of epoxy resin with polydimethylsiloxane-block-poly(ε-caprolactone)-block-polystyrene ABC triblock copolymer, Macromolecules 42 (2009) 327–336, doi:10.1021/ ma8018014.

30. I. Tzoumani, A. Soto Beobide, Z. Iatridi, G.A. Voyiatzis, G. Bokias, J.K. Kallitsis, Glycidyl methacrylate-based copolymers as healing agents of waterborne polyurethanes, Int. J. Mol. Sci. (2022) 23, doi:10.3390/ijms23158118.

31. J.J. Schwartz, A.J. Boydston, Multimaterial actinic spatial control 3D and 4D printing, Nat. Commun. 10 (2019) 1–10, doi:10.1038/s41467-019-08639-7.

32. J. Liu, H.J. Sue, Z.J. Thompson, F.S. Bates, M. Dettloff, G. Jacob, N. Verghese, H. Pham, Nanocavitation in self-assembled amphiphilic block copolymermodified epoxy, Macromolecules 41 (2008) 7616–7624, doi:10.1021/ma801037q

33. D. Carolan, A. Ivankovic, A.J. Kinloch, S. Sprenger, A.C. Taylor, Toughening of epoxy-based hybrid nanocomposites, Polymer (Guildf) 97 (2016) 179–190, doi:10.1016/j.polymer.2016.05.007.

34. Q.H. Le, H.C. Kuan, J. Bin Dai, I. Zaman, L. Luong, J. Ma, Structure-property relations of 55 nm particle-toughened epoxy, Polymer (Guildf) 51 (2010) 4867– 4879, doi:10.1016/j.polymer.2010.08.038.

35. K.B. Manning, N. Wyatt, L. Hughes, A. Cook, N.H. Giron, E. Martinez, C.G. Campbell, M.C. Celina, self assembly–assisted additive manufacturing: direct ink write 3D Printing of epoxy–amine thermosets, Macromol. Mater. Eng 304 (2019) 1–16, doi:10.1002/mame.201800511.

36. K. Chen, X. Kuang, V. Li, G. Kang, H.J. Qi, Fabrication of tough epoxy with shape memory effects by UV-assisted direct-ink write printing, Soft Matter. 14 (2018) 1879–1886, doi:10.1039/c7sm02362f.

37. B.G. Compton, J.A. Lewis, 3D-printing of lightweight cellular composites, Adv. Mater. 26 (2014) 5930–5935, doi:10.1002/adma.201401804.

38. M. Invernizzi, G. Natale, M. Levi, S. Turri, G. Griffini, UV-assisted 3D printing of glass and carbon fiber-reinforced dual-cure polymer composites, Materials (Basel) 9 (2016), doi:10.3390/MA9070583.

39. Q. Shi, K. Yu, X. Kuang, X. Mu, C.K. Dunn, M.L. Dunn, T. Wang, H.J. Qi, Recyclable 3D printing of vitrimer epoxy, Mater. Horizons 4 (2017) 598–607, doi:10.1039/c7mh00043j.

40. C.D. Armstrong, L. Yue, F. Demoly, K. Zhou, H.J. Qi, Unstructured direct ink write 3D printing of functional structures with ambient temperature curing dualnetwork thermoset ink, Adv. Intell. Syst. 5 (2023) 2200226, doi:10.1002/aisy. 202200226.

41. W. Voit, K.V. Rao, W. Zapka, Direct-write process for UV-curable epoxy materials by inkjet technology, Mater. Res. Soc. Symp. - Proc. 758 (2003) 93–99, doi:10. 1557/proc-758-ll3.5.

42. A. Medellin, W. Du, G. Miao, J. Zou, Z. Pei, C. Ma, Vat photopolymerization 3d printing of nanocomposites: a literature review, J. Micro Nano-Manufact. 7 (2019), doi:10.1115/1.4044288.

43. G.A. Appuhamillage, N. Chartrain, V. Meenakshisundaram, K.D. Feller, C.B. Williams, T.E. Long, 110th anniversary: vat photopolymerization-based additive manufacturing: current trends and future directions in materials design, Ind. Eng. Chem. Res. 58 (2019) 15109–15118, doi:10.1021/acs.iecr.9b02679.

44. C. Choi, Y. Okayama, P.T. Morris, L.L. Robinson, M. Gerst, J.C. Speros, C.J. Hawker, J. Read de Alaniz, C.M. Bates, Digital light processing of dynamic bottlebrush materials, Adv. Funct. Mater. (2022) 32, doi:10.1002/adfm.202200883.

45. B. Steyrer, B. Busetti, G. Harakály, R. Liska, J. Stampfl, Hot Lithography vs. room temperature DLP 3D-printing of a dimethacrylate, Addit. Manuf. 21 (2018) 209– 214, doi:10.1016/j.addma.2018.03.013.

46. A. Udagawa, Y. Yamamoto, Y. Inoue, R. Chûjô, Physical properties and photoreactivity of cycloaliphatic epoxy resins cured by UV-induced cationic polymerization, Polym. J. 23 (1991) 1081–1090, doi:10.1295/polymj.23.1081.

47. A. Fantoni, J. Ecker, M. Ahmadi, T. Koch, J. Stampfl, R. Liska, S. Baudis, Green monomers for 3D printing: epoxy-methacrylate interpenetrating polymer networks as a versatile alternative for toughness enhancement in additive manufacturing, ACS Sustain. Chem. Eng. (2023), doi:10.1021/acssuschemeng. 3c02194.

48. I. Binyamin, E. Grossman, M. Gorodnitsky, D. Kam, S. Magdassi, 3D printing thermally stable high-performance polymers based on a dual curing mechanism, Adv. Funct. Mater. (2023) 33, doi:10.1002/adfm.202214368.

49. X. Kuang, J. Wu, K. Chen, Z. Zhao, Z. Ding, F. Hu, D. Fang, H.J. Qi, Grayscale digital light processing 3D printing for highly functionally graded materials, Sci. Adv. 5 (2019) 1–10, doi:10.1126/sciadv.aav5790.

Chapter 6: 3D Printing Self Strengthening Architected Material Through Mechanoacid Induced Crosslinking

This chapter summarizes unpublished work.

Chin, K. C. H.; Ouchi, T.; Craig, S.L.; Boydston, A. J. 3D Printing of Self-Indicating and Self Strengthening Material Through Mechanoacid Induced Crosslinking.

Abstract:

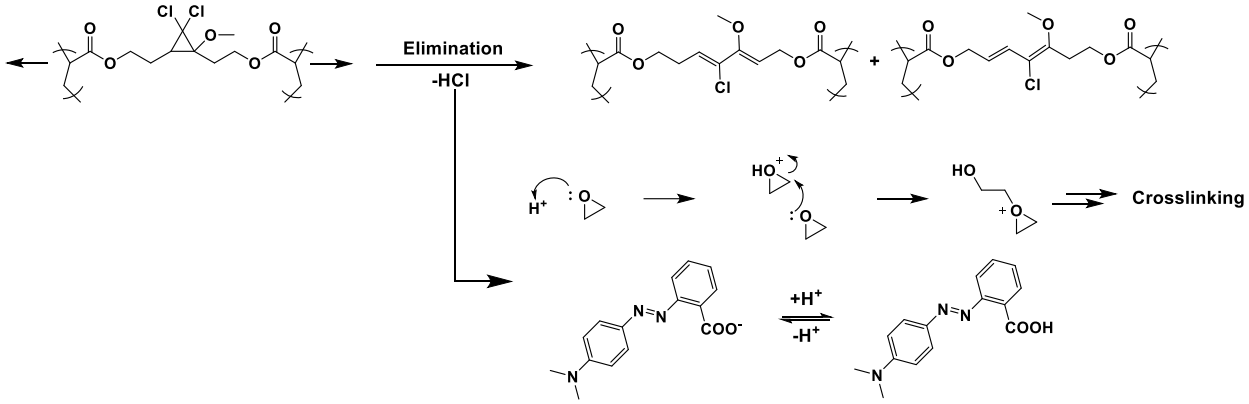

Mechanochemical transduction to yield protons provides pathways toward stress responsive polymeric materials capable of many interesting transformations such as color change, degradation, and strengthening. However, introducing mechanophores into bulk materials is challenging due to low activations. Microstructure has been shown to improve activation of mechanophores in bulk material systems by reducing the strains needed for activation. Complex structures with potential to improve mechanophore activation can be generated using 3D printing. Here we report beginning work toward developing a 3D printing resin that incorporates mechanoacids as the crosslinker. The resin is designed to achieve strains conducive to mechanophore activation as well as incorporate modalities for self-indicating through pH responsive dyes and self-strengthening through additional crosslinking facilitated by ring opening of epoxides.

Introduction:

Access to materials that can change their chemical or physical properties upon applying an external stimulus are of interest for a diverse range of applications from drug delivery,[1] tissue engineering,[2] sensors,[3] coatings,[4] actuators,[5,6] and more.[7–9] These stimuli responsive, also termed 'smart', materials can be designed to be responsive to a range of stimuli from pH,[10] temperature,[11] solvents,[12] light,[13] and even force.[14,15] When triggered, these materials can undergo changes in mechanical properties,[16] shape,[13] color,[17] or reactivity,[14,18] which offers avenues to novel functionality.

Materials capable of responding to force are of special interest due to the possibility of mechanochemical transduction. Mechanochemical transduction is responsible for a range of biological processes such as many of our senses and remodeling in tissue and bone, but difficult to recreate synthetically.[19–22] Polymer mechanochemistry, a field of polymer chemistry focused on creating polymers that respond to external forces, provides a method for highly specific mechanochemical transduction.

The principle behind mechanochemistry stems from early observations by Staudinger in the 1930s that a polymer's molecular weight would reduce when subjected to mastication.[23] Subsequently, Kauzmann and Eyring associate phenomena with mechanical induced breaking of covalent bonds.[24] These bond breaking events were found to predominately occur at the center of a polymer chain where the force is most concentrated during elongation flow.[25,26] It was later found that by introducing weak bonds within a polymer the rate of bond scission increased dramatically[27] and by controlling the location of this weak bond site specific cleavage was possible.[28] This finding was significant as stress sensitive molecules, termed mechanophores, were realized and could be designed and incorporated into a polymer enabling a once destructive event to produce a productive chemical response. Now, many different mechanophores have been discovered enabling diverse range of reactivity and responses.[15,17,18,29–33]

While mechanophore activation in dilute solution has shown a strong dependence on the properties of single chains such as backbone rigidity, molecular weight, and solvent, mechanophore activation in bulk material is less understood due to additional complexity such as chain entanglement, inhomogeneities, and load

transfer from bulk to polymer chains. Furthermore, incorporating mechanophores into solid materials has been met with limited success due to the low activation experienced in bulk polymer networks. Some contributing factors are the high-threshold forces for activation and the requirement of large strains which either prohibits mechanophore activation in the bulk or only facilitates low activation percents.[15] One way to improve activation in bulk materials is through generating architected materials to improve the mechanophore activation at lower strains.[34,35] Therefore, additive manufacturing (AM), commonly referred to as 3D printing, capable of producing materials with complex structures is highly enabling to improve the activation of mechanophores within a network. Beyond this, there is general interest in using AM to create architected materials capable of being manipulated in time and space often leveraging stimuli responsive materials.[7,36]

The proton is one of the most powerful chemical species for a variety of chemical transformations including polymerization/crosslinking[37,38] and polymer degradation.[39,40] Importantly, these transformations often only require catalytic amounts of acid. This versatility makes mechanochemical transduction to create a proton promising for making a variety of valuable stimuli responsive materials. Thus far, several mechanophores that release acid, termed mechanoacids, have been developed.[31,41,42] Of these, Lin et al. synthesized a 2-methoxy substituted gem-dichlorocyclopropane (MeO-gDCC) that is thermally stable and non-scissile. Upon mechanical activation, the mechanophore undergoes rearrangement to a 2,3-dichloroalkene followed by disassociation of chloride and deprotonation.[31] This results in the elimination of HCl which was shown to be generated in dilute pulsed sonication experiments, single molecule force microscopy experiments, and solid-state incorporation in molded silicone elastomers.

With the success of MeO-gDCC previously being incorporated and activated in a polymer network, we wanted to further explore MeO-gDCC by incorporating it as a crosslinker within a photoresin for digital light processing (DLP) AM. Here, we could leverage the unique reactivity of the proton and the geometric freedom AM provides. Additionally, we wanted to leverage the generated acid towards a productive chemical response to create a self-indicating and self-reinforcing materials.

Results and Discussion:

Resin Development

To facilitate mechanophore activation, polymers networks capable of high strains (often exceeding 100%) are needed. Elastomers are preferred as this deformation can be elastic in nature and the initial shape can be recovered if strain to failure is not reached. To form our desired elastomer, 2-hydroxyethyl acrylate (HEA) was chosen as the base monomer which has previously been shown to stretch to over 300% strain,[43] exhibit hyperelasticity under quasistatic tensile conditions,[44] and previously been used with other mechanophores.[45] Additionally, we hypothesized there may be some benefit from the strong hydrogen bonding as such supramolecular interactions can increase the activation of mechanophores by enhancing chain orientation and thus load transfer to mechanophores.[46] We also chose (3,4-epoxycyclohexyl)methyl acrylate (ECMA) as a comonomer to instill self-strengthening by leveraging acid catalyzed cationic ring opening of epoxides to induce crosslinking upon mechanophore activation. Lastly, Phenylbis(2,4,6-trimethylbenzoyl)phosphine oxide (BAPO) was used as the photoinitiator. Compound structures can be found in Figure C1.

Table 6.1. *Resin formulations prepared to screen resins for elastomeric properties and mechanical property changes upon thermal cure of epoxy side groups.*

Resin	HEA (vol %)	ECMA (vol %)	HDDA (vol%)[a]	BAPO (wt%)[b]
R0	100	0	5	1
R1	90	10	5	1
R2	80	20	5	1
R3	70	30	5	1

[a]Vol% compared to total volume of monomers [b]Wt% of compared to total monomers assuming a density of 1 g/mL for each.

First, we tested the mechanical properties of molded material with increasing amounts of ECMA and with 1,6-hexanediol diacrylate (HDDA) as a placeholder crosslinker at a concentration of 5 vol% compared to the total monomer amount (Table 6.1). Increasing the concentration of ECMA would theoretically yield larger changes in mechanical properties upon activation due to higher degree of crosslinking but could be detrimental to the elastomeric properties provided by HEA. To get an idea of the properties of each material tensile samples were prepared by bulk curing with UV light. Quasistatic tensile testing of the samples

showed that increasing the concentration of ECMA resulted in an increase in Young's modulus, and ultimate tensile strength (Figure 6.2). A drop in elongation from ~125% to 90% strain at break was observed with addition of ECMA but increasing amounts from 10 to 20 to 30 vol% did not appear to drop the elongation further below ~90%. The hardness of these samples was also measured and showed that increasing amounts of ECMA led to an increase in the hardness of these materials across the compositions studied.

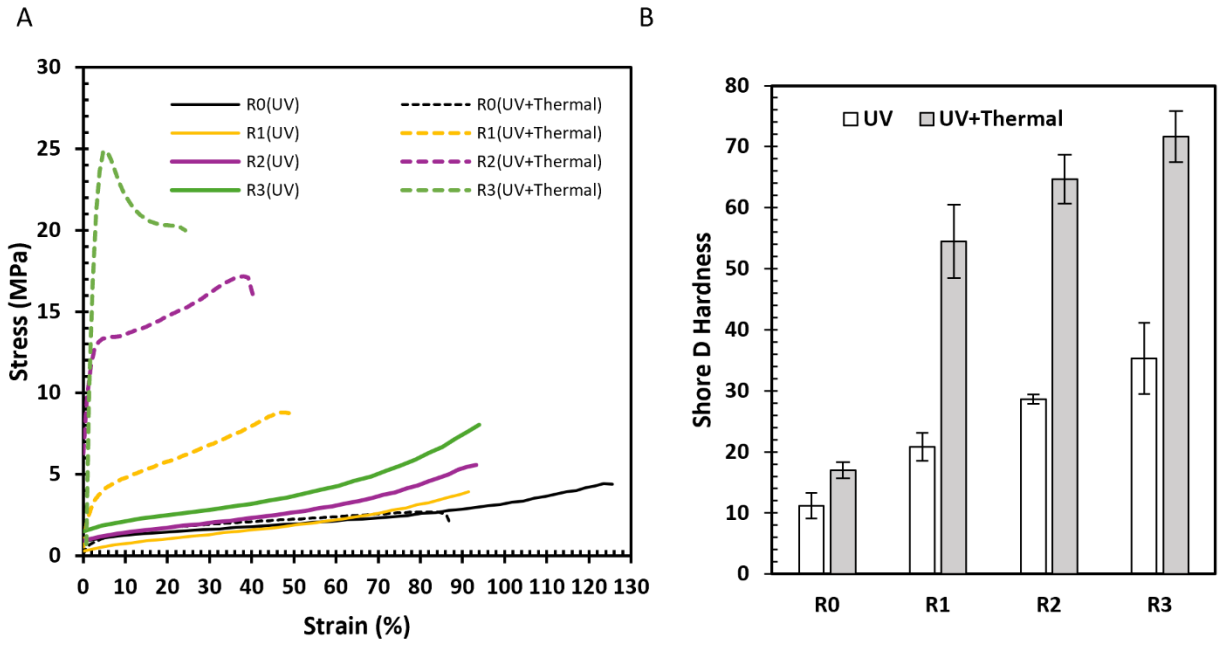

Figure 6.1. *A) Representative stress-strain curves showing the tensile mechanical properties of R0-R3 resins with UV cure and with UV + thermal cure. B) Hardness measurements for R0-R3 samples cured with UV and with UV = thermal cure. Error bars represent the standard deviation of three replicates.*

To better understand the potential change in mechanical property due to additional crosslinking from the pendent epoxy groups, the same resins were bulk cured with UV light and then thermally treated at 200 °C for 1 hour. R1, R2, and R3 had a noticeable change upon removing them from the oven with a slight yellowing occurring, commonly seen in epoxy systems, while R0 appeared relatively unaffected (Figure C2). When tensile properties were retested, R0 which contained no ECMA retained its elastomeric properties, despite a drop in elongation at break to 90%, while R1, R2, and R3 showcased order of magnitude changes in modulus and showcased plasticity. The dramatic change in properties can also be

observed through the changes in shore D hardness of these samples. While all samples had an increase in hardness as a result of thermal treatment, R1, R2, and R3 exhibited large jumps in shore D hardness compared to R0 indicating the pendent epoxy groups are necessary for this change. Additionally, increasing amounts of ECMA appears to increase the upper threshold of modulus, tensile strength, and hardnesses. This is promising if the mechanoacid can induce even a fraction of this change. Notably, thermal crosslinking is not representative of ROP and so mechanical change is not suspected to be the same.

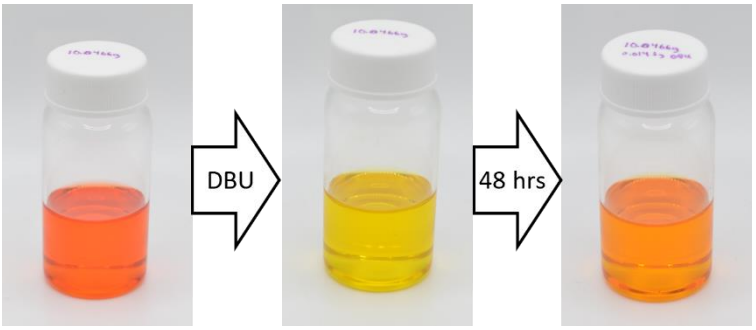

Figure 6.2. *Illustration of the color change that occurs by adding DBU as well as the gradual color shift back to orange.*

To instill self-sensing characteristics, we incorporated methyl red (MR), a known pH responsive dye, as well as 1,8-Diazabicyclo[5.4.0]undec-7-ene (DBU) as a non-nucleophilic organic base to modulate the initial acidity of the network. The idea being we could set the initial acidity such that small changes in pH could result in large changes in color due to the rapid transition from yellow to orange to red intrinsic to methyl red. The amount of DBU was determined by titrating increasing amounts into the resin until color change occurred. Interestingly, within 24 hours the mixture would shift from bright yellow to an intermediate orange color and at 0.2 wt% DBU the mixture was unstable and would polymerize in less than 12 hours presumably via an anionic mechanism. For this reason, we chose 0.15 wt% of DBU which displayed an orange color but was stable from spontaneous polymerization.

To incorporate the MeO-gDCC mechanophore into a network suitable for DLP printing, a derivative was synthesized instilling acrylate functionality to produce MeO-gDCC diacrylate (MeO-gDCC-DA) (Scheme C1). Further experiments and adjustments to formulation are needed to incorporate MeO-gDCC-DA into

the network. Additionally, the ability to achieve high enough activation to induce color change and additional crosslinking will be required. However, initial results are encouraging for a self-sensing and self-strengthening system through mechanoacid incorporation.

Experimental Section

Materials: Phenylbis(2,4,6-trimethylbenzoyl)phosphine oxide (97%), 2-hydroxyethyl acrylate (96 %), 1,6-hexanediol diacrylate (80%), and 1,8-Diazabicyclo[5.4.0]undec-7-ene (98%) were purchased from Sigma Aldrich. Methyl red was purchased from Chem-Cruz. The (3,4-epoxycyclohexyl)methyl acrylate (95%) was purchased from Asta Tech.

Synthesis of MeO-gDCC-DA: MeO-gDCC-DA was synthesized according to previous literature report.[31] Notably, MeO-gDCC-DA was unstable when fully concentrated and so it was synthesized with small amounts of residual solvent. Additionally, 100 ppm of 4-methoxyphenol was used as inhibitor.

Resin Curing in Molds: Resin formulations were cured in a PTFE mold using a 405 nm light source at 10 mW/cm^2 light intensity for 5 minutes. After being removed from the mold, the samples was cured for another 20 minutes on each side at the same intensity.

Tensile Testing: Tensile tests were conducted on a MTS Criterion® Electromechanical Testing System using ASTM D638 type V specimen. The strain rate was set to 10 mm/min for stiff samples and 100 mm/min for elastomeric samples. Tensile strain was measured through video analysis using MATLAB by measuring the distance between series of lines that were drawn on the dogbones in the gauge region prior to testing. Strain was calculated based on the change in distance between the lines on the dogbones. Stress-strain curves were obtained by correlating stress and strain values.

Hardness Measurement: Hardness measurements were conducted using a shore D durometer. Each measurement was taken in triplicate and the average and standard deviation for these measurements reported.

References

1. Yang, Y., Zeng, W., Huang, P., Zeng, X. & Mei, L. Smart materials for drug delivery and cancer therapy. *View* **2**, 20200042 (2021).

2. Municoy, S. *et al.* Stimuli-Responsive Materials for Tissue Engineering and Drug Delivery. *Int. J. Mol. Sci. 2020, Vol. 21, Page 4724* **21**, 4724 (2020).

3. Hu, J. & Liu, S. Responsive polymers for detection and sensing applications: Current status and future developments. *Macromolecules* **43**, 8315–8330 (2010).

4. Hwang, S.-H., Moorefield, C. N. & Newkome, G. R. Stimuli-responsive surfaces for bio-applications. *Chem. Soc. Rev.* **37**, 2512–2529 (2008).

5. van Manen, T., Janbaz, S. & Zadpoor, A. A. Programming the shape-shifting of flat soft matter. *Mater. Today* **21**, 144–163 (2018).

6. Apsite, I., Salehi, S. & Ionov, L. Materials for Smart Soft Actuator Systems. *Chem. Rev.* **122**, 1349–1415 (2022).

7. Xia, X., Spadaccini, C. M. & Greer, J. R. Responsive materials architected in space and time. *Nat. Rev. Mater. 2022 79* **7**, 683–701 (2022).

8. Wei, M., Gao, Y., Li, X. & Serpe, M. J. Stimuli-responsive polymers and their applications. *Polym. Chem.* **8**, 127–143 (2016).

9. Stuart, M. A. C. *et al.* Emerging applications of stimuli-responsive polymer materials. *Nature Materials* vol. 9 101–113 (2010).

10. Dai, S., Ravi, P. & Tam, K. C. pH-Responsive polymers: synthesis, properties and applications. *Soft Matter* **4**, 435–449 (2008).

11. Kotsuchibashi, Y. Recent advances in multi-temperature-responsive polymeric materials. *Polym. J. 2020 527* **52**, 681–689 (2020).

12. Basak, S. & Bandyopadhyay, A. Solvent Responsive Shape Memory Polymers- Evolution, Current Status, and Future Outlook. *Macromol. Chem. Phys.* **222**, 2100195 (2021).

13. Stoychev, G., Kirillova, A. & Ionov, L. Light-Responsive Shape-Changing Polymers. *Adv. Opt. Mater.* **7**, 1900067 (2019).

14. Larsen, M. B. & Boydston, A. J. Investigations in fundamental and applied polymer mechanochemistry. *Macromol. Chem. Phys.* **217**, 354–364 (2016).

15. Abi Ghanem, M. *et al.* The role of polymer mechanochemistry in responsive materials and additive manufacturing. *Nat. Rev. Mater.* doi:10.1038/s41578-020-00249-w.

16. Ramirez, A. L. B. *et al.* Mechanochemical strengthening of a synthetic polymer in response to typically destructive shear forces. *Nat. Chem. 2013 59* **5**, 757–761 (2013).

17. Peterson, G. I., Larsen, M. B., Ganter, M. A., Storti, D. W. & Boydston, A. J. 3D-printed mechanochromic materials. *ACS Appl. Mater. Interfaces* **7**, 577–583 (2015).

18. Hickenboth, C. R. *et al.* Biasing reaction pathways with mechanical force. *Nat. 2007 4467134* **446**, 423–427 (2007).

19. Gillespie, P. G. & Walker, R. G. Molecular basis of mechanosensory transduction. *Nat. 2001 4136852* **413**, 194–202 (2001).

20. Yavropoulou, M. P. & Yovos, J. G. The molecular basis of bone mechanotransduction. *J. Musculoskelet. Neuronal Interact.* **16**, 221 (2016).

21. Martinac, B. Mechanosensitive ion channels: molecules of mechanotransduction. *J. Cell Sci.* **117**, 2449–2460 (2004).

22. Orr, A. W., Helmke, B. P., Blackman, B. R. & Schwartz, M. A. Mechanisms of Mechanotransduction. *Dev. Cell* **10**, 11–20 (2006).

23. Staudinger, H. Über Isopren und Kautschuk, 20. Mitteil.: Über die Kolloidnatur von Kautschuk, Guttapercha und Balata. *Berichte der Dtsch. Chem. Gesellschaft (A B Ser.* **63**, 921–934 (1930).

24. Kauzman, W. & Eyring, H. The Viscous Flow of Large Molecules. *J. Am. Chem. Soc.* **62**, 3113–3125 (1940).

25. May, P. A. & Moore, J. S. Polymer mechanochemistry: techniques to generate molecular force via elongational flows. *Chem. Soc. Rev* **42**, 7497 (2013).

26. Buchholz, B. A., Zahn, J. M., Kenward, M., Slater, G. W. & Barron, A. E. Flow-induced chain scission as a physical route to narrowly distributed, high molar mass polymers. doi:10.1016/j.polymer.2003.11.051.

27. Encina, M. V., Lissi, E., Sarasúa, M., Gargallo, L. & Radic, D. Ultrasonic degradation of polyvinylpyrrolidone: Effect of peroxide linkages. *J. Polym. Sci. Polym. Lett. Ed.* **18**, 757–760 (1980).

28. Berkowski, K. L., Potisek, S. L., Hickenboth, C. R. & Moore, J. S. Ultrasound-induced site-specific cleavage of azo-functionalized poly(ethylene glycol). *Macromolecules* **38**, 8975–8978 (2005).

29. Larsen, M. B. & Boydston, A. J. 'Flex-activated' mechanophores: Using polymer mechanochemistry to direct bond bending activation. *J. Am. Chem. Soc.* **135**, 8189–8192 (2013).

30. Zhang, H. *et al.* Mechanochromism and Mechanical-Force-Triggered Cross-Linking from a Single Reactive Moiety Incorporated into Polymer Chains. *Angew. Chemie Int. Ed.* **55**, 3040–3044 (2016).

31. Lin, Y., Kouznetsova, T. B. & Craig, S. L. A Latent Mechanoacid for Time-Stamped Mechanochromism and Chemical Signaling in Polymeric Materials. (2019) doi:10.1021/jacs.9b12861.

32. Willis-Fox, N., Rognin, E., Aljohani, T. A. & Daly, R. Polymer Mechanochemistry: Manufacturing Is Now a Force to Be Reckoned With. *Chem* **4**, 2499–2537 (2018).

33. Lloyd, E. M., Vakil, J. R., Yao, Y., Sottos, N. R. & Craig, S. L. Covalent Mechanochemistry and Contemporary Polymer Network Chemistry: A Marriage in the Making. *J. Am. Chem. Soc.* **145**, 751–768 (2023).

34. Schwartz, J. J. *et al.* Polymer Chemistry COMMUNICATION Reduced strain mechanochemical activation onset in microstructured materials †. (2020) doi:10.1039/c9py01875a.

35. Rohde, R. C. *et al.* Mechanochromic composite elastomers for additive manufacturing and low strain mechanophore activation. *Polym. Chem.* **10**, 5985–5991 (2019).

36. Shafranek, R. T. *et al.* Stimuli-responsive materials in additive manufacturing. *Prog. Polym. Sci.* **93**, 36–67 (2019).

37. Fu, C., Xu, J. & Boyer, C. Photoacid-mediated ring opening polymerization driven by visible light. *Chem. Commun.* **52**, 7126–7129 (2016).

38. Tsuchimura, T. Recent Progress in Photo-Acid Generators for Advanced Photopolymer Materials.

39. Binauld, S. & Stenzel, M. H. Acid-degradable polymers for drug delivery: a decade of innovation. *Chem. Commun.* **49**, 2082–2102 (2013).

40. Miller, K. A. *et al.* Acid-Triggered, Acid-Generating, and Self-Amplifying Degradable Polymers. *J. Am. Chem. Soc.* **141**, 2838–2842 (2019).

41. Diesendruck, C. E. *et al.* Proton-coupled mechanochemical transduction: A mechanogenerated acid. *J. Am. Chem. Soc.* **134**, 12446–12449 (2012).

42. Nagamani, C., Liu, H. & Moore, J. S. Mechanogeneration of Acid from Oxime Sulfonates. *J. Am. Chem. Soc.* **138**, 2540–2543 (2016).

43. Thrasher, C. J., Schwartz, J. J. & Boydston, A. J. Modular Elastomer Photoresins for Digital Light Processing Additive Manufacturing. *ACS Appl. Mater. Interfaces* **9**, 39708–39716 (2017).

44. Xiang, Y., Schilling, C., Arora, N., Boydston, A. J. & Rudykh, S. Mechanical characterization and constitutive modeling of visco-hyperelasticity of photocured polymers. *Addit. Manuf.* **36**, 101511 (2020).

45. Cao, B., Boechler, N. & Boydston, A. J. Additive manufacturing with a flex activated mechanophore for nondestructive assessment of mechanochemical reactivity in complex object geometries. *Polymer (Guildf).* **152**, 4–8 (2018).

46. Chen, Y. *et al.* Mechanical activation of mechanophore enhanced by strong hydrogen bonding interactions. *ACS Macro Lett.* **3**, 141–145 (2014).

Part Two

Novel 3D Printing Techniques Toward Enhanced Chemical Flexibility

Chapter 7: Additive Manufacturing by Heating at a Patterned Photothermal Interface

Reprinted (adapted) with permission from:

Lee, C.-U., **Chin, K. C. H.** & Boydston, A. J. Additive Manufacturing by Heating at a Patterned Photothermal Interface. *ACS Appl. Mater. Interfaces* **15**, 16072–16078 (2023).

Abstract

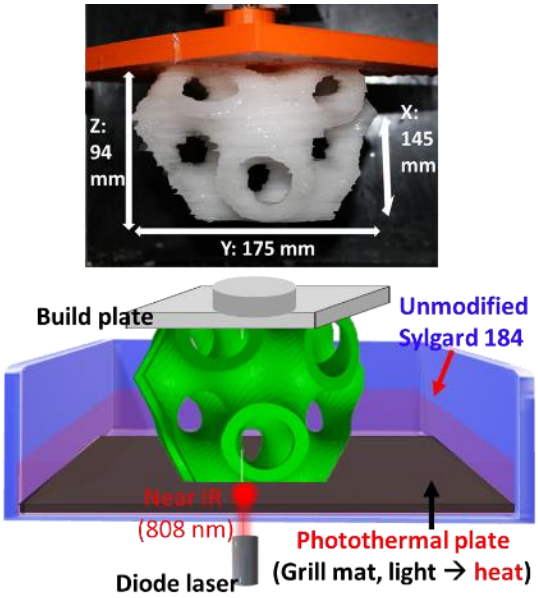

Direct additive manufacturing (AM) of commercial silicones is an unmet need with high demand. We report a new technology, Heating at a Patterned Photothermal Interface (HAPPI), which achieves AM of commercial thermoset resins without any chemical modifications. HAPPI integrates desirable aspects of stereolithography with the thermally driven chemical modalities of commercial silicone formulations. In this way, HAPPI combines the geometric advantages of vat photopolymerization with the materials properties of, for example, injection molded silicones. We describe the realization of the new technology, HAPPI printing using commercial Sylgard 184 PDMS resin, comparative analyses of material properties, and demonstration of HAPPI in targeted applications.

Introduction

Additive manufacturing (AM), often referred to as 3D printing (3DP), creates objects from digital design models often through deposition of build material via layer-by-layer assembly.[1] This offers several advantages to traditional manufacturing as it circumvents molds or other fixed tooling methods and facilitates the direct production of end-use objects. Additionally, this production method gives access to challenging geometric features such as hollow voids, overhangs, and structurally graded designs which are prohibitively difficult to obtain through alternative methods. Furthermore, AM enables multimaterial parts, thus giving new outlooks in design and function.[2] These advantages, along with innovations in materials, hardware, and software, have broadened applications beyond rapid prototyping to fields such as health, personalized medicine, tissue engineering, automotive, aerospace, athletics, and electronics.[3]

Seven AM techniques are summarized in ISO/ASTM 52900: vat photopolymerization (VP), material jetting, binder jetting, material extrusion, power bed fusion (also referred to as selective laser sintering), sheet lamination, and directed energy deposition.[4] Among those techniques, VP is one of the most successful and wide-spread options. In VP, resin is solidified into objects through application of light either volumetrically or in a layer-by-layer fashion. In layer-by-layer techniques, including stereolithography (SLA) and digital light processing (DLP), a layer as thin as 12 μm is cured using light.[5] VP offers excellent geometric freedom and is efficient for producing complex structures that include overhangs or voids. Another advantage in VP is the versatility in processing and types of resins. For example, DLP can be extended to continuous DLP/continuous liquid interface production and SLA to two-photon lithography.[5] Collectively, photocurable resins enable access to a wide range of properties, such as high rigidity, elasticity, and flexibility, as well as formulations that produce ceramics (after VP and then sintering), wax-like parts that can be used as sacrificial molds, and compositions that can be rendered biocompatible.[5]

One of the obvious requirements in light-based technology such as VP is that resins should be photocurable. Acrylates have been found to be the most efficient functional groups for rapid photocuring, and as a result, physical and mechanical properties anticipated from VP are those of photocured acrylates. While the

material properties of these systems can vary, in general, acrylate-based AM gives rise to parts with poor mechanical properties (low modulus and elongation at break) and poor biocompatibility.[6,7] For AM to be more competitive compared to manufacturing by molding and injection, there is high demand for an expanded scope of materials and properties. This makes moving to higher performing thermosets enticing.

Products made from thermoset resins, such as crosslinked urethanes, epoxies, silicones, cyanate esters, or isocyanates, have been of great interest in AM due to their superior physical properties compared to parts made from acrylate-based resins. However, as the name implies, thermoset resins primarily require thermal impetus for curing. Unfortunately, at present, very few AM methods allow for thermally cured thermosets because of the difficulty in producing patterned heat. Thus, the apparent dichotomy exists of having either the geometric freedom of AM or the desirable materials properties of thermosets.

Among thermoset resins, AM of polydimethylsiloxane (PDMS, silicone) elastomers is in high demand for a variety of applications. Silicones have proven biocompatibility, are regarded as food-safe, and display superior mechanical properties compared to products made from acrylate-based resins.[6] Additionally, it has been of great interest to additively manufacture features with complex structures composed of commercial silicone resins, which has motivated various strategies for compatibilizing silicone-based materials with existing AM equipment.[8] Reports show that AM of silicones has been accomplished by direct-ink writing (material extrusion),[9–14] VP,[15–17] and material jetting.[12] Notably, current printing of silicone resins required modification either by imparting photocurable functional groups (i.e., acrylates[16,17] or thiol-ene[15] functionalities) or inclusion of rheological modifiers and fillers.[9–11,13] Unfortunately, compositional changes to the resin that enable AM bring along the caveat of compromised properties. Although it is possible to optimize a new resin toward a particular performance metric, we considered whether there would be a more direct way to enable AM with unmodified, readily available silicones that simply uses traditional Pt-catalyzed hydrosilylation chemistry for curing.

Lear and co-workers reported photothermal curing of silicone resin (Sylgard 184) mixed with photothermal gold nanoparticles by irradiation with 532-nm laser light.[18,19] Doping the resin with photothermal particles

rendered the entire resin sensitive to photothermal transduction, thus enabling spatially resolved curing of the resin. However, adding photothermal dopants modified the chemical and physical properties of the resin as well as the printed parts. For example, incorporation of gold nanoparticles in the resin reduced the Young's modulus by 68% for printed tensile test specimens.[20] AM of silicone resins without any chemical modifications or support bath has rarely been reported.[21] A noteworthy recent advance used focused ultrasound to directly heat specific volumes of silicone resin within the 3D build space.[22] In order to preserve the geometric advantages and broad familiarity of VP with the unaltered materials properties of commercial silicones, we designed a system wherein a photothermal vat is used to achieve AM of a material which otherwise could not be printed in a vat-type setup. We refer to this process as Heating at a Patterned Photothermal Interface (HAPPI) AM.

Results and Discussion

To control the spatial formation of unmodified commercial thermosets using photothermal methods, the energy from the light source would need to be efficiently transduced to heat, which in turn would need to transfer to the resin for localized curing. Inspired by the work of Lear et al.,[18,19] which used photothermal particles distributed within the resin, we envisioned patterned heating of a photothermal plate to circumvent the need for chemical modifications to resins. Taking inspiration from SLA and DLP hardware and workflow designs, we envisioned using a photothermal plate rather than FEP film that would absorb the light's energy with high photothermal efficiency rather than let the light pass through. By controlling the laser or light projection, the light's energy could be transferred to the photothermal plate with spatial precision enabling us to cure resins into specific patterns. By iterating in a layer-by-layer manner, printing of complex objects could be accomplished.

Although using heat for printing gives access to thermoset materials, it adds additional complexity to processing. This is because thermal generation and depletion is not quasi-instantaneous in contrast to photocuring (cf. SLA and DLP). Therefore, for HAPPI to work, judicious choice of the photothermal plate is required to ensure rapid heating (for curing efficiency) as well as cooling (to avoid uncontrolled outgrowth). A photothermal plate should possess the following properties: 1) high light absorptivity, 2)

high photothermal activity for localized heating and fast cooling, 3) low surface adhesion after resin curing, and 4) thermal stability and mechanical durability to endure multiple heating and cooling cycles during printing. These properties will be directly dependent on the physical properties of the material (e.g., heat capacity, density, thermal conductivity, thermal diffusivity, absorptivity, physical dimensions, etc.). Although for most materials these are tabulated quantities, the balance of these for optimal performance in HAPPI was not clear at the outset. For example, high thermal conductivity may lead to fast heat transfer, but says little about the localization of heat. For this, a metric such as thermal diffusivity is required. However, finding a balance between a high thermal conductivity and low thermal diffusivity is nontrivial as this relationship is inversely proportional. In our studies, we adopted an empirical approach to identifying photothermal plates for HAPPI AM.

Table 7.1. *Results of curing Sylgard 184 on photothermal plates using a diode laser*

Photothermal plate	Plate Thickness [mm]	Laser power [W]	Cur Time [sec.]
Black polycarbonate	1.5	4	< 5
		3	< 5
		2	20 ~ 30
		1	No curing
Black plexiglass (PMMA) plate	1.5	4	< 5
		3	10 ~ 15
		2	20 ~ 25
		1	No curing
Crosslinked PDMS with carbon black (1 wt %)	1	4	< 5
		3	< 5
		2	15 ~ 20
		1	No curing
Black PTFE	0.75	4	< 5
		3	5
		2	10
		1	No curing
Black grill mat (fiberglass coated with black PTFE)	0.2	4	< 3
		3	< 3
		2	< 5
		1.5	5 ~ 10
		1	60
Black PTFE A4 thin sheet	0.1	4	< 3
		3	< 3
		2	5
		1	No curing

		4	5
Blue-black steel plate	0.1	3	15 ~ 20
		2	No curing

To identify suitable photothermal materials, we looked at the temperature profiles of seven materials that were commercially available as thin black sheets, each illuminated with an 808-nm laser (Table 7.1, Figure D2 and Table D1). The materials included polycarbonate, acrylic, steel, silicone, and PTFE of various thicknesses. Important metrics were the cure time for a thin layer of Sylgard 184 silicone resin, the size of a localized heating area, and time to cool down after curing (Table D1).[21] For fast curing of Sylgard 184 on a photothermal plate, the local temperature should reach at least 120 °C. Immediate curing (within 5 seconds) of the resin was observed on each of the plastic plates with thicknesses from 0.1 to 1.5 mm. In contrast, it took at least 15 seconds for the steel plate to reach 120 °C (thickness = 0.1 mm). The localized heating area from the plastic plates was found to be much smaller than that from the steel plate, likely due to higher thermal conductivity (250-fold) and thermal diffusivity (80-fold) of the steel plates. Among the plastic plates of similar thermal conductivities, the thinner (0.1- or 0.2-mm thickness) PTFE grill mat or sheet showed smaller heating areas, as well as higher rates of heating and cooling, than thicker ones (1- or 1.5-mm thickness) (Table D1). Additionally, PTFE showed low surface adhesion of the cured resin. The PTFE mat, composed of woven glass fiber with black PTFE coating, showed promising thermal stability and mechanical durability during multiple curing cycles compared to the other plates. As a result, we selected a black PTFE mat as the photothermal plate for HAPPI AM.

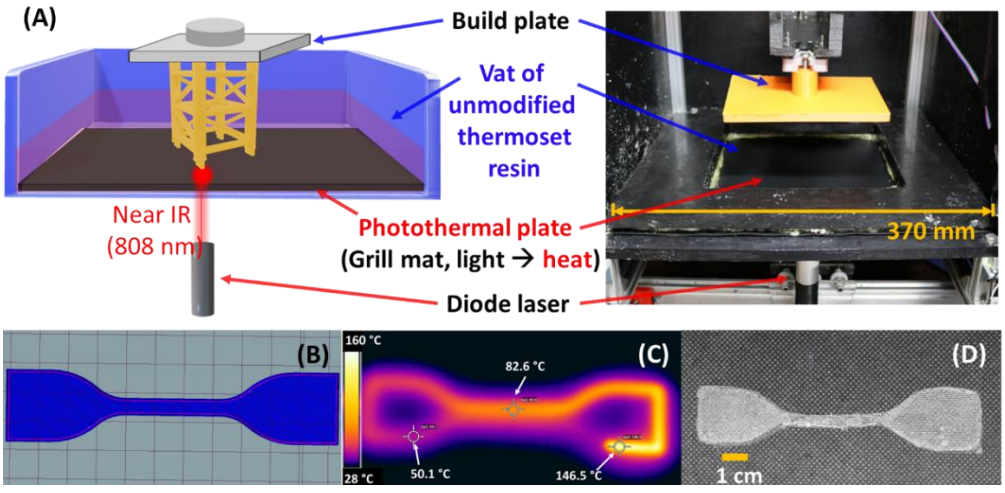

Figure 7.1. *(A) Simplified diagram and actual image of the HAPPI printer. (B) Dogbone CAD model, (C) Photothermal image showing the temperature evolution during printing, and (D) Final single-layer dogbone produced by HAPPI.*

HAPPI AM incorporates many of the desirable design features of classic SLA printing (Figure 7.1). The main differences are the addition of the grill mat on the vat base as well as an 808-nm diode laser to replace a UV- or visible-light laser system. The x-y motion of the diode laser is controlled via a gantry under the vat, while the z-axis build plate position is controlled by an additional stepper motor. Fans assist in dissipating heat from the bulk resin and build plate as well as controlling the temperature of the printing environment. For safety, we operated HAPPI AM inside a light-blocking enclosure. One of the major motivations for HAPPI was the prospect of printing commercial resins without compositional modifications. To investigate this, Sylgard 184, a commercial PDMS resin produced by DOW, was chosen. Initially, single layer samples were produced to prove viability of the HAPPI method (Figure 7.1B, C and D). Cured material that remained intact was observed at print peed of 200 mm/min or less. Altering the raster speed slower than 200 mm/min resulted in severe outgrowth (Figure D3). The best resolution was found to be 2.9 mm as shown in Figure D3.

Despite identical chemical compositions, processing methods can alter final material properties. One concern was whether forming the part through a rastering process would impact the material properties compared to curing of resin in a mold. To investigate, mechanical properties of single layer tensile samples produced from a 10:1 weight ratio of base to curing agent were compared with molded samples of the same composition. We found that the Young's modulus, tensile strength, and elongation at break of single-layer HAPPI samples were comparable with those of molded samples (Figure 7.2A and Table 7.2). As we moved toward multilayer prints, we found that adjusting the base to curing agent ratio to 10:4 by weight, and including a common diluent (1,3-divinyltetramethyldisiloxane) in small quantities provided a lower viscosity formulation as well as an extended resin pot life (4 to 6 hours), which were advantageous. To test the effect of layers produced during HAPPI AM, we examined multilayered tensile and compression samples made from a 10:4:0.5 weight ratios of base, curing agent, and diluent. The results showed that the Young's modulus of the HAPPI samples reached 72% that of molded variants (Table 7.2). Strain at break

of the HAPPI samples was comparable with that of molded samples for uniaxial tensile testing of dogbone specimens (Figure 7.2A and B). The compressive modulus and strength of the HAPPI samples, assessed for cylindrical test specimens, reached 66% and 70% of molded samples, respectively (Figure 7.2C). We speculate that the lower Young's modulus and properties under compression from HAPPI are a result of layer adhesion issues and small bubbles within the final parts. These bubbles are likely introduced during the movement of the build stage between layers as even resin that had been degassed was prone to small amounts of bubble formation during printing. In contrast, no bubbles formed when a single layer dogbone was cured without the build plate (Figure 7.2A).

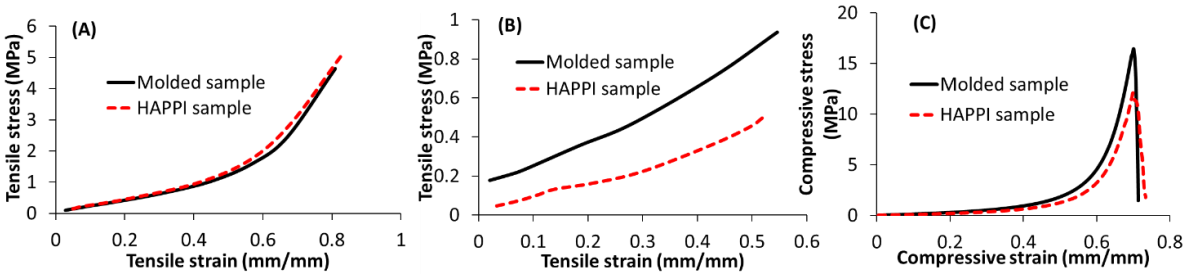

Figure 7.2. *Representative comparisons between samples produced by HAPPI versus traditional molding. (A) Results from tensile tests on single-layered dogbones (ASTM D412-C), (B) Results from tensile tests on multi-layered dogbones (ASTM D412-C, 20 layers), and (C) Results from compressive tests on multi-layered cylinders (ASTM 575-91, 120 layers).*

Table 7.2. *Comparisons between samples produced by HAPPI versus traditional molding shown in Figure 7.2.*

Loading[a)]	Formulation[b)]	Elastic Modulus [MPa]		Ultimate Strength [MPa]		ε at break [%]	
		HAPPI	Molded	HAPPI	Molded	HAPPI	Molded
Tensile (A)	10:1:0	1.8 ± 0.4	2.1 ± 0.2	4.4 ± 0.7	3.9 ± 0.7	86 ± 3	75 ± 5
Tensile (B)	10:4:0.5	0.8 ± 0.1	1.1 ± 0.3	0.51 ± 0.04	0.8 ± 0.1	50 ± 2	49 ± 6
Compression (C)	10:4:0.5	0.77 ± 0.03	1.17 ± 0.09	12 ± 1	16.9 ± 0.9	70 ± 0.7	70 ± 2

a) All the samples were post-cured at 150 ˚C for 15 minutes. Values for molded samples are listed in parentheses. Values represent average of three experiments, errors represent one standard deviation. b) Weight ratio of base, curing agent, and diluent.

We also studied the effect of layers on anisotropic mechanical properties in final objects. Cubes were prepared and subjected to uniaxial compression testing along different orientations. Figure 7.3 and Table

7.3 show results from compressive tests on cubes at 0° and 90° orientation relative to the print direction. The compressive modulus and strain at break from samples at 0° were comparable with those at 90°. When samples ruptured, we noticed that failure upon compression at 90° was localized to regions between layers. The weaker interfaces between layers explains the resulting ultimate compressive strength for compression at a 90° orientation being about 47% of the value obtained for compression at a 0° orientation.

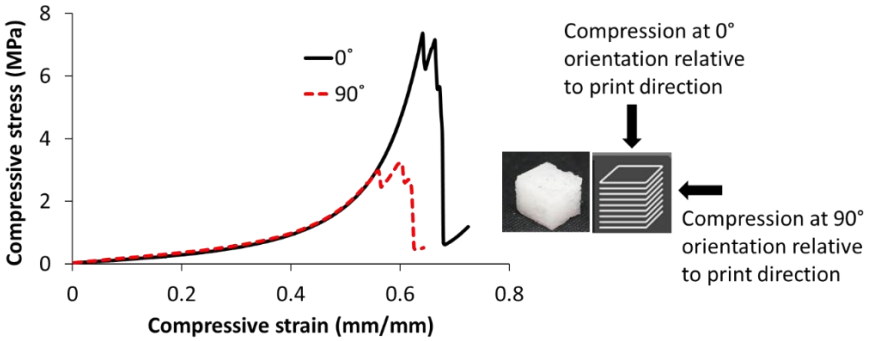

Figure 7.3. *Results from compressive tests on cubes made by HAPPI, compressed at 0- or 90-degree orientation to the print direction.*

Table 7.3. *Results from compressive tests on cubes at 0- or 90-degree orientation to the print direction.*

Orientation	Elastic Modulus [MPa]	Ultimate Strength [MPa]	ε at break [%]
0°	1.3 ± 0.1	6.6 ± 0.7	66 ± 2
90°	1.59 ± 0.03	3.1 ± 0.2	61 ± 1

Samples prepared by HAPPI AM also showed comparable swelling behavior, gel fraction, and thermal stability when compared with parts produced via molding. Table 7.4 shows swelling percentages by volume and mass for samples produced by HAPPI AM and molding. We evaluated swelling and gel fraction in toluene and xylenes, which are good solvents for the base and curing agent of Sylgard 184, and in 2-propanol since it is a common wash solvent for AM processing. In toluene, HAPPI samples showed 209% increase by volume and 187% increase by mass, whereas molded parts showed 215% increase by volume and 191% increase by mass. Across all solvents, each of the HAPPI samples maintained their shape for at least two weeks without any visible signs of delamination. The high extent of curing as well as the consistent chemical composition between HAPPI and molded parts was also supported by thermogravimetric analysis (TGA) data (Figure 7.4). TGA thermograms of parts made from each of the formulations studied herein

showed similar behavior between HAPPI and molded samples. For samples made from the 10:1 weight ratio of base to curing agent, the TGA profile of HAPPI and molded samples were essentially identical up to 450 °C, where only slight deviation was observed at higher temperatures. For samples made from the 10:4:0.5 weight ratio of base, curing agent, and diluent, the TGA profile of HAPPI samples was found to be the same as that of molded samples up to 500 °C before any slight deviations were noticeable.

Table 7.4. *Swelling behavior and gel fraction of HAPPI and molded samples*

Solvent	Volume change [%][a)]		Mass change [%][a)]		Gel fraction [%][b)]	
	HAPPI	Molded	HAPPI	Molded	HAPPI	Molded
toluene	209 ± 9	215 ± 10	187 ± 12	191 ± 9	96 ± 0.2	95 ± 1
xylenes	226 ± 10	202 ± 2	200 ± 5	190 ± 8	96 ± 0.01	95 ± 1
2-propanol	122 ± 5	125 ± 7	117 ± 1	118 ± 4	96 ± 0.3	96 ± 0.2

a) Samples were submerged in the solvent for 72 h. Volumes were calculated based on the dimensions using a digital caliper and masses were recorded by analytical balance. b) Gel fraction was calculated by the ratio of mass of an original sample to that of the dried sample after soaking in the solvent.

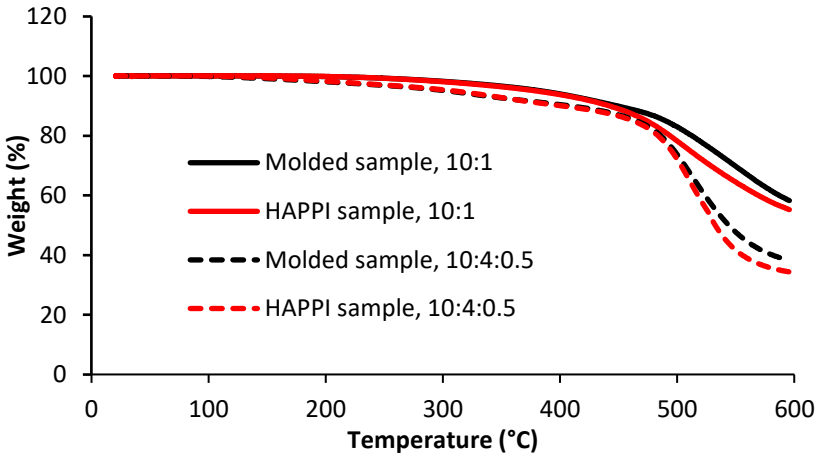

Figure 7.4. *TGA thermograms of HAPPI (red) and molded (black) samples produced from 10:1:0 (solid lines) or 10:4:0.5 (dashed lines) weight ratios of base to curing agent to diluent.*

We next investigated the dimensional accuracy and utility of HAPPI when challenged by objects with complex geometries. HAPPI AM of multi-layered, three-dimensional objects was done without any chemical modifications or supports. Successful HAPPI prints of an overhang, open tube, and gyroid are each depicted in Figure 7.5. For comparison across the series of HAPPI prints, we compared the dimensions of the as-designed (digital files, Figure D4) objects with the as-printed outcomes. Agreement along the x- and y-axis were excellent in each case, whereas heights of the HAPPI objects along the z-axis were found

to be ca. 13 - 16% less than those specified in the digital files. The z-axis disparity was likely due to mechanical compression of the layers as the build plate was brought down into near-contact with the vat bottom.

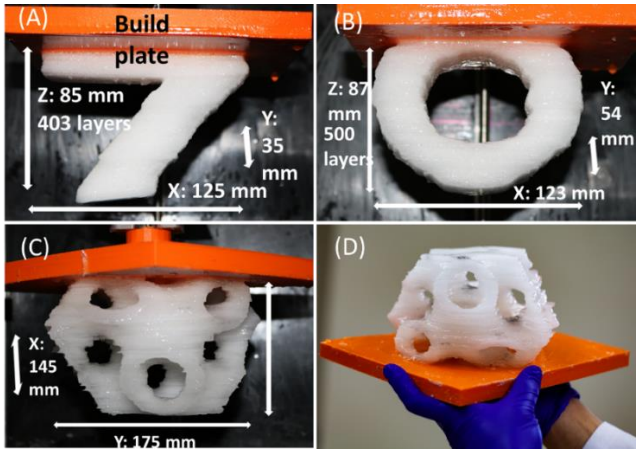

Figure 7.5. *HAPPI AM of multi-layered objects of Sylgard 184 (A) Overhang (403 layers), (B) Open tubes (500 layers), and (C), (D) Gyroid (562 layers); each printed without any supports.*

We next examined an open tube structure via SEM with representative results depicted in Figure 7.6. For reference, the HAPPI printed open tube structure is shown in Figure 7.5B. In Figure 7.6A, interfaces between layers were found to be strong without any delamination, which may be caused by hot bonding between a layer undergoing curing and the preceding layer. The layer spacing was found to 10 to 50 µm as assessed by ImageJ, which is much lower than the as-designed layer thickness of 200 µm. These results support the z-axis disparity observed between the as-designed and as-printed structures, and further suggest new layers were cured on the previous layers by the residual heat. Pores or bubbles were also observed across the section (Figure 7.6B), where stress concentrations would occur during tensile tests, causing lower mechanical properties of multilayered dogbones as detailed in Figure 7.2 and Table 7.2. Pore sizes varied from 10 to 88 µm with an average of 32 (± 25) µm by ImageJ analysis on 12 pores in the image.

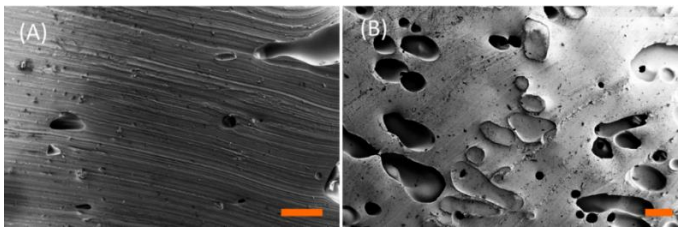

Figure 7.6. *SEM cross-sectional images of an open tube in Figure 5 (A) across or (B) along layer lanes (scale bar = 300 µm).*

Notably, HAPPI can achieve relatively large print areas. For example, we applied the HAPPI technology to AM of a skull cap of Sylgard 184 with an end-to-end length of 195 mm (Figure 7.7). Once again, the final part was achieved without the use of supports, as can be seen in the intermediate pictures taken after 154 and 263 layers were printed (Figure 7.7B and 7.7C, respectively). In consideration of potential applications of devices such as a skull cap for impact testing, we also investigated the ability to use HAPPI to produce mechanochromic silicone parts by incorporating a spiropyran (SP) mechanophore into the resin formulation. We used a divinyl-terminated SP mechanophore at 0.2 wt% in Sylgard 184 and additively manufactured the skull cap by HAPPI. Figure 7E shows the printed skull cap, mechanochromism after applied mechanical force, and photochromism after irradiation with UV light from a laser pointer. These results show the mechanochromic activities of the skull cap by HAPPI AM, indicating that the SP was covalently bonded to Sylgard 184 during HAPPI. Although the temperature exceeded 120 °C during HAPPI (above the decomposition temperature of the SP moiety), rapid cooling within 5 seconds after curing the resin sufficiently precluded the decomposition of SP, preserving the mechanochromic and photochromic activities (Figure 7.7F and 7.7G).

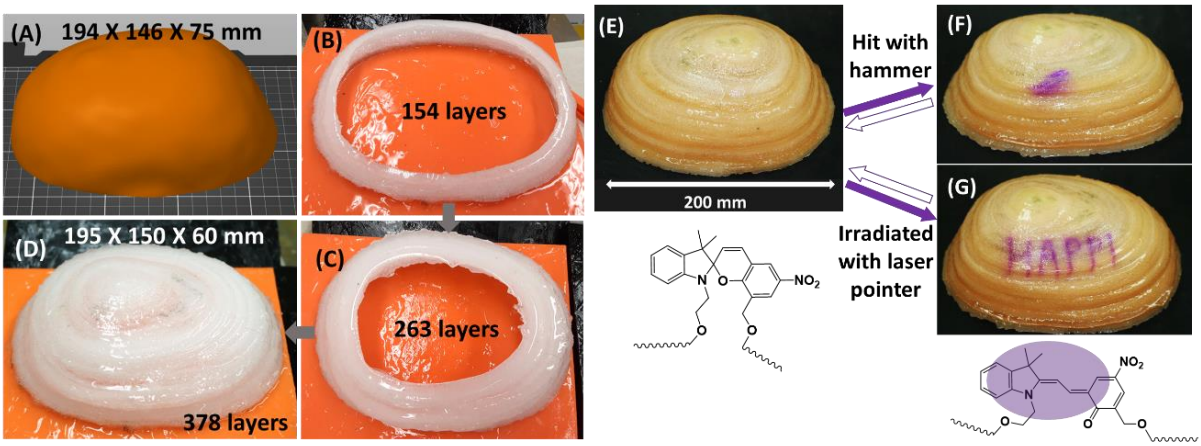

Figure 7.7. *HAPPI AM and activation of a skull cap of Sylgard 184: (A) Digital file image, (B), (C) and (D) printed skull cap at 154, 263, and 378 layers, respectively, showing an empty space inside of the skull cap, (E) skull cap of Sylgard 184 with SP mechanophores (0.2 wt%), F) the skull cap after mechanical impact, and (G) after irradiation with a laser pointer.*

Conclusion

This study reports a new AM technology for processing thermally cured thermoset resins using patterned heat. By combining the geometric freedom of VP setups with a photothermal plate, we demonstrated AM of simple silicone dogbones to overhangs and complex gyroids all without any chemical modifications of the resin or supports. Mechanical, tensile, and compressive properties of HAPPI samples were found to be comparable to those of molded ones. In future developments, we anticipate HAPPI AM could be compatible with other thermoset resins including oligomers or monomers containing high performance functional groups such as epoxides, urethanes, cyanate esters, trifluorovinylether or phenylethynyl groups, as well as polyamic acids.

Experimental Section

Materials: Sylgard 184 silicone elastomer kit was purchased from Ellsworth. Diluent 1,3-divinyltetramethyldisiloxane was purchased from TCI Chemicals. GPL 107 fluorinated oil was purchased from Krytox. PTFE grill mats of 0.2-mm thickness and A4 sheets of 0.1-mm thickness were each purchased from Amazon.com. Carbon black was purchased from Alfa Aesar. Black polycarbonate of 1-mm thickness and black acrylic sheet of 1.5-mm thickness were each purchased from ePlastics. Black steel shim sheets were purchased from Precision Brand. All materials purchased from commercial sources were used as received. Pentenoyl-functionalized spiropyran mechanophore was prepared from reports by Peterson et al. and Gossweiler et al.[23,24]

Resin Preparation: For single layer printing, the resin was prepared by mixing base and curing agent (10:1 by weight). For multi-layers, resin was prepared by mixing base and crosslinker (10:4 by weight) without or with a small molecule diluent, 1,3-divinyltetramethyldisiloxane at the amount up to 0.5 wt% of the resin (Figure D1). The additional crosslinker was used to reduce the viscosity of the system while the small molecule diluent helped to increase the pot life. Resin containing mechanophore was was prepared by mixing base and crosslinker (10:4 by weight) with an additional 0.2 wt% mechanophore. Resin was used immediately after preparation due to the pot life of the resin under ambient conditions.

Printing: GPL 107 was spread manually on the grill mat to reduce surface adhesion. The resin was then added to the vat. The vat was a square cylinder (370×370 mm, void: 300×300 mm) made from HDPE plates. The open bottom of the vat was covered by a grill mat that was glued to the HDPE vat. Repetier-host was used to load STL files slice and operate printing. The STL files were converted to G code files using Slic3r. Diode laser with a wavelength of 808 nm was purchased from Opto Engine LLC (Midvale, UT, USA). The laser light is directed through a fiber optic cable and a collimator creating a 365 um beam diameter. Laser power was set to 5 W and print speeds were varied by altering the G code to control degree of curing. Distance between the collimator of the laser and bottom of vat was fixed to 15 mm. Major print speed was set to 600 mm/min for multilayers and 3000 mm/min for single layers. The cured layers on the build plate were cooled between layers from 20 seconds for small objects (cylinders or cubes) to 60 seconds

for large ones (gyroids or skull cap). Layer thickness was set to 0.2 mm. STL files for gyroid and ASTM 412-C tensile samples were obtained from open sources, GrabCAD or Thingiverse. The STL file for the skull cap was obtained from Army Research Lab. All other STL files were created by using Autodesk Tinkercad. Marlin, the open-source firmware, was used to run the G codes.

Mechanical Testing: ASTM D412-C samples for tensile testing and ASTM D575-91 samples for compressive testing were prepared by HAPPI or Teflon molds. The multilayered tensile samples consisted of 20 layers while the multilayered compression samples were 120 layers. The multilayer cubes (approximately 15 × 15 × 15 mm^3, 75 layers) were cut from a printed rectangular prism (123 × 30 × 15 mm^3). All samples were post-cured at 150 °C for 15 minutes. Tensile testing was conducted using the MTS Criterion Model 43 with 50kN load cell at an extension rate of 254 mm/min.[25] For uniform pressure distribution across the silicone elastomer, PMMA plates (23 × 20 × 4 mm^3) were attached on both sides of the sample grips with an adhesive tape.[25] Elongation of the sample with line-marks were recorded by taking videos and strain was calculated by image analysis. Average values from three runs were reported. Compressive tests were done by the MTS machine at 20 mm/min of crosshead velocity. To prevent excessive friction between disks and samples and barreling,[25] GPL 103 was applied to both surfaces of cylinders prior to testing.

Swelling behavior, gel fraction, thermal analysis and SEM: Swelling behavior of HAPPI samples (single layer) and molded ones was studied by submerging the samples in toluene, xylenes, or isopropyl alcohol for 72 h, removing, and patting on paper. Average masses of three samples were recorded by analytical balance and volumes were calculated based on the dimensions using a digital caliper. Gel fraction was calculated by the ratio of mass of an original sample to that of dried sample after soaking in the solvent. Thermogravimetric analysis (TGA) was conducted on a TA TGA Q50 under nitrogen from room temperature to 600 °C at a rate of 10 °C/min. Samples for SEM were cut across or along layer lines of an open tube (shown in Figure 7.5) using a razor blade. The samples were then sputter-coated using the Leica EM ACE600 with a 10 nm layer of gold. Scanning electron microscopy (SEM) was conducted using a Zeiss Gemini SEM 450 at an accelerating voltage of 5 to 10 kV.

References

1. Lee, C.-U.; Vandenbrande, J.; Goetz, A. E.; Ganter, M. A.; Storti, D. W.; Boydston, A. J. Room Temperature Extrusion 3D Printing of Polyether Ether Ketone Using a Stimuli-Responsive Binder. *Addit. Manuf.* **2019**, *28*, 430–438.

2. Schwartz, J. J.; Boydston, A. J. Multimaterial Actinic Spatial Control 3D and 4D Printing. *Nat. Commun.* **2019**, *10*, 1–10.

3. Appuhamillage, G. A.; Chartrain, N.; Meenakshisundaram, V.; Feller, K. D.; Williams, C. B.; Long, T. E. 110th Anniversary: Vat Photopolymerization-Based Additive Manufacturing: Current Trends and Future Directions in Materials Design. *Ind. Eng. Chem. Res.* **2019**, *58*, 15109–15118.

4. ASTM International. Additive Manufacturing, Design, Functionally Graded Additive Manufacturing, ISO/ASTMTR52912-EB; West Conshohocken, PA, 2021. DOI: 10.1520/20200034

5. Pagac, M.; Hajnys, J.; Ma, Q. P.; Jancar, L.; Jansa, J.; Stefek, P.; Mesicek, J. A Review of Vat Photopolymerization Technology: Materials, Applications, Challenges, and Future Trends of 3d Printing. *Polymers (Basel)* **2021**, *13*, 1–20.

6. Eggbeer, D.; Bibb, R.; Evans, P.; Ji, L. Evaluation of Direct and Indirect Additive Manufacture of Maxillofacial Prostheses. *Proc. Inst. Mech. Eng. H* **2012**, *226*, 718–728.

7. Sano, Y.; Matsuzaki, R.; Ueda, M.; Todoroki, A.; Hirano, Y. 3D Printing of Discontinuous and Continuous Fibre Composites Using Stereolithography. *Addit. Manuf.* **2018**, *24* (October), 521–527.

8. Liravi, F.; Toyserkani, E. Additive Manufacturing of Silicone Structures: A Review and Prospective. *Addit. Manuf.* **2018**, *24* (January), 232–242.

9. Ji, Z.; Jiang, D.; Zhang, X.; Guo, Y.; Wang, X. Facile Photo and Thermal Two-Stage Curing for High-Performance 3D Printing of Poly(Dimethylsiloxane). *Macromol. Rapid Commun.* **2020**, *41*, 1–8.

10. Zhou, L. Y.; Gao, Q.; Fu, J. Z.; Chen, Q. Y.; Zhu, J. P.; Sun, Y.; He, Y. Multimaterial 3D Printing of Highly Stretchable Silicone Elastomers. *ACS Appl. Mater. Interfaces* **2019**, *11*, 23573–23583.

11. Tang, Z.; Jia, S.; Zhou, C.; Li, B. 3D Printing of Highly Sensitive and Large-Measurement-Range Flexible Pressure Sensors with a Positive Piezoresistive Effect. *ACS Appl. Mater. Interfaces* **2020**, *12*, 28669–28680.

12. Liravi, F.; Toyserkani, E. A Hybrid Additive Manufacturing Method for the Fabrication of Silicone Bio-Structures: 3D Printing Optimization and Surface Characterization. *Mater. Des.* **2018**, *138*, 46–61.

13. Duoss, E. B.; Weisgraber, T. H.; Hearon, K.; Zhu, C.; Small IV, W.; Metz, T. R.; Vericella, J. J.; Barth, H. D.; Kuntz, J. D.; Maxwell, R. S.; Spadaccini, C. M.; Wilson, T. S. Three-Dimensional Printing of Elastomeric, Cellular Architectures with Negative Stiffness. *Adv. Funct. Mater.* **2014**, *24*, 4905–4913.

14. Zhang, H.; Qi, T.; Zhu, X.; Zhou, L.; Li, Z.; Zhang, Y. F.; Yang, W.; Yang, J.; Peng, Z.; Zhang, G.; Wang, F.; Guo, P.; Lan, H. 3D Printing of a PDMS Cylindrical Microlens Array with 100% Fill-Factor. *ACS Appl. Mater. Interfaces.* **2021**, *13*, 36295–36306.

15. Zhao, T.; Yu, R.; Li, S.; Li, X.; Zhang, Y.; Yang, X.; Zhao, X.; Wang, C.; Liu, Z.; Dou, R.; Huang, W. Superstretchable and Processable Silicone Elastomers by Digital Light Processing 3D Printing. *ACS Appl. Mater. Interfaces* **2019**, *11*, 14391–14398.

16. Thrasher, C. J.; Schwartz, J. J.; Boydston, A. J. Modular Elastomer Photoresins for Digital Light Processing Additive Manufacturing. *ACS Appl. Mater. Interfaces* **2017**, *9*, 39708–39716.

17. Bhattacharjee, N.; Parra-Cabrera, C.; Kim, Y. T.; Kuo, A. P.; Folch, A. Desktop-Stereolithography 3D-Printing of a Poly(Dimethylsiloxane)-Based Material with Sylgard-184 Properties. *Adv. Mater.* **2018**, *30*, 5950-5935.

18. Fortenbaugh, R. J.; Lear, B. J. On-Demand Curing of Polydimethylsiloxane (PDMS) Using the Photothermal Effect of Gold Nanoparticles. *Nanoscale* **2017**, *9*, 8555–8559.

19. Lear, B. J.; Fortenbaugh, R. J. Photothermal Curing of Thermoset Resins. WO2018204817A1, 2018.

20. Fortenbaugh, R. J.; Carrozzi, S. A.; Lear, B. J. Photothermal Control over the Mechanical and Physical Properties of Polydimethylsiloxane. *Macromolecules* **2019**, 52, 3839–3844.

21. Boydston, A. J.; Lee, C.-U. Additive Manufacturing with Curable Compositions. US 20200406539A1, 2020.

22. Habibi, M.; Foroughi, S.; Karamzadeh, V.; Packirisamy, M. Direct Sound Printing. *Nat. Commun.* **2022**, *13*, 1–11.

23. Peterson, G. I.; Larsen, M. B.; Ganter, M. A.; Storti, D. W.; Boydston, A. J. 3D-Printed Mechanochromic Materials. *ACS Appl. Mater. Interfaces* **2015**, *7*, 577–583.

24. Gossweiler, G. R.; Hewage, G. B.; Soriano, G.; Wang, Q.; Welshofer, G. W.; Zhao, X.; Craig, S. L. Mechanochemical Activation of Covalent Bonds in Polymers with Full and Repeatable Macroscopic Shape Recovery. *ACS Macro. Lett.* **2014**, *3*, 216–219.

25. Johnston, I. D.; McCluskey, D. K.; Tan, C. K. L.; Tracey, M. C. Mechanical Characterization of Bulk Sylgard 184 for Microfluidics and Microengineering. *J. Micromech. Microeng.* **2014**, 035017 (7pp).

Chapter 8: Design, Development, and Application of an Open-Source Powder Material Extrusion 3D Printer

Abstract:

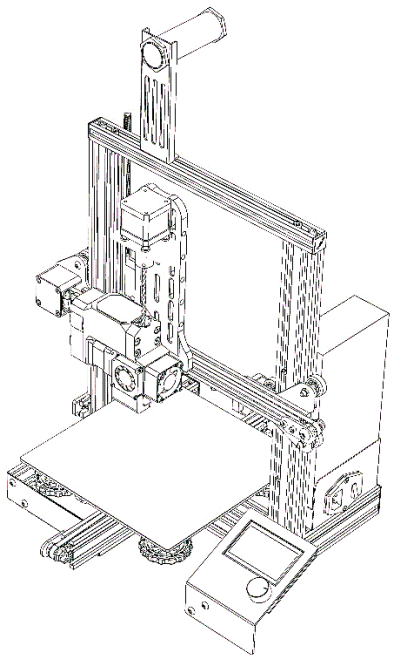

Powder material extrusion (PME) additive manufacturing (AM) is a convenient and practical method to study novel materials by circumventing the need for filamentation or compounding of materials. However, few researchers use this approach due to lack of readily accessible printing systems. In this work, we present the design, development, and testing of an open-source PME printer. The open-source PME 3D printer achieves print quality on par with commercial material extrusion 3D printers in terms of dimensional accuracy, print quality, and mechanical performance. Additionally, we demonstrate this system to be versatile and robust through printing of recycled materials, polymer composites, polymer blends, and functional polymers with thermally sensitive moieties. The broad range of build materials illustrates the diverse capabilities accessible with this system, which enabled access to properties and functions such as phosphorescence, ferromagnetism, shape memory, and mechanochromism. By improving the accessibility of PME AM and demonstrating its versatility, we hope to enable others to explore novel material systems.

Introduction

Additive Manufacturing (AM), also commonly referred to as 3D printing (3DP), encompasses technologies for producing complex objects from computer aided design models.[1] Object function is instilled through material and geometry choices that impart unparalleled design freedom. This freedom has made AM technologies popular in academia and industry[2,3] resulting in new structure property relationships,[4,5] novel 4D,[6–10] smart,[11–14] biomimetic materials,[7,15–18] and revelations in personalized healthcare.[19–21] Such innovations are made possible through advancements in hardware, material scope, and software – collectively the pillars of the AM ecosystem.

Material extrusion (MEX) AM is a subclass of AM characterized by the controlled dispensing of softened material through a nozzle.[1] The most popular type of MEX is fused filament fabrication (FFF) which utilizes a rastering hot end extruder to dictate the deposition of melted thermoplastic polymer around a build platform. FFF systems have undergone extensive advancements over the past decade yielding inexpensive, easy to operate, modifiable, multimaterial-capable, and high-performance printers.[22–24]This has made FFF widely used for fabrication of end-user products, in prototyping, and in research settings.[3]

The materials compatible for FFF are predominately thermoplastics that must be formed into spooled filaments.[24,25] Common materials for FFF printing are polylactic acid (PLA), polycarbonate (PC), polyethylene terephthalate (PET), and acrylonitrile-butadiene-styrene (ABS). Although these materials are suitable for many applications, the desire for higher performing and specialty materials is ever growing.[24–26] One challenge with studying novel material systems in FFF is the non-trivial process for forming filament spools. This process requires an understanding of rheology, material flow, and heat transport, as well as specialized equipment[25]. Additionally, research-scale filament extruders can be costly and often require quantities of material that are difficult to produce in a purely research setting, which makes experimental iteration cumbersome. Furthermore, the additional filamenting process can be a challenge for materials that exhibit thermal sensitivity making direct extrusion without filamenting appealing.[27,28]

Direct MEX printing of granulated material as opposed to filament would address many of the issues outlined above.[29] This has motivated exploration of MEX methods such as screw-assisted material extrusion printers.[30] These printers offer several possible advantages including broader material scope, larger design freedom, and reduced feedstock cost in comparison with those that require precisely formed filament.[24,26,29,31–33] Screw-assisted printing technologies have shown significant potential, especially in their ability to continuously print a diverse range of granulated materials. These include directly recycled substances,[32,34,35] biological materials,[33,36] and economically efficient metals and ceramics.[34,37] Notably, many screw-assisted systems are optimized for processing pellets (granulated materials larger than 1 mm), which offers cost advantages due to the direct use of bulk-distributed materials. However, a limitation arises when printing composites with varied granule sizes. In such cases, an initial compounding step followed by pellet formation is necessary. In contrast, using finer powders (less than 1 mm in size) in a powder material extrusion (PME) printer could directly create composite objects, bypassing the need for compounding. This approach highlights the unique capabilities of PME printers in handling a wider range of material sizes and types.

Although there are various commercial screw-assisted printers available for granulate printing, most face significant barriers to widespread adoption, primarily due to their cost and complexity. In contrast, a low-cost, customizable, and versatile open-source printer could offer a more accessible option. Such a printer would allow researchers to experiment with a broader range of materials and functionalities without the constraints of filament-based systems. While several groups have developed printers aimed at this goal, challenges remain.[26,29,30,38] Most notably, existing designs are often highly proprietary, struggle to match the print quality of FFF methods and have not fully tapped into the potential of novel build materials.

Recognizing the potential of PME printers, we set out to develop an open-source PME printer with print quality comparable to commercial FFF printers. To this end, we introduce a low-cost, open-source PME 3D printer and demonstrate print characteristics on par with those achieved with commercial FFF printers. Additionally, we showcase facile preparation and printing of recycled plastics, polymer blends, polymer

composites, and specialty polymers. We briefly explore the useful properties of these material combinations and discuss future opportunities. By doing this, we showcase the expanded design freedom a completely open-source and modular PME system offers and create a versatile, robust, and cost-effective platform for others to explore novel material systems.

Results and Discussion

Technical Design

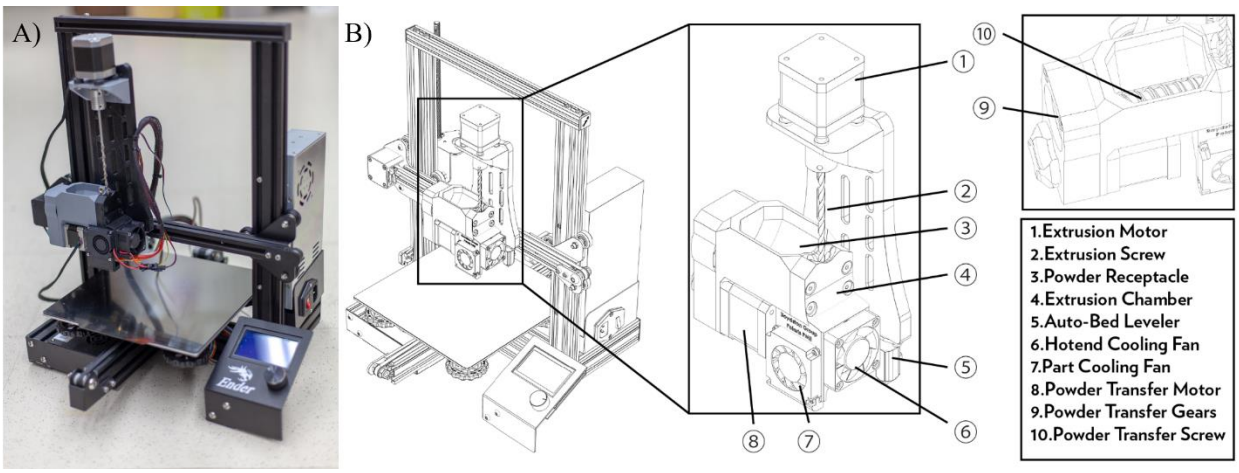

Figure 8.1. *A) PME printer build B) PME printer design with the print head parts identified.*

In the development of a PME 3D printer, we focused on establishing a cost-effective, open-source system with performance comparable to commercial FFF printers. The Ender 3 desktop 3D printer by Creality was selected as the base 3D printer, primarily for its open-source architecture (Figure 8.1). This choice facilitated the integration of a custom print head while also allowing the use of the original Ender-3 parts in the design, effectively reducing both costs and complexity.

The primary challenge in 3D printing, and a key focus for the PME printer, was achieving consistent material delivery. In both PME and FFF systems, this requires maintaining a continuous and even flow of material into the printer's hot end. The initial design iteration, taking inspiration from Boyle et al.[26], featured a funnel and a single screwhead extruder powered by a NEMA 17 stepper motor. This configuration, however, resulted in inconsistent extrusion patterns, as evidenced by a coefficient of determination (R2) of

0.9425 and gradual decrease in powder flow over time (Figure 8.2). To address this, the design was revised to include an additional lateral chamber for powder storage and an extra feed screw, which significantly improved powder delivery consistency, reflected in an improved R^2 value of 0.9988 (Figure 8.2).

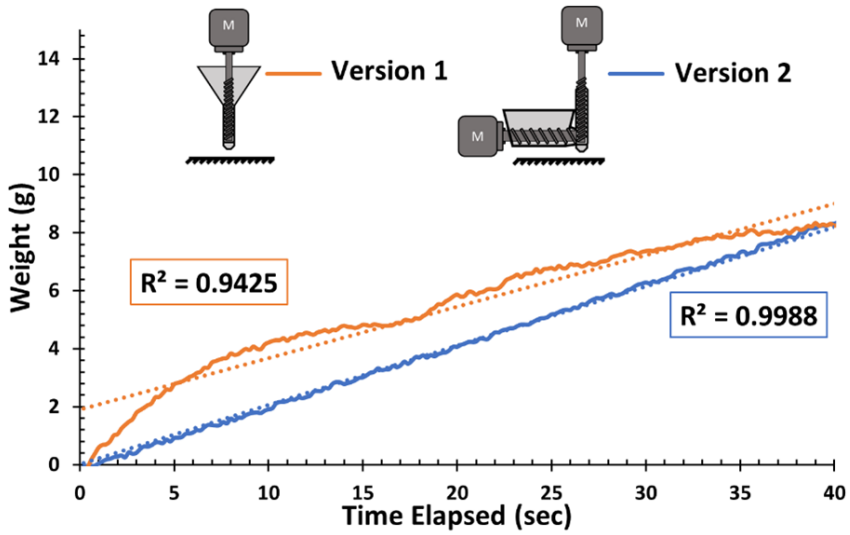

Figure 8.2. *Powder transfer comparison between the original design (orange) and the version 2 design (blue). Dotted lines and R^2 values show the linear best fit for each curve.*

Further refinements led to the incorporation of a 1:3 ratio synchronous gear belt drive system (Figure 8.3A). This system was engineered to compact the material transfer system's size and amplify the motor's torque, optimizing space and enhancing power transmission efficiency.

In adapting the Ender-3's hotend for the PME printer, the Bowden tube's removal created space for a 4 mm diameter pathway, originally designed for the Bowden tube, to accommodate the extrusion drill bit (Figure 8.3B). Crucially, this modification maintained much of the hotend's original structure, enabling the reuse of the existing heater, thermistor, and, importantly, the nozzles. This reuse of original components not only eased integration into the PME printer but also contributed to cost savings and waste reduction.

The modification of the hotend necessitated the design of a new fan shroud to accommodate both the part cooling fan and the hotend cooling fan (Figure 8.3A). Additionally, a mounting mechanism for the NEMA 17 extrusion stepper motor was engineered to drive the extrusion screw. A flexible coupler was employed to connect the motor's shaft to the extrusion screw (Figure 8.1B). This setup is compatible with

various stepper motors including different sizes and gear ratios to accommodate a wider range of extrusion speed and strength.

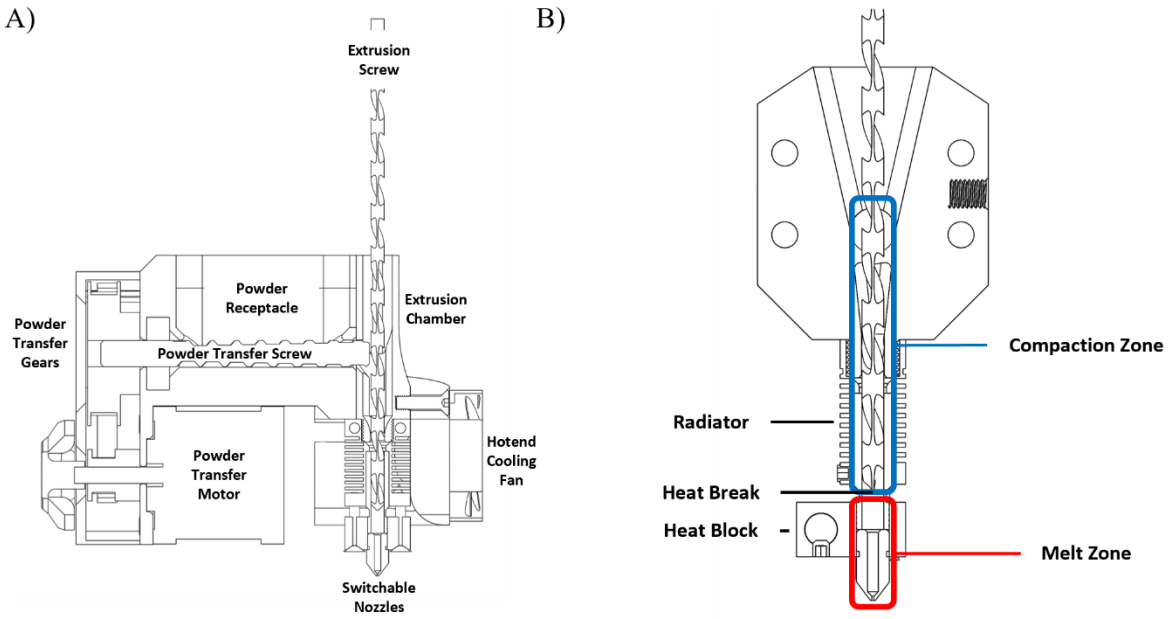

Figure 8.3. *A) Cross section of open-source PME printer head with main components labeled. B) Cross section of the hot end design showing the compaction zone and melt zones.*

The entire assembly, including the modified hotend and motor components, was then mounted onto a 3D printed scaffold. This scaffold provided a stable and precise platform for the components, ensuring proper alignment and functionality. Furthermore, a custom stepper motor controller was developed to manage the operation of the material transfer motor, allowing for precise control over the material extrusion process.

Figure 1 shows the entire printer and print head design. The design consists of a side powder receptacle which facilitates the consistent transfer of powder from the receptacle to the extrusion chamber by a powder transfer screw driven by the powder transfer motor and powder transfer gears (Figure 8.1B). Once the powder is in the extrusion chamber, it is moved toward the hot end by the extrusion screw which also compresses the powder (Figure 8.1B). The powder softens and melts as it nears the hot end tip and is extruded onto the build platform (Figure 8.3B). The final cost at the time of publication was comparable to entry-level FFF 3D printer (Table E1).

Validation

To examine the printer's performance, common filamented materials spanning a range of print temperatures and materials properties were selected for testing: polylactic acid (PLA), polycaprolactone (PCL), and thermoplastic polyurethane (TPU) (Table E2, Figures E3(A-E), Figure E4(A-E)). Print parameters for the PME and FFF were determined empirically (Table E3). We assessed the performance of the PME 3D printer compared to a conventional FFF machine by comparing dimensional accuracy, print quality, and mechanical properties of the printed test specimens.

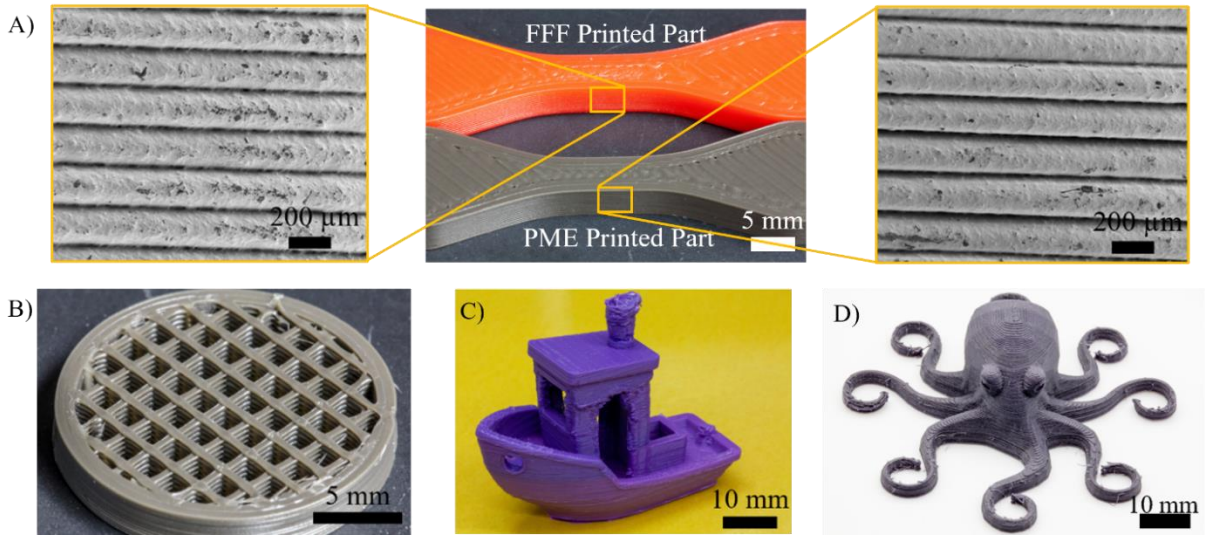

Figure 8.4. *(A) SEM images showing the layer lines of PCL printed with the PME and FFF printer (B) Optical image showing a single infill of a PME printed object (C) PME printed benchmark model (D) PME printed octopus.*

The print accuracy along each print axis (x,y,z) was determined by printing 20 × 20 × 20 mm^3 cubes from PCL and measuring the length across each axis using digital calipers (Figure E6**)**. A 0.6-mm nozzle was used for the prints. The PME average error percent across the x-, y-, and z-axis were 0.5 ± 0.2%, 0.5 ± 0.3%, and 1.0 ± 0.7%, respectively, which corresponds to no larger than 0.5 mm of error in each print (Table E4). The error from the PME was found to be comparable to that of same cube design printed with a commercial FFF printer using the same nozzle size (average error percents across the x-, y-, and z-axis of 0.7 ± 0.1%, 0.5 ± 0.2%, and 0.7 ± 0.2%, respectively; Table E4).

Print quality between FFF and PME printed parts were evaluated using scanning electron microscopy (SEM) and optical images of test prints. SEM images along the z-axis of printed parts for PCL reveal exceptional layer line consistency, smooth finish of the extruded layers, and little difference compared with parts printed using a FFF printer (Figure 8.4A). Comparison of SEM images for layer line quality of FFF and PME printed parts for TPU and PLA also show near indistinguishable layer line quality and consistency between PME and FFF printed objects (Figure E7). Additionally, optical images display the print quality achievable with the PME printer (Figure 8.4A-D). Standard benchmark models of a tugboat and an octopus were printed using PCL and TPU, respectively (Figure 8.4C, D). Overall, the printer was able to handle challenging geometric features including overhangs, edges, curves, and pillars. Additionally, various infill geometries (e.g., grid, cubic, lines, gyroid, triangles, cubic subdivision, trihexagon, octet, quarter cubic) and infill percentages (triangles at 15, 30, 45, and 60%) were printed (Figure 8.4B, Figure E8, Figure E9). The PME printer performed each of these operations without issue.

We assessed mechanical properties through quasistatic tensile testing of ASTM D638 type V samples printed using PME and FFF printers using PCL, TPU, and PLA as build materials (Figure E10). The Young's modulus, elongation to break, and yield stresses were compared (Figure 8.5, Table 8.1). Values obtained from each print method were found to be comparable with one another. (Figure 8.5, Table 8.1). We found that PCL printed with the PME had a higher elongation at break than parts printed with the FFF printer (Figure 8.5, Table 8.1). We hypothesized that the differences in the PCL samples were either due to print speed (the PME prints slower than FFF printers, Table E3) or to the grinding of polymer into powder. Notably, polymer processing conditions and polymer mastication have each been shown to alter the properties of the resulting material.[39,40] To better understand this, we printed PCL on a FFF printer at the same print speeds as the PME printer, which resulted in more similar properties between the printed test samples (Figure 8.5A, Table 8.1). Additionally, the tested samples were reprocessed into powder and reprinted into tensile test specimens (Figure 8.5A). Reprocessing resulted in reduced the Young's modulus and tensile strength of the parts, but retained comparable elongation at break (Figure 8.5, Table 8.1).

Collectively, the tests establish that PME printed parts can achieve the same mechanical properties as those produced by FFF printers, but the print parameters and effects of polymer mastication should be considered.

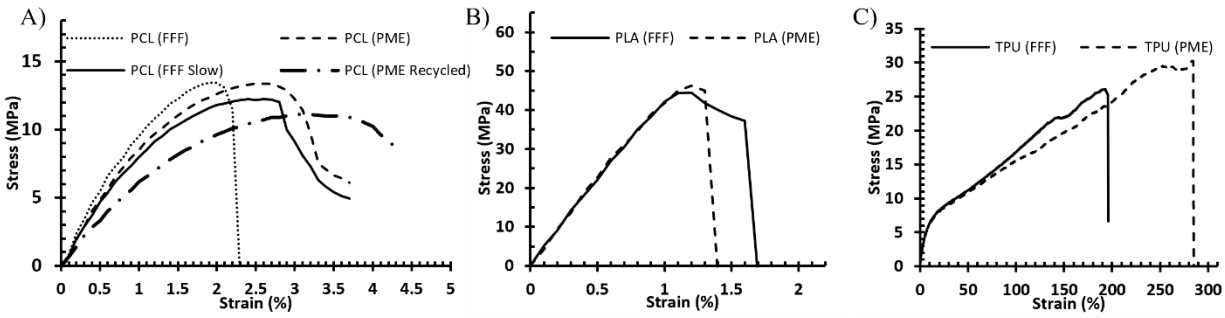

Figure 8.5. *Uniaxial tensile testing data showing the stress-strain behavior of representative samples from three replicate trials (Figure E10) for ASTM D638 type V tensile samples printed from A) PCL printed with FFF (dotted), PME (dashed), FFF at slower print speeds (solid), and PME recycled from previous prints (dash dot). B) PLA printed with FFF (solid) and PME (dashed). C) TPU printed with FFF (solid) and PME (dashed).*

Table 8.1. *Summary of the tensile properties of printed PCL, PLA, and TPU ASTM D638 type V samples from PME and FFF printers.*

Samples[a]	Young's Modulus (Mpa)	Yield Stress (Mpa)	Elongation at Break (%)
PCL (FFF)	1240 ± 90	14.7 ± 0.2	2.4 ± 0.2
PCL (PME)	1120 ± 60	14.3 ± 0.4	3.7 ± 0.3
PCL (FFF Slow)	1030 ± 40	13.5 ± 0.2	3.5 ± 0.3
PCL (PME Recycled)	900 ± 100	12.4 ± 0.6	4.0 ± 0.5
PLA (FFF)	4600 ± 300	43 ± 7	1.9 ± 0.2
PLA (PME)	4700 ± 200	49.6 ± 0.8	1.43 ± 0.06
TPU (FFF)	61 ± 5	8 ± 1	200 ± 30
TPU (PME)	57 ± 3	9.2 ± 0.1	260 ± 40

[a]*Averages and standard deviations represent the results from three replicate experiments.*

Case Studies

An advantage of PME printers is the potential to expedite materials research due to the simplicity in materials preparation and mixing. We hope the accessibility and robustness of this system will promote breakthroughs in sustainability and material discovery through rapid testing of a variety of material systems. To illustrate this, several model systems were explored, demonstrating the printing of recycled commodity plastics, polymer composites, polymer blends, and a functional mechanophore-containing polymer.

Commodity Plastics

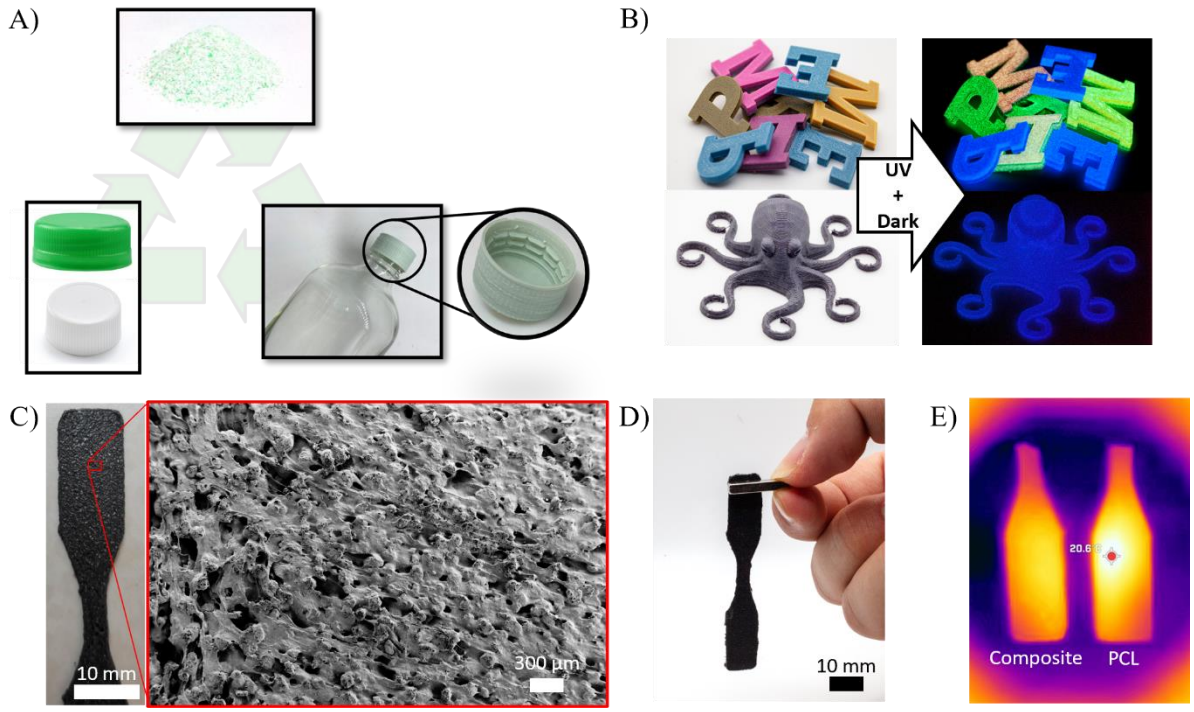

Figure 8.6. *A) Transformation of combined waste plastic back into useable items. B) Printed strontium aluminate composites and demonstration of their glow in the dark properties. C) Printed iron oxide and PCL composite along. Corresponding SEM shows the iron oxide particles along the surface of the printed part. D) Iron oxide and PCL composite suspended using a magnet. E) IR thermal camera image of iron oxide PCL composite being cooled next to a pure PCL part.*

Mechanical recycling is a widely employed method for recycling plastic solid waste, but comes with challenges including contamination of feedstock, reduced mechanical properties, and separation of multilayered plastics.[41,42] PME printing offers a mode for the study and implementation of the mechanical recycling process on a reduced scale and turns recycled polymer directly into printed objects. To demonstrate mechanical recycling of commodity plastics, high density polyethylene (HDPE) lids taken from laboratory scintillation vials and from plastic soda bottles were processed into powder. Notably, no additional pretreatment steps were used, and the HDPE comes from two different sources. The resulting powder mix, as expected, exhibited two melt and crystallization temperatures (Figure E3E). The powder HDPE can easily be recycled into additional printed objects using PME printing, effectively demonstrating material recycling as a potential use (Figure 8.6A, Table E3). Even this simple demonstration is

encouraging and creates prospects for studying the recycling of commodity plastics from multiple material streams or the reprocessing of multilayered plastics.

Polymer Composites

The relative narrow range of FFF 3D printable materials and resulting properties has motivated the development of composite materials[43–46]. These polymer composite materials give access to properties typically not available from accessible polymer materials as well as properties that can even outperform those of the individual components[47]. Often, the processing of composite materials is a challenge, which motivates direct formation of composite objects during the AM printing process. To show the ease of creating novel composite systems, strontium aluminate, a common phosphor found in glow-in-the-dark products, was mixed with TPU in a ratio of 80:20 by weight (TPU:strontium aluminate). The composite system could then be printed into objects with various shapes and geometric complexities, and the parts were phosphorescent after exposure to UV light (Figure 8.6B).

Separately, iron oxide could be mixed with PCL and printed to form composites (Figure 8.6C-E). Printed composites contained a matte-like and rough surface that, upon closer inspection by SEM, shows the incorporations of the iron oxide throughout the thermoplastic matrix (Figure 8.6C). Increased loadings of inorganic fillers often require increased nozzle diameters. We briefly explored printing with nozzle diameters ranging from 0.4 to 1 mm using PCL (Figure E11). Print parameters only required minor alteration to accommodate for the changes in pressure drop and volumetric flowrate for the different nozzles (Table E5). We also determined that we were able to print compositions consistent with the mixture loadings of iron oxide and PCL. By loading a 60 wt% iron oxide 40 wt% PCL mixture into the hopper we were able to print objects and used TGA to determine the composition of the part (Figure E12). TGA showed good agreement with loaded mixture as 62.2% of material was left after thermally removing the PCL. We were also able to reach up to 80 wt% loadings of iron oxide in PCL using a 0.8 mm nozzle with compositions confirmed by TGA (Figure E12). While there are many uses for thermoplastic composites, the ability to reach 80 wt% iron oxide loadings reveals potential for printing metals and ceramics where

debinding and sintering would be needed to form the final part. We are excited about this potential area of study and hope to examine new binder systems in the future more suitable for printing of high loadings of inorganic materials. Notably, the printed parts exhibited ferromagnetic properties and could be attracted by standard bar magnets (Figure 8.6D). We also observed an increase in the overall thermal conductivity of the parts. Additionally, comparison of PCL objects with and without iron oxide (~50 wt.% of iron oxide) resulted in differences in their cooling rate with the composite part cooling faster than the pure PCL part (Figure 8.6E).

Polymer Blends

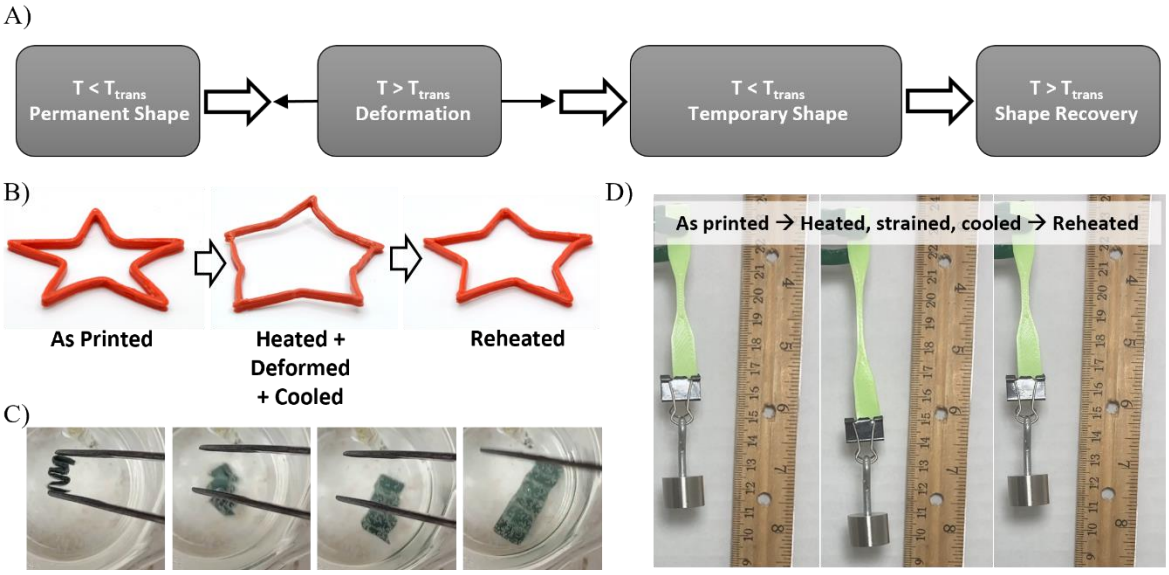

Figure 8.7. *A) Demonstration of thermally responsive shape memory material below and above it transition temperature (T_{trans}). B) 3D printed star from a PCL/TPU blend that allows for 3D printing (left), heating and deforming of material into a temporary shape (middle), and then reheating to reform original shape (right). C) Demonstration of rapid shape transformation of PCL/TPU blend printed in a panel design with unfolding shown in images from left to right as material is placed into 60 ℃ water. D) Ability to store elastic energy using thermally responsive shape memory materials.*

Formation of polymer blends can be a powerful method to obtain materials with improved properties and interesting phase behavior[48,49]. PME printing offers a mode for simple implementation and study of these properties. For example, by printing a PCL/TPU polymer blend, we achieved thermally responsive shape memory materials [50,51]. These thermally responsive shape memory materials can be printed into a permanent shape which, when heated above a thermal transition temperature (T_{trans}), can be deformed and subsequently

cooled below T_{trans} locking in the temporary shape until being reheated above T_{trans} to return the object to its permanent form (Figure 8.7A). In the case of PCL/TPU blends, the shape memory properties are derived from the distinct 116hermosmechanical properties of the individual polymers. Dynamic mechanical analysis (DMA) of each individual polymer reveals neither material alone exhibits shape memory behavior within the temperature range measured (Figure E13). TPU maintains a steady storage modulus and tan δ while PCL has a drastic decrease in storage modulus and increase in tan δ as it forms a polymer melt where the viscous properties begin to dominate and shape fidelity is lost (Figure E13). Contrasting these behaviors, a 40/60 by weight blend of TPU/PCL allows for a more moderate decrease in storage modulus that plateaus resulting in only a slight increase in the tan δ (Figure E13). This softening allows for the blended polymers to be deformed above the melting temperature of PCL, locked into place by cooling and reforming of the stiff PCL crystalline domains, and then returned to the original shape through additional heating (Figure 8.7A). This process is shown by printing a star, heating and deforming, allowing it to cool to retain its temporary shape, and then reheating to form the original star shape (Figure 8.7B). Additionally, this shape transformation can be fairly rapid when used in thin designs where heat transfer can be fast. This was shown through printing of a panel design that can be folded and fixed into shape, but when reheated transforms back into its original shape in seconds (Figure 8.7C). Furthermore, the shape memory properties of the polymer blend can be tuned by altering the composition of the TPU/PCL which was explored by bending tests (Figure E14, Table E6). The 20/80 and 80/20 mixtures of TPU/PCL show lower shape memory properties than mixtures of 40/60 and 60/40 TPU/PCL. This is likely due to minority components being unable to form continuous networks. Interestingly, these polymer blends can also be used to store elastic energy to be released later upon thermal heating. By heating a printed part from a 60/40 mixture of TPU/PCL to 60 °C, straining the sample, and then cooling the sample, elastic energy is stored. The release of this stored energy is shown by attaching a 20 g weight to the sample and reheating (Figure 8.7D).

Specialty Polymers

In many instances, researchers are interested in 3D printing novel or functional polymers that are not commercially available and may be difficult to synthesize at multigram scales. In these instances, the PME may be an appropriate platform for printing and exploring the properties of these materials. One exciting avenue is the printing of mechanophore containing polymers. This was explored by the synthesis of PCL containing a chain centered spiropyran, P1 (Figure 8.8A). Under either mechanical force or UV light the spiropyran undergoes isomerization to its merocyanine form (Figure 8.8A). Parts can be printed from P1 into arbitrary geometries (Figure 8.8B). When printed objects are exposed to UV light, they undergo a stark change in color (Figure 8.8C). Mechanical force can also be used for strain induced mechanophore activation (Figure 8.8D).

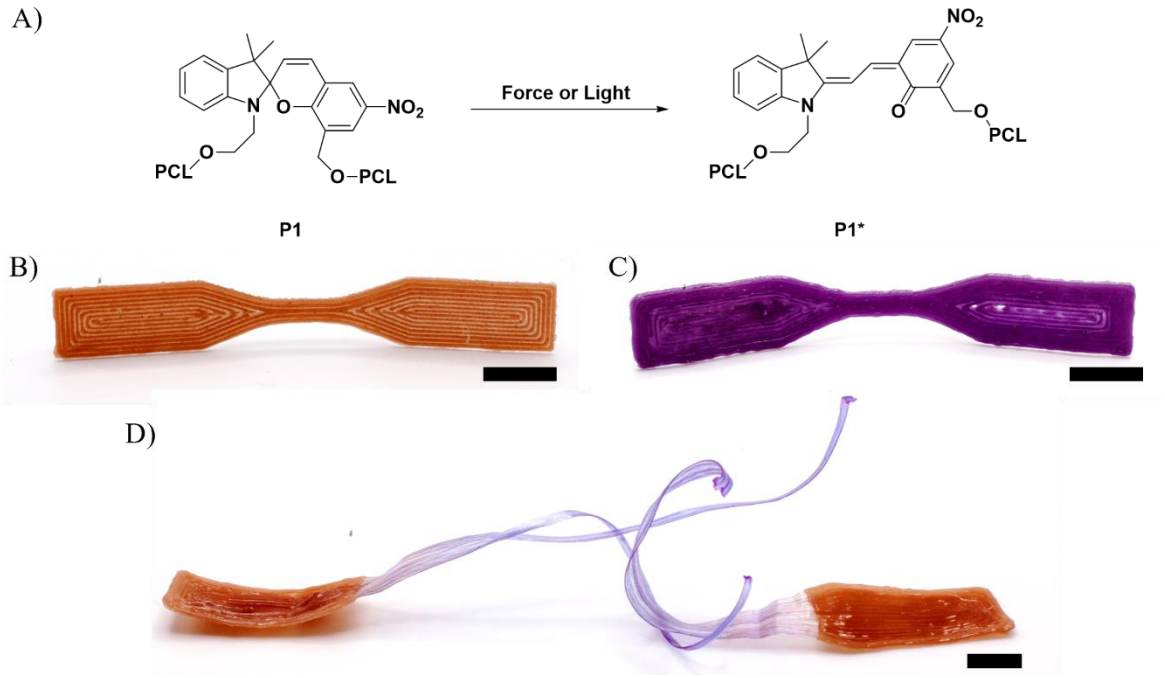

Figure 8. *A) Generalized depiction of mechanical and UV induced isomerization of Spiropyran containing polymer, P1, to its merocyanine form, P1* B) Part printed from P1 C) Image of the P1 printed part after exposure to UV light D) Image of P1 after being manually stretched. All scale bars indicate 10 mm.*

Conclusion and Future Work

The development and application of the open-source PME 3D printer successfully addresses a gap in the AM landscape by providing an accessible, low-cost, and versatile PME printing system. Filling this gap is

particularly beneficial for providing access to chemical and material spaces incompatible with filamenting and compounding materials and impactful for research and development purposes.

Our findings demonstrate that the open-source PME printer can achieve print quality comparable to commercial FFF systems, particularly in terms of resolution, appearance, and mechanical properties. This is a noteworthy achievement considering the intrinsic complexities of PME systems compared to FFF. The PME system's ability to handle a broad spectrum of materials, including recycled plastics, polymer blends, composites, and specialty polymers, underlines its versatility and potential for broader application in material science research.

The PME printer's capacity to work with a diverse suite of materials, ranging from thermoplastic polymers to complex composites, opens new avenues for material exploration. The successful printing of materials with special properties like phosphorescence, ferromagnetism, shape memory, and mechanochromism is particularly significant. These capabilities indicate the potential for developing advanced materials with customized functionalities tailored for specific applications, ranging from biomedical devices to smart materials.

While the PME printer marks a significant step forward, challenges remain, particularly in achieving consistent material delivery over longer timescales and handling a wide range of material granule sizes. Future work could focus on refining the printer design for even more consistent powder delivery and exploring novel material systems, such as compatibilized multi-stream plastics and organic-inorganic composites. Additionally, further development of the printer to facilitate in-line mixing of materials could pave the way for smoother material gradients and multi-material printing.

In conclusion, the open-source PME 3D printer offers a promising platform for the rapid prototyping and testing of novel material systems. Its accessibility, cost-effectiveness, and versatility make it a valuable tool for both academic research and industrial applications. By bridging the gap between material availability

and printing technology, the PME system has the potential to significantly accelerate the exploration and development of new materials and their applications in various fields.

Experimental Section

Materials: SainSmart TPU filament, Overlook PLA filament, MSNJ PCL filaments, strontium aluminate-based glow powder, and iron oxide powder were purchased from Amazon. The Spiropyran difunctional initiator was prepared as previously reported[52,53]. Stannous octoate (92.5-100%), ε-caprolactone (97%), and tetrahydrofuran (>99.9) were purchased from Sigma Aldrich. HDPE for recycling via PME 3DP was obtained from laboratory scintillation vial caps and soda bottle caps.

Thermogravimetric Analysis, Differential Scanning Calorimetry, and Dynamic Mechanical Analysis: TGA was conducted on a TA TGA Q50 under nitrogen from room temperature to 600 °C with a heating rate of 10 °C/min. DSC was conducted on a TA DSC Q200 calorimeter under air. Samples were sealed in a Tzero aluminum pan and lid. Testing was run under a heat-cool-heat cycle with 10 °C/min heating and cooling rates. The first cooling and second heating are reported. The three-point bending test DMA experiments were performed on a TA Instruments RSA III in a 3-point bending configuration performed at 0.01% strain and 1 Hz.

PME Printing: To print non-powdered thermoplastic materials with the PME printer, the given material was ground into powder using a coffee grinder and by periodically adding dry ice to embrittle the polymers. The resulting powder was separated through a 35 mesh sieve and the powder was recovered and stored in a desiccator to remove residual moisture. Although more elaborate operation of the PME printer can be found in the Supporting information PME Build Guide, in brief, stl files were loaded into Cura and sliced using the desired print parameters. The Gcode file was loaded onto the printer. Powdered material was then fed into the material hopper and the powder transfer was started. Once material was being fed into the extruder chamber, the print was started. All prints were done with a 0.6 mm nozzle unless directly indicated otherwise.

Particle Size Determination: Particle size distribution was determined through optical microscopy followed by image analysis. For measurement, a small amount of powder was dispersed in water and sandwiched between two glass slides. The glass slide was imaged using a Nikon Eclipse Ti-2 microscope. The

microscopy image was then analyzed using imageJ to determine particle size distribution. The resulting powder had an average particle size of 140 ± 40 μm (Figure E5).

Scanning Electron Microscopy: The Prep-Leica ACE600 was used to sputter coat samples with a 10 nm thick layer of platinum with settings of 30 mA, a 2.5×10^{-2} mbar operating pressure, working distance of 50 mm, and sputter rate of 0.13 nm/s. Samples were then imaged on a Zeiss GeminiSEM 450 scanning electron microscope.

Tensile Testing: Tensile testing was performed on an MTS universal testing machine. ASTM D638 type V dogbone samples were prepared for each material. For rigid materials (PLA and PCL), a strain rate of 10 mm/min was used. For soft materials (TPU), a strain rate of 100 mm/min was used. Three replicates were performed for each material and the average and standard deviation of those measurements reported.

Bending Test: ASTM D638 type V dogbone samples were printed with various ratios of TPU to PCL. The parts were then submerged in 60 °C water for 1 minute. After 1 minute, the samples were bent to an angle of 180° around a 3 mm diameter post and held in that position until completely cooled. The samples were resubmerged in 60 °C water and their relaxation tracked by video. Angles were determined by analyzing each frame of video using MATLAB.

Synthesis of PCL-Spiropyran-PCL: The mechanochromic PCL, P1, was prepared as previously reported (M_n = 37.2 kDa and Đ = 1.45) (Figure E15) [52,54]. Gel permeation chromatography (GPC) was performed using an Agilent Technologies 1260 Infinity II pump with two inline Agilent Plgel (part #: PL1113-6300) columns, Wyatt Technology mini-DAWN light scattering, and Agilent 1260 Infinity II RI detectors, using uninhibited HPLC grade THF as the mobile phase.

References:

1. ASTM 52900. Additive Manufacturing - General Principles - Terminology. *ASTM Int.* **2021**, 1–14 (2021).
2. Berman, B. 3-D printing: The new industrial revolution. *Bus. Horiz.* **55**, 155–162 (2012).
3. Ahmed, A. *et al.* Discovering the technology evolution pathways for 3D printing (3DP) using bibliometric investigation and emerging applications of 3DP during COVID-19. *Clean. Environ. Syst.* **3**, 100042 (2021).
4. Bobrin, V. A. *et al.* Nano- to macro-scale control of 3D printed materials via polymerization induced microphase separation. *Nat. Commun.* **13**, 3577 (2022).
5. Cipriani, C. E. *et al.* Structure–Processing–Property Relationships of 3D Printed Porous Polymeric Materials. *ACS Mater. Au* **1**, 69–80 (2021).
6. Zhou, L.-Y., Ye, J.-H., Fu, J.-Z., Gao, Q. & He, Y. 4D Printing of High-Performance Thermal-Responsive Liquid Metal Elastomers Driven by Embedded Microliquid Chambers. doi:10.1021/acsami.9b22433.
7. Gladman, A. S., Matsumoto, E. A., Nuzzo, R. G., Mahadevan, L. & Lewis, J. A. Biomimetic 4D printing. *Nat. Mater.* **15**, 413–418 (2016).
8. Jung, K. *et al.* Designing with Light: Advanced 2D, 3D, and 4D Materials. *Adv. Mater.* **32**, 1903850 (2020).
9. Kuang, X. *et al.* Advances in 4D Printing: Materials and Applications. *j* **29**, (2019).
10. Pinho, A. C., Buga, C. S. & Piedade, A. P. The chemistry behind 4D printing. *Applied Materials Today* vol. 19 100611 (2020).
11. Boydston, A. J. *et al.* Additive manufacturing with stimuli-responsive materials. *J. Mater. Chem. A* **6**, 20621–20645 (2018).
12. Wang, T., Wang, H., Shen, L. & Zhang, N. Multicolor mechanochromism of a multinetwork elastomer that can distinguish between low and high stress. *Polym. Chem.* **12**, 3832–3841 (2021).
13. Shafranek, R. T. *et al.* Stimuli-responsive materials in additive manufacturing. *Prog. Polym. Sci.* **93**, 36–67 (2019).
14. Nadgorny, M. & Ameli, A. Functional Polymers and Nanocomposites for 3D Printing of Smart Structures and Devices. (2018) doi:10.1021/acsami.8b01786.
15. Ritchie, R. O. The conflicts between strength and toughness. *Nat. Mater.* **10**, 817–822 (2011).
16. Yang, C. *et al.* 3D-Printed Biomimetic Systems with Synergetic Color and Shape Responses Based on Oblate Cholesteric Liquid Crystal Droplets. *Adv. Mater.* **2006361**, 1–7 (2021).
17. Sydney Gladman, A., Matsumoto, E. A., Nuzzo, R. G., Mahadevan, L. & Lewis, J. A. Biomimetic 4D printing. *Nat. Mater.* **15**, 413–418 (2016).
18. Du Plessis, A. *et al.* Beautiful and Functional: A Review of Biomimetic Design in Additive Manufacturing. (2019) doi:10.1016/j.addma.2019.03.033.
19. Ligon, S. C., Liska, R., Stampfl, J., Gurr, M. & Mülhaupt, R. Polymers for 3D Printing and Customized Additive Manufacturing. *Chem. Rev.* **117**, 10212–10290 (2017).

20. Yan, Q. *et al.* A Review of 3D Printing Technology for Medical Applications. *Engineering* vol. 4 729–742 (2018).

21. Murphy, S. V. & Atala, A. 3D bioprinting of tissues and organs. *Nat. Biotechnol.* **32**, 773–785 (2014).

22. Bilton, N. Disruptions: 3-D Printing Is on the Fast Track. *The New York Times* Bits https://nyti.ms/3DyS2GM (2013).

23. Jones, R. *et al.* RepRap-the replicating rapid prototyper. *Robotica* **29**, 177–191 (2011).

24. Zhang, P., Wang, Z., Li, J., Li, X. & Cheng, L. From materials to devices using fused deposition modeling: A state-of-art review. *Nanotechnol. Rev.* **9**, 1594–1609 (2020).

25. Park, S. & Fu, K. (Kelvin). Polymer-based filament feedstock for additive manufacturing. *Compos. Sci. Technol.* **213**, 108876 (2021).

26. Boyle, B. M., Xiong, P. T., Mensch, T. E., Werder, T. J. & Miyake, G. M. 3D printing using powder melt extrusion. *Addit. Manuf.* **29**, 100811 (2019).

27. Abdella, S. *et al.* 3D Printing of Thermo-Sensitive Drugs. *Pharm. 2021, Vol. 13, Page 1524* **13**, 1524 (2021).

28. Zhou, Z., Salaoru, I., Morris, P. & Gibbons, G. J. Additive manufacturing of heat-sensitive polymer melt using a pellet-fed material extrusion. *Addit. Manuf.* **24**, 552–559 (2018).

29. Justino Netto, J. M. *et al.* Screw-assisted 3D printing with granulated materials: a systematic review. *Int. J. Adv. Manuf. Technol. 2021 1159* **115**, 2711–2727 (2021).

30. Justino Netto, J. M. *et al.* Screw-assisted 3D printing with granulated materials: a systematic review. *Int. J. Adv. Manuf. Technol. 2021 1159* **115**, 2711–2727 (2021).

31. Nurhudan, A. I., Supriadi, S., Whulanza, Y. & Saragih, A. S. Additive manufacturing of metallic based on extrusion process: A review. *J. Manuf. Process.* **66**, 228–237 (2021).

32. Alexandre, A., Cruz Sanchez, F. A., Boudaoud, H., Camargo, M. & Pearce, J. M. Mechanical Properties of Direct Waste Printing of Polylactic Acid with Universal Pellets Extruder: Comparison to Fused Filament Fabrication on Open-Source Desktop Three-Dimensional Printers. *3D Print. Addit. Manuf.* **7**, 237–247 (2020).

33. Whyman, S., Arif, K. M. & Potgieter, J. Design and development of an extrusion system for 3D printing biopolymer pellets. *Int. J. Adv. Manuf. Technol. 2018 969* **96**, 3417–3428 (2018).

34. Kim, H. & Lee, S. Printability and physical properties of iron slag powder composites using material extrusion-based 3D printing. *J. Iron Steel Res. Int.* **28**, 111–121 (2021).

35. Byard, D. J. *et al.* Green fab lab applications of large-area waste polymer-based additive manufacturing. *Addit. Manuf.* **27**, 515–525 (2019).

36. Wang, C., Zhang, L., Fang, Y. & Sun, W. Design, Characterization, and 3D Printing of Cardiovascular Stents with Zero Poisson's Ratio in Longitudinal Deformation. *Engineering* **7**, 979–990 (2021).

37. Lengauer, W. *et al.* Fabrication and properties of extrusion-based 3D-printed hardmetal and cermet components. *Int. J. Refract. Met. Hard Mater.* **82**, 141–149 (2019).

38. Justino Netto, J. M. *et al.* Design and validation of an innovative 3D printer containing a co-rotating

twin screw extrusion unit. *Addit. Manuf.* **59**, 103192 (2022).

39. Alexandre, A., Cruz Sanchez, F. A., Boudaoud, H., Camargo, M. & Pearce, J. M. Mechanical Properties of Direct Waste Printing of Polylactic Acid with Universal Pellets Extruder: Comparison to Fused Filament Fabrication on Open-Source Desktop Three-Dimensional Printers. *3D Print. Addit. Manuf.* **7**, 237–247 (2020).

40. Hsueh, M. H. *et al.* Effect of Printing Parameters on the Thermal and Mechanical Properties of 3D-Printed PLA and PETG, Using Fused Deposition Modeling. *Polymers (Basel).* **13**, (2021).

41. G Schyns, Z. O., Shaver, M. P., G Schyns, Z. O. & Shaver, M. P. Mechanical Recycling of Packaging Plastics: A Review. *Macromol. Rapid Commun.* **42**, 2000415 (2021).

42. Li, H. *et al.* Expanding plastics recycling technologies: chemical aspects, technology status and challenges. *Green Chem.* **24**, 8899–9002 (2022).

43. Parandoush, P. & Lin, D. A review on additive manufacturing of polymer-fiber composites. *Compos. Struct.* **182**, 36–53 (2017).

44. Kalsoom, U., Nesterenko, P. N. & Paull, B. Recent developments in 3D printable composite materials. *RSC Adv.* **6**, 60355–60371 (2016).

45. Wang, X., Jiang, M., Zhou, Z., Gou, J. & Hui, D. 3D printing of polymer matrix composites: A review and prospective. *Compos. Part B Eng.* **110**, 442–458 (2017).

46. Singh, S., Ramakrishna, S. & Berto, F. 3D Printing of polymer composites: A short review. *Mater. Des. Process. Commun.* **2**, e97 (2020).

47. Wegst, U. G. K., Bai, H., Saiz, E., Tomsia, A. P. & Ritchie, R. O. Bioinspired structural materials. *Nat. Mater.* **14**, 23–36 (2015).

48. Abdilla, A. *et al.* Silicone-based polymer blends: Enhancing properties through compatibilization. *J. Polym. Sci.* **59**, 2114–2128 (2021).

49. Koning, C., Van Duin, M., Pagnoulle, C. & Jerome, R. Strategies for compatibilization of polymer blends. *Prog. Polym. Sci.* **23**, 707–757 (1998).

50. Bhattacharya, S., Hailstone, R. & Lewis, C. L. Thermoplastic Blend Exhibiting Shape Memory-Assisted Self-Healing Functionality. *ACS Appl. Mater. Interfaces* **12**, 46733–46742 (2020).

51. Jing, X., Mi, H. Y., Huang, H. X. & Turng, L. S. Shape memory thermoplastic polyurethane (TPU)/poly(ε-caprolactone) (PCL) blends as self-knotting sutures. *J. Mech. Behav. Biomed. Mater.* **64**, 94–103 (2016).

52. Peterson, G. I., Larsen, M. B., Ganter, M. A., Storti, D. W. & Boydston, A. J. 3D-printed mechanochromic materials. *ACS Appl. Mater. Interfaces* **7**, 577–583 (2015).

53. O'Bryan, G., Wong, B. M. & McElhanon, J. R. Stress sensing in polycaprolactone films via an embedded photochromic compound. *ACS Appl. Mater. Interfaces* **2**, 1594–1600 (2010).

54. McFadden, M. E. & Robb, M. J. Generation of an Elusive Permanent Merocyanine via a Unique Mechanochemical Reaction Pathway. *J. Am. Chem. Soc.* jacs.1c03865 (2021) doi:10.1021/jacs.1c03865.

Part Three

Multimaterial 3D Printing Via Dual Wavelength Vat Photopolymerization

Chapter 9: Multi-Color Dual Wavelength Vat Photopolymerization 3D Printing Via Spatially Controlled Acidity

This chapter was reproduced from a manuscript that has been submitted.

Chin, K. C. H.; Ovsepyan, G.; Boydston, A. J. Multi-Color Dual Wavelength Photopolymerization 3D Printing Via Spatially Controlled Acidity. **2024**. Under Review.

Abstract

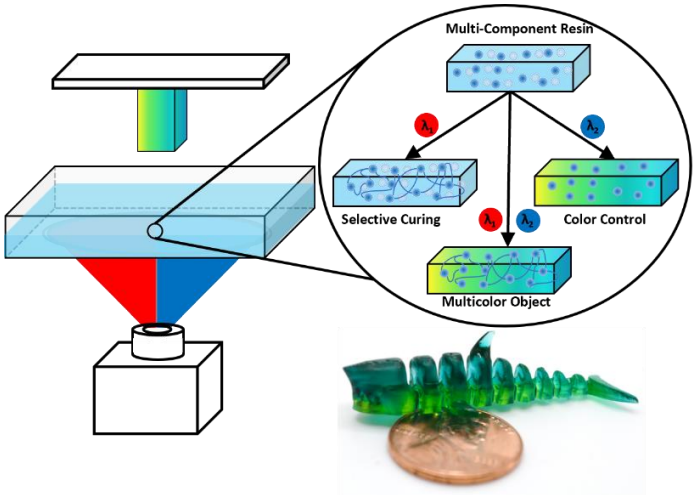

Dual wavelength vat photopolymerization (DW-VP) has emerged as a powerful approach to create multimaterial objects. However, thus far only a limited range of properties have been showcased, mainly focusing on controlling stiffness. In this work, we report the 3D printing (3DP) of multi-color objects from a single resin vat using DW-VP. This was accomplished by concurrently curing resin with visible light and modulating local resin color with 365-nm ultraviolet (UV) light. The key advance was to use a photoacid generator (PAG) in combination with pH responsive dyes in the 3DP resins. In this way, a single component of the resin can give rise to a range of colors, and a single photochemical event can be used to modulate the color. The specific color is then dictated by the extent of reaction, or local acidity in our case. Specifically, the final color of a voxel was controlled by the dosage and pattern of UV light applied. Multi-color object formation was implemented in two-step processes involving first 3DP to set the object structure, followed by UV exposure, as well as single processes that leveraged DW-VP. With these strategies, we demonstrated recreation of camouflage patterns as well as complex multi-color architectures. Additionally, we showcase the compatibility of this approach with multiple dyes to achieve broad ranges of vibrant colors.

Introduction

Additive manufacturing (AM), commonly referred to as 3D printing (3DP), is a powerful method of creating objects from computer-aided design models and provides unprecedented control over object shape and function[1–3]. Although most AM methods focus on printing single materials, there is a growing desire to print multiple materials at once[4–7]. These multimaterial AM systems further expand design freedom by providing spatial control over various properties of interest throughout an object which can give rise to a myriad of useful, interesting, and novel functions. Thus far, several properties have been explored across AM methods such as disparate stiffness[8–11], thermomechanical properties[12,13], conductivity[14], color[15,16], and solubility[17].

The most common multimaterial AM methods are deposition-based systems, where object formation is achieved by directly depositing material to specified locations such as melt material extrusion, material jetting, and direct ink write material extrusion. These AM approaches enable multimaterial approaches centered around delivery of materials to the print head[8,18]. In contrast, vat photopolymerization (VP) AM methods build objects through light-patterned curing of a homogeneous liquid from a material reservoir. The homogeneity of the resin vat makes multimaterial VP challenging due to a general inability to deliver varied materials to a prescribed voxel within a single vat. Despite this difficulty, multimaterial VP is attractive due to its high resolution, smooth surface finish, and fast print times.

Most efforts toward multimaterial VP focus on methods to change out the entirety of a resin for a new one[5]. This is predominantly accomplished by either swapping of resin vats[19–21] or with fluidic devices[15,22,23]. However, these approaches can suffer from increased print times, additional manufacturing complexity, resin contamination, a need to design multiple co-compatible resins, and limitations on the diversity of materials and thus properties. Additionally, although exchanging resins can lead to multiple materials within a single layer, it is tedious as a single layer needs to be addressed multiple times (separately for each material). Therefore, these approaches often restrict material changes to individual layers, which limits the freedom in material placement throughout an object (i.e., only z-axis material variation is enabled).

An alternative method for multimaterial VP leverages chemistry-centered solutions that allow for a single homogeneous vat of resin to be used. In this, the chemistry of the cured material is manipulated during the printing process by altering the properties of light (i.e wavelength and/or intensity)[5,24]. Simply by tuning the intensity of light, a range of properties have been achieved using a single resin vat through control of the local degree of monomer conversion [4,25–28]. However, these approaches often require post-processing to set the final properties or result in minimal disparity in properties.

By manipulating light intensity and wavelength simultaneously, additional levels of control can be gained over the printing process[5,29]. The principle for this method leverages photochemical orthogonality within resin design. This strategy allows for distinct chemistries to be controlled by exposure to different wavelengths of light[24,29,30]. Several works have utilized this method toward dual wavelength multimaterial VP[9,10,31,32]. Specifically, Schwartz et al.[9] and Dolinksi et al.[10] dictated radical and cationic photopolymerizations while Rossegger et al.[32] paired thiol-ene click and coumarin photocycloaddition reactions to control the local stiffnesses of an object.

Thus far, controlling the stiffness of a material has been the primary demonstration for multimaterial VP 3DP, which motivated us to consider if we could design resins to target additional properties. One property of interest was altering the color of a 3D printed object using dual wavelength VP. Beyond aesthetics, producing multi-color objects is of interest for applications in data storage[18], camouflage[33], and education[34,35]. Previously, Peng. et al. utilized gradient light intensity to create multi-color objects from a single resin vat by spatially controlling the generation of radicals and including an anthraquinone-based dye that, when oxidized, changes color[16]. Although this was an excellent step toward multi-color VP 3DP, we noted that the printing process and color modulation are necessarily coupled. We wondered if we could introduce an additional wavelength of light for color modulation independent of the wavelength (and chemistry) that dictates object formation.

Results and Discussion

Development of Multi-Color Resins

Inspired by the vibrant color changes obtainable in acid/base titration, we envisioned a dual wavelength approach to creating multi-color objects that relied on controlling the local acidity within a part via the use of photoacid generators (PAGs). Onium salt PAGs undergo photolysis under UV light resulting in the creation of a Brønsted acid[36,37]. The strength of the generated acid depends on the counter ion species and is often designated a superacid due to bulky and weakly-coordinating anions such as hexafluoroantimonate, hexafluorophosphate, tetrafluoroborate[37]. We wondered if the resulting acid generation could be controlled with light dosage and allow for the protonation of pH-responsive dyes. To explore this, a pH-responsive dye, bromocresol green (BG), was chosen due to its need for only moderate pH changes and its distinct color change from blue to green to yellow (See Figure F1 for chemical structures). UV illumination of a solution of a PAG, triarylsulfonium hexafluorophosphate salts (TAS), BG, and aqueous 1 M NaOH (added to adjust the initial solution acidity) resulted in a distinct change in solution color from blue to green to yellow indicative of a change in solution acidity (Figure 9.1A). The final solution color could be dictated by the duration of the light exposure.

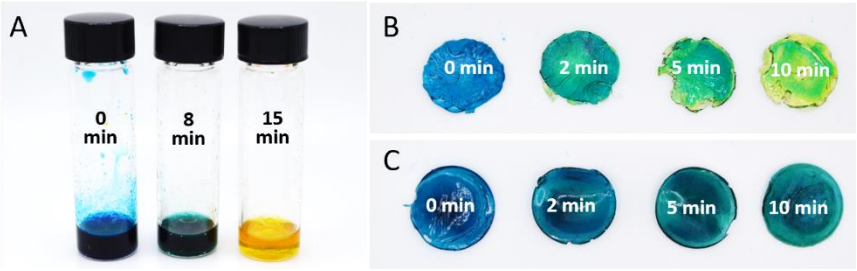

Figure 9.1. *A) Solution of TAS, bromocresol green, and aqueous 1 M NaOH after various duration of 10 mW/cm^2 365-nm light. B) F1 that had been cured with white light and then exposed to different durations of 10 mW/cm^2 365-nm light. C) F2 that that had been cured with white light and then exposed to different durations of 10 mW/cm^2 365-nm light.*

Although color change was accomplished in solution, decreased mobility of reactive species within a crosslinked network could inhibit the same result in solid samples. To test this, a resin formulation consisting of polyethylene glycol diacrylate (M_n = 250 Da), phenylbis(2,4,6-trimethylbenzoyl)phosphine

oxide (BAPO), TAS, BG, and aqueous 3 M NaOH, F1 (Table 9.1, Figure F1), was cured with white light and then subsequently exposed to increasing dosages of UV light. To our delight, the cured sample began to change from blue to green to yellow (Figure 9.1B). To ensure this was due to formation of acid and not a radical-induced side reaction, a similar resin containing no TAS, F2 (Table 9.1), was treated in the same fashion and the sample's color change was monitored. We observed some shifting of the blue color, however, the color change was qualitatively different and resulted in a muting of the blue color rather than shifting the color to green and yellow (Figure 9.1C). The change in blue color is consistent with prior reports of BG degradation due to UV photolysis[38,39]. In our studies, we quickly focused in on PEGDA-based resin systems given that PEGDA is known to be soluble in water as well as many organic solvents, and is compatible with a range of ionic, hydrophobic, and hydrophilic compounds. Notably, when we briefly examined nonpolar monomers isobornyl acrylate and butyl acrylate we observed solubility limitations from the TAS (Figure F2). We speculate that other photoacid generators could be suitable for use with nonpolar monomers, although this was not explored in our study.

Table 9.1. *Composition of compounds in each resin formulation. Compounds with their structure, full name, and corresponding acronym can be found in Figure S1.*

Resin	Dye	PEGDA-250 (wt%)[a]	BAPO (wt%)[b]	TAS (wt%)[b]	Dye (wt%)[b]	3 M NaOH (wt%)[b]	HQ (wt%)[b]	CQ (wt%)[b]	EDMAB (wt%)[b]
F1	BG	100	0.4	3	0.05	1	0	0	0
F2	BG	100	0.4	0	0.05	1	0	0	0
F3	MR	100	0.4	3	0.05	1	0	0	0
F4	BG+MR[c]	100	0.4	3	0.05	1	0	0	0
F5	BG	100	0	6	0.01	1	0.2	0.4	0.4

[a] Considered monomer component [b] Weight percent compared to total monomer weight [c] Mixture of bromocresol green and methyl red in a ratio of 3:1, 1:1, 1:3 by weight

We then explored 3DP of F1 using an Elegoo Mars 3 LCD printer equipped with a single 405-nm light source. With 12 second layer times and 50-µm layer thicknesses (Table F1), objects were printed with good resolution and complexity (Figure 9.2A-D, Figure F3, Figure F4). Line slits as small as 100 µm, walls as

thin as 200 µm, sharp features, and horizontal overhangs were each achieved (Figure 9.2A, Figure F4). Also, complex objects could be printed such as lattices, frogs, and gyroids (Figure 9.2B-D). The bulk colors of these final objects could be modulated by exposure to UV light after printing (Figure 9.2C). In this way, multi-color objects were achieved from a single resin vat. Using physical masks or applying projections results in spatial patterning of objects (Figure 9.2D). For thicker objects, color change was less readily accessible due to limitations in light penetration governed by the Beer-Lambert law. To probe this, 10 ×5 × 1 mm^3 samples were illuminated along their top, and the color change recorded as a function of depth (Figure F5, Figure F6). This showed that only shallow penetration of light occurs and color alteration deeper into the sample only takes place after complete discoloration of the outside layers. This is a limitation in the sequential approach to color modulation for thick (> 1 mm) object architectures, yet it is encouraging for VP 3DP since unwanted color modulation into already printed layers can be avoided.

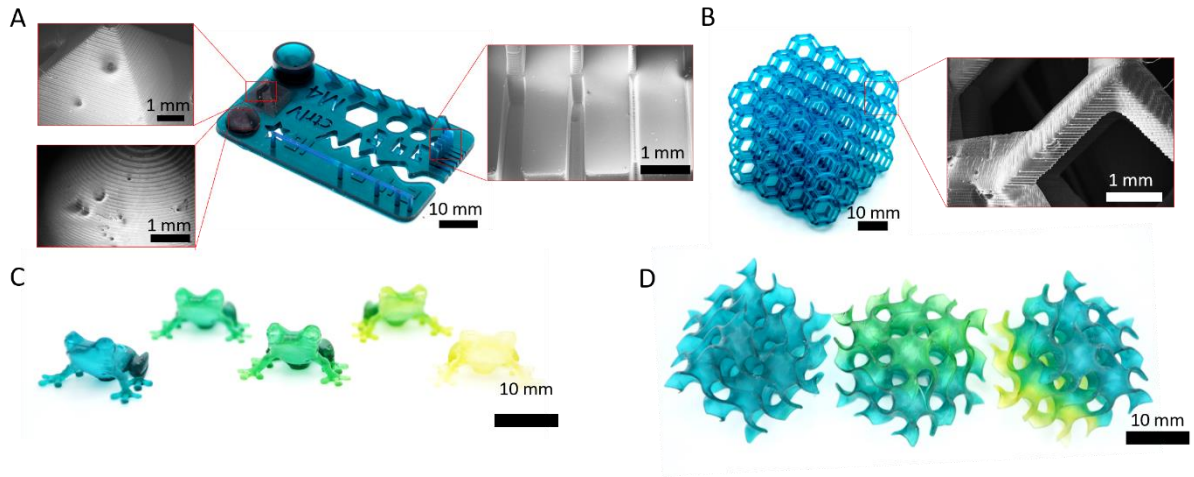

Figure 9.2. *A) 3D printed sample showcasing the printability and resolution of multi-color resins. SEM image insets showing specific features of the test print. Left insets show a zoomed in image of the pyramid and half dome architectures revealing consistent ~50 µm layers and the right inset reveals feature size resolutions (~100 µm) of 3D printed positive and negative pillars. B) Complex lattice with SEM inset of a single beam within a unit cell of the lattice. C) 3D printed frogs using F1 resin and their final color after being altered by 365 nm light for 0, 2, 5, 7, and 15 minutes as you go from left to right. D) 3D printed gyroids with their color altered by 365 nm light and physical masks.*

We also investigated the effect of light wavelength on the color change of 200-µm thick printed cylinders by exposing printed parts to either 365-, 405-, or 455-nm light (Figure F7). Use of 365-nm light produced the most drastic color change of the wavelengths tested for samples exposed to increasing light dosages.

Use of 405-nm light evoked moderate color change but had a sluggish response, only beginning to show small signs of color change after 5 minutes and 456-nm light exhibited no effect on the color of printed objects even after long exposures. This aligns well with the absorption profile of TAS, which has negligible absorption of light beyond 390 nm (Figure F8). Importantly, this showcases the ability to decouple the color change from resin curing to still allow postcuring of objects, which can be crucial for setting the final properties of printed objects.

We characterized two important components of the environmental stability of the parts: color stability upon exposure to light, and color leaching when submerged in water. In ambient light without any measures to preclude color changes, we noticed the color of parts gradually evolved toward the color associated with their most acidic form (Figure F9). This effect seemed to be due to ambient light as parts stored in the dark retained their color (Figure F9). Over six weeks of color tracking, the blue and green pixel values stayed rather steady while the red pixel values increased more significantly as the samples changed from appearing blue to green to yellow (Figure F10). To mitigate this, samples were printed from F1 with 0.2 wt% avobenzone, a common UV absorber. Avobenzone has a strong absorption within the UVA region (Figure S8). When these samples were exposed to 365-nm light, no color change was observed which was determined by tracking the RGB values of samples, compared to the distinct color change of F1 (Figure F11). The color stability improved with the addition of the UV blocker, albeit at the expense of rapid color modification during 3DP. We speculate that a UV coating applied after printing and designed to absorb UV-A and UV-B light could solve this issue when a part is made ready for a specific application. Additionally, we investigated color change due to leaching by submerging samples printed from F1 into a solution of water and monitoring the sample color change visually as well as leached pH dye by UV-Vis spectroscopy of the water. No color change was observed (Figure F12) and nearly no detectable leaching of BG into the surrounding water was seen in the absorption spectra over the four weeks (Figure F13). This is attributed to the highly crosslinked nature of the resulting parts which limits the swelling and chance for

diffusion of species out of the sample. Notably, other factors that impact swelling, such as affinity of polymer network to solvent, could affect the leaching dynamics of printed objects.

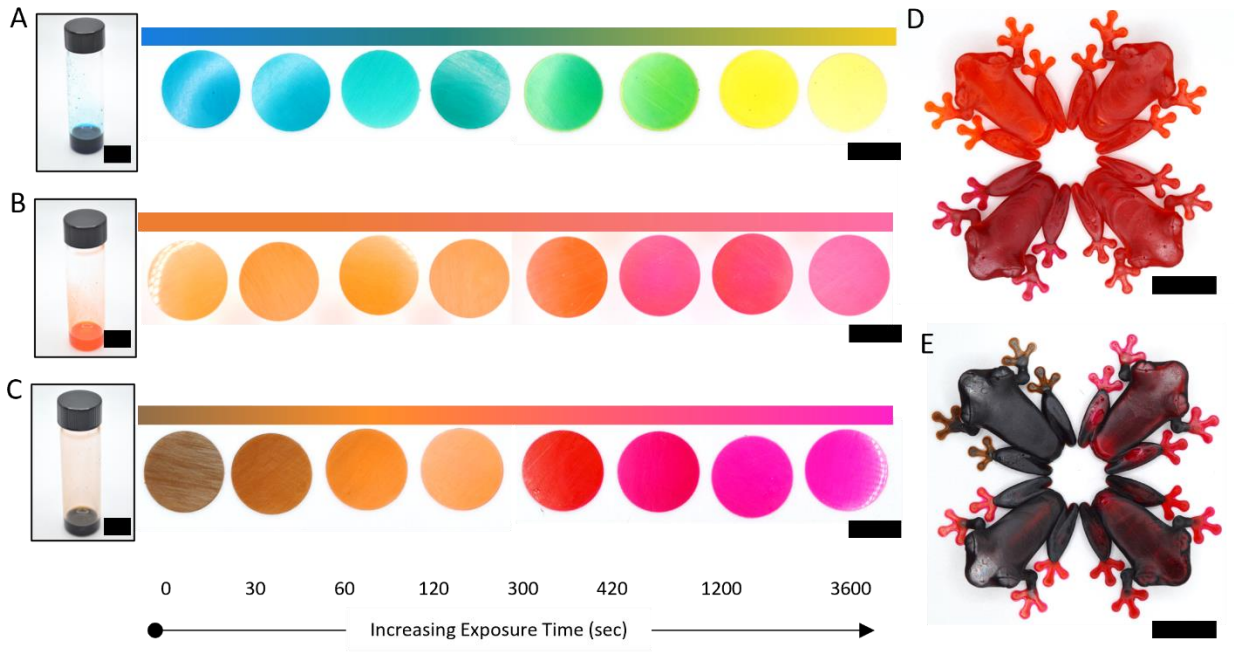

Figure 9.3. *A) F1 resin next to printed samples exposed to various exposures of 10 mW/cm^2 365-nm light. B) F3 resin next to printed samples exposed to various exposures of 10 mW/cm^2 365-nm light. C) F4 resin next to printed samples exposed to various exposures of 10 mW/cm^2 365-nm light. D) 3D printed frogs using F3 resin and their final color after being altered by 365-nm light for 0, 2, 7, and 15 minutes (clockwise starting from top left). E) 3D printed frogs from F4 resin with 1:1 ratio BG and MR and their final colors after being altered by 365-nm light. All scale bars represent 10 mm 0, 2, 7, and 15 minutes (clockwise starting from top left).*

We next investigated accessing a broader range of colors. To do this, we selected methyl red (MR) due to its color change under similar pH ranges as bromocresol green. MR undergoes a distinct transition from yellow to orange to red upon exposure to a more acidic environment. We were able to simply replace MR for BG at the same weight percent to create F3 (Table 9.1). The print parameters for F3 were determined iteratively and, overall, the addition of MR had little impact on printing parameters or resolution compared to F1 (Table F1, Figure F14). Sample prints along with post print exposure to varying dosages of 365-nm light led to a spectrum of vibrant colors ranging from orange to red, which was distinct compared to the colors accessed from F1 (Figure 9.3A, 9.3B, 9.3D). Conveniently, by mixing BG and MR dyes (F4, Table 9.1), new and distinct color combinations were possible (Figure 9.3C and 9.3E) and by controlling the ratio

of BG and MR, such as from ratios of 3:1, 1:1, and 1:3 BG:MR, the color palettes could vary dramatically (Figure 9.3E, Figure F15). These capabilities highlight the flexibility of this approach toward designing resins that can produce a multitude of colors.

Grayscale Patterning

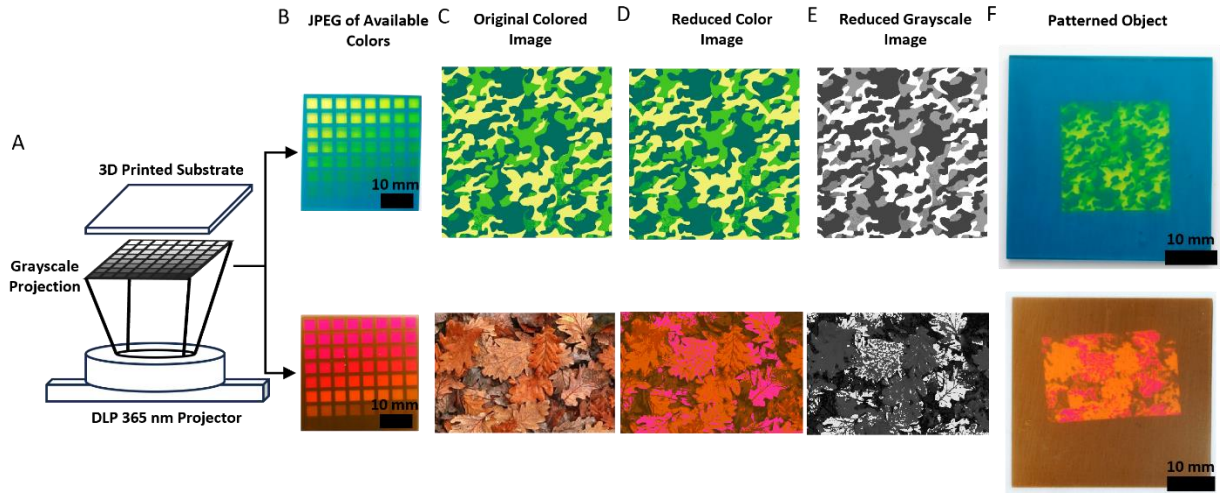

Figure 9.4. *Depiction of the process of patterning objects with a desired pattern using multi-color resins. A) Patterning a 3D printed substrate with grayscale values (0 – 255). B) Photograph of patterned substrate showing the colors obtainable with F1 (top) and F4 (bottom). C) Image that will be replicated. Camouflage pattern designed with the color palette of F1 (top) and fall leaves image that uses similar colors to F4 (bottom). D) Reduced color image of each of the original target images. E) Reduced color images translated to the grayscale version for patterning of a substrate F) Patterned substrate using the reduced grayscale images as projections for camouflage pattern using F1 resin (top) and fall leaves using F4 resin (bottom).*

We next wanted to determine if we could recreate patterns of our choice by controlling the local dosage of light in specified regions. To do this, we created a platform for generating grayscale projections to create target patterns. In this approach, an experiment is conducted to determine the color palette of a resin, which provides data to relate grayscale pixel value (0 to 255) to the resulting color that can be generated by a given resin. With this information, one can move on to transitioning a desired colored image into a grayscale projection that can be used to pattern the target sample. Ideally, desired patterns would be designed with the available color palette in mind, therefore providing simple conversion from the designed projection to the necessary grayscale image using the determined calibration data. However, manipulating any image into a reduced color image that includes only the available colors can be accomplished via minimum variance quantization. The reduced color image can then be translated back into grayscale through the

acquired conversion system giving a final projection suitable for printing individual layers. A flowchart showing this process can be found in Figure F16.

We tested our workflow for recreation of target multi-color patterns using F1 and F4 resin formulations. We determined the available colors for each resin using a 500-μm thick square 3D printed with uniform light exposure. That sample square was then patterned onto with the grayscale calibration pattern consisting of pixel intensities ranging from 0 to 255 (Figure 9.4A). The resulting sample, now displaying a range of colors, was photographed and the available color information extracted (Figure 9.4B). We then used MATLAB to extract the colormaps from the grayscale pattern and the swath of available colors, which provided information for translating between the two. Next, we selected an image of a camo pattern and another of fall leaves based on the visual similarity in colors between the images and either the F1 or F4 resins (Figure 9.4C). The sample image was fed into MATLAB and went through minimum variance quantization to create a reduced color image (Figure 9.4D). The camo pattern was generated in MATLAB using the colors extracted from F1's available colors and needed no alteration. The reduced color images could be translated into grayscale (Figure 9.4E) using our obtained translational information and, finally, this could be used to pattern an object with our desired pattern (Figure 9.4F). Visually there is good agreement between the target reduced color image and the patterned object. However, developing resins with a specific color palette in mind shows promise toward inspiring formulations for coatings, paints, or 3D printing resins geared specifically for creating camouflage materials or tailoring resins to prepare patterns with specified color palettes.

Dual Wavelength Multi-Color Printing

We next took aim at a single process dual wavelength VP 3DP approach. To accomplish this, we employed a custom dual wavelength printer (Figure F17) outfitted with a UV projector (365 nm, max light intensity of ~2 mW/cm^2) and a visible light projector (max light intensity of ~200 klux). The printer was operated using MATLAB with psychtoolbox[40] to control the individual projectors and serial commands to control the z-axis stepper motor. The visible projections were aligned to the UV projector by first undergoing a

keystone correction to straighten the image to the projection plan and then applying a geometric transformation to each image from the visible projection area to the UV projection area (Figure F18). Notably, print parameters for the visible projector were kept constant for each resin and determined iteratively (Table F2). In the future, controlling the visible light dosage within a given layer with grayscale offers additional opportunity to control more properties, such as stiffness, in conjunction with color.

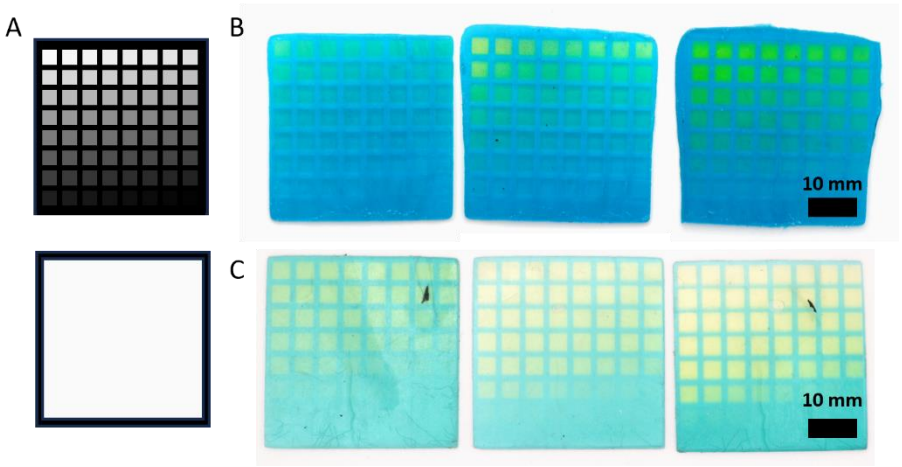

Figure 9.5. *A) UV (top) and visible (bottom) image slices used to determine necessary UV times to express full color range of resins. B) 3D printed sample printed from F1 resin using 4-sec visible layer cure time and 60- (left), 120- (middle), and 180-sec (right) UV layer time. C) 3D printed sample printed from F5 resin using 25 sec visible layer cure time and 60- (left), 120- (middle), and 180-sec (right) UV layer time.*

To determine the necessary UV projector time to obtain the full color range, a square was illuminated with white light and overlaid by a gradient intensity of UV light and 1-mm thick samples were printed using a layer thickness of 100 μm and systematically increasing UV layer times (Figure 9.5A). Although multi-color objects were printed with multiple colors on a single layer, the printing was overall met with limited success due to excessive UV layer times required to reach the full color change (>3 min/layer) resulting in outgrowth (Figure 9.5B). The outgrowth likely stemmed from BAPO's absorbance at 365 nm (Figure F8). To mitigate these issues, the amount of TAS was increased to 6 wt% to aid in faster color change, 0.2 wt% of hydroquinone (HQ) radical inhibitor was added to limit outgrowth, and a type II initiating system consisting of camphorquinone (CQ; λ_{max} = 470 nm), and ethyl 4-(dimethylamino)benzoate (EDMAB) tertiary amine coinitiator was introduced to reduce radical photoinitiator reactivity at 365 nm (F5, Table 9.1). Use of CQ had the added benefit of overlapping the absorption profile of the protonated form of BG,

essentially rendering BG as an opaquing agent to the CQ initiator throughout the print and preventing outgrowth at long UV exposure times (Figure F8). Additionally, dye concentration was reduced to better display the color change throughout thicker printed parts. Printing with F5 resulted in faster color change (UV layer times of < 3 min/layer) and a discernible reduction in outgrowth (Figure 9.5C). Although not explored here, we speculate that shorter layer times could be achieved through use of more efficient PAGs, higher light intensities, or larger concentrations of PAG. However, we found our print parameters to be reasonable to showcase 3DP of these resin formulations. With printability determined, we wondered if the color change was impacting the final properties of 3D printed objects. To test this, we produced blue and yellow ASTM standard type V samples from F5. Quasistatic tensile testing of these samples revealed no statistical difference in ultimate tensile strength, modulus, or elongation to break between the blue and yellow samples printed from the same resin vat (Figure F19).

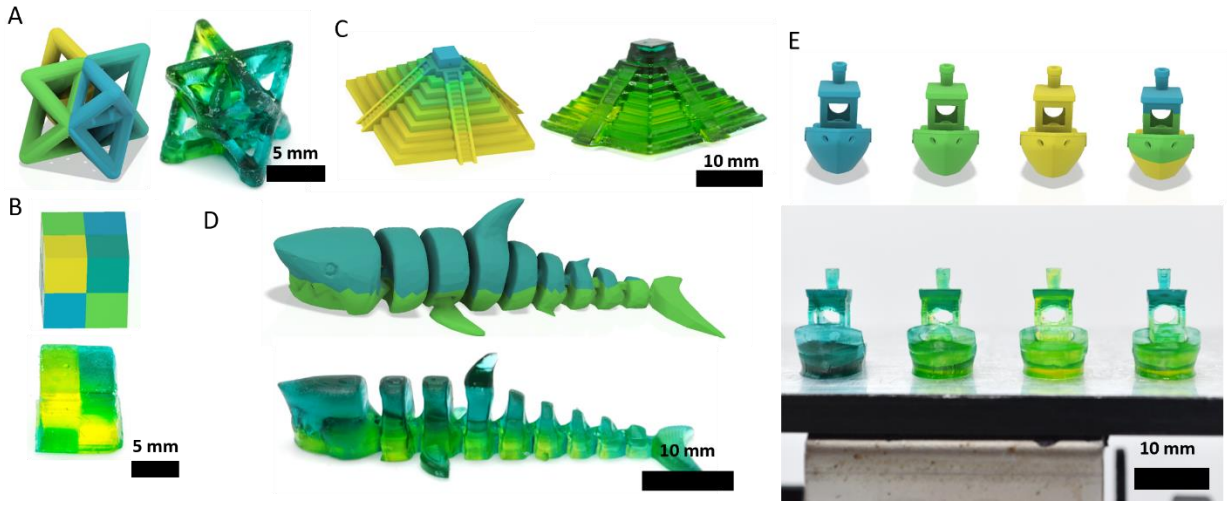

Figure 9.6. *A) Multi-color octet truss (CAD model (left) printed object (right)) B) Multi-color cube (CAD model (left) printed object (right)) C) Gradient multi-color pyramid (CAD model (left) printed object (right)) D) Two-toned shark (CAD model (left) printed object (right)) E) Multi-color benchy (CAD model (top) printed objects as printed on build plate (bottom))*

We next wanted to test our ability to print a range of multi-color structures. To start, we wanted to demonstrate objects can be printed with multiple colors that would be difficult to produce via subtractive manufacturing. To do this, we printed a multi-color octet truss printed with four different grayscale values (Figure 9.6A). We also wanted to show the ease of changing colors along the z axis by printing a cube

consisting of multiple colors that switch their arrangement halfway up the sample's height as well as a gradient-colored pyramid (Figure 9.6B,C). This coloring can also be applied to countershading, a camouflage method used in nature where the topside of an animal is darker colored than the bottom side allowing it to appear flat. Similar to how they appear in nature, a two-toned shark was printed with a darker top half than bottom (Figure 9.6D). Additionally, this approach can be used to not only create multi-color objects, but also produce different colored objects from a single resin vat. To showcase this, four benchy models were printed simultaneously on a single build plate resulting in a yellow, green, blue, and multi-color benchy (Figure 9.6E).

Conclusion:

We demonstrated a versatile approach for 3DP of multi-color parts via two-step (3DP followed by UV exposure) and single process (dual wavelength) 3DP processes each from single resin vats. Visible light was used to cure the resin setting final object architecture while 365-nm UV light was used to control the color of an object. While traditional radical curing of acrylates was responsible for object formation, color was modulated by controlling the localized acidity within a part. This was accomplished through the inclusion of TAS PAG and various pH-responsive dyes and by controlling the dosage of UV light. Additionally, this approach to multi-color printing was versatile showing compatibility with multiple pH-responsive dyes that can also be mixed using color mixing rules to achieve an even more diverse range of colors. In the future, we hope to explore additional resin systems that may yield control of new properties in VP using a single resin vat as well as controlling more than a single property through grayscale control of both visible and UV light.

Experimental Section

Materials: Bromocresol green (95%), mixed triarylsulfonium hexafluorophosphate salt (50 wt% in propylene carbonate), Phenylbis(2,4,6-trimethylbenzoyl)phosphine oxide (97%), poly(ethylene glycol) diacrylate average M_n 250, poly(ethylene glycol) diacrylate average M_n 575, poly(ethylene glycol) diacrylate average M_n 700, 2-hydroxyethyl acrylate (96 %), Isobornyl acrylate (technical grade), butyl acrylate (≥98%), sodium hydroxide (≥98%), ethyl 4-(dimethylamino)benzoate (≥99%), and camphorquinone (97%) were purchased from Sigma-Aldrich. Methyl red was purchased from Chem-Cruz. Hydroquinone (99.5%) was purchased from Acros Organics. Avobenzone (97.8%) was purchased from AmBeed. All chemicals were used as received.

Modifying Solution Color: A mixture of 3 g of TAS, 0.0015 g BG, and 0.05 g 1M NaOH was prepared. The solution was thoroughly mixed until homogenous. Contents were then split into three separate vials and a Teflon stir bar was added to each. Each vial was exposed to 10 mW/cm^2 365 nm light while being stirred at 200 rpm for either 0, 8, or 15 minutes.

Resin PTFE Mold Color Change: F1 and F2 resin (0.5 g) was placed into a cylindrical Teflon mold and illuminated with a white light lamp for 15 seconds until the resin solidified. The cured resin was rinsed with IPA and allowed to dry. Each sample was then illuminated with 10 mW/cm^2 of 365 nm light for either 0, 2, 5, or 10 minutes.

Resin Preparation: Resin components were mixed in amber borosilicate vials with PTFE caps. Each material was added sequentially (order of addition not important) in the specified amounts. After mixing, the resin was stirred in the dark for 24 hours allowing all components to dissolve.

*Commercial 3D Printing:*3D printing was done on a commercial Elegoo Mars 3 printer. To print, 3D object files were added to Lychee Slicer and arranged to fit on the build plate. The print profile for each resin was determined iteratively and can be found in Table F1. The build plate was levelled before each print. Resin was added to the vat and the print started. After printing, the printed object was rinsed with IPA and

carefully separated from the build plate. The parts were then submerged and rinsed in IPA for 5 minutes to remove uncured resin from the print surface before being postcured with 10 mW/cm^2 405 nm light for 1 min.

UV-Vis Spectroscopy: UV-Vis spectroscopy was performed on a Cary 60 UV-Vis spectrophotometer with quartz vials with a 1 cm pathlength at ambient pressure and temperature. A range from 250 nm to 800 nm was scanned.

*Penetration Depth Determination***:** Sample were 3D printed with dimensions of 10x5x1 mm (h-l-t). The sides and bottom of each sample were covered using black electrical tape leaving just the top face of the sample exposed. The top of the sample was exposed to 50 mW/cm^2 for times from 0 to 1800 sec. The tape was then removed, and the samples photographed (Figure F5). The photos were fed into MALTAB and the color along each height percent of a sample averaged and plotted (Figure F6).

RGB Tracking: Images for RGB tracking were taken with a Nikon D3200 DSLR camera with aperture set to 5.6, shutter speed 1/60, ISO 100, and fine resolution (6016x4000). The white balance and focus were set to auto and the camera was 20 cm away from the samples. To ensure consistency between images, a red, green, and blue color swatch was placed in each photo and RGB values extracted to ensure RGB values remained comparable (Figure S10). RGB values for the images were extracted from each sample by taking the average pixel value for ten points on each sample for three replicates.

Scanning Electron Microscopy: Samples were sputter-coated using the Leica EM ACE600 with a 10 nm layer of gold. SEM was subsequently conducted on a Zeiss Gemini SEM 450 at an accelerating voltage of 5 kV.

Multiwavelength Testing: Sample were 3D printed that were 500 μm thick and 15 mm in diameter. Either a 365 or 457 nm Kessil lamp or 405 nm projector was positioned to deliver a 10 mW/cm^2 light intensity onto a given sample. Intensity was measured using a light meter with the corresponding detector. Samples

were then placed under the light for various amounts of time and the resulting colors were captured with a Nikon D3200 camera.

Photopatterning: Photopatterning was done with a PDC05-5 projector with 365 nm light purchased from Xiamen Zhisen Electro. Equip. Co., LTD that could reach 2 mW/cm^2 at the print surface. 40x40x 0.5 (w x l x t) mm 3D printed sample substrates were placed above the projector and the grayscale calibration pattern displayed for 3 hours. After 3 hours, the sample was removed and photographed using a Nikon D3200 camera. The image was then fed into MATLAB where the grayscale counterpart was generated. The grayscale image was then projected onto a new sample for 3 hours. Ater 3 hours the substrate was removed from the projection area now displaying the desired pattern.

Dual Wavelength 3D Printing: Dual wavelength 3D printing was accomplished on a custom 3D printer equipped with a Acer X152H visible light projector and a PDC05-5 365 nm light projector purchased from Xiamen Zhisen Electro. Equip. Co., LTD. Print files were prepared in MALTAB. MATLAB was also used to run the printer by controlling projectors via Psychtoolbox[40] and sending G code commands via the serial port.

Tensile Testing: Tensile tests were conducted on a MTS Criterion® Electromechanical Testing System using ASTM D638 type V specimen. The strain rate was set to 10 mm/min. Tensile strain was measured through video analysis using MATLAB by measuring the distance between series of lines that were drawn on the dogbones in the gauge region prior to testing. Strain was calculated based on the change in distance between the lines on the dogbones. Stress-strain curves were obtained by correlating stress and strain values.

*Measuring Light Sources Emission Spectra***:** General emission spectra for each light source were recorded using a Flame Miniature Spectrometer by Ocean Optics (Figure F21). To do this, the spectrometer was placed into a dark enclosure to reduce background noise. The light source of interest was then positioned in front of the light input slit and positioned far enough away so that a reasonable signal to noise was

reached with the signal also did not overload the detector. The spectra were then recorded for each light source and data normalized to the wavelength with the maximum intensity value.

Photoacid Generators (PAGs) Solubility Tests in Different Monomers: A solution of 3 wt% TAS each monomer was prepared in a borosilicate vial. The solution was then lightly perturbed using a vortexer every hour for four hours and dissolution observed. The solutions were left overnight and resulting solubility recorded.

References:

1. ASTM 52900. Additive Manufacturing - General Principles - Terminology. *ASTM Int.* **2021**, 1–14 (2021).
2. Huang, S. H., Liu, P., Mokasdar, A. & Hou, L. Additive manufacturing and its societal impact: A literature review. *Int. J. Adv. Manuf. Technol.* **67**, 1191–1203 (2013).
3. Lipson, H. & Kurman, M. Printing in layers. *Fabr. new world 3D Print.* 65–81 (2013).
4. Shaukat, U., Rossegger, E. & Schlögl, S. A Review of Multi-Material 3D Printing of Functional Materials via Vat Photopolymerization. *Polymers (Basel).* **14**, (2022).
5. Sampson, K. L. *et al.* Multimaterial Vat Polymerization Additive Manufacturing. *ACS Appl. Polym. Mater.* **3**, 4304–4324 (2021).
6. Nazir, A. *et al.* Multi-material additive manufacturing: A systematic review of design, properties, applications, challenges, and 3D printing of materials and cellular metamaterials. *Mater. Des.* **226**, 111661 (2023).
7. Rafiee, M., Farahani, R. D. & Therriault, D. Multi-Material 3D and 4D Printing: A Survey. *Adv. Sci.* **7**, 1902307 (2020).
8. Skylar-Scott, M. A., Mueller, J., Visser, C. W. & Lewis, J. A. Voxelated soft matter via multimaterial multinozzle 3D printing. *330 | Nat. |* **575**, 330–335 (2019).
9. Schwartz, J. J. & Boydston, A. J. Multimaterial actinic spatial control 3D and 4D printing. *Nat. Commun.* **10**, 1–10 (2019).
10. Dolinski, N. D. *et al.* Solution Mask Liquid Lithography (SMaLL) for One-Step, Multimaterial 3D Printing. *Adv. Mater.* **30**, 1800364 (2018).
11. Ge, Q. *et al.* 3D printing of highly stretchable hydrogel with diverse UV curable polymers. *Sci. Adv.* **7**, (2021).
12. Ge, Q. *et al.* Multimaterial 4D Printing with Tailorable Shape Memory Polymers. *Sci. Reports 2016 61* **6**, 1–11 (2016).
13. Sun, Y. C., Wan, Y., Nam, R., Chu, M. & Naguib, H. E. 4D-printed hybrids with localized shape memory behaviour: Implementation in a functionally graded structure. *Sci. Reports 2019 91* **9**, 1–13 (2019).
14. Wu, S. Y., Yang, C., Hsu, W. & Lin, L. 3D-printed microelectronics for integrated circuitry and passive wireless sensors. *Microsystems Nanoeng. 2015 11* **1**, 1–9 (2015).
15. Lipkowitz, G. *et al.* Injection continuous liquid interface production of 3D objects. *Sci. Adv.* **8**, eabq3917 (2022).
16. Peng, X. *et al.* Multi-Color 3D Printing via Single-Vat Grayscale Digital Light Processing. *Adv. Funct. Mater.* **32**, 2112329 (2022).
17. Xu, Z. *et al.* Vat photopolymerization of fly-like, complex micro-architectures with dissolvable supports. *Addit. Manuf.* **47**, 102321 (2021).
18. Bader, C. *et al.* Making data matter: Voxel printing for the digital fabrication of data across scales and domains. *Sci. Adv.* **4**, 8652 (2018).
19. Grigoryan, B. *et al.* Development, characterization, and applications of multi-material

stereolithography bioprinting. *Sci. Reports 2021 111* **11**, 1–13 (2021).

20. Cheng, J. *et al.* Centrifugal multimaterial 3D printing of multifunctional heterogeneous objects. *Nat. Commun.* **13**, 7931 (2022).

21. Gu, Y. *et al.* Photoswitching topology in polymer networks with metal–organic cages as crosslinks. *Nat. 2018 5607716* **560**, 65–69 (2018).

22. Chen, D. & Zheng, X. Multi-material Additive Manufacturing of Metamaterials with Giant, Tailorable Negative Poisson's Ratios. *Sci. Reports 2018 81* **8**, 1–8 (2018).

23. Han, D., Yang, C., Fang, N. X. & Lee, H. Rapid multi-material 3D printing with projection micro-stereolithography using dynamic fluidic control. *Addit. Manuf.* **27**, 606–615 (2019).

24. Lu, P. *et al.* Wavelength-selective light-matter interactions in polymer science. *Matter* **4**, 2172–2229 (2021).

25. Kuang, X. *et al.* Grayscale digital light processing 3D printing for highly functionally graded materials. *Sci. Adv.* **5**, (2019).

26. Peterson, G. I. *et al.* Production of Materials with Spatially-Controlled Cross-Link Density via Vat Photopolymerization. *ACS Appl. Mater. Interfaces* **8**, 29037–29043 (2016).

27. Yue, L. *et al.* Single-vat single-cure grayscale digital light processing 3D printing of materials with large property difference and high stretchability. *Nat. Commun. 2023 141* **14**, 1–12 (2023).

28. Huang, S. *et al.* One-pot ternary sequential reactions for photopatterned gradient multimaterials. *Matter* **6**, 2419–2438 (2023).

29. Ehrmann, K. & Barner-Kowollik, C. Colorful 3D Printing: A Critical Feasibility Analysis of Multi-Wavelength Additive Manufacturing. *J. Am. Chem. Soc.* (2023) doi:10.1021/JACS.3C09567.

30. Ma, Y. *et al.* Photoswitching Cationic and Radical Polymerizations: Spatiotemporal Control of Thermoset Properties. *J. Am. Chem. Soc.* **143**, 21200–21205 (2021).

31. Wang, B. *et al.* Stiffness control in dual color tomographic volumetric 3D printing. *Nat. Commun. 2022 131* **13**, 1–10 (2022).

32. Rossegger, E. *et al.* Wavelength Selective Multi-Material 3D Printing of Soft Active Devices Using Orthogonal Photoreactions. *Macromol. Rapid Commun.* 2200586 (2022) doi:10.1002/marc.202200586.

33. Price, N., Green, S., Troscianko, J., Tregenza, T. & Stevens, M. Background matching and disruptive coloration as habitat-specific strategies for camouflage. *Sci. Reports 2019 91* **9**, 1–10 (2019).

34. Martin, H., Eisner, E. & Klosterman, J. K. Accessible 3D Printing: Multicolor Molecular Models from Consumer-Grade, Single Filament 3D Printers. *J. Chem. Educ.* **100**, 4860–4865 (2023).

35. Dzulkifli, M. A. & Mustafar, M. F. The Influence of Colour on Memory Performance: A Review. *Malays. J. Med. Sci.* **20**, 3 (2013).

36. Crivello, J. V. & Lam, J. H. W. Diaryliodonium Salts. A New Class of Photoinitiators for Cationic Polymerization. *Macromolecules* **10**, 1307–1315 (1977).

37. Crivello, J. V. The Discovery and Development of Onium Salt Cationic Photoinitiators. *J Polym*

Sci A Polym Chem **37**, 4241–4254 (1999).

38. Matyszczak, G., Krzyczkowska, K. & Krawczyk, K. Removal of Bromocresol Green from aqueous solution by electro-Fenton and electro-Fenton-like processes with different catalysts: laboratory and kinetic model investigation. *Water Sci. Technol.* **84**, 3227–3236 (2021).

39. Revilla Pacheco, C. *et al.* Adsorption and degradation of rhodamine B and bromocresol green by FeOCl under advanced oxidation process. *Arab. J. Chem.* **16**, 105049 (2023).

40. Brainard, D. H. The Psychophysics Toolbox. *Spat. Vis.* **10**, 433–436 (1997).

Part Four

3D Printing as an Enabling Technology

Chapter 10: Dependence of the kinetic energy absorption capacity of bistable mechanical metamaterials on impactor mass and velocity

Reprinted (adapted) with permission from:

R. Fancher, I. Frankel, **K.C.H. Chin**, M. Abi Ghanem, B. MacNider, L.S. Shannahan, J.F. Berry, M. Fermen-Coker, A.J. Boydston, N. Boechler. Dependence of the kinetic energy absorption capacity of bistable mechanical metamaterials on impactor mass and velocity, Extreme Mechanics Letters (2023),

Abstract

Using an alternative mechanism to dissipation or scattering, bistable structures and mechanical metamaterials have shown promise for mitigating the detrimental effects of impact by reversibly locking energy into strained material. Herein, we extend prior works on impact absorption via bistable metamaterials to computationally explore the dependence of kinetic energy transmission on the velocity and mass of the impactor, with strain rates exceeding 10^2 s^{-1}. We observe a large dependence on both impactor parameters, ranging from significantly better to worse performance than a comparative linear material. We then correlate the variability in performance to solitary wave formation in the system and give analytical estimates of idealized energy absorption capacity under dynamic loading. In addition, we find a significant dependence on damping accompanied by a qualitative difference in solitary wave propagation within the system. The complex dynamics revealed in this study offer potential future guidance for the application of bistable metamaterials to applications including human and engineered system shock and impact protection devices.

Introduction

The local magnification of mechanical forces as a result of a dynamic collision (impact) and their detrimental effects on natural and engineered systems have been studied extensively [1–4]. A relatively new approach for the mitigation of damage induced by impact is the use of bistable structures, which in contrast to the more ubiquitous mechanisms of dissipation and scattering [5–8], reduces the effect of impact by reversibly ‘‘locking’’ some of the energy imparted by a shock or impact into the form of strain energy [9,10]. Both the performance and reversibility of bistable structures for impact mitigation are attractive, as the energy locking mechanism could be used in conjunction with other mechanisms [11], such as dissipation, and the structures can ostensibly be reset in a controllable fashion for reuse. In addition to studies of the impact absorption characteristics of single bistable structures [9,10], more recently, the energy absorption properties of bistable structures configured into multiunit-cell mechanical metamaterials has been explored [10–18]. In such studies, the material response has been studied in either relatively low rate regimes [12–18] (where in some cases the response was suggested to be rate independent [12]), or, in high rate regimes (e.g. up to 600 s^{-1}), the impact response was not related to wave propagation in the material [11]. This can be placed in contrast with other studies of nonlinear solitary, or ‘‘transition’’, wave propagation in similar materials, which show significant dependence on the system excitation [19–27]. A notable work that brings these two features (impact absorption via bistability and nonlinear waves) together is that of Ref. [28], which described the effect that the shape of the bistable potential has on energy trapping and solitary wave emission, however, they did not study the dependence of absorption performance on impact conditions. Energy dissipation in bistable systems exhibiting transition waves was also studied in an earlier work [29,30], however the model involved irreversibility and only a few impact conditions were studied. We further note that, closely related to energy dissipation, transition waves in bistable media have also been studied in the context of energy harvesting [31].

In this work, we computationally study the dependence of kinetic energy transmission in a bistable mechanical metamaterial (shown in Fig. 1) on the velocity and mass of the impactor, in wave dominated

regimes (wavelengths less than the absorbing material's reference length) with maximum strain rates of approximately 195 s^{-1}. Kinetic energy (KE) transmission is used as a performance metric herein as it has been previously shown to be closely related to damaging effects, for instance, in the case of behind armor blunt trauma [32,33]. The computational model of our mechanical metamaterial is a discrete element model (DEM) composed of a one-dimensional (1D) chain of masses connected by bistable nonlinear springs, with linear intersite damping, and a contact spring at the boundary that allows release of the impactor under tension during rebound. We find a large dependence of KE transmission on both impactor mass and velocity, ranging from significantly better to worse performance than a comparative linear material. We correlate said performance to solitary wave formation and give analytical estimates of idealized energy absorption capacity under dynamic loading. In addition, a significant effect is found from the inclusion of the intersite damping, accompanied by a qualitative difference in solitary wave propagation within the system. The complex dynamics revealed in this study offer potential future guidance for applications including improved packaging to prevent damage during shipment [12], personal protection equipment [7,12,34], and crash mitigation for vehicles [12,16,35].

Results and Discussion

Description of metamaterials to be modeled

The conceptual setup described herein is the impact of a relatively rigid ‘‘impactor’’ block onto an arbitrarily-sized ‘‘absorbing’’ material block. The dimensions of the absorbing block were chosen as 2d (height) by d (both width and depth), with d = 5 cm. Our designed absorbing material consists of a bistable mechanical metamaterial composed of a periodic array of structured unit cells based upon the geometry from Ref. [12]. The unit cell of our bistable mechanical metamaterial is composed of two elastic beams surrounded by a lower-aspect ratio monolithic ‘‘frame’’. Fig. 10.1(a,b) shows a 3D printed representation (with fewer unit cells and layers than modeled herein) of the bistable mechanical metamaterial, where the beams are composed of a rubber simulant material and the frame composed of an acrylic simulant. The thickness to length aspect ratio of the beam elements r = T/L (where T is the beam thickness and L is its length) and the angle of the beam θ was chosen such that r = 0.14 and θ = 60 degrees.

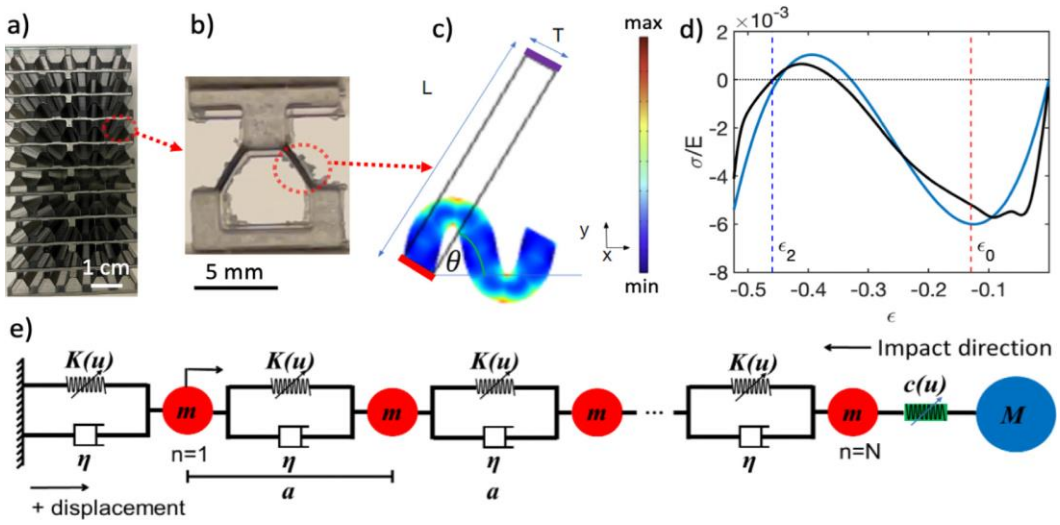

Figure 10.1. *Concept and modeling overview. (a) Photograph of a 3D printed model of the bistable mechanical metamaterial (with fewer unit cells than modeled herein). (b) Photograph of a 3D printed unit cell. (c) One beam in the unit cell design, showing the displacement of the beam near* ϵ_2 *simulated using FEM, where the colorscale denotes the von Mises stress (arb.). (d) Non-dimensionalized effective stress and strain of the mechanical metamaterial (for* $r = 0.14$ *and* $\theta = 60$ *degrees), based upon experimental compression measurements (solid black line), and the 3rd order polynomial fit of the experimentally measured curve (solid blue line), which is used in the DEM model. The vertical dashed red and blue lines denote* ϵ_0 *and* ϵ_2*, respectively, and the horizontal dotted black line denotes zero stress. (e) Illustration of the DEM model.*

Large deformation finite element method (FEM) simulations of beam deformation under compression are shown in Fig. 1(c), assuming a Neo-Hookean material model (Lamé Parameters: $\lambda = 47.191$ GPa, $\mu = 25$ GPa), fixed boundaries on the bottom end (red), with a prescribed y-direction displacement on the top end (purple, fixed in the x-direction), and free boundaries otherwise. We model the beam separately from the frame, because we approximate the frame itself to undergo minimal deformation as it is much thicker (structurally stiffer) than the beams. Furthermore, we assume that the two beams within the unit cell deform symmetrically with respect to each other. As such the mechanical response of a single beam can be extrapolated to determine the elasticity of the metamaterial. The choice of the beam aspect ratio was chosen to obtain moderately high energy locking without self-contact [12], but without too small of an energy barrier before unsnapping. The size of the frame was chosen to avoid self-contact while maintaining rigidity without excessive density per unit volume of the unit cell. Both the frame and geometry are natural candidates for future optimization studies. We note that FEM simulations serve three purposes in this study, as they: (i) Serve as an aid in visualizing the deformation of the snap through mechanism (Fig. 10.1(c)), (ii)

help support the origin of the force–displacement behavior measured (Fig. 10.1(d)) for the printed bistable sample, and (iii) served as a tool to select a highly absorbing beam aspect ratio r for the printed structure (for which the mechanical response was measured, and fitted to serve as the force–displacement relation in the DEM simulations).

Measurement of quasi-static bistable material response

Fig. 10.1(d) shows the experimentally measured mechanical response of a single 3D printed layer of bistable metamaterial (composed of the same material and geometry as in Fig. 10.1(a,b), but less depth in the direction going into the page), along with a 3rd order polynomial fit of the measurement. The response of the layer was measured using a mechanical test frame in displacement control, where the rigid (acrylic simulant) top and bottom parts of the layer were attached to grips in a mechanical testing frame, allowing measurement of tension, as well as compression, following the snap through event. Herein a ‘‘layer’’ is defined as a row of unit cells where the normal is in the direction of the impactor velocity vector and along the long axis of the absorbing block. In Fig. 10.1(d), σ and ε are the effective bistable mechanical metamaterial stress and strain, respectively, and E = 8.42e5 N/m2 is the measured small strain elastic modulus of the rubber simulant beam material. The transition to negative stiffness can be seen to occur in the fit at $\epsilon_0 = -0.13$ and the second stability point at $\epsilon_2 = -0.46$.

Discrete element model

Fig. 10.1(e) shows a visualization of the DEM used to simulate the dynamics of the metamaterial undergoing impact. Each layer of unit cells in the absorbing material were described as lumped mass layers of mass m connected by massless springs and dampers, with the impactor of mass M interacting with the absorber via a contact spring. A DEM was chosen as a reasonable model due to the following key assumptions: (i) That the model is designed to describe uniaxial loading of the impactor on the absorber block with minimal off axis loading effects; (ii) near zero effective Poisson’s ratio of the lattice; and (iii) The lattice is composed of stiffer and larger masses lumped within the material, separated by softer, lower mass elements. Regarding the third assumption, more precisely, the vibrational frequencies of the separate

mass and spring components must be much higher than the modal frequency of the two elements combined, where the spring deforms as the mass moves like a rigid body, such that the higher frequencies can be reasonably ignored. The sample mass was divided into equal ‘‘mass layers’’ in number equal to the amount of unit cells along the height of the material (N). For the N = 100 lattice, which we study herein, the layer mass m = 1.2 g, with layer spacing a = 1 mm.

A ‘‘contact spring’’ with nonlinear stiffness, based on the Hertzian contact model [36], between the top unit cell and the impactor mass was modeled to describe the impactor hitting the top of the sample and allowing the impactor to freely bounce rather than stick to the top of the lattice after impact. The equations of motion for the impactor particle (i.e. particle n = N + 1) is thus:

$$M\ddot{y}_{N+1} = C_1([y_N - y_{N+1}]_+)^{\frac{3}{2}} \qquad \text{(Eq 10.1)}$$

where the $[]_+$ denotes spring's inability to support tension (if the value in brackets is negative it equals zero), y_n is the displacement of the nth layer, and C_1 is a fitting parameter (set to −8.51e8). As such, the contact stiffness (shown in Fig. 1(e)) is $c(u) = -3/2\ C_1([-u]_+)^{1/2}$, where u is the spring stretch (positive in tension for both u and c(u)). In addition to allowing the impactor to rebound, the use of a contact spring allowed for a better estimation of real impact conditions, including roughly describing the impactor coming into contact with the sample at a slight relative angle, or having asperities on the two surfaces.

We then define the force–displacement relation of an individual layer:

$$F_L(u) = \beta_3(u)^3 + \beta_2(u)^2 + \beta_1(u) \qquad \text{(Eq 10.2)}$$

where F_L is positive in tension. For an N = 100 particle long chain, coefficients β_1 = 2.257e5 N/m, β_2 = 1.187e9 N/m, and β_3 = 1.524e12 N/m, which are extracted from the fit of the mechanical response measured for the 3D printed bistable layer (shown in Fig. 10.1(d)). The stiffness is thus defined as $K(u) = \partial F_L(u)/\partial u$ (shown in Fig. 10.1(e)). Eq. (10.2) is used in all other elements of the DEM (corresponding to the metamaterial layers), where the top layer of the absorber (n = N) is:

$$m\ddot{y}_N = C_1(y_N - y_{N+1})^{\frac{3}{2}} - F_L(y_N - y_{N-1}) - \eta(\dot{y}_N - \dot{y}_{N-1}) \qquad \text{(Eq 10.3)}$$

where $\dot{y}_N$ and η are the velocity of the nth particle and η the damping coefficient, respectively.

The equations of motion for layers from n = 2 to n = N – 1 are given by:

$$m\ddot{y}_n = F_L(y_{n+1} - y_n) - \mathrm{F_L}(\mathrm{y}_n - \mathrm{y}_{n-1}) + \eta(\dot{y}_{n+1} - \dot{y}_n) - \eta(\dot{y}_n - \dot{y}_{n-1}) \qquad \text{(Eq 10.4)}$$

The equation of motion for the n = 1 mass, next to the fixed boundary is then:

$$m\ddot{y}_1 = F_L(y_2 - y_1) - \mathrm{F_L}(\mathrm{y}_1) + \eta(\dot{y}_2 - \dot{y}_1) - \eta(\dot{y}_1) \qquad \text{(Eq 10.5)}$$

The equations of motion were numerically integrated using the ODE45 integrator in MATLAB [37], given an initial velocity V applied to the impactor mass, to solve for particle displacements and velocities as a function of time.

Analytical estimate of nominal impact conditions

The kinetic energy transmitted through the half-way-point of the absorbing block (with respect to the impactor velocity vector), or unit cell n = N/2, was chosen as the performance metric (so as to avoid boundary effects), which was then compared against that of a linearly coupled (with the exception of the contact spring) absorbing material.

We then endeavored to estimate the impactor parameters to minimize KE transmission through n = N/2 of our chosen bistable mechanical metamaterial. The nominal impact velocity was estimated as:

$$V_0 = 2c_0\epsilon_0 \qquad \text{(Eq 10.6)}$$

where c_0 is the long wavelength linear soundspeed of the lattice, with $c_0 = \sqrt{\beta_1/m}a$ (such that c_0 = 13.7 m/s for the lattice parameters simulated herein). Eq. (10.6), which is derived for an elastic projectile hitting a bar of the same diameter and material [2], is meant to estimate the minimum velocity threshold such that the snap through to the second stable state is induced, and results in V_0 = 3.6 m/s for our simulated chain. In an ideal scenario, the entire material between the n = N/2 and the impactor would then snap to the second

stable state, and have locked the entire KE from the impactor into stored potential energy (PE). The PE absorbed from the first half of the absorber is then:

$$PE = \frac{N}{2}\int_0^{a\epsilon_2} F_L(u)du \qquad \text{(Eq 10.7)}$$

The nominal impactor mass M_0 was solved as the only remaining unknown when impactor KE (i.e. $MV^2/2$) was set equal to PE. For our simulated chain, M_0 = 18 g.

With regards to this estimate of nominal impact conditions, we highlight several issues related to the bistable material impact energy absorption strategy. As noted in prior works (e.g. Ref. [38]), a bistable element can only lock a fraction of the incident energy. This can be seen from the effective stress–strain curve of a bistable element, e.g., Fig. 10.1a, where, for bistability to exist, the curve must pass above the σ = 0 axis, and as such will always release some energy that was used to snap it into the closed stable state. The limit of this is when the curve just touches the σ = 0 axis, however, in this case, vanishingly small tensile stresses are needed to unsnap and open the bistable element, which releases any stored energy back into the system. Such tensile stresses can be readily expected in a dynamic impact scenario. In the case of a bistable metamaterial, where there are many bistable elements in series, this issue may be less pronounced, as each bistable element can be imagined to lock in a comparatively small portion of the impact pulse energy, such that the remaining re-released fraction, in an ideal scenario as described in Eq. (10.7), would be less than for a single bistable element. Similarly, one can then further speculate that a metamaterial with a uniform array of bistable elements may not be an ideal solution. For instance, a better solution may be to use a gradient of bistable elements (as has been used in related studies [38]), such that, approximately, the first bistable element encountered by the impact pulse requires the largest energy to lock, then the next element requires less energy to lock and is matched to the ‘‘leftover’’ or re-released energy from the first element, and so on. In such a strategy one could imagine potentially having nearly complete energy absorption for specific impact stimuli, although we do not explore this configuration herein.

Simulated dependence on impact conditions for a conservative material

To assess the performance of the bistable mechanical metamaterial, the linear ‘‘control’’ material was simulated using a linear stiffness corresponding to the slope between zero force and the force at ε0 for the bistable material (equal to $1.77\beta_1$), identical mass, contact spring and damping parameters to the bistable sample. Simulations with varied impactor mass and velocity using an undamped linear material showed negligible difference in KE transmission at the n = N/2 (approximately 1% maximum), between linear materials of different stiffnesses, when analyzed from impact time until the time the first wavefront hits the bottom of the sample. We thus define a ‘‘KE ratio’’, as the maximum KE of the N/2 mass of the control lattice divided by the maximum KE of the N/2 mass of the bistable lattice, where a value greater than one indicates the bistable material is outperforming the linear material in terms of minimizing KE transmission.

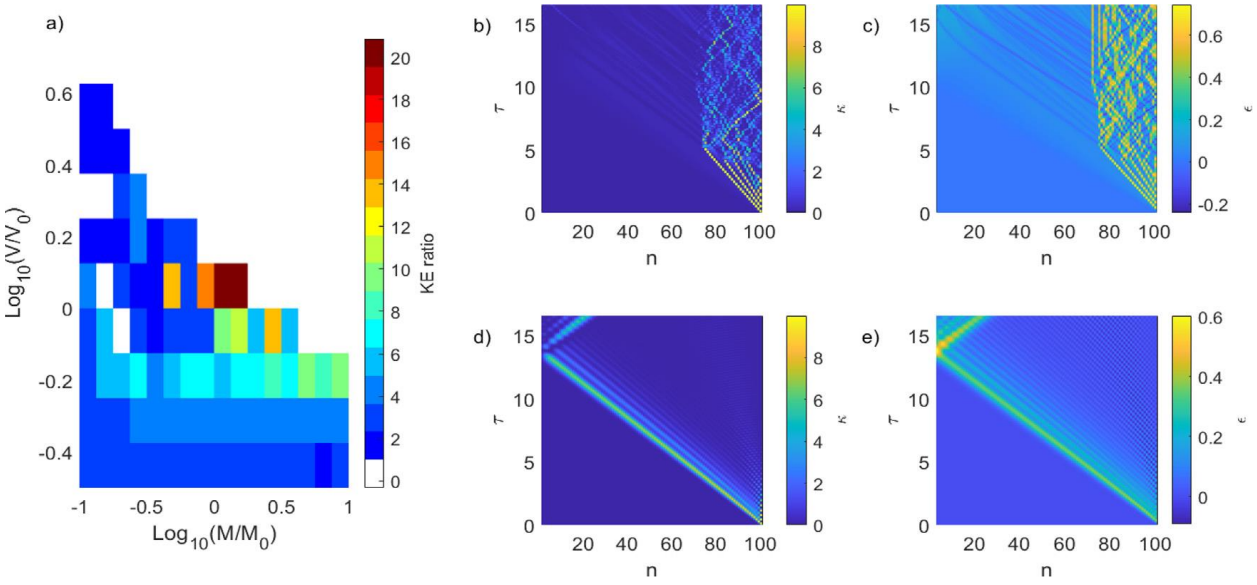

Figure 10.2. *Undamped simulations. (a) KE ratio as a function of impactor conditions. Non-dimensionalized KE, κ, for bistable (b) and linear (d) materials at nominal impact conditions (M_0, V_0). The colorbar is saturated at $KE_I/10$. Layer strain, ϵ, for bistable (c) and linear (e) materials at nominal impact conditions (M_0, V_0).*

We initially simulated the response of N = 100 layer conservative (i.e. η = 0) materials for duration $T_s = 1.2\tau_l$ where τ_l is the time for the linear wave to travel across the material once (based on c_0). Fig. 10.2(a) shows the KE ratio for varied M and V, wherein the bistable material outperforms the linear material by up to 21x, while performing worse than the linear material particularly for impactor conditions where $M > M_0$

and $V > V_0$. There is a reduction in performance above the nominal impact conditions of M_0 and V_0 as they represent the point where the kinetic energy of the impactor could be equally distributed across the first half of the material and stably locked into strain energy. This is consistent with the approximate iso-energy diagonal threshold that can be observed in Fig. 10.2(a) that separates KE ratios above and below unity. This however opens the question as to why the bistable material would perform less well than the linear material without any energy locking capability. To address this question we proceed to study the spatiotemporal response for both systems.

To study the spatiotemporal response of the absorber materials at specific impact conditions, we define a normalized KE $\kappa = N(KE_n/KE_I)$, where KE_n is the KE of the nth particle and KE_I is the KE of the impactor, and strain $\epsilon = u/a$. The simulation time t is expressed in terms of $\tau = t\sqrt{\beta_1 m}$. Fig. 10.2(b,c) shows κ and ϵ at impactor conditions M_0, V_0, and Fig. 10.2(d,e) shows the linear sample at the same impact conditions. We note that the impactor is not shown in the plots of ϵ, although it is included as the $n = N + 1$ layer in the κ diagrams.

Fig. 10.2(d,e) shows a minimally dispersive pulse that propagates through the linear sample. In contrast, the bistable material (Fig. 10.2(b,c)) shows nonlinear effects, demonstrating the richness of the bistable system. In Fig. 10.2(b,c), we see solitary, transition wave emission from the initial impact, as shown by the straight, yellow lines that progress ~25 particles into the sample from the point of impact. The identification of these as transition waves is noted by strains exceeding ε_2. Looking first at each of these emissions, we see that the first wave is the fastest, then the next two are progressively slower, which is consistent with the amplitude dependent wavespeed of many solitary waves [25]. Beyond $\tau \sim 4$, between the 80–100th particles, we see a complex oscillatory behavior, likely a combination of low amplitude vibrations and dynamic snapping and unsnapping of the bistable layers. Crucially, past ~25 particles from the impactor, very little KE is transmitted further into the material.

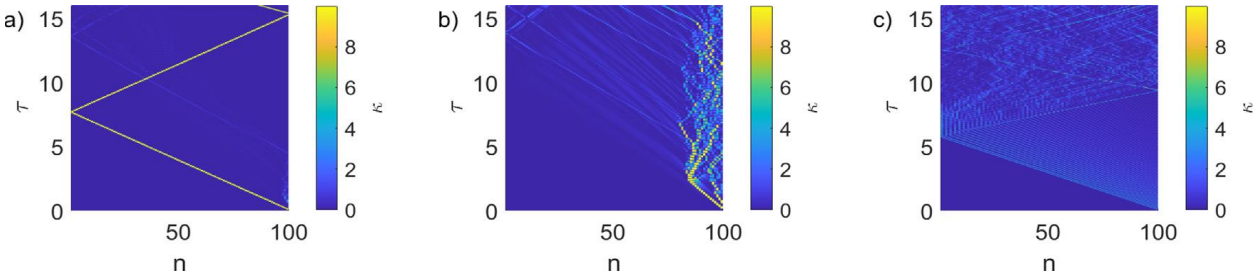

Figure 10.3. *Normalized KE, κ, for the simulated undamped bistable material shown in Fig. 2(a) for the (a) worst performance (low mass and high velocity, $M/M_0 = 10^{-1}$ and $V/V_0 = 10^{0.75}$), (b) good performance (close to nominal mass and velocity, $M/M_0 = 10^{-0.625}$ and $V/V_0 = 10^{0.25}$), and (c) poor performance (high mass and high velocity, $M/M_0 = 10^{0.75}$ and $V/V_0 = 10^{0.75}$).*

In order to investigate the changing performance shown in Fig. 10.2(a), we study three different impactor conditions. Fig. 10.3(a) shows a location to the top left of Fig. 10.2(a), which also corresponds to the worst performance of the sweep. At these impactor conditions ($M/M_0 = 10^{-1}$ and $V/V_0 = 10^{0.75}$), a high amplitude, short wavelength, transition wave travels throughout the sample, at speeds faster than the waves in the linear material, resulting in a KE ratio of 0.0848x. Defining $M_R = M/m$, $M_R = 1.5$ and the formation of a single solitary wave in this instance agrees with previous studies, for instance in granular chain impacts [4], favoring single solitary wave formation when impactor and layer mass are closely matched. Within the context of solitary waves, nonlinear self-localization likely contributes to the poor performance seen in such cases. Fig. 10.3(b) shows impactor conditions: $M/M_0 = 10^{-0.625}$ and $V/V_0 = 10^{0.25}$ representative of good performance (KE ratio = 4.44x), but not as good as the nominal conditions shown in Fig. 10.2(b). A side by side comparison reveals qualitative differences in the behavior; namely longer lasting and more initial solitary waves generated in Fig. 10.2(b), which transition to an oscillatory phase encompassing more particles than Fig. 10.3(b). Additionally, close inspection at the n = N/2 location in Fig. 10.3(b) show wave-fronts that travel through particle n = N/2 of higher KE density than any of the crossing wave-fronts in Fig. 10.2(b). We observe that these wavefronts occur later in time than the time it would take for the first solitary wave to reach n = N/2 and appear to stem from dynamic unsnapping of the unit cells. Fig. 10.3(c) shows an example for high M and V ($M/M_0 = 10^{0.75}$ and $V/V_0 = 10^{0.75}$), where $M_R = 87$, and parallels could be drawn with known ‘‘shock’’ cases in granular chains [39]. A ‘‘train’’ of solitary waves is emitted after impact, and appear to continue to do so along the right side of Fig. 10.3(c). The KE density magnitude of

subsequent emitted waves appears to decrease, and the highest KE density solitary wave, which is also the wave that triggers the maximum κ, is the first wave emitted from the time of initial impact. We note the fastest transition wavespeeds are shown under these high-energy impact conditions. The KE ratio was 0.246x, which we note, does not occur at the first passage of the first transition wave but rather after the reflection of the first wave off the fixed bottom (after $\tau \approx 5$). Reflections and interference are representative of the complications of longer simulation duration in undamped simulations. Finally, we note that the maximum strain experienced during this high energy simulation is $\varepsilon = 1.95$, which in a physical scenario would imply self-contact. While we do not model self-contact herein to maintain simplicity, we suggest that this is an important effect to consider in higher fidelity models.

Effect of damping on system response

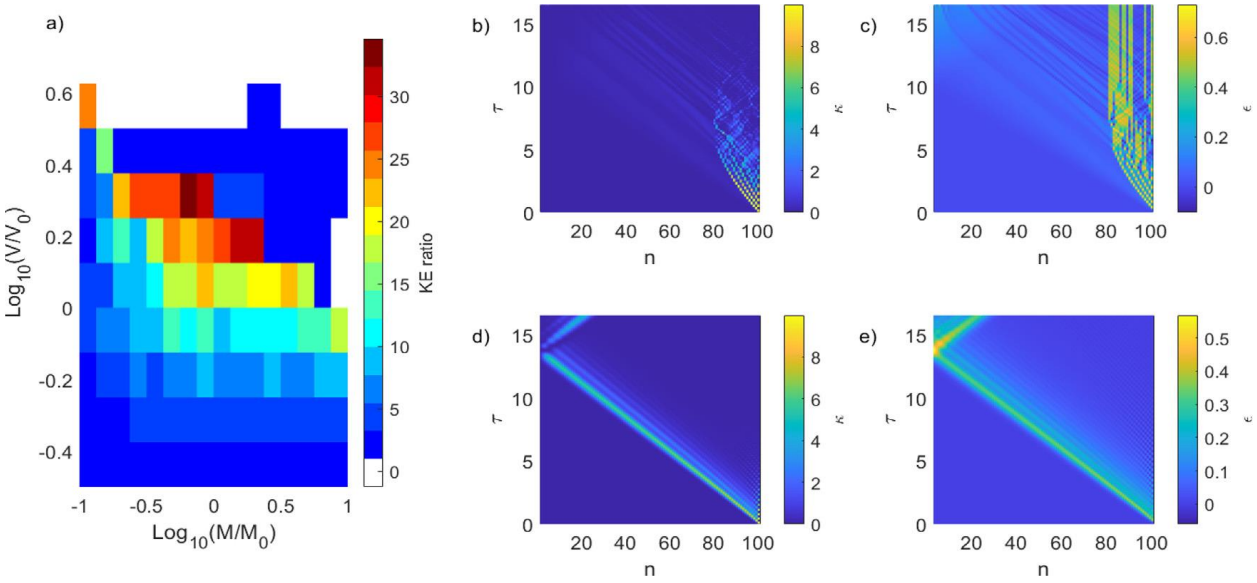

Figure 10.4. *Damped simulation. (a) KE ratio as a function of impactor conditions. Non-dimensional kinetic energy, κ, for bistable (b) and linear (d) materials at nominal impact conditions (M_0, V_0). The colorbar axis is saturated at $KE_I/10$. Layer strain, ε for bistable (c) and linear materials (e) at nominal impact conditions (M_0, V_0).*

The effect of the addition of a predetermined amount of damping to the simulations is assessed by implementing an intersite damping value of $\eta = 0.164$ Ns/m, or a normalized value of $\eta V_0/\beta_1\varepsilon_2 a = 5.8e-3$ which represents the ratio of viscous to elastic effects. Otherwise, the simulation setup is identical to the prior section. Fig. 10.4 shows the results of the damped simulations in the same format as shown

previously in Fig. 10.2. As before, Fig. 10.4(b,c) shows the bistable material response at impactor conditions M_0, V_0, and Fig. 10.4(d,e) shows the linear material response at the same conditions. The maximum KE ratio in the sweep in Fig. 10.4(a) was 34.58x, which occurred at impactor conditions: $M/M_0 = 10^{-.25}$ and $V/V_0 = 10^{.25}$, noting a shift in the optimal impact conditions with the addition of damping. The maximum KE ratio from the sweep in Fig. 10.4(a) is higher than any values observed from the undamped sweep (Fig. 10.2(a)). In addition, Fig. 10.4(a) also shows more regions where the bistable material outperforms the linear material, as indicated by fewer regions of white color in the figure (noting the threshold of white to blue in the plot in Fig. 10.2(a) and Fig.10. 4(a) is a KE ratio of one).

Fig. 10.4(b) shows four solitary waves that propagate in succession after impact, then transition to the oscillatory region by approximately n = 80. In contrast to the undamped case, the wavespeed of each transition wave decreases after the point of impact, as could be expected by the damping-induced reduction of amplitude coupled with the amplitude dependent wavespeed of the solitary waves. Fig. 10.4(c) shows regions with layers that have snapped to their secondary stable state and remained there, ostensibly aided by damping. Fig. 10.4(d,e) show similar behavior of the damped linear sample as was seen in the undamped linear sample in Fig. 10.2(d,e), with the exception of a lower maximum κ value at n = N/2 when damping is included.

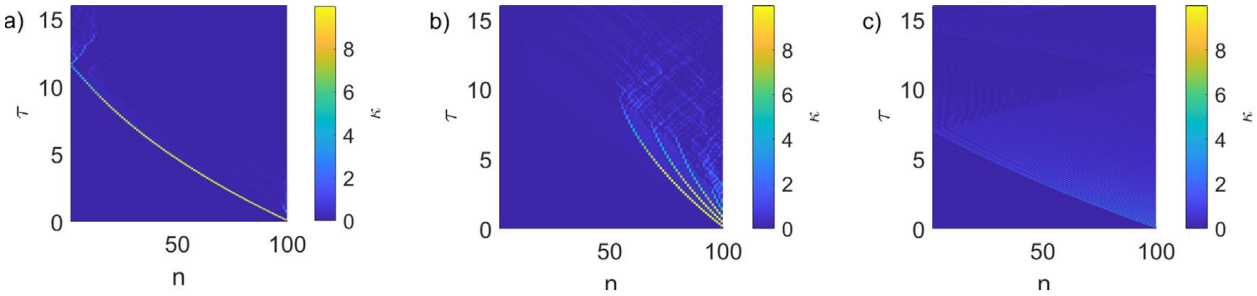

Figure 10.5. *Normalized KE, κ, for the simulated damped bistable material shown in Fig. 4(a) for the (a) worst performance (low mass and high velocity, M/M0 = 10−1 and V/V0 = 100.75), (b) best performance (close to nominal mass and velocity, M/M0 = 10−0.25 and V/V0 = 100.25), and (c) poor performance (high mass and high velocity, $M/M_0 = 10^{0.75}$ and $V/V_0 = 10^{0.75}$).*

Further comparison of κ for three chosen impactor conditions picked from within Fig. 10.4(a) are shown in Fig. 10.5. Fig. 10.5(a) shows impactor conditions corresponding to the top left corner and the worst

performance within Fig. 10.4(a), representing impactor mass $M/M_0 = 10^{-1}$ and velocity $V/V_0 = 10^{0.75}$, and a KE ratio of 0.2073x. It is also the same impactor conditions that resulted in the worst performance from the undamped sweep. Fig. 10.5(b) shows the best performance, a KE ratio of 34.58x, at impactor conditions $M/M_0 = 10^{-0.25}$ and $V/V_0 = 10^{0.25}$. Qualitatively, some similarities are observed when Fig. 10.5(b) is compared with the undamped high performance cases (Figs. 10.2(b) and 10.3(b)). We see an initial solitary wavefront that transitions (in time) to an oscillatory region prior to crossing particle n = N/2 (noting again the slowing wavespeed). Crucially, there appears to be an interaction between the solitary wave fronts and damping such that when multiple solitary wave emissions occur, it is possible that the waves slow as they reduce in amplitude (due to damping) such that they approach, but do not pass, the n = N/2 location. This may further be a synergistic effect in the sense that the damping-induced speed reduction gives the solitary waves even more time to decay in amplitude, and eventually vanish, before reaching the halfway point. Fig. 10.5(c) shows impactor conditions $M/M_0 = 10^{0.75}$ and $V/V_0 = 10^{0.75}$, which is a region in the upper right corner of the sweep in Fig. 10.4(a), showing poor performance. A comparison of Fig. 10.5(c) to the undamped case (Fig. 10.3(c)) at the same impactor conditions shows similar behavior with the exception of the slowing transition waves in the damped case.

Conclusion

The kinetic energy transmission performance in response to impact of a simulated bistable mechanical metamaterial was found to be highly dependent on the impactor conditions (mass and velocity). In the undamped simulations, the performance of a N = 100 sample ranged from worse (0.08x) to far superior (20.9x) in comparison to the linear control lattice. Similarly, in the damped sweep, the performance again ranged from worse (0.21x) to far superior (34.6x). The presence of damping was seen to have a beneficial, potentially synergistic, effect on the performance of the system, as indicated by both higher maximum KE ratio values and higher minimum KE ratio values for the same set of impactor conditions. One likely reason for this is the higher amount of ‘‘permanent’’ snapping of layers prior to the n = N/2 point. This permanent

snapping is aided by damping both by the viscous resistance to unsnapping and reduction of traveling waves that may cause unsnapping at later times after subsequent reflections and constructive interference.

Two significant additional implications of the findings regarding impact conditions and damping are the following. First, the bistable mechanism has the potential to yield significant performance benefits in terms of KE abatement if the material and impact conditions are well paired, but if not well paired, the bistable material can underperform a more traditional material, sometimes by a substantial margin. These high performance conditions were found, via simulation, to match well with predictions made using simple analytical estimates (namely, Eqs. (10.6) and (10.7)). Second, while only a single viscosity was used in the damped examples, the performance improvement as a result of the addition of damping leads the authors to suspect that subsequent ‘‘tuning’’ of the damping may significantly affect the performance of these systems.

We further suggest several potential avenues for future study in the context of both the fundamental understanding of energy transmission in bistable systems as well as their application in impact mitigation systems. The simulations considered herein idealized the response of a physically realized bistable mechanical metamaterial by not considering self contact (or full compaction) of the physical unit cells. The future inclusion of self contact will be critical for accurately describing the response of such systems, and can be expected to modify ranges of poor and superior impact performance. In addition, we suggest that computational optimization has a key future role to play, particularly given the strong nonlinearities involved herein. This may take the form of shape optimization of the unit cell aimed at maximizing energy absorption per unit mass density considering the metamaterial’s dynamic response. One may also consider optimizing the unit cell to broaden the envelope of impactor conditions (e.g. Figs. 10.2 and 10.4) wherein the bistable material gives superior impact absorption response. There may also exist additional rich dynamics and unique capabilities for impact absorption with bistable media in higher dimensions, such as in the case of localized point impacts, instead of the 1D (plate-impact-like) scenarios considered herein. Finally, we note that many impact absorption problems involving high strain rates also involve inelastic

material behavior [2]. For the case of elastomeric materials, we expect this will manifest primarily in the form of viscoelasticity, which can be roughly accounted for by our inclusion of viscous elements in the model. However, for most other materials, we expect that high energy and strain rate impact scenarios will introduce a range of additional important material behavior including strain rate dependent material properties of the constituent materials forming the bistable elements, plasticity, and fracture. Indeed, there exist many impact scenarios where the energies are so large – which could be approximated as where the kinetic energy of the impactor is much greater than the elastic strain energy Eϵ2d3 of a fully dense (non-bistable) material – such a bistable mechanism would not be expected to be effective. However, considering the former regime, one can imagine that plasticity and fracture can work in concert with bistable mechanisms and result in increased energy absorption. While aspects of this interaction have been previously studied (see, e.g., Refs. [29,30,40]), we suggest open questions remain concerning the use of bistable metamaterials for impact mitigation in high energy and strain rate, destructive regimes.

References

1. W. Schiehlen, The long history of impact mechanics, rolling contact and multibody system dynamics, PAMM 17 (1) (2017) 165–166.

2. M.A. Meyers, Dynamic Behavior of Materials, John wiley & sons, 1994.

3. C.M. Harris, A.G. Piersol, Harris' Shock and Vibration Handbook, Vol. 5, McGraw-Hill, New York, 2002.

4. V. Nesterenko, Dynamics of Heterogeneous Materials, Springer Science & Business Media, 2013.

5. R. Lakes, R.S. Lakes, Viscoelastic Materials, Cambridge University Press, 2009.

6. R. Bouferra, H. Pron, J.-F. Henry, C. Bissieux, J. Beaudoin, Study of the intrinsic dissipation associated to the plastic work induced by a ball impact, Int. J. Therm. Sci. 44 (2) (2005) 115–119.

7. Y. Li, H. Fan, X.-L. Gao, Ballistic helmets: Recent advances in materials, protection mechanisms, performance, and head injury mitigation, Composites B (2022) 109890.

8. W. Mason, H. McSkimin, Energy losses of sound waves in metals due to scattering and diffusion, J. Appl. Phys. 19 (10) (1948) 940–946.

9. K.-W. Wang, R.L. Harne, Harnessing Bistable Structural Dynamics: For Vibration Control, Energy Harvesting and Sensing, John Wiley & Sons, 2017.

10. Y. Cao, M. Derakhshani, Y. Fang, G. Huang, C. Cao, Bistable structures for advanced functional systems, Adv. Funct. Mater. 31 (2106231) (2021) 1–23.

11. S. Jeon, B. Shen, N. Traugutt, Z. Zhu, L. Fang, C. Yakacki, T. Nguyen, S. Kang, Synergistic energy absorption mechanisms of architected liquid crystal elastomers, Adv. Mater. 34 (2200272) (2022) 1–8.

12. S. Shan, S.H. Kang, J.R. Raney, P. Wang, L. Fang, F. Candido, J.A. Lewis, K. Bertoldi, Multistable architected materials for trapping elastic strain energy, Adv. Mater. 27 (29) (2015) 4296–4301.

13. T. Frenzel, C. Findeisen, M. Kadic, P. Gumbsch, M. Wegener, Tailored buckling microlattices as reusable light-weight shock absorbers, Adv. Mater. 28 (28) (2016) 5865–5870.

14. B. Haghpanah, A. Shirazi, L. Salari-Sharif, A. Guell Izard, L. Valdevit, Elastic architected materials with extreme damping capacity, Extreme Mech. Lett. 17 (2017) 56–61.

15. A. Guell Izard, R. Fabian Alfonso, G. McKnight, L. Valdevit, Optimal design of a cellular material encompassing negative stiffness elements for unique combinations of stiffness and elastic hysteresis, Mater. Des. 135 (2017) 37–50.

16. L. Wu, X. Xi, B. Li, J. Zhou, Multi-stable mechanical structural materials, Adv. Eng. Mater. 20 (2) (2018) 1700599.

17. C.S. Ha, R.S. Lakes, M.E. Plesha, Design, fabrication, and analysis of lattice exhibiting energy absorption via snap-through behavior, Mater. Des. 141 (2018) 426–437.

18. T. Raj Giri, R. Mailen, Controlled snapping sequence and energy absorption in multistable mechanical metamaterial cylinders, Int. J. Mech. Sci. 204 (106541) (2021) 1–12.

19. A.M. Balk, A.V. Cherkaev, L.I. Slepyan, Dynamics of chains with nonmonotone stress–strain relations. I. Model and numerical experiments, J. Mech. Phys. Solids 49 (1) (2001) 131–148.

20. A.M. Balk, A.V. Cherkaev, L.I. Slepyan, Dynamics of chains with nonmonotone stress–strain relations. II. Nonlinear waves and waves of phase transition, J. Mech. Phys. Solids 49 (1) (2001) 149–171.

21. B.F. Feeny, A.R. Diaz, Twinkling phenomena in snap-through oscillators, in: International Design Engineering Technical Conferences and Computers and Information in Engineering Conference, Vol. 80296, American Society of Mechanical Engineers, 2001, pp. 2393–2398.
22. B. Deng, P. Wang, V. Tournat, K. Bertoldi, Nonlinear transition waves in free-standing bistable chains, J. Mech. Phys. Solids 136 (2020) 103661.

23. N. Nadkarni, A.F. Arrieta, C. Chong, D.M. Kochmann, C. Daraio, Unidirectional transition waves in bistable lattices, Phys. Rev. Lett. 116 (24) (2016) 244501.

24. J.R. Raney, N. Nadkarni, C. Daraio, D.M. Kochmann, J.A. Lewis, K. Bertoldi, Stable propagation of mechanical signals in soft media using stored elastic energy, Proc. Natl. Acad. Sci. 113 (35) (2016) 9722–9727.

25. T. Dauxois, M. Peyrard, Physics of Solitons, Cambridge University Press, 2006.

26. M. Frazier, D. Kochmann, Band gap transmission in periodic bistable mechanical systems, J. Sound Vib. 388 (2017) 315–326.

27. S. Katz, S. Givli, Solitary waves in a nonintegrable chain with double-well potentials, Phys. Rev. E 100 (3) (2019) 032209.

28. S. Katz, S. Givli, Solitary waves in a bistable lattice, Extreme Mech. Lett. 22 (2018) 106–111.

29. A. Cherkaev, E. Cherkaev, L. Slepyan, Transition waves in bistable structures. I. Delocalization of damage, J. Mech. Phys. Solids 53 (2) (2005) 383–405.

30. L. Slepyan, A. Cherkaev, E. Cherkaev, Transition waves in bistable structures. II. Analytical solution: wave speed and energy dissipation, J. Mech. Phys. Solids 53 (2) (2005) 407–436.
31. M. Hwang, A.F. Arrieta, Input-independent energy harvesting in bistable lattices from transition waves, Sci. Rep. 8 (1) (2018) 3630.

32. N.R. Council, et al., Opportunities in Protection Materials Science and Technology for Future Army Applications, National Academies Press, 2011.

33. A. Sondén, D. Rocksén, L. Riddez, J. Davidsson, J.K. Persson, D. Gryth, J. Bursell, U.P. Arborelius, Trauma attenuating backing improves protection against behind armor blunt trauma, J. Trauma Acute Care Surg. 67 (6) (2009) 1191–1199.

34. X.Q. Wang, The failure analysis and the innovative design of hammer head on hammer crusher based on TRIZ theory, in: Applied Mechanics and Materials, Vol. 741, Trans Tech Publ, 2015, pp. 85–90.

35. J.A. Sherwood, C.C. Frost, Constitutive modeling and simulation of energy absorbing polyurethane foam under impact loading, Polym. Eng. Sci. 32 (16) (1992) 1138–1146.
36. H. Hertz, Uber die Berührung fester elastischer Körper. (On the contact of elastic solids), J. Reine Angew. Math. 92 (1882) 156–171.

37. MATLAB, Version 9.7.0.1216025 (R2019b Update 1), The MathWorks Inc., Natick, Massachusetts, 2022.

38. H. Yang, L. Ma, Multi-stable mechanical metamaterials by elastic buckling instability, J. Mater. Sci. 54 (2019) 3509–3526.

39. A. Molinari, C. Daraio, Stationary shocks in periodic highly nonlinear granular chains, Phys. Rev. E 80 (5) (2009) 056602.

40. X. Tan, S. Chen, S. Zhu, B. Wang, P. Xu, K. Yao, Y. Sun, Reusable metamaterial via inelastic instability for energy absorption, Int. J. Mech. Sci. 155 (2019) 509–517.

Chapter 11: Enhanced Energy Absorption and Dynamic Properties Controllability in Gyroid Lattice Structures by Exploiting Structural Gradients

This chapter was produced from a manuscript that is in preparation.

Cai, J.; **Chin, K. C. H.**; Boydston, A. J.; Thevamaran, R.; Enhanced Energy Absorption and Dynamic Properties Controllability in Gyroid Lattice Structures by Exploiting Structural Gradients. **2024**. In Preparation.

Abstract

Developing structural materials with a hierarchical design and gradient functional characteristics allows for unparalleled control over both static and dynamic mechanical performance, while simultaneously achieving a reduction in weight. Contrasting with the randomly microstructured open-cell foams that are frequently used to absorb and mitigate impact forces for enhanced safety, specific cellular configurations like gyroid lattices, characterized by their significant structural design capabilities, provide exceptional mechanical performance advantages and more efficient material utilization. By employing additively manufactured elastomeric gyroid lattices with tailored structures as model cellular systems, we uncover a significant dependence of the energy absorption, deformation characteristics, and dynamic mechanical performance of the gyroid structures on their relative density and structural gradient under compressive loads. Gyroid lattices with a gradient in their structural density exhibit enhanced structural stability and increased capacity for energy absorption and dissipation, stemming from the graded mechanical properties and deformation modes along the loading direction induced by continuous geometrical variation. In the dynamic regime, leveraging structural gradients in the gyroid structure results in an outstanding controllability of dynamic stiffness, while maintaining their inherent damping capabilities. Our study demonstrates the potential of architected cellular structures with deliberately tailored structural density distributions as advanced, lightweight structural materials that offer optimized static and dynamic mechanical performance for extreme damping and shock-absorbing applications.

Introduction

Creating lightweight structural materials with synergistic achievement of high stiffness, strength, and toughness is crucial for effectively mitigating the high-velocity impact, mechanical waves, and vibration in extreme environments[1–7]. However, these properties are usually mutually exclusive within conventional engineering materials characterized by a homogeneous structure with a relatively consistent composition and microstructure[1]. Implementation of intentionally engineered spatial heterogeneities or gradients with a gradual transition in a single material has been demonstrated to be a promising structural design strategy to overcome the traditional property trade-off in homogeneous material system [2,7–10]. By positioning optimized compositions or architectures in specific regions, this approach allows for the combination of multiple benefits within the material, from alleviating stress concentration to introducing unique functionalities, thereby resulting in superior overall properties. The creation of heterogeneous gradient nano-grained (GNG) structure in metal leads to unnatural plastic deformation distribution in a gradient stress field[2], which possesses significant potential to overcome the strength-ductility trade-off found in conventional polycrystalline metals. Synthesis-tailored structural hierarchy and gradients in vertically aligned carbon nanotube (VACNT) foams enable the achievement of a dramatic tunability of the material's dynamic stiffness using static precompression while maintaining its near-constant damping capacity[9]. Dimensionally varied thermal characteristics in thermal gradient materials efficiently alleviate the thermal stress concentration caused by mismatches in the coefficient of thermal expansion [11].

In contrast to their solid material counterparts, cellular materials are an emerging class of lightweight material structures with exceptional specific properties. They demonstrate great promise in engineering fields where structural weight and material efficiency are critical design factors, including automotive, aerospace, and sports industries [12–15]. The porous nature associated with the tailorable topological features across multiple lengthscales offers the cellular materials great opportunity to achieve high stiffness-to-weight ratio, mechanical energy absorption, thermal and sound insulation through deliberately engineering their structural density and functional gradient. Unlike random porous cellular materials like

foam, architected cellular materials featuring well-organized structural patterns, such as octet-truss[16], honeycomb[17], gyroid lattices[18], exhibit significant enhancement in their specific mechanical performance and better controllability over deformation and failure modes. The polymeric lattices with an octet-truss unit cell shows 11% higher energy absorption efficiency than conventional open cell aluminum foam [19]. Furthermore, incorporation of spatial gradient structures in cellular materials leads to gradient properties, enhanced energy absorption, and well-defined deformation and failure modes [20]. Polymer honeycomb structures with discrete and continuous-density gradient show increased densification strain as well as a combination of high strength and enhanced energy absorption while maintaining the low structural weight [21].

The advancement in additive manufacturing techniques allows for the precise production of largescale architected cellular materials with sophisticated architectures like the smooth transition of cellular topologies and continuous gradient of structural density. This development facilities the customized design and optimization of the mechanical behaviors of cellular materials targeted for various applications. However, the manufacturing defects presented at the connection nodes in 3D-printed truss-based structures lead to the premature failure of the material, therefore hindering the achievement of optimal mechanical performance as envisioned in the designs [22]. In contrast, as a member of the Triply Periodic Minimal Surfaces (TPMS) family, gyroid lattices are featured by a continuous, interconnected network of curved surfaces throughout the entire structure. Such structural smoothness and continuity allow for more uniform material flow during the 3D printing process, therefore effectively reducing the likelihood of defects such as voids and incomplete infill that may occur in truss-based lattices. Additionally, it enables a more evenly load distribution [23] and reduced stress concentration at joints with sharp angles[24]. Therefore, 3D printed gyroid structures demonstrate outstanding mechanical performance, including elastic stiffness, strength, and toughness, as well as tunable property anisotropy [25–27].

The mechanical properties of the gyroid lattices are tailorable by independently designing their constituent materials and architectural parameters, like the relative density (the ratio of the density of structure to the

density of the solid materials) and its distribution within the structure. Based on Gibson-Ashby Model[12], the stiffness ($E_{lattice}$) and strength ($S_{lattice}$) of lattice structures can be obtained as functions of relative density using the following equations, as $E_{lattice} = E_{bulk}\, C_1(1-\varphi)^{n_1}$ and $S_{lattice} = S_{bulk}\, C_2(1-\varphi)^{n_2}$, where E_{bulk} and S_{bulk} are the stiffness and strength of bulk materials, φ is porosity of the material and C and n are empirically determined coefficients. The energy absorption capability of gyroid lattice is proportional to the relative density of the materials—increasing the relative density leads to increased energy absorption[25, 28]. Like other cellular structures, functionally graded gyroid lattices show tunable deformation behavior and enhanced mechanical performance. The distinct progressive layer-by-layer collapsing deformation modes existed in additive manufactured metallic gyroid structures result in enhanced energy absorption under compressive loading [29]. In contrast to rigid materials, elastomers are particularly effective in applications involving damping and shock absorption, due to their highly flexible and deformable nature, hysteresis behavior, viscoelastic characteristics, and resistance to brittleness[30,31]. While the mechanical properties of rigid material based gyroid lattices have been explored, the impact of structural features on the mechanical behaviors, particularly the dynamic performance, of gyroid lattices composed of soft elastomeric polymers remain elusive, which substantially restricts their use in applications which involves energy absorption.

Here, we employ stereolithography (SLA) 3D printed gyroid structures using a viscoelastic elastomeric polymer as a model system to examine the effects of relative density and its gradient on the quasistatic energy absorption, modes of deformation, and dynamic mechanical performance of soft gyroid lattices. We showed, under quasi-static compression, elastomeric gyroid-structure exhibits a strong density-dependent mechanical behavior and energy absorption capacities. Unlike a uniform structure, the introduction of a continuous density gradient in gyroid lattices significantly increases the structural stability and enhances the performance in energy absorption and dissipation at large compressive strain deformations. In dynamic regime, functionally graded gyroid-structure demonstrates outstanding dynamic stiffness tunability by applying static precompression with near constant damping ability of the materials. The insights gained

from this research will facilitate the creation of optimal impact-absorbing structural materials and various other protective material systems, utilizing architected cellular materials with strategically customized structures. Furthermore, due to the exceptional mechanical properties of gradient gyroid lattices, this model system can be directly integrated either as a three-dimensional interconnected reinforcement structure in a composite or used independently to augment the performance of protective materials.

Results and discussion

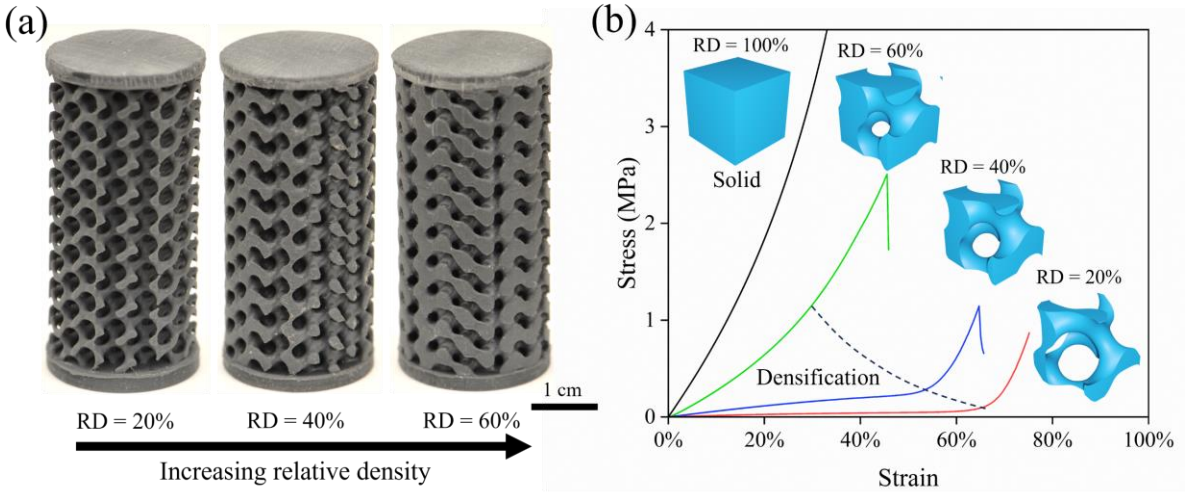

Figure 11.1. *(a) 3D printed cylindrical gyroid lattices with uniform relative density (RD), RD = 20%, 40% and 60%. (b) Compressive stress-strain curves of the solid cylinder (RD = 100%) and cylindrical gyroid lattices with RD = 20%, 40% and 60%.*

The gyroid lattices with tailorable structures were defined by the following mathematical equation,

$$\sin\left(\frac{2\pi}{a}\cdot x\right)\cos\left(\frac{2\pi}{a}\cdot y\right)+\sin\left(\frac{2\pi}{a}\cdot y\right)\cos\left(\frac{2\pi}{a}\cdot z\right)+\sin\left(\frac{2\pi}{a}\cdot z\right)\cos\left(\frac{2\pi}{a}\cdot x\right)=t$$

where a is the unit cell size, and parameter *t* governs the relative density and its distribution within the structure. By setting *t* as a constant number throughout the whole structure, ranging from -1.5 to 1.5, gyroid lattices with a uniform unit cell size (a) and Relative Density (RD) are achieved, varying from 0% to 100%. The cylindrical gyroid lattices with uniform RD (RD = 20%, 40% and 60%) without structural defects are manufactured by SLA 3D printing (Fig.11.1a). By setting *t* = f (x,y,z) as a function of the locations within the gyroid lattice, non-uniform structural density throughout the structure could be obtained. In this work,

a linear function of t = f (z) is applied to generate the gyroid lattice with gradient RD along the z axis, increasing linearly from 20% to 60% (Fig.11.3a).

The compressive stress-strain curves of cylindrical gyroid lattices with RD=20%, 40% and 60% are presented in Fig.11.1b, all of which start with a near-linear, continuous increase in stress as the applied strain increases. Gyroid lattices possessing a higher RD demonstrate increased nominal stress in the structures under the same applied strain, all of which remain lower than that of the solid cylinder sample. In gyroid lattices composed of rigid materials, the typical stages characterized by different deformation behaviors, such as elastic deformation, yielding, and plateau regimes, are not distinctly evident in elastomeric soft gyroid lattices [26,29]. Instead, the stiffness of the gyroid lattice, indicated by the slopes of the stress-strain curves, gradually rises with the applied strains during the initial loading stage, and then transitions into a regime with a reduced slope value, akin to the plateau regime. As all layers of the sample

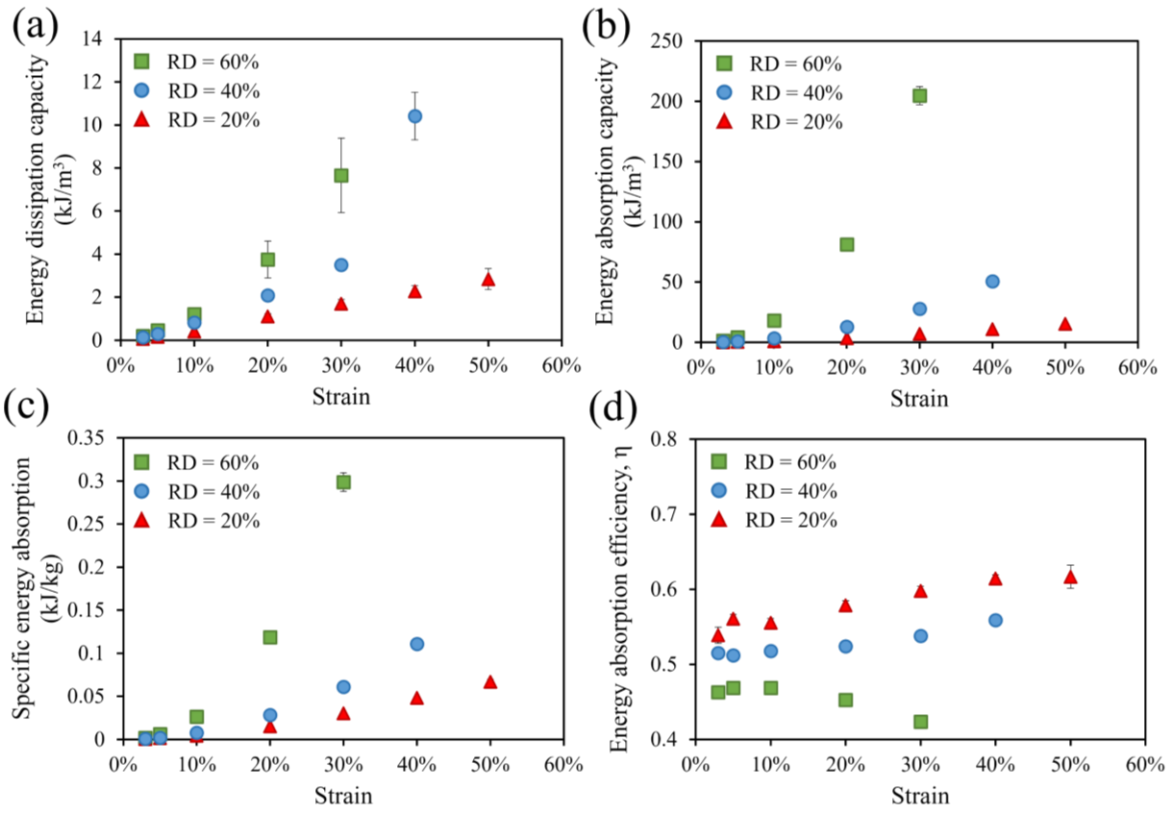

Figure 11.2. *(a) Energy dissipation capacity, (b) energy absorption capacity, (c) specific energy absorption and (d) energy absorption efficiency of gyroid lattices with RD = 20%, 40% and 60%.*

collapse and the structural elements deform sufficiently to begin contacting each other, the bulk sample shows densification, with stress increasing exponentially with the applied strain. This is a characteristic deformation behavior in bending-dominated structures[29,32]. The onset strains of densification in gyroid lattices are highly dependent on their RD. The densification of the gyroid lattice with RD = 20% starts at about ε=65%, which is much larger than the sample with RD = 60%, starting at about ε<30%.

The energy dissipation capacity of the gyroid lattice, defined as energy dissipation per unit volume of material, is determined from the area enclosed by the loading-unloading cycle in the stress-strain curves under compressive loading. In the compression process, as the struts within the gyroid lattice collapse and bend, energy is thermally dissipated through the viscoelastic behavior of the constituent polymeric materials. With the increase in compressive strain, there is a consistent rise in the energy dissipation capacity of the lattice structures. Higher RD leads to better energy dissipating performance of the gyroid lattice, as it involves more viscoelastic polymeric materials in the process of energy dissipation. The trend is alike for both energy absorption capacity (energy absorbed per unit volume) and specific energy absorption (energy absorbed per unit weight), indicating that structures with a higher RD demonstrate enhanced energy absorption performance. The energy absorption efficiency (EAE) η is obtained by,

$$\eta = \frac{\int_0^{\varepsilon} \sigma(\varepsilon) d\varepsilon}{\sigma_{max}\varepsilon}$$

where σ_{max} is the maximum stress before the specified strain and ε is the strain applied to the materials. The EAE has been demonstrated as an effective parameter to understand the energy absorbing features of the cellular materials under different loading conditions [33,34]. In contrast to the total energy absorption capacities, gyroid lattices with lower RD exhibit higher EAE, due to its lower nominal stress level within the structure during the compressive deformation process with the same applied strain. For RD =20% and 40%, since the applied strain is lower than their densification strain (Fig.11.1b), there is an increase of the EAE as increasing the strain due to the expanding area of the plateau regime[34]. For RD = 60%, since the densification of the gyroid structures starts at a much lower applied strain (ε<30%), the EAE starts to

decrease as increasing the applied strain due to the rapidly increasing nominal stress. Therefore, by deliberately engineering the structural density of the gyroid structures, the deformation behavior and energy absorption performance of the structures can be optimized aiming at diverse energy absorption applications.

In addition to adjusting the structural density of the uniform gyroid lattice, the distribution of density within the structure can also be tailored. Gyroid lattices featuring gradient RD, which increases linearly from 20% to 60% along the z-axis, is fabricated using SLA 3D printing. The lattice has an equivalent bulk density to the sample with a uniform RD = 40% (Fig.11.3a). The stress-strain curves reveal distinct mechanical responses under compression between these two samples (Fig.11.3b). The uniform gyroid lattice exhibits a consistent rise in stress as the applied strain increases. At around ε= 55%, the compressive curve transitions into the densification regime, where the stress starts to increase exponentially (Fig.11.1b). However, the deformation process shows that, at ε=50%, the entire cylindrical gyroid structure begins to buckle, signaling the onset of structural failure under compressive load (Fig.11.4a).

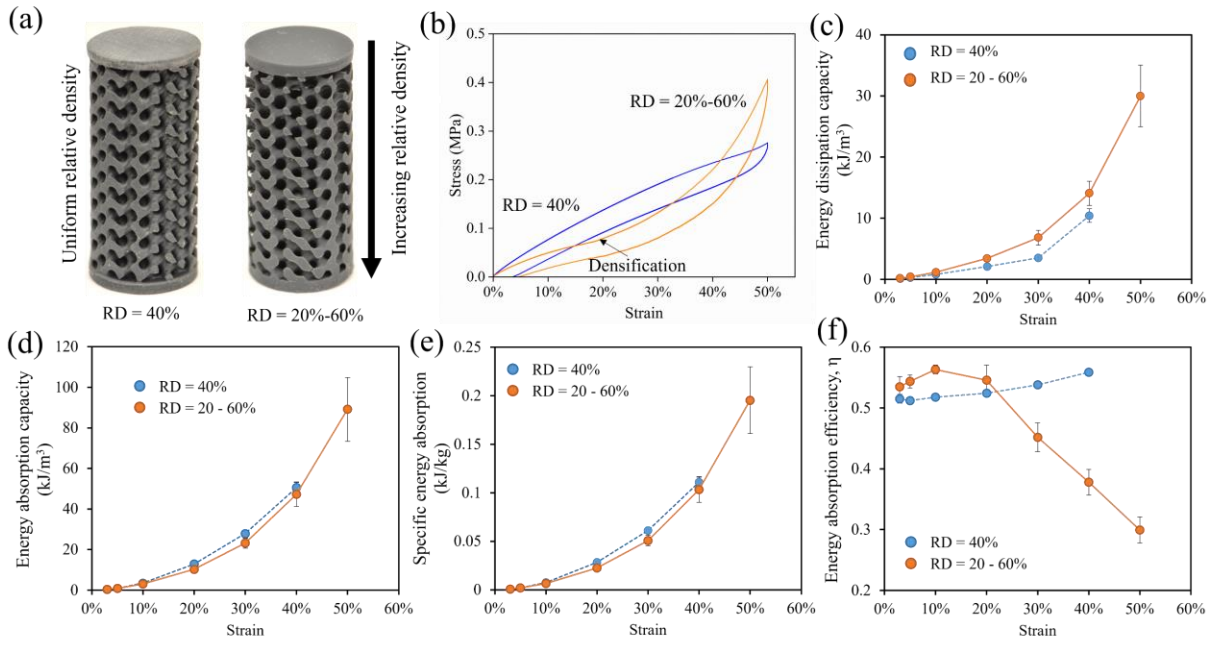

Figure 11.3. *(a) 3D printed cylindrical gyroid lattices with different RD distribution, uniform (RD = 40%) and gradient (RD = 20% - 60%). (b) stress-strain curve, (c) energy dissipation capacity, (d) energy absorption capacity, (e) specific energy absorption and (f) energy absorption efficiency η of gyroid lattices with RD = 40% and RD = 20 – 60%.*

Conversely, with the gradient gyroid structure, at low compressive strains, the stress level is lower compared to the uniform sample (Fig.11.3b). This is because deformation predominantly occurs in the region with lower relative density (Fig.11.4). With the increasing of applied strain, the structure undergoes a rapid increase in stiffness. This is attributed to the ongoing collapse of the structural elements in the low-density region, resulting in an uneven deformation behavior within the structure along the z-aixs (Fig.11.4b). At an equivalent global strain, the lower density region in gradient sample undergoes a higher local strain compared to the uniform structure. As the applied strain reaches 42%, the stress in the gradient sample exceeds that of the uniform sample and escalates more rapidly with the continued increase in the applied strain. The distinct deformation behaviors caused by the density gradient lead to differences in energy dissipation and absorption performance among gyroid lattices. The gradient gyroid structure shows a greater capacity for energy dissipation, stemming from the increased local strain in the low-density region, which induces higher energy dissipation through extensive non-linear viscoelastic deformation of the constituent polymer materials. Nonetheless, at a lower compressive strain ($\varepsilon<50\%$), both the energy absorption capacity and specific energy absorption of gradient gyroid structure are lower than those of the uniform structure, owing to its lower nominal stress level. When the stress in the gradient structure exceeds that of the uniform structure at $\varepsilon=42\%$, the energy absorption ability of the gradient structure begins to increase more rapidly than that of the uniform sample as the applied strain continues to rise. At $\varepsilon=50\%$, gradient structure demonstrates enhanced energy absorption capacity and specific energy absorption compared to the uniform gyroid structure, which experiences buckling failure at this same strain level. The variation of EAE in response to applied strain likewise indicates the unique deformation behaviors observed between these two structures. In the low compressive strain regime ($\varepsilon<20\%$), the gradient structure exhibits a higher efficiency in energy absorption, attributed to the highly localized deformation in the lower-RD region. As the level of applied strain rises, this efficiency quickly declines, a consequence of the structure's densification and the resultant increase in nominal stress. This pattern aligns well with the mechanical behavior observed in foam materials [34]. Consequently, the gradient distribution of structural density within gyroid lattices results in uneven deformation behavior and varied energy absorption performance

under compressive loading. This not only contributes to a higher failure compressive strain and improved energy absorption at larger strains but also enables tailorable mechanical responses while preserving the material's overall bulk density. Moreover, the shape of the gradient gyroid lattice is fully recovered after applying 60% compressive strain.

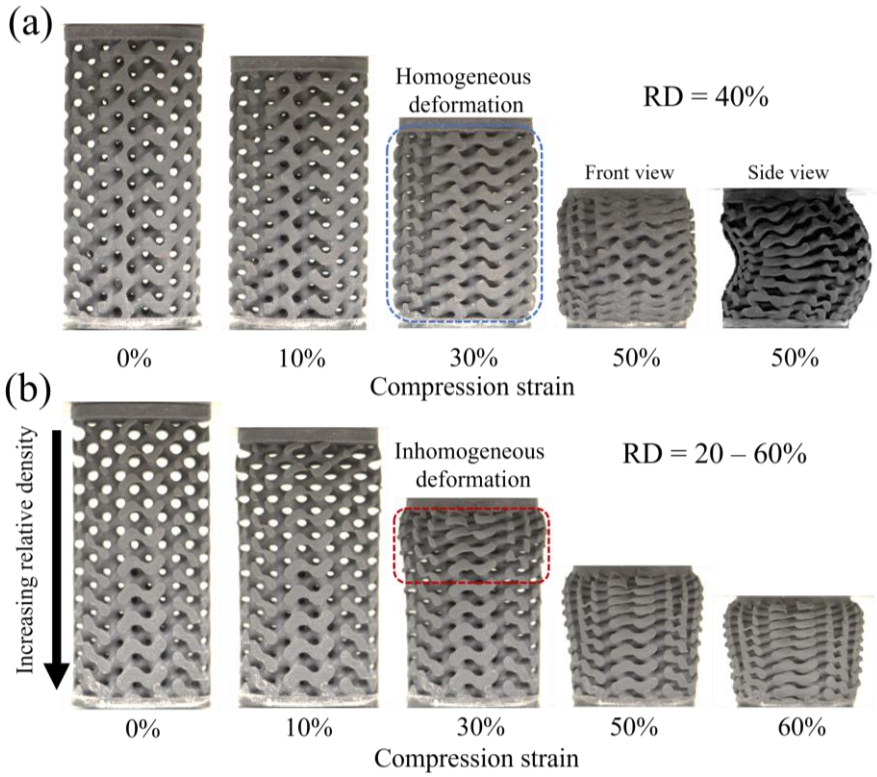

Figure 11.4. *Deformation processes of cylindrical gyroid lattices with (a) uniform density distribution (RD = 40%) and gradient density distribution (RD = 20-60%) under compression with increasing strains.*

In dynamic regime, the dynamic mechanical properties of the gyroid lattice are determined by analyzing the stress-strain responses under the cyclic load. The storage modulus E' and loss modulus E'' are the real and imaginary parts of the complex modulus of the viscoelastic material, which represent the abilities of material to store energy elastically and dissipate stress through heat, respectively. The dynamic stiffness of the material, given by $|E^*| = \sqrt{E'^2 + E''^2}$, measures the material's resilience against vibrations and deformations triggered by dynamic loads. The loss tangent indicates the ratio between thermally dissipated energy and elastically stored energy of material, given by $tan\delta = \frac{E''}{E'}$.

The dynamic stiffness and loss tangent of the gyroid lattices with uniform structural density as a function of the applied static precompression strains are presented in Fig.11.5a, b. The variation of dynamic stiffness in response to precompression strain is directly related to the density-dependent structural densification behavior of the gyroid lattice when subjected to axial compression. As shown in the previous section, the gyroid lattices with different RDs begin densification at different levels of applied strain. Subjecting the gyroid lattice with RD of 20% to a precompression strain of up to 50% is insufficient to trigger structural densification, hence leading to a minimal change in dynamic stiffness. Gyroid lattice with higher structural density exhibits increased dynamic stiffness. Increasing the precompression strain in gyroid lattice with RT=40% results in a rise in dynamic stiffness ($\varepsilon<10\%$), followed by a subsequent decrease ($10\%<\varepsilon<30\%$). This phenomenon may stem from the ongoing collapse and bending of struts within the gyroid lattice. When the strain reaches $\varepsilon=40\%$, the struts within the structure begin to make contact with each other, consequently causing an increase in dynamic stiffness due to structural densification. Increasing the RD to 60% further pushes forward the strain at which the densification occurs, resulting in a continuous rise of dynamic stiffness as the precompression strain increases. The loss tangent of the uniform gyroid lattices also exhibits a strong dependency on structural density, indicating improved damping of materials with an increase in structural density. The origin of this unique behavior might be attributed to the different deformation modes present in gyroid lattices of varying densities. A gyroid lattice with a high structural density (RD = 60%) undergoes more compressive deformation of its struts, leading to increased viscoelastic energy dissipation. This results in its loss tangent being comparable to that of a solid sample. In contrast, in a low-density gyroid lattice (RD = 20%), strut bending initiates at lower precompression strains. This bending is the dominated mode of deformation, leading to reduced energy dissipation from the bending deformation than from compression. With the increase of applied static precompression in gyroid lattices with RD = 40%

and 60%, the struts within the structure begin to collapse and bend, resulting in a decrease in the loss tangent.

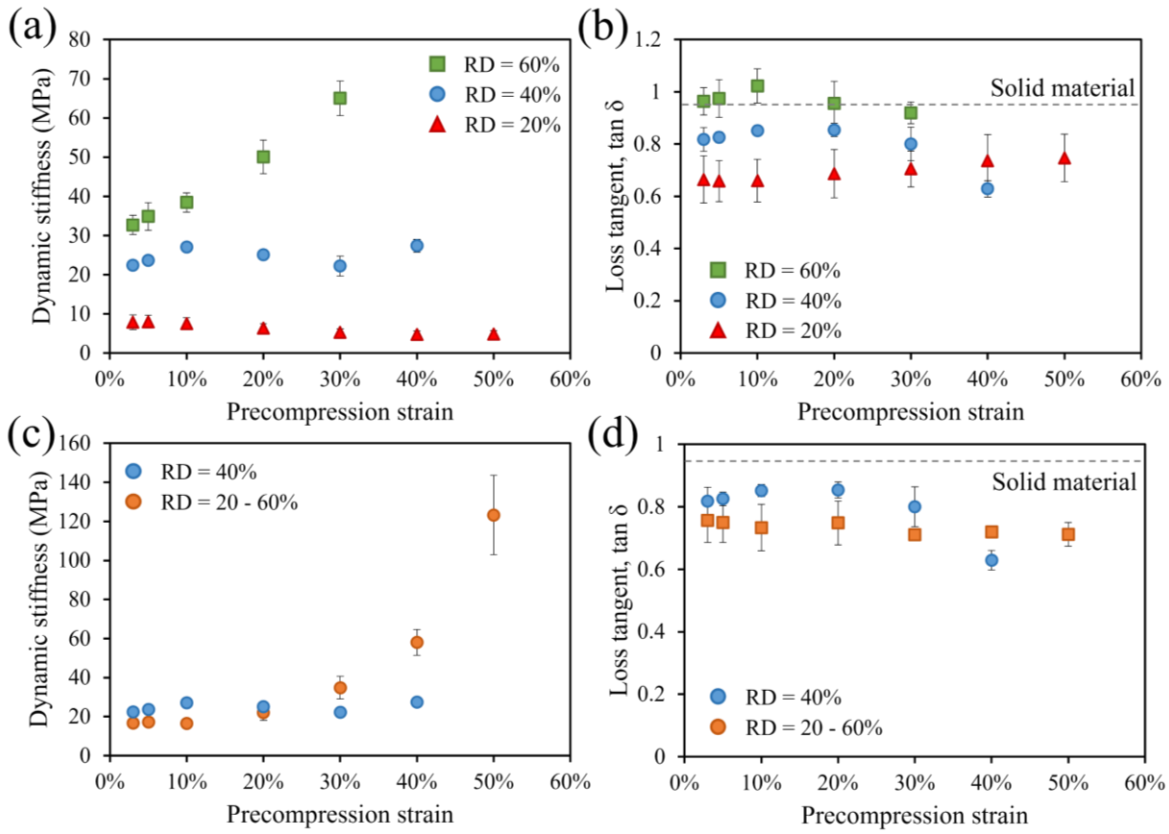

Figure 11.5. *(a) Dynamic stiffness and (b) loss tangent, tan δ of gyroid lattices with uniform density distribution (RD = 20%, 40% and 60%). (c) Dynamic stiffness and (d) loss tangent, tan δ of gyroid lattices with gradient density distribution (RD = 20-60%). The dash line labels the loss tangent of solid cylinder material made by 3D printing.*

Beyond controlling structural density, incorporating a density gradient into gyroid lattice leads to more prominent tunability of its dynamic performance, particularly the dynamic stiffness. Unlike the relatively constant dynamic stiffness in uniform gyroid materials across various precompression strains, the dynamic stiffness of the gradient gyroid dramatically increases from 16.7 to 123 MPa (an increase of over 600%) when the precompression strain is increased from 3% to 50%. This substantial change is due to the intrinsic structural density gradient and the resulting stiffness gradient, which cause inhomogeneous deformation in the material, as observed in the quasi-static compression study (Fig.11.5c). Despite the dramatic increase in dynamic stiffness, the damping capability of the material remains nearly unchanged (Fig.11.5d), similar

to the that of uniform structure. The stiffness and damping in materials generally exhibit mutually exclusive characteristics; hence, creating a material system that simultaneously achieves high stiffness and substantial loss is a notably challenging endeavor [9,35–37]. Polymeric foam, commonly utilized in protective materials, excels in energy absorption. Yet, its lack of sufficient stiffness and strength restricts its application in the development of load-bearing structural components. Our research indicates that by customizing the intrinsic structural density gradient of architected cellular materials, their dynamic properties can be effectively modulated across a wide spectrum. This approach enables a significant enhancement in dynamic stiffness while preserving the loss tangent of the materials. Together with its ability for tailorable energy absorption and dissipation under quasi-static compression, the 3D-printed lightweight gyroid-structure material, featuring a deliberately engineered intrinsic density distribution, demonstrates significant potential as a foundational component in creating hierarchically architected impact-absorbing helmet liners for traumatic brain injury prevention[6,38,39] and protective materials for aerospace applications[40].

Conclusion

Employing 3D-printed gyroid lattices made from viscoelastic elastomers of various structures as model systems, we demonstrate that the mechanical responses and performance of soft gyroid-structure cellular material are significantly influenced by its relative density and density distribution under various loading conditions, ranging from quasistatic to dynamic. Increasing the structural density of gyroid lattices leads to enhanced quasi-static energy dissipation and absorption. The incorporation of a structural gradient induces distinct uneven deformation behavior, which in turn enhances the structure's stability and energy absorption capacity at large compressive strain. Moreover, in dynamic regime, tailoring the relative density and its gradient distribution in the gyroid structure leads to dramatic tunability of the dynamic stiffness, from the applied static precompression induced varying stress conditions in the materials, while simultaneously maintaining the damping capability of the material. This research demonstrates the great potential of applying additively manufactured architected elastomeric cellular materials with judiciously designed

structural gradient for creating highly efficient structural materials with tailorable quasistatic and dynamic mechanical performance for extreme damping and impact mitigating applications.

Experimental Section

Gyroid lattice samples were printed by a Formlabs Form 2 SLA printer using Formlabs Flexible V2 resin (FLFLGR02). The fully cured resin exhibits a good combination of high elongation (80%) and tensile strength (7.7-8.5 MPa), which is particularly suitable for fabricating bendable or compressible part by 3D printing. To print, STL files were loaded into the PreForm slicing software and oriented such that the flat surface of the cylindrical gyroid sample was parallel to the print environment surface. A raft was added and support structures with a 1.6 mm touch point were placed along only the bottom of the part as to not affect the sample geometry. Note, a generous amount of support structures was needed to prevent samples from detaching from the build plate during printing. Flexible V2 resin was selected as the material in PreForm before the file was sliced and sent to the printer. After printing, samples were carefully removed from the build plate using a straight edge. The removed samples were submerged in a clean beaker filled with isopropyl alcohol (IPA) and allowed to sonicate for 30 minutes. The samples were then removed and submerged into a fresh beaker filled with clean IPA and sonicated for another 30 minutes. After the second sonication, samples were patted dry and left to air dry for 3 hours before being placed into a 60 °C oven for 60 minutes to post-cure. Once post-cured, the supports were removed using a straight edge.

We studied the mechanical behavior of 3D printed gyroid lattices by performing quasistatic compression up to 70% strain at a strain rate of 0.01 S^{-1} using an Instron Electropulse E3000. Nominal stress applied on the material is calculated from the measured force normalized by cross-sectional area and the strain is obtained from the imposed displacement normalized by height of material. We use the Instron Electropulse E3000 to perform dynamic analyses in compression mode with frequency of 10 Hz and at excitation amplitude of 0.25 mm (0.5%) with different applied static precompressions (3% - 50%) on the samples. Three gyroid samples with different structures are fabricated and tested to avoid the effects of manufacturing defects on the performance of the structures and obtain the average mechanical performance.

References

1. R.O. Ritchie, The conflicts between strength and toughness, Nat. Mater. 10 (2011) 817–822.

2. E. Ma, T. Zhu, Towards strength–ductility synergy through the design of heterogeneous nanostructures in metals, Mater. Today 20 (2017) 323–331.

3. J. Cai, M. Naraghi, Non-intertwined graphitic domains leads to super strong and tough continuous 1D nanostructures, Carbon 137 (2018) 242–251.

4. J. Cai, C. Griesbach, R. Thevamaran, Extreme Dynamic Performance of Nanofiber Mats under Supersonic Impacts Mediated by Interfacial Hydrogen Bonds, ACS Nano 15 (2021) 19945–19955.

5. C. Griesbach, J. Cai, S.-J. Jeon, R. Thevamaran, Synergistic strength and toughness through impact-induced nanostructural evolutions in metals, Extreme Mech. Lett. 62 (2023) 102037.

6. K. Chawla, A. Gupta, R. Thevamaran, Disrupting Density-Dependent Property Scaling in Hierarchically Architected Foams, ACS Nano 17 (2023) 10452–10461.

7. X. Li, L. Lu, J. Li, X. Zhang, H. Gao, Mechanical properties and deformation mechanisms of gradient nanostructured metals and alloys, Nat. Rev. Mater. 5 (2020) 706–723.

8. K. Lu, Making strong nanomaterials ductile with gradients, Science 345 (2014) 1455–1456.

9. D. Murgado, R. Thevamaran, Independent control of dynamic material properties by exploiting structural hierarchy and intrinsic structural gradients, Mater. Today Commun. 23 (2020) 100865.

10. J. Cai, M. Naraghi, The formation of highly ordered graphitic interphase around embedded CNTs controls the mechanics of ultra-strong carbonized nanofibers, Acta Mater. 162 (2019) 46–54.

11. P.G. Lashmi, P.V. Ananthapadmanabhan, G. Unnikrishnan, S.T. Aruna, Present status and future prospects of plasma sprayed multilayered thermal barrier coating systems, J. Eur. Ceram. Soc. 40 (2020) 2731–2745.

12. L.J. Gibson, M.F. Ashby, Cellular Solids: Structure and Properties, second edition, Cell. Solids Struct. Prop. Second Ed. (2014) 1–510.

13. L.J. Gibson, Cellular Solids, MRS Bull. 28 (2003) 270–274.

14. T.A. Schaedler, W.B. Carter, Architected Cellular Materials, Annu. Rev. Mater. Res. 46 (2016) 187–210.

15. M.F. Ashby, The properties of foams and lattices, Philos. Trans. R. Soc. Math. Phys. Eng. Sci. 364 (2005) 15–30.

16. L. Dong, V. Deshpande, H. Wadley, Mechanical response of Ti–6Al–4V octet-truss lattice structures, Int. J. Solids Struct. 60–61 (2015) 107–124.

17. A. Ajdari, B.H. Jahromi, J. Papadopoulos, H. Nayeb-Hashemi, A. Vaziri, Hierarchical honeycombs with tailorable properties, Int. J. Solids Struct. 49 (2012) 1413–1419.

18. Z. Qin, G.S. Jung, M.J. Kang, M.J. Buehler, The mechanics and design of a lightweight three-dimensional graphene assembly, Sci. Adv. 3 (2017) e1601536.

19. M. Mohsenizadeh, F. Gasbarri, M. Munther, A. Beheshti, K. Davami, Additively-manufactured lightweight Metamaterials for energy absorption, Mater. Des. 139 (2018) 521–530.

20. O. Rahman, K.Z. Uddin, J. Muthulingam, G. Youssef, C. Shen, B. Koohbor, Density-Graded Cellular Solids: Mechanics, Fabrication, and Applications, Adv. Eng. Mater. 24 (2022) 2100646.

21. O. Rahman, B. Koohbor, Optimization of energy absorption performance of polymer honeycombs by density gradation, Compos. Part C Open Access 3 (2020) 100052.

22. D. Qi, W. Hu, K. Xin, Q. Zeng, L. Xi, R. Tao, H. Liao, Y. Deng, B. Liao, W. Wu, In-situ synchrotron X-ray tomography investigation of micro lattice manufactured with the projection micro-stereolithography (PμSL) 3D printing technique: Defects characterization and in-situ shear test, Compos. Struct. 252 (2020) 112710.

23. J. Plocher, A. Panesar, Effect of density and unit cell size grading on the stiffness and energy absorption of short fibre-reinforced functionally graded lattice structures, Addit. Manuf. 33 (2020) 101171.

24. L. Yang, Y. Li, Y. Chen, C. Yan, B. Liu, Y. Shi, Topologically optimized lattice structures with superior fatigue performance, Int. J. Fatigue 165 (2022) 107188.

25. C. Zhang, H. Zheng, L. Yang, Y. Li, J. Jin, W. Cao, C. Yan, Y. Shi, Mechanical responses of sheet-based gyroid-type triply periodic minimal surface lattice structures fabricated using selective laser melting, Mater. Des. 214 (2022) 110407.

26. D.W. Abueidda, M. Elhebeary, C.-S. (Andrew) Shiang, S. Pang, R.K. Abu Al-Rub, I.M. Jasiuk, Mechanical properties of 3D printed polymeric Gyroid cellular structures: Experimental and finite element study, Mater. Des. 165 (2019) 107597.

27. K. Kim, G. Kim, H.G. Kim, H.J. Kim, N. Kim, Customizing the mechanical properties of additively manufactured metallic meta grain structure with sheet-based gyroid architecture, Sci. Rep. 12 (2022) 19897.

28. D. Li, W. Liao, N. Dai, Y.M. Xie, Comparison of Mechanical Properties and Energy Absorption of Sheet-Based and Strut-Based Gyroid Cellular Structures with Graded Densities, Mater. Basel Switz. 12 (2019) 2183.

29. L. Yang, R. Mertens, M. Ferrucci, C. Yan, Y. Shi, S. Yang, Continuous graded Gyroid cellular structures fabricated by selective laser melting: Design, manufacturing and mechanical properties, Mater. Des. 162 (2019) 394–404.

30. J. Huang, Y. Xu, S. Qi, J. Zhou, W. Shi, T. Zhao, M. Liu, Ultrahigh energy-dissipation elastomers by precisely tailoring the relaxation of confined polymer fluids, Nat. Commun. 12 (2021) 3610.

31. H. Kim, S.H. Tawfick, W.P. King, Buckling elastomeric springs and lattices for tailored energy absorption, Mater. Today Commun. 35 (2023) 106417.

32. C.W. Haney, H.R. Siller, Properties of Hyper-Elastic-Graded Triply Periodic Minimal Surfaces, Polymers 15 (2023) 4475.

33. H. Ren, H. Shen, J. Ning, Effect of Internal Microstructure Distribution on Quasi-Static Compression Behavior and Energy Absorption of Hollow Truss Structures, Materials 13 (2020) 5094.

34. J. Baumeister, J. Banhart, M. Weber, Aluminium foams for transport industry, Mater. Des. 18 (1997) 217–220.

35. R. Lakes, Viscoelastic Materials, Cambridge University Press, 2012.

36. A.P. Unwin, P.J. Hine, I.M. Ward, M. Fujita, E. Tanaka, A.A. Gusev, Escaping the Ashby limit for mechanical damping/stiffness trade-off using a constrained high internal friction interfacial layer, Sci. Rep. 8 (2018) 2454.

37. Z. Xu, C.S. Ha, R. Kadam, J. Lindahl, S. Kim, H.F. Wu, V. Kunc, X. Zheng, Additive manufacturing of two-phase lightweight, stiff and high damping carbon fiber reinforced polymer microlattices, Addit. Manuf. 32 (2020) 101106.

38. G. Kulkarni, X.-L. Gao, S.E. Horner, J.Q. Zheng, N.V. David, Ballistic helmets – Their design, materials, and performance against traumatic brain injury, Compos. Struct. 101 (2013) 313–331.

39. P. Siegkas, D.J. Sharp, M. Ghajari, The traumatic brain injury mitigation effects of a new viscoelastic add-on liner, Sci. Rep. 9 (2019) 3471.

40. Z. Jia, Y. Yu, S. Hou, L. Wang, Biomimetic architected materials with improved dynamic performance, J. Mech. Phys. Solids 125 (2019) 178–197.

Chapter 12: Thesis for the Layperson

Thank you to the Wisconsin Initiative for Science Literacy, specifically Cayce Osborne, Elizabeth Reynolds, and Bassam Shakhashiri, for this opportunity to explain my thesis work to the public. I believe scientific literacy is important on multiple levels:

- From an **individual** level, leveraging professional expertise allows one to make informed decisions that could be crucial to your health or wellbeing.
- From an **educator** level, understanding scientific literacy and improving science communication can break down barriers in education.
- From a **professional** level, scientific literacy enables you to connect your expertise to others' expertise. Notably, an expert in one area is often a layperson in another, nonetheless the connection between those two areas could have huge implications.
- On a **societal** level, the public often funds much of the research being done and scientists have an obligation to justify the funds. Additionally, at some point we hope non-scientists will be able to use the results of our research in some meaningful way and people should have the option to understand how it works.
- From a **personal** level, writing this chapter prepares me for future effective collaboration. Additionally, during my PhD, in conversation with fellow graduate students, someone said, "I feel like I know less now than when I started". Of course, this is not meant literally, but represents how disconnected you can get from what is general knowledge and what is specialized. As you dive deeper into your field, more questions arise than you can answer, and so by writing this chapter, hopefully, I can appreciate how far I have come.

Q: What will this chapter cover?

Throughout my thesis work, I have delved into the world of polymer materials and 3D printing (more on these in a bit!). Specifically, I examined how we can design materials for 3D printing with both improved properties (for example, stronger materials), new functions (for example, materials that respond to their environment), and better sustainability. This chapter is for anyone in the public who is interested in learning more about how scientists think about designing new materials. In contrast to the other sections of this thesis, this chapter will be limited in technical jargon or any assumptions about the reader's prior knowledge. Through this chapter, I will answer the following questions:

1. *What is the role of a material scientist?*
2. *How do material scientists go about designing new materials?*
3. *What is a polymer?*
4. *What is 3D printing and how can one 3D print a polymer?*
5. *What are some materials I made during my PhD?*

Hopefully, by the end of this chapter you understand a bit more about the motivation behind developing new materials and how I and other material scientists think about designing new materials. I hope you enjoy learning about my PhD work!

Q: What is the role of a material scientist?

Materials have been extremely important throughout human history. So important, that entire time periods have been described by their defining materials. Some examples are the stone age and metal age, which each brought unprecedented changes to civilizations and technology. In fact, even the present is defined by two materials—plastics (found everywhere from water bottles to clothing to medicines) and silicon (used in computers and other electronic devices). While materials have substantially evolved from those materials that can naturally be found, such as wood and stone, to synthetic materials, such as steel and Kevlar, the material scientists' role is never done. Material scientists are constantly developing materials with ever improving properties to solve some of the world's most pressing problems, such as clean and renewable energy, sustainability, space travel, human health, computing, and more.

When I came to graduate school, I decided I wanted to learn how to design better materials. While I was not entirely sure what materials I would design, I knew I wanted to understand how to transfer fundamental understanding of physics and chemistry to desired properties and functions. Early on in my graduate school coursework, I came to understand that better control of a material's structure was key to achieving this, and that 3D printing was a revolutionary technology. I also came to the realization that polymers are an important class of materials that offer huge opportunities for developing novel functionality, but also have a pressing need to improve their sustainability. For the last five years, I have been exploring these aspects, growing as a material scientist, and learning to tackle pressing challenges that could be solved by developing new materials. I hope you enjoy reading about what I learned and some of the materials that I developed.

Q: How do material scientists go about designing new materials?

Aspiring material scientists learn early on the importance of the relationship between a material's structure, processing, property, and performance (Figure 12.1). Importantly, a fundamental lesson is that each of these elements are interconnected, and that by changing one, you affect another. While this can complicate material design, it also creates a vast number of variables that can be changed, yielding enormous room for growth and discovery. However, it also makes it clear that the more control we have over this design space, the more we can learn and improve.

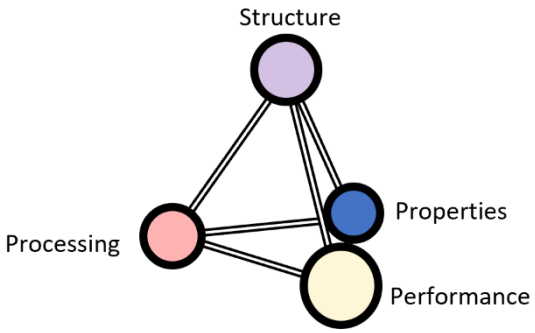

Figure 12.1. *Material science tetrahedron showing the relationship between structure, processing, properties, and performance.*

One way material scientists can improve materials is through controlling the structure of a material across length scales: from the molecular to the macroscopic. So, what does this mean? Well imagine you want to make a Lego™ model. When you dump out the pieces you would likely see they come in many shapes, sizes, and connectivity. If you connect each piece in the precise location with compatible pieces one at a time, perhaps building smaller subunits first before assembling them together, you will eventually form the desired final structure. Depending on how these pieces are connected your final structure can take on very different properties. For example, maybe it can fold, be quite rigid, be easy or difficult to be unassembled, or have room to expand on in the future. Taking a step back, you can see that you have used the structure and properties of your smaller individual building blocks to create a larger structure with new properties, shape, and function. Material scientists attempt to do this with similar levels of precision, but with building blocks so small they are impossible to see or touch. So how do we do this?

Well first, we need to put into context material scientists' building blocks, atoms. Atoms are the basic building blocks of all the matter around us and compose everything we can see, touch, and smell. Each atom is composed of three subatomic particles called the proton, neutron, and electron (Figure 12.2A). The proton and neutrons are housed in the nucleus of the atom, while the electrons fill the volume around the nucleus. For simplicity, one could envision it being like the way planets orbit the sun (Figure 12.2B). The sun, in this case, is the nucleus, while the planets are electrons. However, the entire size of an atom is around an Angstroms (Å), which is 10 billion times smaller than a meter. Notably, an atom can have different numbers of protons, neutrons, and electrons, and a single type of atom is known as an element. All the known elements are represented on the periodic table. Therefore, the periodic table contains all the building blocks material scientists can use to design materials. Some of the elements you have likely heard of before, for example hydrogen, oxygen, nitrogen, copper, and gold. Notably, just like Lego™ blocks, elements come in many different shapes, sizes, and connectivity, which controls how they will interact with atoms identical to themselves or other elements in the periodic table.

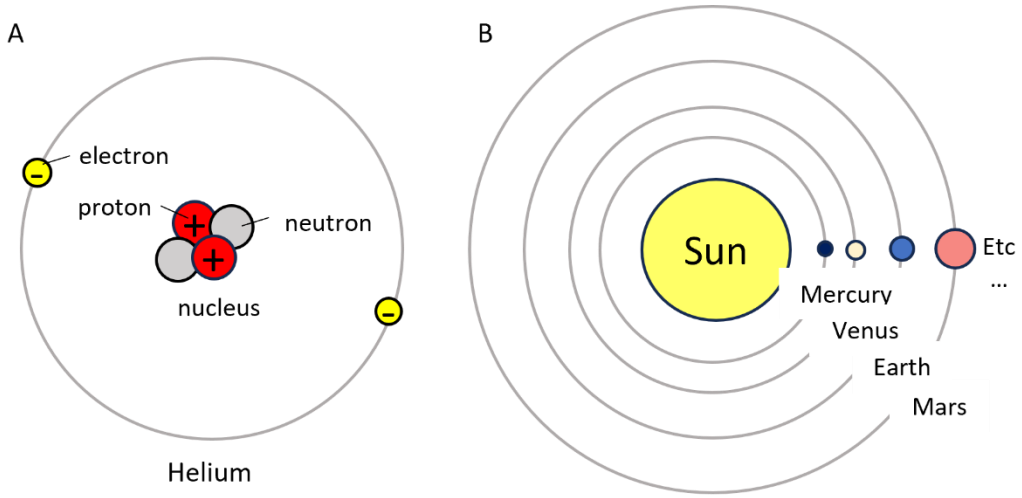

Figure 12.2. *A) Picture of an atom of the element helium (He) B) General diagram of planets orbiting the sun.*

In reality, not many pure elements are found in nature, but rather elements are commonly assembled into structures called molecules. A chemist's job is to figure out ways to take elements or molecules and react them with one another to form new useful molecules. For example, two hydrogen atoms (H) and one oxygen

atom (O) can react to form water (H_2O) (Figure 12.3). Notably, molecules can also react with one another to form new molecules, which will become important later in this chapter. While there are rules for how molecules react with one another, this is quite complicated, and so for now, understanding that we can make a wide variety of molecules made up of atoms is key!

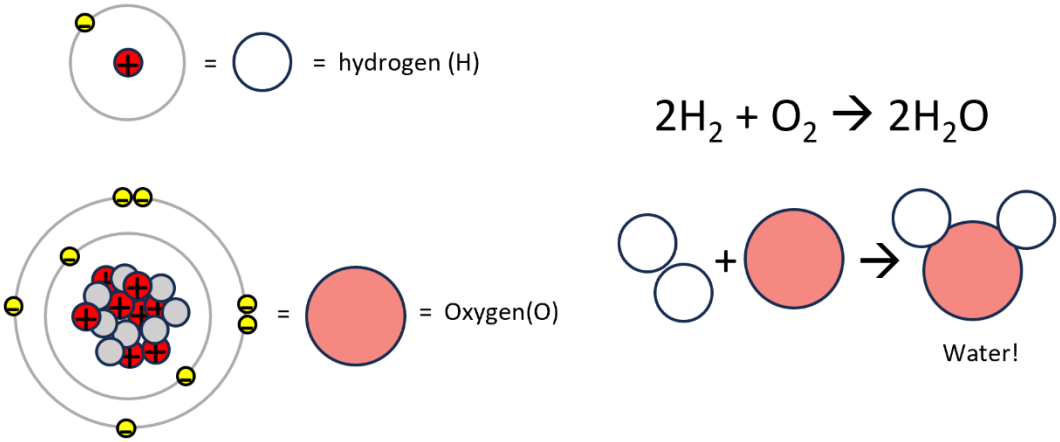

Figure 12.3. *Diagram of oxygen, hydrogen, and the water molecules as well as the general reaction of hydrogen and oxygen to form water.*

With atoms and molecules, we can do quite a lot. By controlling how they are arranged in space, we can form larger structures that we can begin to see and manipulate (Figure 12.4). For example, we can take many water molecules from our faucets and fill a glass with them. In the glass, the individual water molecules are around one another in a disordered fashion, and can move relatively freely. Because of this, the molecules make a liquid that we can readily pour into a new glass, or ice mold. However, by altering how we process the water, its properties can change drastically. For example, when we sufficiently cool water down it freezes, the molecules become ordered and get locked into place, losing mobility, and the water becomes solid ice. Suddenly it has become quite hard, and we can no longer smoothly pour it. Additionally, if we heat the ice up, the water will return to its liquid state. If we continue to heat it up, it may suddenly begin to boil into gaseous steam. Now, we can no longer contain it in a glass, but we can use it to power things, like trains, using steam engines. This illustrates the drastic effects that the processing of a material has on its physical properties.

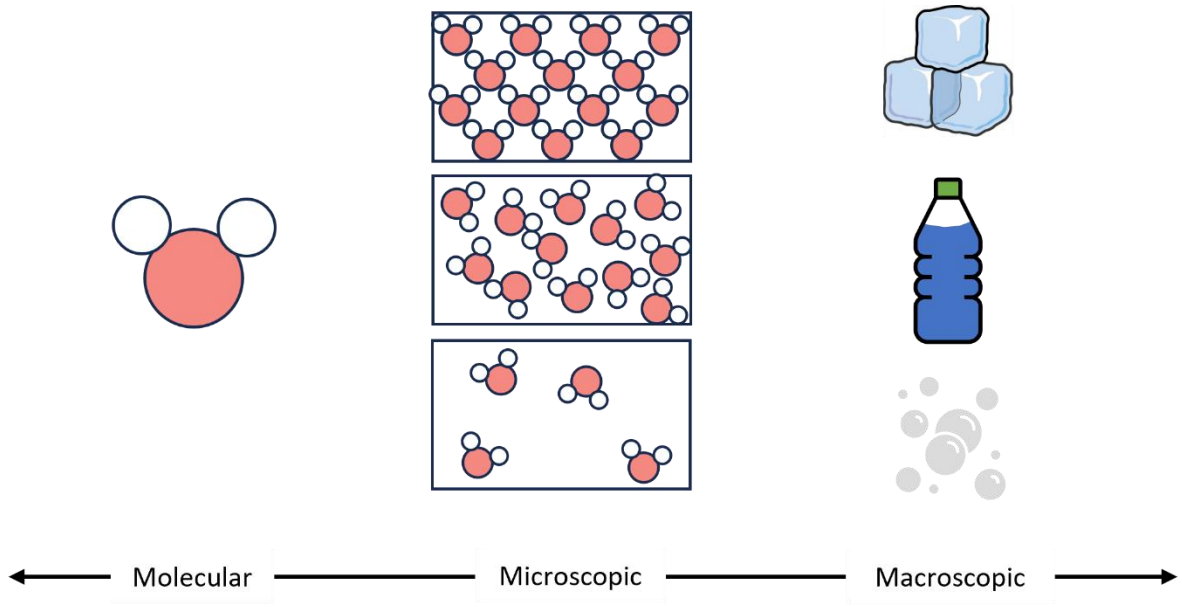

Figure 12.4. *Visualization of water at different length scales. This illustrates that the way water is structured on the molecular and microscopic level has a profound effect on water on the macroscale.*

In summary, material scientists use structure and processing to control the properties and final performance of a material. To do so, they use building blocks, called atoms, and structures made of atoms, called molecules, to build useful materials. New materials can be made by reacting different atoms or molecules together to form new molecules. Notably, even a single material's properties can vary dramatically depending on how it is processed. Now that we have this level of understanding, I will narrow the scope to a single class of material that we can make with molecules, called a polymer, which is the focus of the next section.

Q: What is a polymer?

Polymers, composition of the Greek words *poly* and *meros*, meaning many parts, are large molecules (aptly termed macromolecules) composed of many repeating sub units called monomers. These macromolecules can simply be thought of as a paper clip chain where each individual paper clip is a monomer, and the entire chain is the polymer (Figure 12.5). The process of forming a polymer is called polymerization and entails linking monomers together to form a longer chain. Notably, polymers can be made from a single type of monomer, termed a homopolymer, or multiple types of monomers, called a copolymer. For the case of copolymers, they can be arranged into different patterns such as random, blocks, or alternating (Figure 12.5). It turns out different patterns can drastically alter the properties of the polymer.

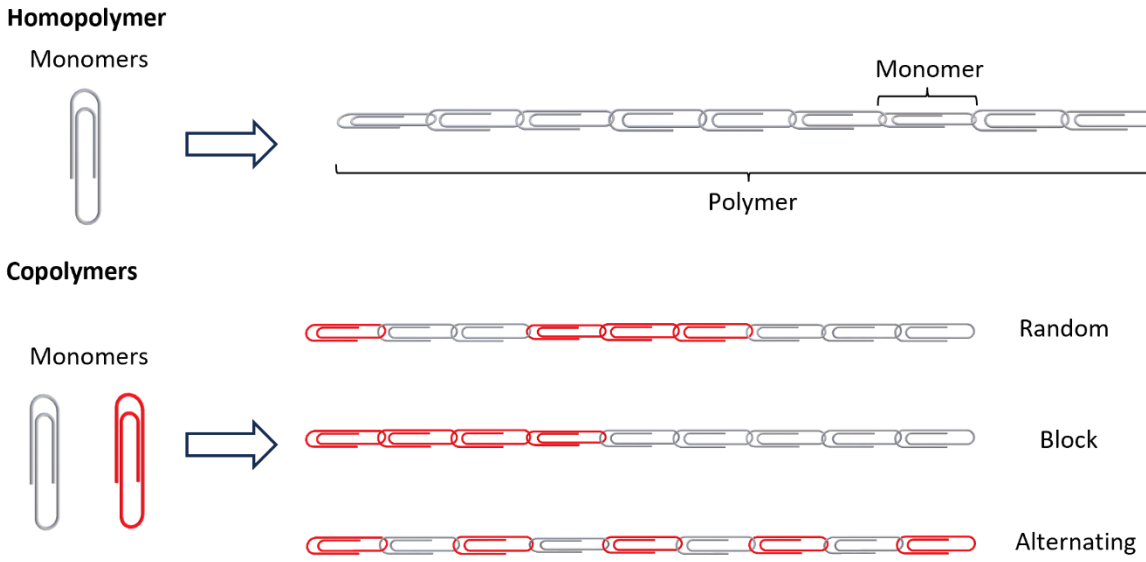

Figure 12.5. Example of a polymerization reaction to form a homopolymer or a copolymer illustrated with paper clips.

Polymers are found virtually all around us (Figure 12.6). This is because a polymer's macromolecular nature instills many properties that are advantageous, such as being light, tough, and chemically resistant. Frequently encountered polymers are materials such as polystyrene in packing peanuts, polyethylene in grocery bags, polypropylene in cups, acrylonitrile-butadiene-styrene in Lego™ bricks, polybutadiene in

tires (rubber), and polyester in our clothing. Natural polymers are also all around us, such as cellulose in tree bark. Even our DNA is a polymer.

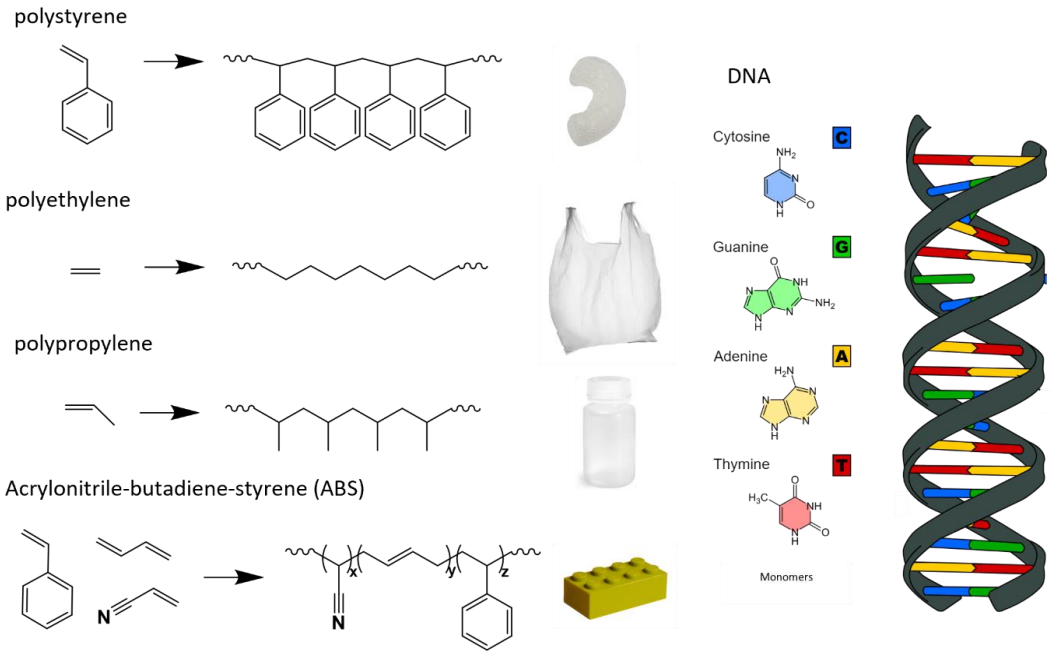

Figure 12.6. *The formation of commonly encountered polymers from their monomers next to an example of where you would likely encounter that material.*

Synthetic polymers can be categorized in two categories, thermoplastics and thermosets. Thermoplastics are polymer chains entangled in one another; you can imagine a pile of paper clip chains. It might be difficult and take a while, but you can separate them all out into individual chains. Thermosets on the other hand, are polymer chains connected to one another with permanent bonds and form a fence like structure. You could imagine in the example of the paper clip chains, if I connect each chain to another by paper clip bridges. Now, the individual polymer chains cannot be separated into individual chains. On a molecular level, this has large implications, as the extra mobility of thermoplastics allows these materials to flow when heated, and dissolve when placed in compatible liquids, while thermosets cannot be reprocessed. This is important when we consider the future of polymers and improving their sustainability. For this reason, the most used thermoplastics are labeled with numbers that enable their sorting for reprocessing and recycling. On the other hand, tires are an example of a thermoset, unable to be reprocessed. Instead, they are ground up and often utilized as cushioning material in turf fields.

Q: What is 3D printing and how can one 3D print a polymer?

3D printing describes a process of manufacturing an object layer-by-layer from a 3-dimensional model constructed on a computer. There are many different types of 3D printing methods that span metals, ceramics, and polymers. Because objects are built in layers, we can produce complex structures that you would not otherwise be able to make, such as lattices, or customized objects specifically for an individual. This contrasts with more traditional methods of making objects, such as filling molds or sculpting. So far, this capability has been used to make customized products, such as dental implants, replacement organs, and foams used in football helmets and shoes (Figure 12.7). While 3D printing is still very much in development, it is being looked at as a revolutionary technology that could shift the manufacturing paradigm.

Figure 12.7. *Showcase of applications of 3D printing technology and demonstration of the types of structures that can be formed.*

The main 3D printing technology I utilized in my thesis is called vat photopolymerization. Vat photopolymerization is a 3D printing process that takes a liquid and turns it into a solid using light (Figure 12.8). For this reason, we call the liquid a photoresin. Importantly, only the areas we expose to light will solidify. By doing this in thin layers (around the thickness of a human hair) and building layers one on top of the next, we can build up a fully 3-dimensional object. You might think this sounds like magic, but in fact it is polymer chemistry, and the reaction triggered by light is polymerization! You can think about this transformation like baking a cake. For a cake, you need certain ingredients that when mixed in the correct

proportions make up your batter. After baking your batter in the oven at high temperatures, the liquid batter can react and solidify into a sugary treat. By baking many layers and stacking those layers, you can create an even taller structure.

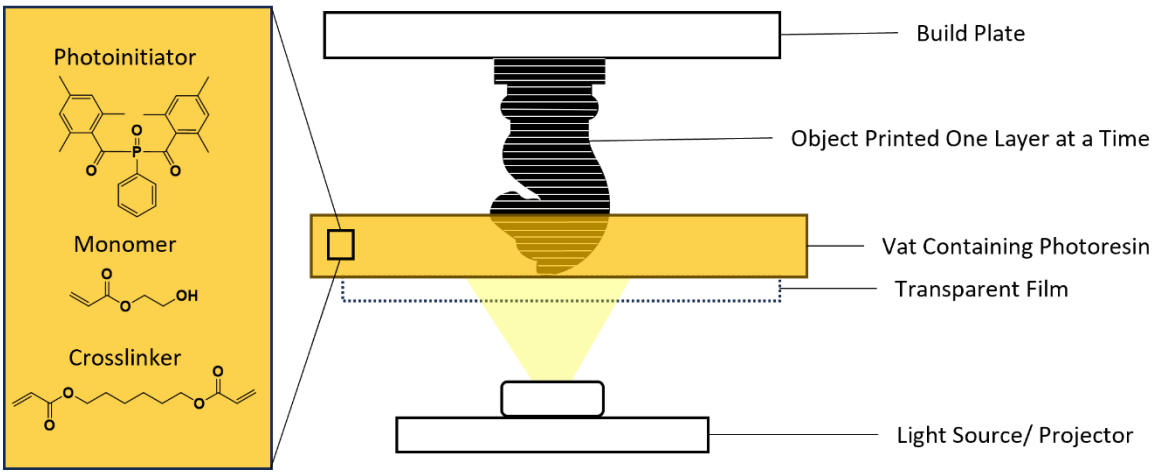

Figure 12.8. *Schematic of a simplified vat photopolymerization printer with the different components labeled. Additionally, the basic ingredients to a photoresin are shown along with examples of what a specific ingredient might look like on a chemical level.*

Similarly, the ingredients (chemicals) and proportions (concentrations) of these ingredients I put into our photoresins determine how well the photoresin will print and what the final properties of the object will be. In the case of our photoresin, the three crucial ingredients are photoinitiator, monomer, and crosslinker (Figure 12.8). The photoinitiator is the chemical that reacts with the light and tells the polymerization reaction to start. The monomer is the major component to the photoresin, and will dictate the chemical structure of the polymer and therefore the material's properties. Lastly, the crosslinker enables the liquid to be converted into solid quickly. The more crosslinker you add, the faster the material will solidify, but often this comes at the cost of making your part more brittle. Importantly, adding a crosslinker turns the object that is being produced into a thermoset. Remember, thermosets are those materials that have a polymer chain connected into a fence like structure, meaning they typically cannot be reprocessed.

What specific materials did I make during my PhD?

1. **Tougher Materials**

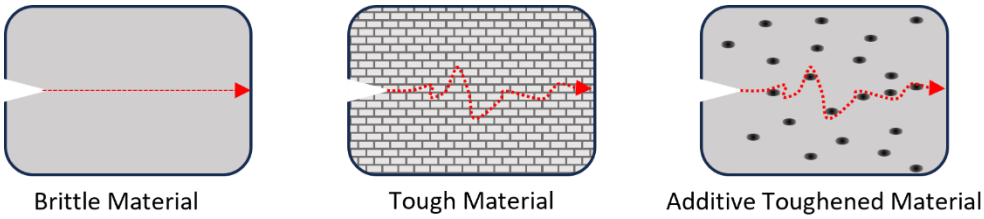

Figure 12.9. *diagram showing the path crack of a brittle material, tough material, and a brittle material reinforced with a soft additive.*

A material breaks when a crack is formed and can propagate all the way through a material (Figure 12.9). One way to make a material less susceptible to breaking is by making the path the crack takes to reach the other side longer. A Common way that material scientists do this is by mixing the material you hope to toughen with soft additives. The role of these soft additives is to block the pathway of the crack, either by stopping the crack by absorbing its energy or by forcing it to take another pathway. However, these additives must be carefully designed, as they can also weaken the material by adding defects along the boundary between the additive and the material it is housed in.

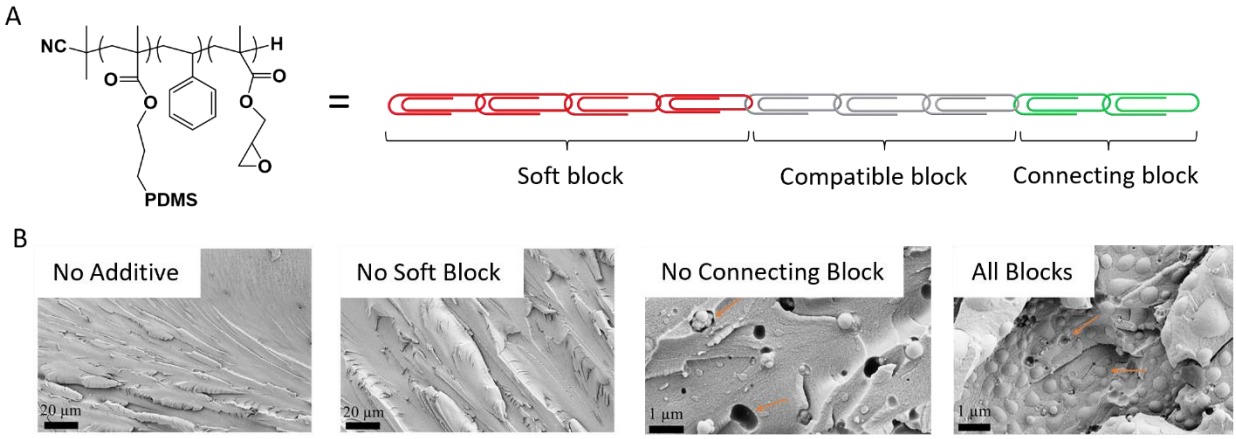

Figure 12.10. A) Image of the exact polymer used in this study along with a diagram showing its triblock nature in terms of a paperclip copolymer B) Scanning electron microscope images of the bulk materials reinforced with polymers leaving out various blocks.

During my PhD, I worked on a highly collaborative project combining the expertise of a polymer chemist, chemical engineer, and mechanical engineer. The project incorporated carefully designed polymers as an

additive in a bulk material to improve its strength and toughness. Here, the strength of the material can be thought of as how much force it takes to break it, while the toughness is how much energy it takes to break it. The polymer was a triblock copolymer. The first block was soft and used to arrest and deflect a crack, the second block was used to make the polymer compatible with the bulk material, and the third block connected the bulk material to the polymer, ensuring it would not act as a defect. The molecular structure next to a paper clip model is shown in (Figure 12.10A).

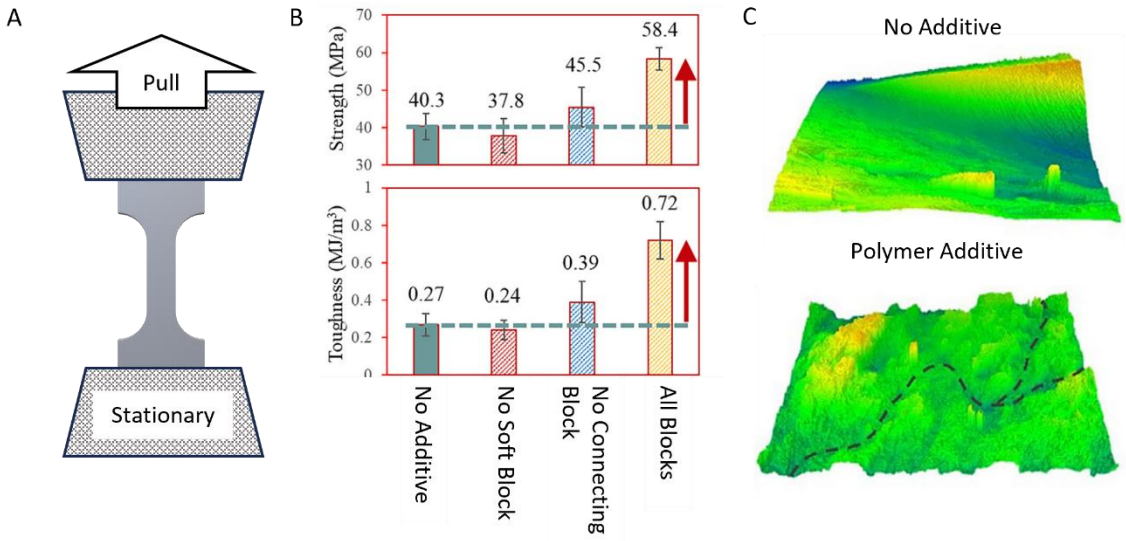

Figure 12.11. *Schematic of the type of testing done on the materials, plot showing the strength and toughness of the materials with different polymer variations incorporated into the bulk material, and mapping of the fracture surface of a bulk material without additive and with polymer additive.*

To test this polymer, I 3D printed test samples consisting of a resin with the new triblock copolymer as an additive. Collaborators and I then looked at how it behaved in the bulk material. To do so, a collaborator who specialized in microscopy took pictures of the sample at high magnification to visually look at how the polymer arranges in the material (Figure 12.10B). We saw something very interesting. Firstly, without the polymer, the bulk material looks rather smooth. This did not change when we added a polymer with only the compatible and connecting blocks to the material. This means it is being cohesively incorporated into the material. However, when we added a polymer with a soft block into the resins, little pockets began to form within the material. These pockets form because the soft block is incompatible with the bulk material. Like oil and water, it does not like to mix, and so it tends to coil into a ball. However, these pockets

are sometimes missing the polymer because it was not connected to the bulk material and came dislodged. When all blocks are present, we see the best effect: small pockets of soft material are housed and connected within the bulk material.

So does this lead to a stronger and tougher material? To test this, I printed samples that look like dog bones and pulled on them (Figure 12.11A), measuring the amount of force and energy required to pull the material apart, which indicates the material's strength and toughness. Using these additives, we were able to strengthen the material by ~1.5x and toughen the material by ~2x (Figure 12.11B). We saw no improvement in strength or toughness when there was no soft block, and marginal improvement without the connecting block. This shows us that all three blocks are needed for the best effect. We could also look at the surface of the broken sample where it cracked and map it (Figure 12.11C). You can clearly see that the sample with the additive is much rougher, indicative of the longer crack path during breaking.

2. More Sustainable Materials

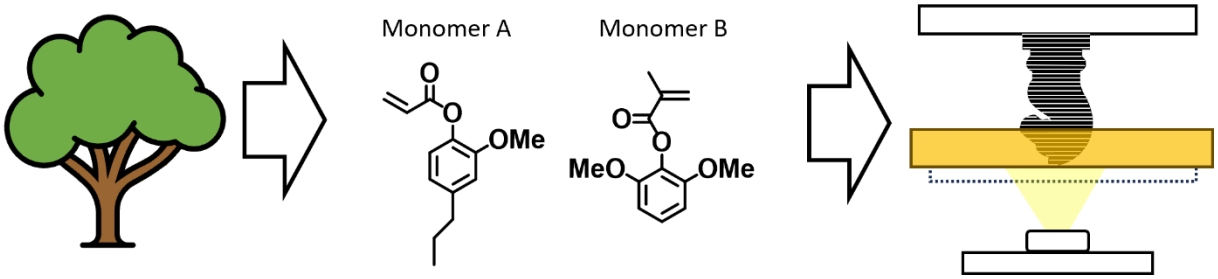

Figure 12.12. *Diagram of the main idea behind the testing of more sustainable materials for 3D printing.*

Currently, vat photopolymerization resins are made from photoinitiators, monomers, and crosslinkers that are derived from petroleum feedstocks. As the world tries to reduce its carbon footprint, we want to move chemical production away from fossil fuels and toward more sustainable alternatives. One way to do this is to use biomass (materials from plants!). The most abundant biomass on the planet is that of lignocellulosic biomass (think of trees). Lignocellulosic biomass is made of three different polymers: cellulose, hemicellulose, and lignin. While cellulose components are used to make paper, the lignin component is often regarded as trash. This provides a huge opportunity, since we can now pull from a source that is already widely produced but not used. This is important, as increasing demand for biomass could lead to negative side effects, like deforestation.

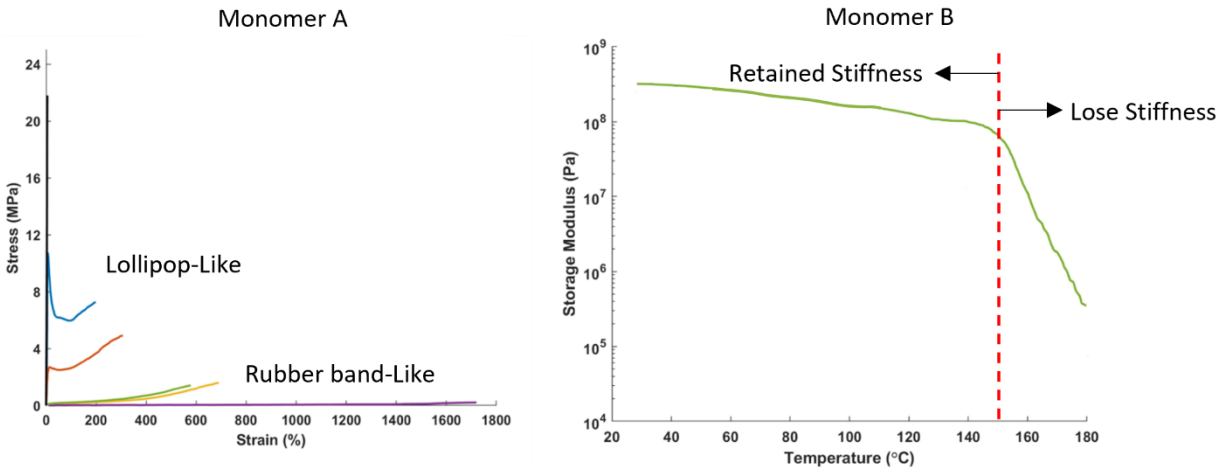

Figure 12.13. *A) Mechanical response of different materials made from monomer A. B) Stiffness of a material made with monomer B with increasing temperature.*

To use lignin to make materials for 3D printing, lignin must first be deconstructed into usable smaller molecules. Many researchers are currently examining how lignin can be deconstructed, and how those different methods affect what molecules are produced. In my work, I looked at two different lignin derivable monomers (Figure 12.12), which I will call monomer A and monomer B, and examined those materials' properties, like strength, thermal properties, and how they react to different chemicals. Interestingly, I found that when I mixed monomer A with other bioderivable monomers, materials with highly tunable mechanical properties were produced. By stretching the different materials and measuring how far the samples stretched (also called strain) and how much force it takes to stretch (called stress), I observed highly varied responses, ranging from as stretchy as a rubber band to as stiff as a lollipop.

On the other hand, monomer B could be heated to over 100 °C (the temperature that water boils at) without softening. I tested this by measuring the storage modulus at increasing temperatures (12.13B). You can think of the storage modulus as how solid-like (or stiff) that material feels at a certain temperature. Typically, as you raise the temperature of a polymer, it will soften and become less solid-like, and this correlates with a drop in the storage modulus. Additionally, to print these materials, I did not need to add a crosslinker. This is uncommon, and enables printing of thermoplastic materials that can be reprocessed and recycled into new materials when placed into select liquids!

3. Stimuli Responsive Materials

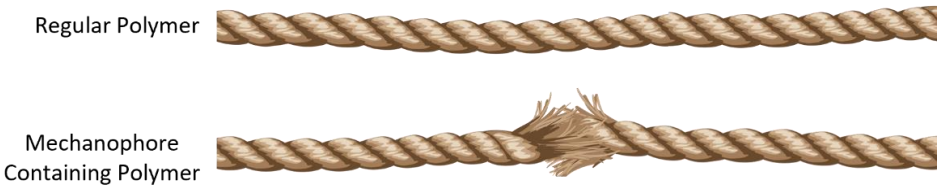

Figure 12.13. *diagram of a polymer with and without mechanophore illustrated by a rope with and without a fray. The fray indicates the idea behind incorporating a mechanophore into a polymer.*

When bone fractures, it can repair itself. Not only does it repair itself, but it can reconfigure, reinforcing those areas from future damage. Developing materials like bone would enable materials to adapt to fracture or cracking without any intervention from humans. Could you imagine a road that could fill its own potholes? Wouldn't that be great! One-way material scientists are beginning to think about this is by using mechanochemical transduction. This word may sound intimidating, but breaking this word down we have "mechano" meaning mechanical force, "chemical" meaning chemistry, and "transduction" meaning to convert. Therefore mechanochemical transduction is converting mechanical force into a chemical response.

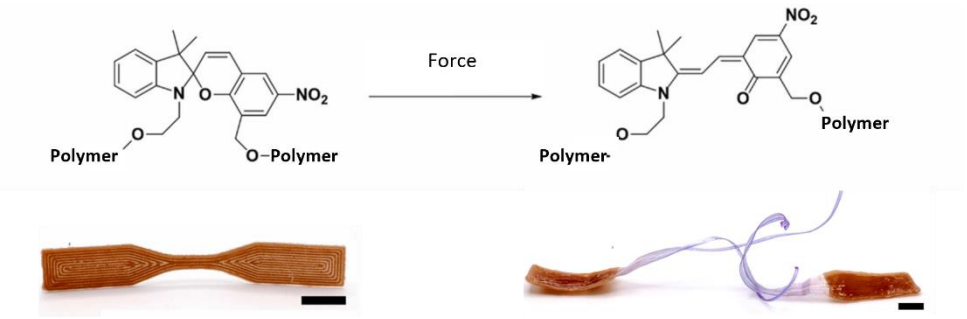

Figure 12.14. *Example of a mechanophore used in our lab that changes color with force. At a molecular level the mechanophore called spiropyran changes its structure resulting in the color change.*

To do this, material scientists are designing polymers with mechanically sensitive units built into them. These mechanically sensitive components are called mechanophores. A simple way to think about these polymers is thinking about a game of tug of war. In a normal game, two teams will pull on a rope. If the teams are evenly matched, the rope will either stay where it is, or if they pull with enough force, the rope

may even break near the center where the force was highest. However, what happens if we fray the rope in the middle? Now, when the teams pull, the rope will likely break at a much lower force than before at the exact location of the fray. This is essentially what a mechanophore does in a polymer. It acts as a weak point in the chain. However, this weak point can be designed to not only break the polymer chain, but also to change the structure of a molecule, which can cause a color change (as shown in Figure 12.14), or even release new chemicals.

4. Multimaterial 3D printing

Making an object from multiple materials can simply be done by mixing two materials together and then forming it into your desired shape. However, in this approach, you have no control over where each material will end up in the final structure. Making a multimaterial object, where you control the precise location of each material within the final object, is much more challenging. I have been approaching this problem utilizing a technique developed in our research group, where we use the color of light to form materials that have different properties. By controlling where we project different colors of light, we can then control the specific material that forms in that location. Importantly, this all occurs from a single photoresin!

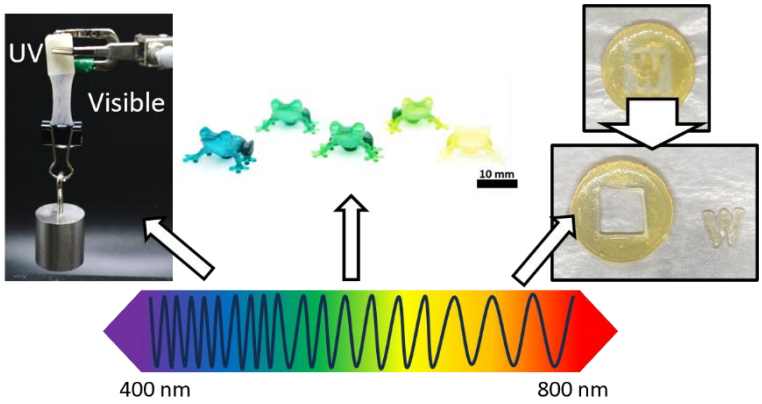

Figure 12.15. *Examples of using different wavelengths of light to alter materials properties.*

This works by recognizing that different colors of light are each a different wavelength and contain different amounts of energy. Interestingly, molecules can be designed to respond to only specific wavelengths of light. This is similar to a radio. Each radio station is like a different wavelength of light. By tuning our radio to a specific channel, we can hear a range of content, including music, news, interviews, or sports. Our system works almost exactly like this, but rather than different content, we express different materials properties (Figure 12.15). For example, we are able to make materials that are soft with visible light and stiff with UV light. Additionally, I designed photoresins that can make materials that can dissolve with visible light, but that will not dissolve with UV light. Lastly, I developed a photoresin which uses visible light to form the object, and UV light to change its color.

Summary

In conclusion, material scientists are important because they develop new materials to solve pressing problems in society. Material scientists do this by controlling the structure of a material across various length scales to achieve specific properties and performance. The building blocks used to do this are called atoms and molecules, which material scientists can design and carefully arrange into materials. One material that can be formed from atoms are polymers! Polymers are defined by the presence of large molecules with repeating units of monomers. These large molecules are lightweight and durable, making them very useful for creating many of the materials found all around us. One exciting avenue to explore using polymers is 3D printing. Using 3D printing, materials with complex structures can be made. During my PhD, I designed several polymer materials for 3D printing, including tougher materials, more sustainable materials, stimuli responsive materials, and precise multimaterials. Importantly, all of this was done by considering the properties of individual molecules used to make the materials.

Where do we go from here?

Over the past five years, I have been able to design a range of polymers for 3D printing with improved strength and toughness, sustainability, stimuli responsiveness, and localized control over material properties. Through this experience, I have gained valuable insight into how to think about designing polymers from individual molecular building blocks, and how this affects their final properties and function. I hope I can use this understanding to better design the polymers of the future. From my perspective, the largest challenge facing the future of polymers comes from a sustainability standpoint. By 2050, the global production of plastics is forecasted to be 34 billion tons. This number, in combination with the growing plastic accumulation crisis and the formation of microplastics, necessitates solutions. Many of these solutions can come from better design of polymers at the molecular level, enabling improved biodegradability, recyclability, and a more circular plastic lifecycle.

To begin working on this problem, I will be joining a small team of material scientists and polymer chemists at RockyTech Ltd. in Boulder, Colorado. Our mission is to improve the nationwide recycling rate and simplify the current plastic recycling process. To do this, we will use a two-part strategy to upcycle existing plastics and develop novel polymer materials and composites with the material's entire lifecycle in mind. This enables us to better utilize the large accumulation of existing plastics while designing new plastics for the future.

Image References

Packing Peanut: https://www.officedepot.com/a/products/578376/Office-Depot-Brand-Loose-Fill-Packing/

Plastic bag: https://cen.acs.org/articles/92/i37/Breaking-Plastic-Bag-Habit.html

Polypropylene bottle: https://www.fishersci.com/shop/products/polypropylene-wide-mouth-bottles-6/02896B

Lego™ brick: https://commons.wikimedia.org/wiki/File:Light_Green_Lego_Brick.jpg

DNA: https://en.wikipedia.org/wiki/Nucleic_acid

Football helmet: https://www.ntop.com/software/capabilities/lattice-structures/

Mouth model: https://www.dentistrytoday.com/2021-the-year-of-3d-printing-in-dentistry/

Shoe: https://www.cnet.com/health/fitness/adidas-running-shoes-with-3d-printed-midsoles-push-your-feet-forward/

Chapter 13: Summary

This dissertation explored how 3D printing can be used to go from molecules to functional models. In chapter one and two, I introduced the history of 3D printing, potential implications it has on manufacturing, and how polymers are printed using different 3D printing techniques. In chapter three, I gave a research perspective on 3D printing of polymeric materials. Emphasis was placed on the ability to achieve hierarchical control over a materials structure, taking inspiration from nature, and the unique advantages 3D printing has in doing this. Additionally, I introduced going beyond materials properties found in nature using new object geometries. Chapter four, five, and six detailed investigations of new materials for 3D printing using a bottom-up approach to material design that starts at the monomer level. The investigations detailed show that: (1) stronger and tougher epoxy materials can be formed by including novel triblock copolymers consisting of a soft block, synergizing block, and crosslinking block. (2) more sustainable materials can be produced from lignin derivable monomers and that these materials can have tunable mechanical properties, favorable thermomechanical properties, and provide new outlooks on VP 3D printed object's lifecycle. (3) Stimuli responsive materials with the potential to be self-reporting and self-strengthening may be possible by incorporating mechanoacid into 3D printing resins. In chapter seven and eight, I showcase two new 3D printing techniques toward enhanced chemical flexibility. One of which was capable of printing thermally cured thermosets through heating at a patterned photothermal interface while the other applied an open-source powder material extrusion printer to rapidly screen new thermoplastic and thermoplastic composite materials without needing to make filament. In chapter nine I outline the continued efforts in the Boydston group to develop new chemistries for DW-VP. Specifically, I formulated a material system for printing multicolor objects from a single resin vat by localizing regions of controlled acidity to alter the color of pH responsive dyes using UV light and printing of the 3D object with visible light. Lastly, in chapter ten and eleven, I explored two complex geometries (bistable mechanical metamaterial and gradient gyroid lattices) to better control mechanical wave propagation within these materials. In this investigation we found that the performance of bistable metamaterials is greatly dependent on impactor mass and velocity and that gradient gyroid lattices enable enhanced energy absorption capacity.

Appendix A: Supporting Information for Chapter 4

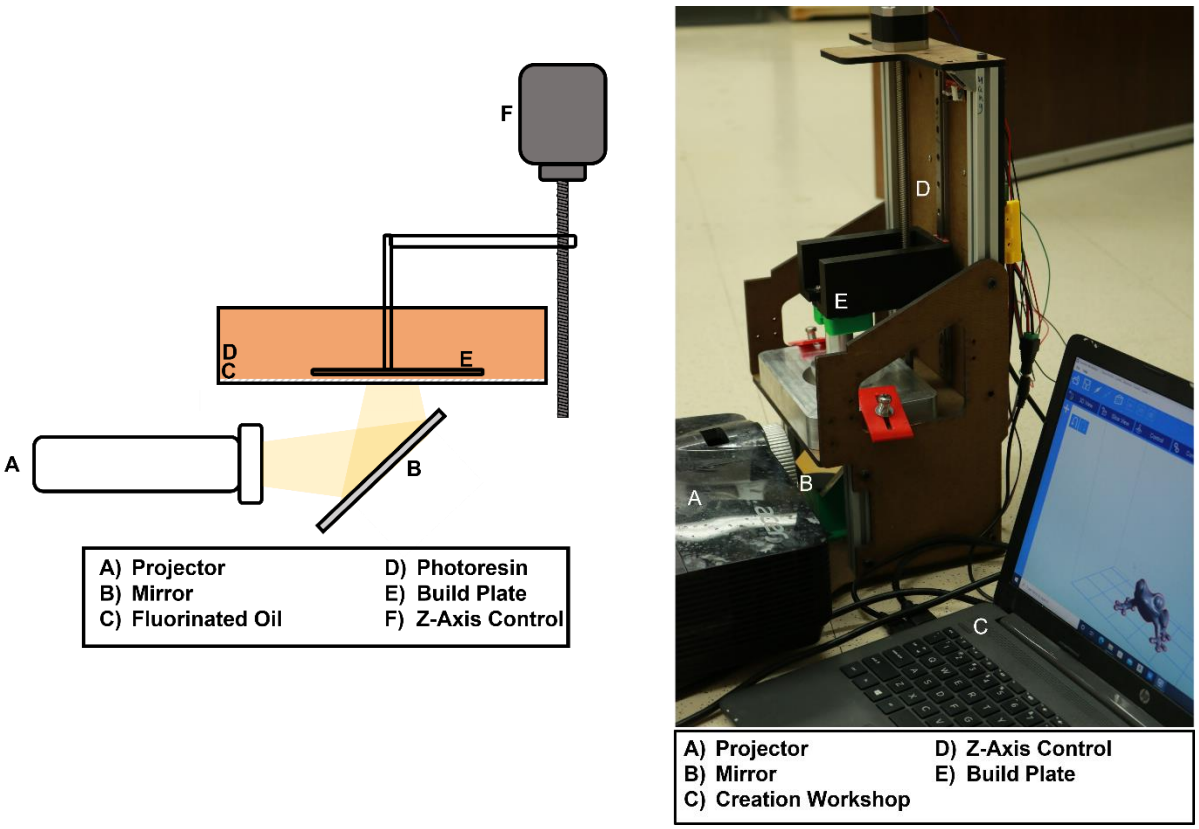

Figure A1. Left) Diagram of the bottom-up printing setup used to print parts from 4-pGA-based resins. In this system, images are projected from beneath the resin vat. Right) Actual Little RP printer setup used to print the parts from 4-pGA-based resins along with the Creation Workshop program used to control the printer.

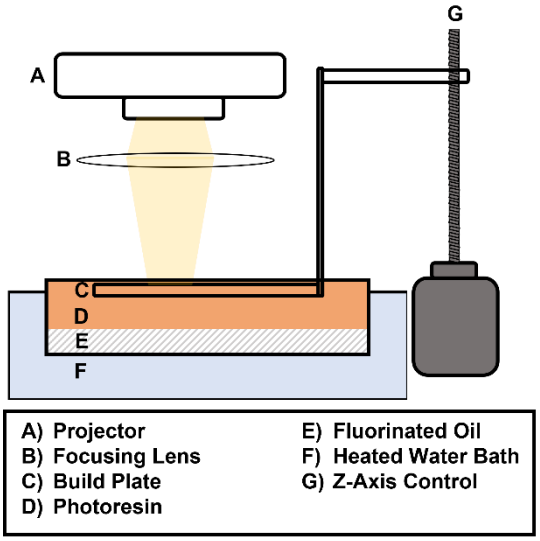

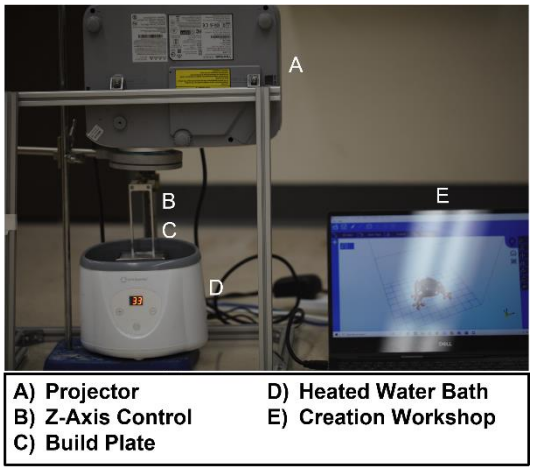

Figure A2. Left) Diagram of the top-down printing setup used to print parts from SMA-based resins. In this system, images are projected from above the resin vat. Right) Actual Little RP printer setup used to print the parts from SMA-based resins along with the Creation Workshop program used to control the printer.

To determine cure times, a simple test was used to sequentially illuminate squares within liquid resin. Each square could be assigned an individual illumination time and intensity. Upon washing with isopropyl alcohol, a pattern was left indicating which exposures were sufficient to solidify material. The shortest time displaying solid material was used for layer times, while double this time was used for bottom layers of objects to ensure adhesion to the build plate.

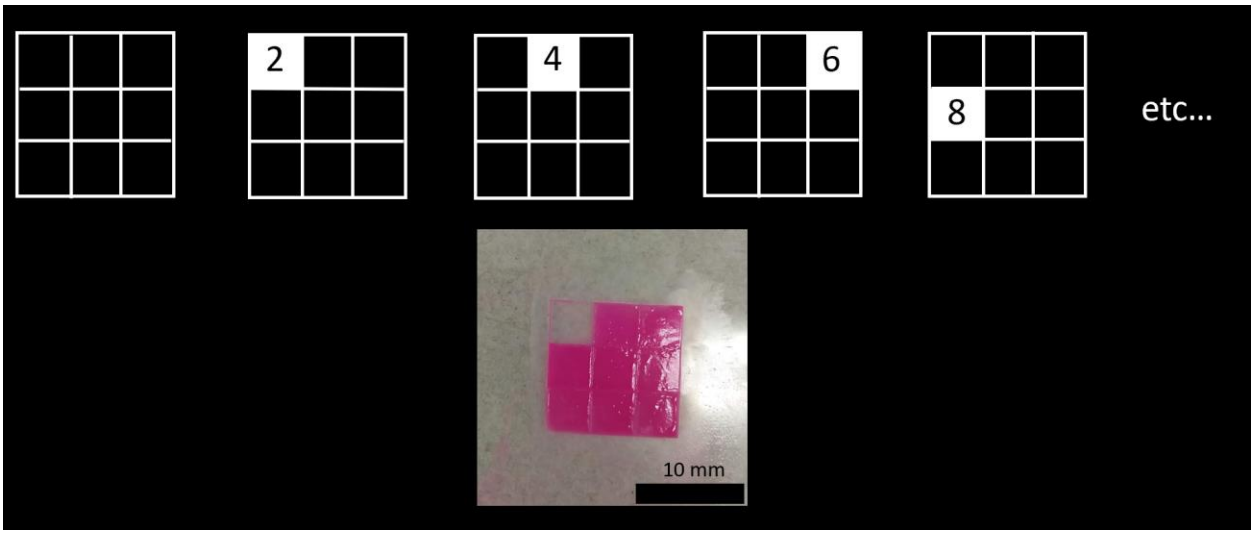

Figure A3. Example of the method for determining print parameters. Sequential images of a grid are projected for increasing amounts of time (example 2, 4, 6, 8 s). An example of the resulting part from this simple test is shown. In this example, a cure time of 4 s per layer and 8 s for bottom layers would be used for printing objects with this resin.

Table A1A. Compilation of the print parameters used to print each resin via our custom print setups.

Resin	4-pGA (wt %)[a]	LA (wt %)[a]	SA (wt %)[a]	Bottom Layer Time (s)	Number of Bottom Layers	Normal Exposure Time (s)	Layer Height (mm)
4-pGA-1	91	9	0	20	5	10	0.1
4-pGA-2	83	17	0	24	5	12	0.1
4-pGA-3	66	34	0	50	5	25	0.1
4-pGA-4	50	50	0	60	5	30	0.1
4-pGA-5	25	50	25	70	5	35	0.1
4-pGA-6	60	10	30	50	5	25	0.1

[a]Weight percent of monomer component. [*]All resins contained 0.04 wt % 4-pG as inhibitor and 0.2 wt % Irg 819 as photoinitiator relative to the total monomer weight.

Table A1B. Compilation of the print parameters used to print each resin via our custom print setups.

Resin	SMA (wt %)[a]	LMA (wt %)[a]	Irg 819 (wt %)[b]	Bottom Layer Time (s)	Number of Bottom Layers	Normal Exposure Time (s)	Layer Height (mm)
SMA-1	100	0	0.2	28	5	14	0.1
SMA-2	50	50	0.2	70	5	35	0.1
SMA-3	100	0	1	10	5	5	0.1

[a]Weight percent of monomer component. [b] Weight percent relative to total monomer components.

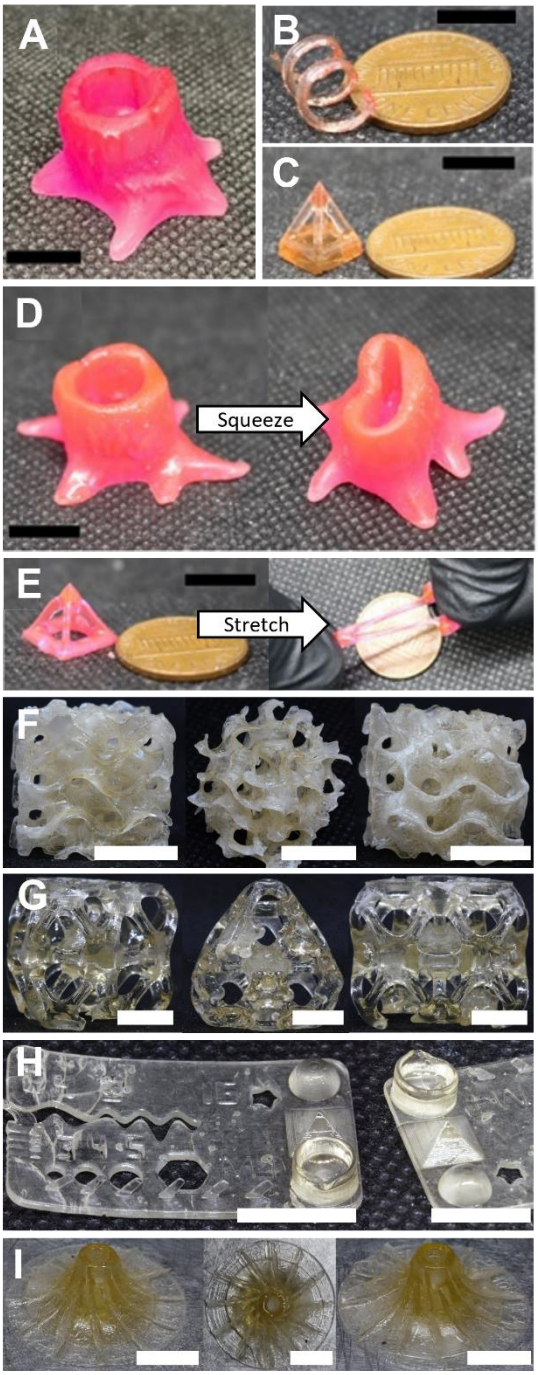

Figure A4. Images of 3D-printed parts from 4-pGA-3, SMA-1, and SMA-3 resins. Colored samples contain Nile red. Scale bars = 10 mm in each image. A) Tree stump printed from SMA-1. B) Printed helix from SMA-1. C) Printed pyramid from SMA-1. D) Tree stump printed from pGA-3 resin as-printed and squeezed. E) As-printed pyramid and stretched pyramid from 4-pGA-3. F) Several angles of a printed gyroid from SMA-3. G) Several angles of a printed octet truss from SMA-3. H) Common testing print with zoomed in half sphere, pyramid, and inset half sphere from SMA-3. I) Several angles of a printed impeller from SMA-3.

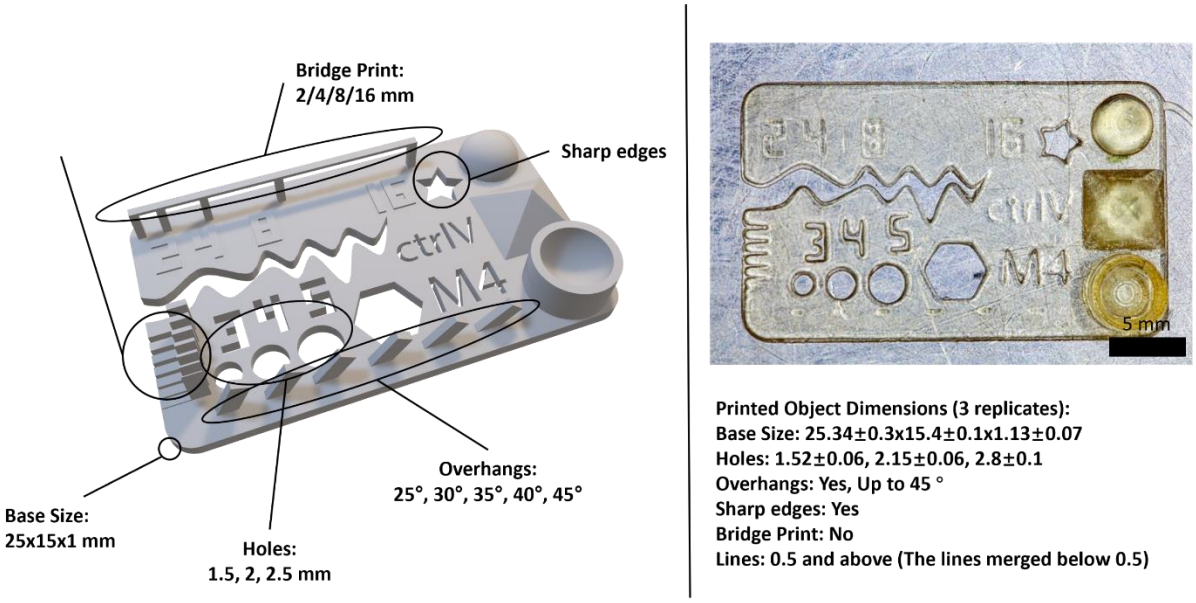

Figure A5. Left) Printed test object with the features, their dimensions, and qualitative elements indicated. Right) Image of a printed object along with measured feature dimensions across 3 replicates and qualitative assessment of additional features.

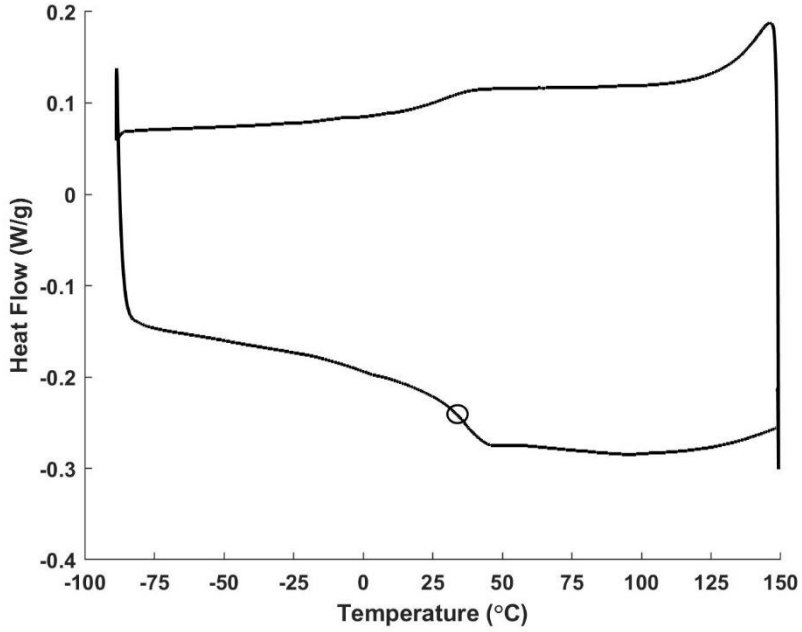

Figure A6A First cooling and second heating from DSC experiment with a heating and cooling rate of 10 °C/min for a 4-pGA homopolymer prepared with 0.2 wt% Irg 819 and exposed to UV light. Only a single T_g was observed at 38 °C.

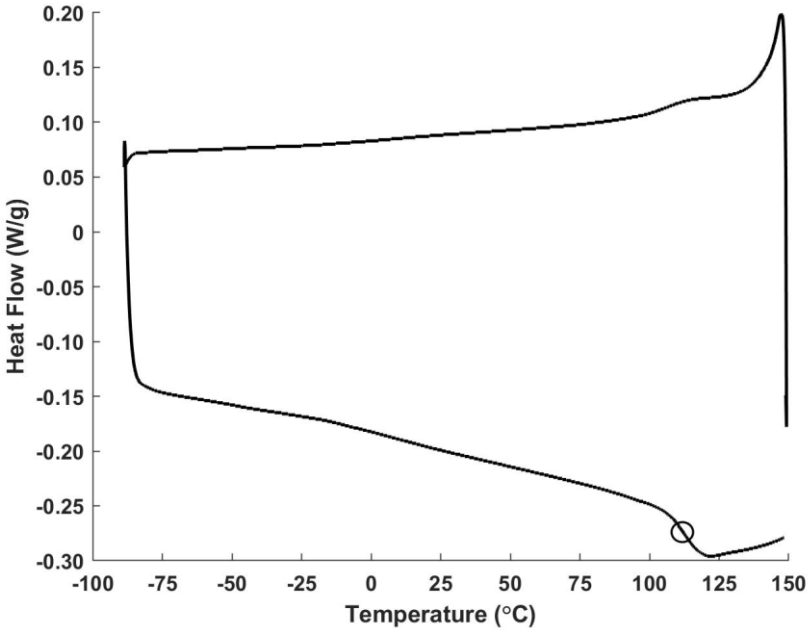

Figure A6B. First cooling and second heating from DSC experiment with a heating and cooling rate of 10 °C/min for a SA homopolymer prepared with 0.2 wt% Irg 819, exposed to UV light, and postcured at 140 °C. Only a single T_g was found at 113 °C.

Fox Equation

$$\frac{1}{T_g} = \frac{w_1}{T_{g,1}} + \frac{w_2}{T_{g,2}} \ldots \qquad eq.A1$$

Where T_g is the glass transition temperature for the resulting polymer, w_1 and w_2 are the weight fractions of each monomer component, and $T_{g,1}$ and $T_{g,2}$ are glass transitions for the homopolymers of each component.

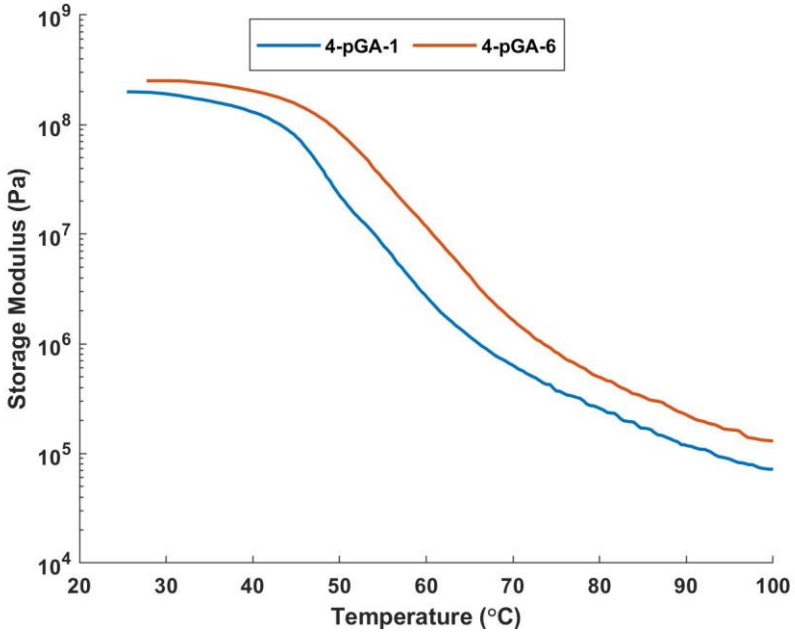

Figure A7. DMA data for parts printed from 4-pGA-1 and 4-pGA-6 resins. Data were obtained with 0.03 strain, 1 Hz frequency, and a 3 ℃/min heating rate.

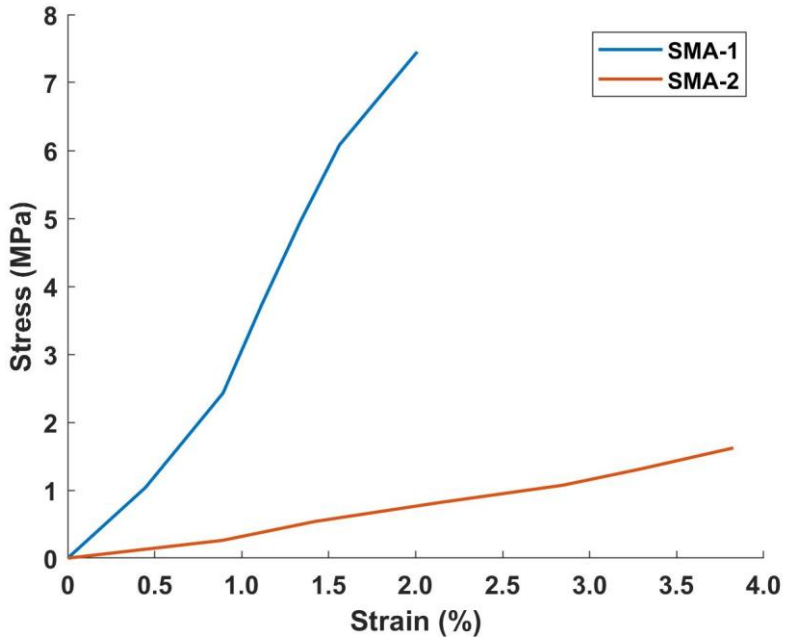

Figure A8. Representative tensile stress-strain curves for samples produced from SMA-1 and SMA-2 resins that were postcured at 40 °C for 1 h. Five replicates were performed at a strain rate of 10 mm/min.

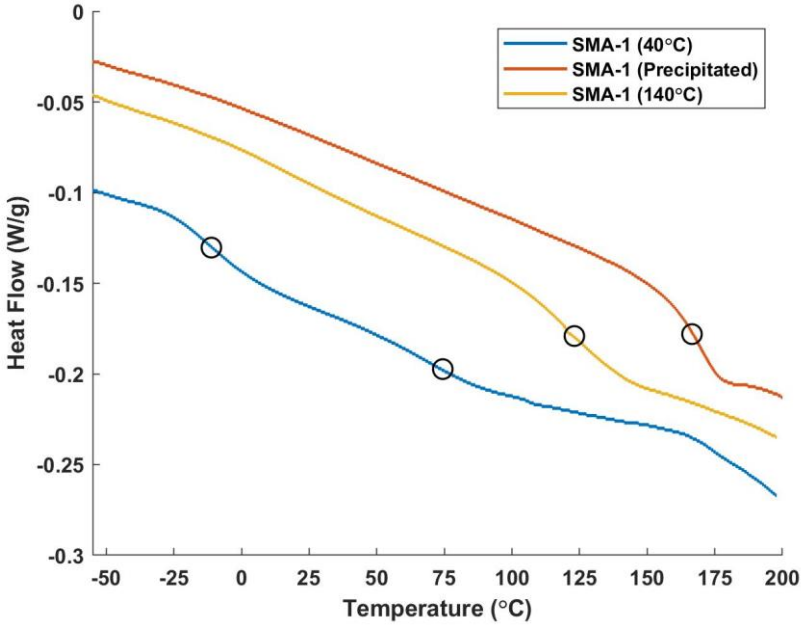

Figure A9. Second heating from DSC experiment with a heating and cooling rate of 10 °C/min for samples printed from SMA-1 resin. SMA-1 (40 °C) was postcured for 1 h at 40 °C and shows multiple glass transitions indicative of an undercured sample and plasticization. SMA-1(Precipitated) is the high molecular weight portion of the SMA-1 (40 °C) sample obtained by dissolving SMA-1 (40 °C) in dichloromethane and precipitating the polymer in excess 0 °C methanol. A single T_g of 166 °C was observed. To obtain better cured parts, samples printed from SMA-1 resin were postcured for 1 h at 140 °C (SMA-1 (140 °C)). A single T_g of 122 °C was observed. DSC curves have been shifted vertically for clarity.

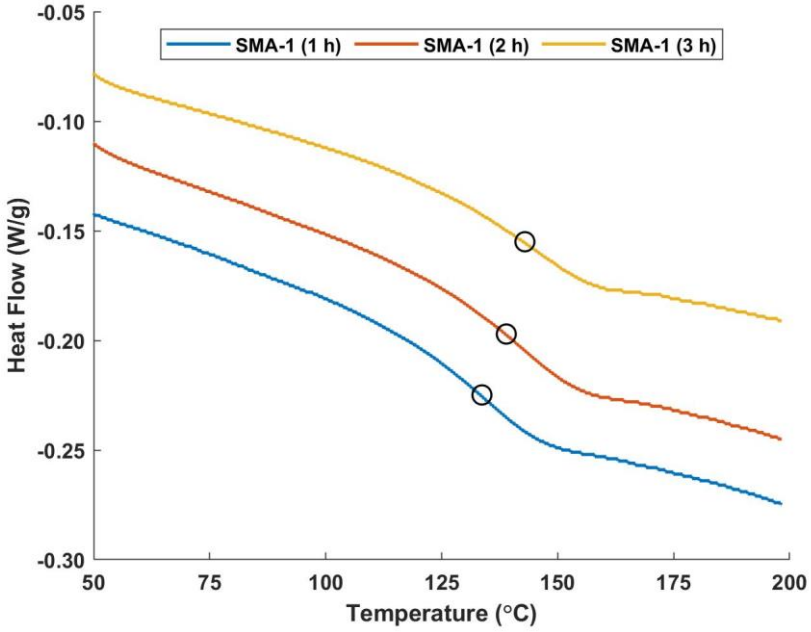

Figure A10. Second heating from DSC experiment with a heating and cooling rate of 10 °C/min for samples printed from SMA-1 resin that had been postcured at 140 °C for 1, 2, and 3 h. Only small shifts in the T_g were observed from increasing post-cure time. DSC curves have been shifted vertically for clarity.

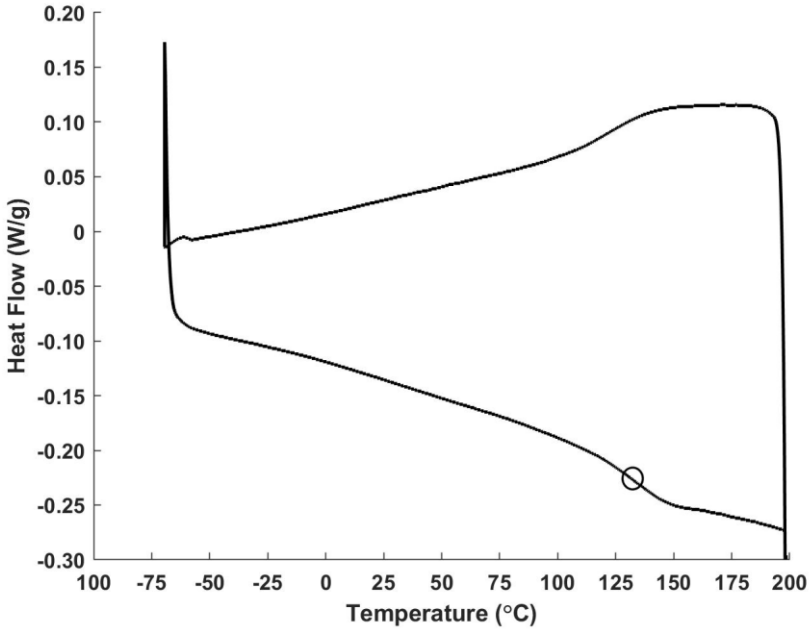

Figure A11. First cooling and second heating from DSC experiment with a heating and cooling rate of 10 °C/min for samples printed from SMA-3 resin that had been postcured at 140 °C for 1 h. Only a single T_g was observed at 132 °C. No crystallization is observed upon cooling.

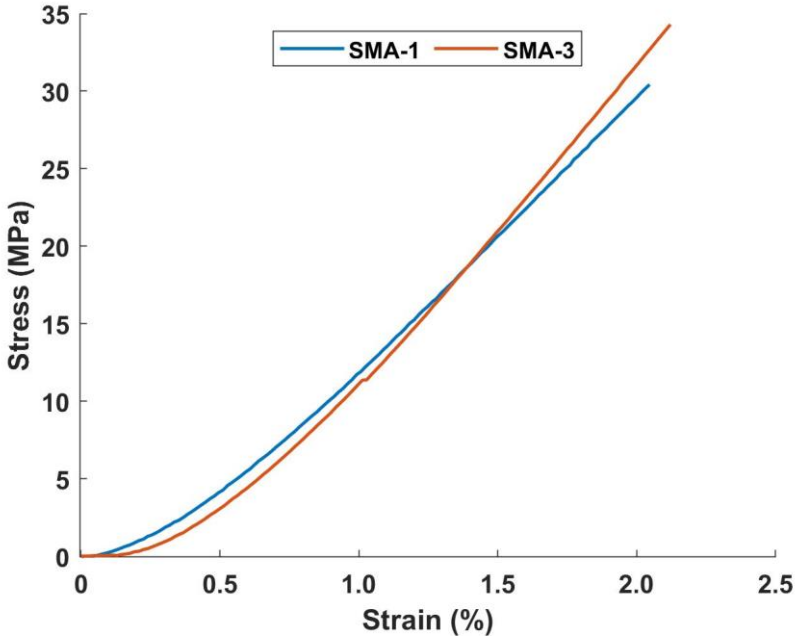

Figure A12. Representative compressive stress-strain curves for samples produced from SMA-1 and SMA-3 resins each postcured at 140 °C for 1 h. Five replicates were performed at a compressive strain rate of 1 mm/min.

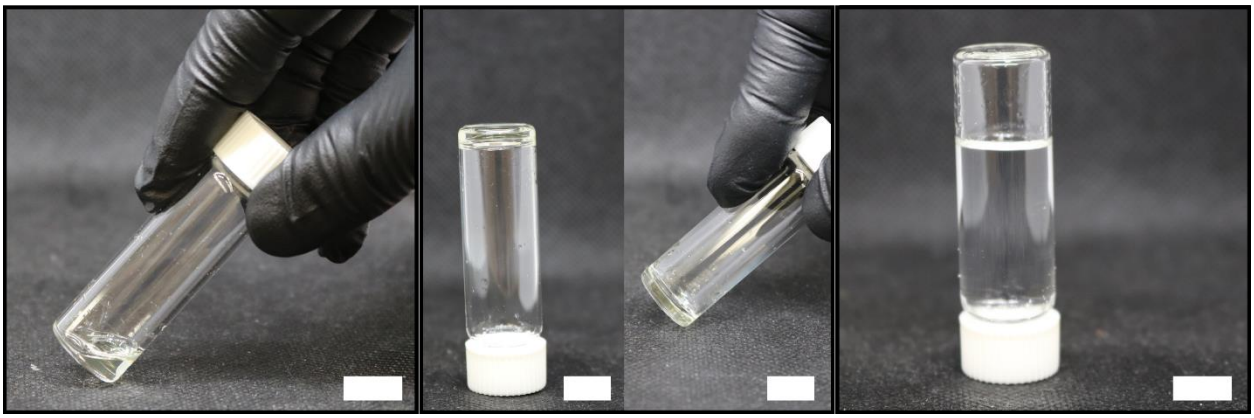

Figure A13A. Left) Liquid 4-pGA-3 resin prior to light exposure. Middle) 4-pGA-3 resin after light exposure held upside down and at an angle. The resin solidified and no longer flowed. Right) Solidified resin after being dissolved in dichloromethane. It no longer adhered to the bottom of the vial and dissolved in solvent. Scale bars indicate 10 mm in each image.

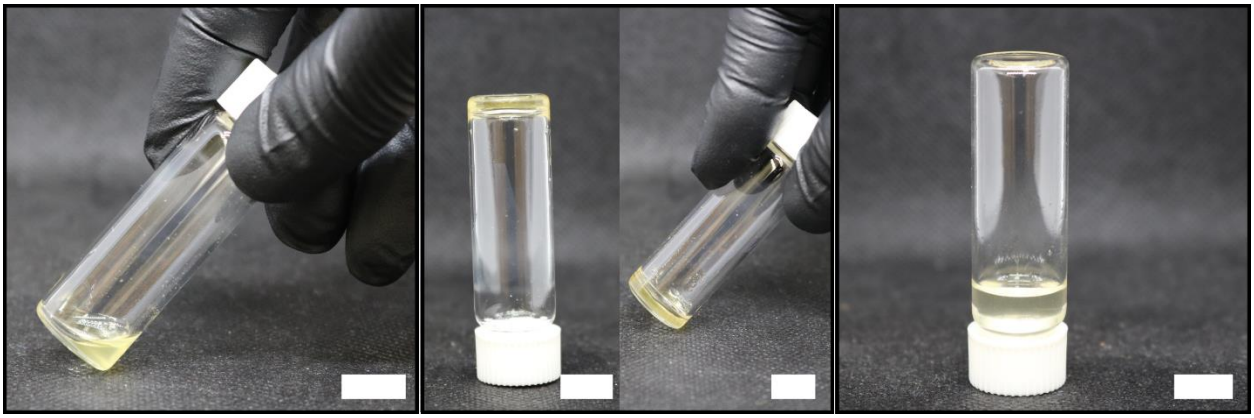

Figure A13B. Left) Liquid SMA -3 resin prior to light exposure Middle) SMA-3 resin after light exposure held upside down and at an angle. The resin solidified and no longer flowed. Right) Solidified SMA-3 resin after being dissolved in dichloromethane. It no longer adhered to the bottom of the vial and dissolved in solvent. Scale bars indicate 10 mm in each image.

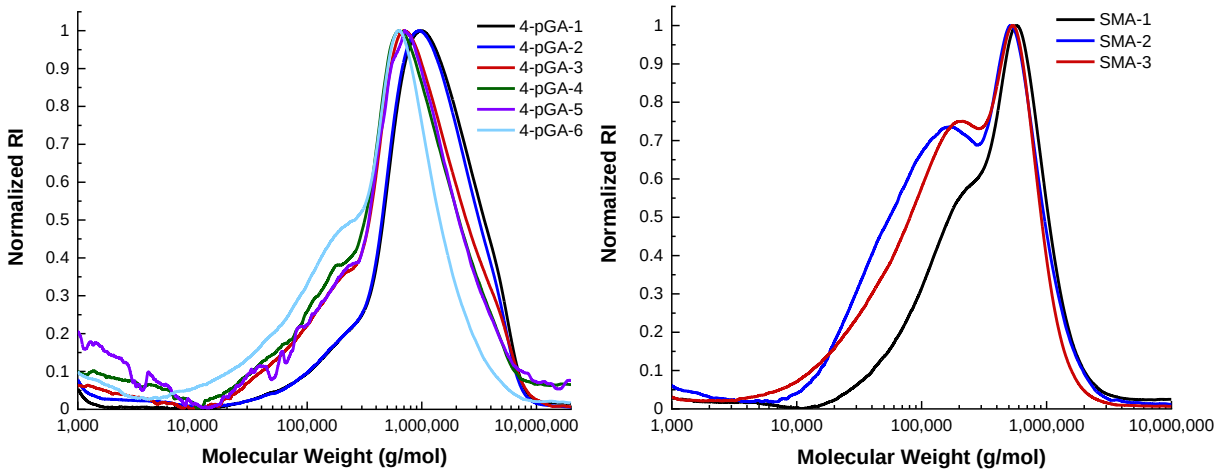

Figure A14a. Molecular weight distributions of printed parts were measured by SEC using chloroform as the effluent and polystyrene standards for calibration. Chromatograms showing the normalized refractive index detector response vs. log_{10}(molecular weight) are shown below for 4-pGA and SMA prints, respectively. Tabular molecular weight data are shown in Table 3 in the main text.

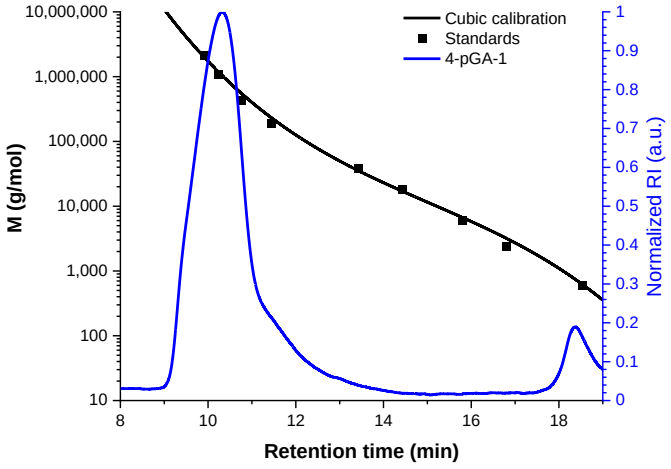

Figure A14b. Chromatogram of 4-pGA-1 with the retention times of polystyrene standards and the cubic calibration curve.

Note: In our initial study of polymer solubility, several parts from 4-pGA-based resins contained small insoluble portions upon dissolution. To investigate this phenomenon, gas chromatography-mass spectrometry (GC-MS) along with ^{1}H NMR and ^{13}C NMR spectroscopy were used to inspect starting materials for impurities. The technical-grade LA contained significant amounts of impurities. By switching to a higher purity LA (>98%), the solubility of these samples improved significantly. This result highlights the importance of monomer purity and sourcing on solubility outcomes.

Table A2. Summary of solubility results for parts printed with 4-pGA-3 and SMA-3 resins. Solubility was tested at room temperature at a concentration of 5 mg/mL. The lower purity LA was used in the 4-pGA-3 resin in this study. Solubility was assessed visually and by the ability to push solution through a 0.45 µm poly(tetrafluoroethylene) syringe filter.

	Room Temperature Solubility	
Solvent	**4-pGA-3**	**SMA-3**
Dichloromethane	Yes	Yes
Chloroform	Yes	Yes
Tetrahydrofuran	Yes	No
Toluene	Yes	No
Isopropyl Alcohol	No	No
(+/-)Limonene	Yes	No
p-Xylene	Yes	No
L-Fenchone	Yes	No

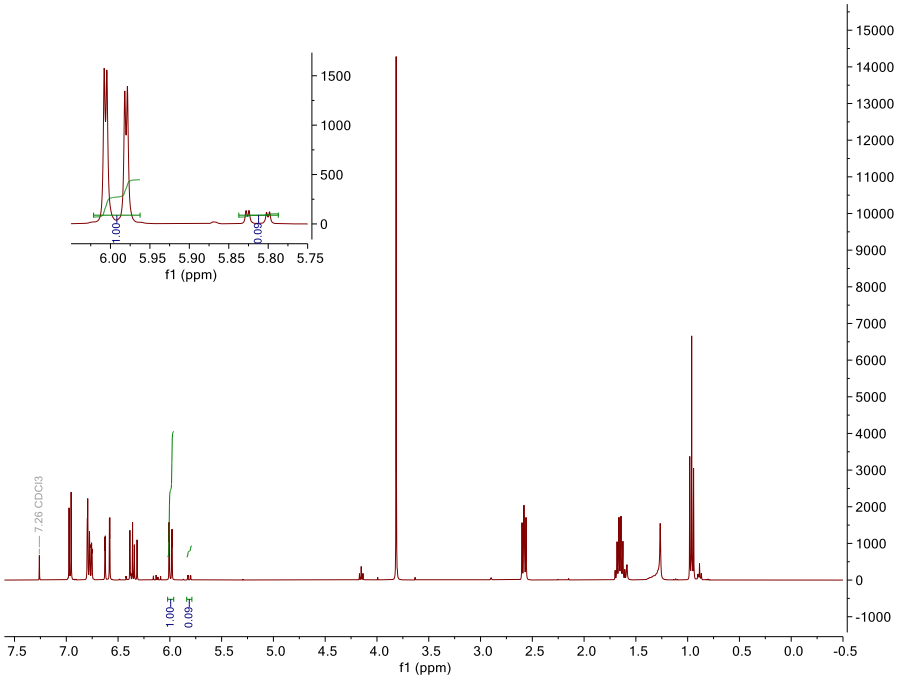

Figure A15A. ^{1}H NMR spectrum of uncured 4-pGA-1 resin before printing illustrating molar ratio of 4-pGA to LA of 1.00:0.09. Inset shows integration for the peaks used to compare monomer ratios.

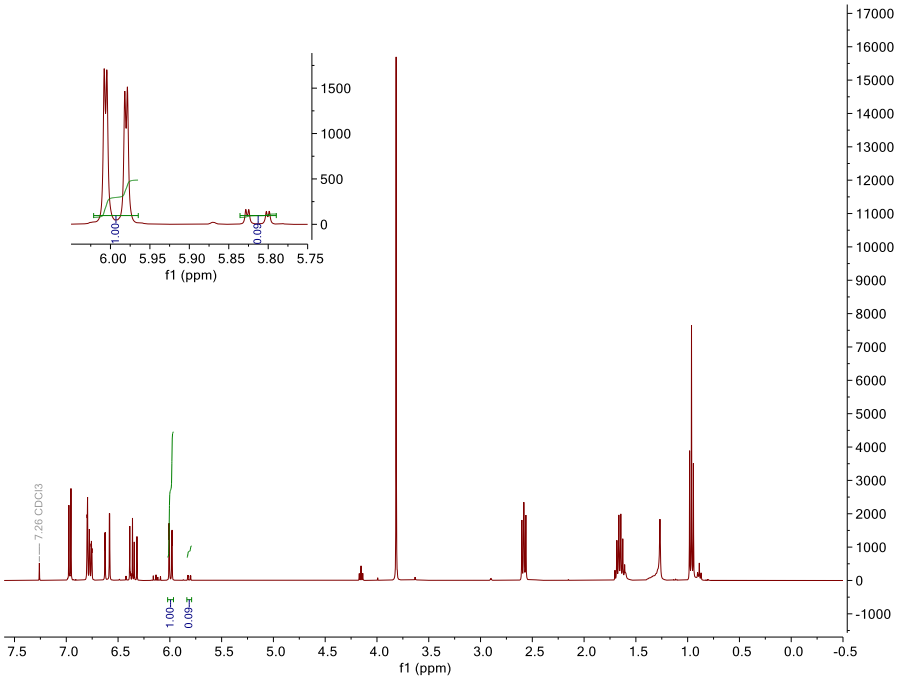

Figure A15B. ^{1}H NMR spectrum of uncured 4-pGA-1 resin after printing illustrating unchanged molar ratio of 4-pGA to LA of 1.00:0.09. Inset shows integration for the comparison peaks of interest for each monomer in the resin.

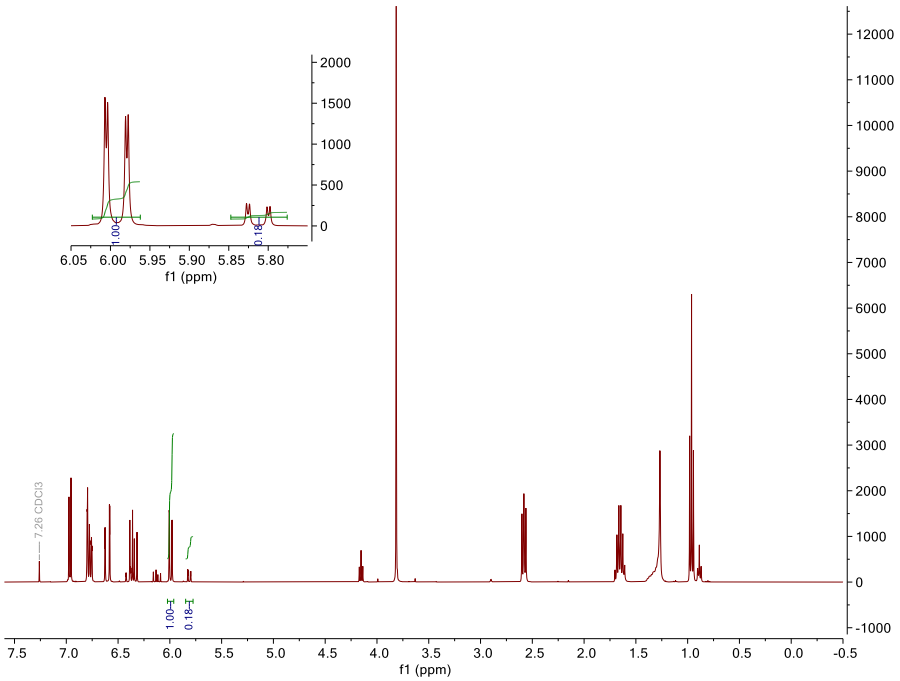

Figure A15C. ^{1}H NMR spectrum of uncured 4-pGA-2 resin before printing illustrating molar ratio of 4-pGA to LA of 1.00:0.18. Inset shows integration for the peaks used to compare monomer ratios.

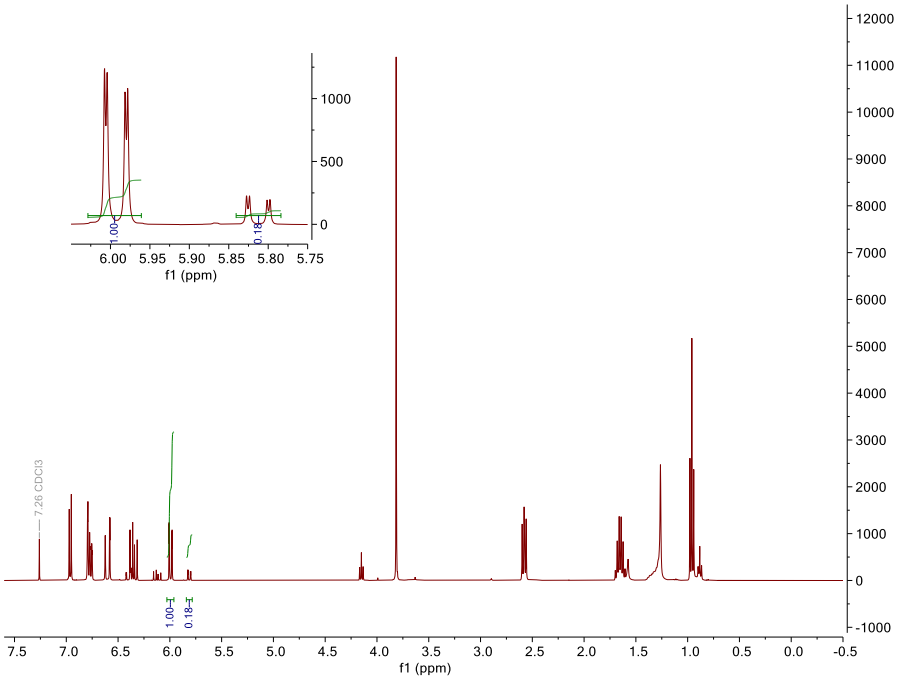

Figure A15D. ^{1}H NMR spectrum of uncured 4-pGA-2 resin after printing illustrating unchanged molar ratio of 4-pGA to LA of 1.00:0.18. Inset shows integration for the peaks used to compare monomer ratios.

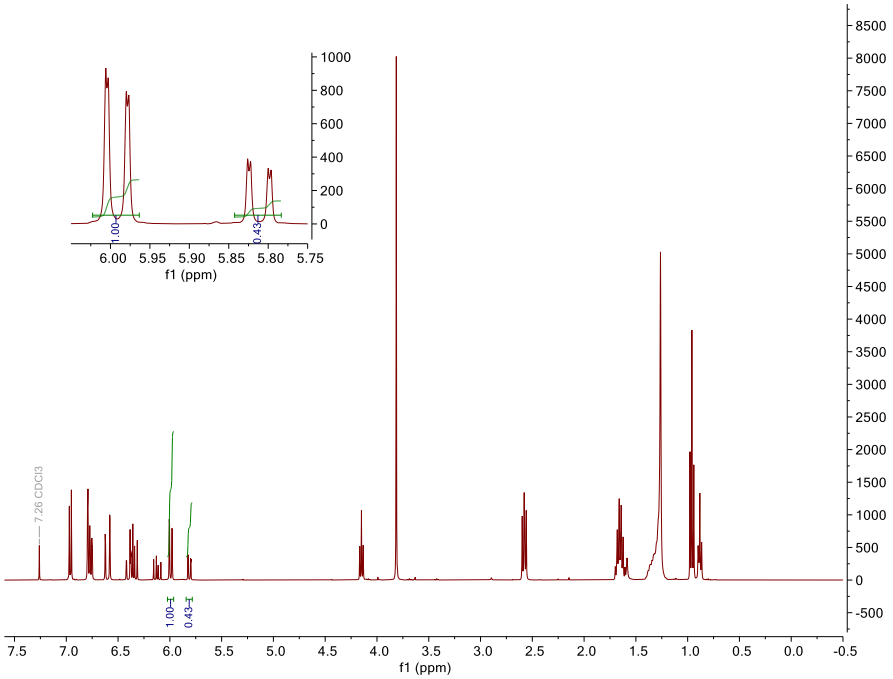

Figure A15E. ^{1}H NMR spectrum of uncured 4-pGA-3 resin before printing illustrating molar ratio of 4-pGA to LA of 1.00:0.43. Inset shows integration for the peaks used to compare monomer ratios.

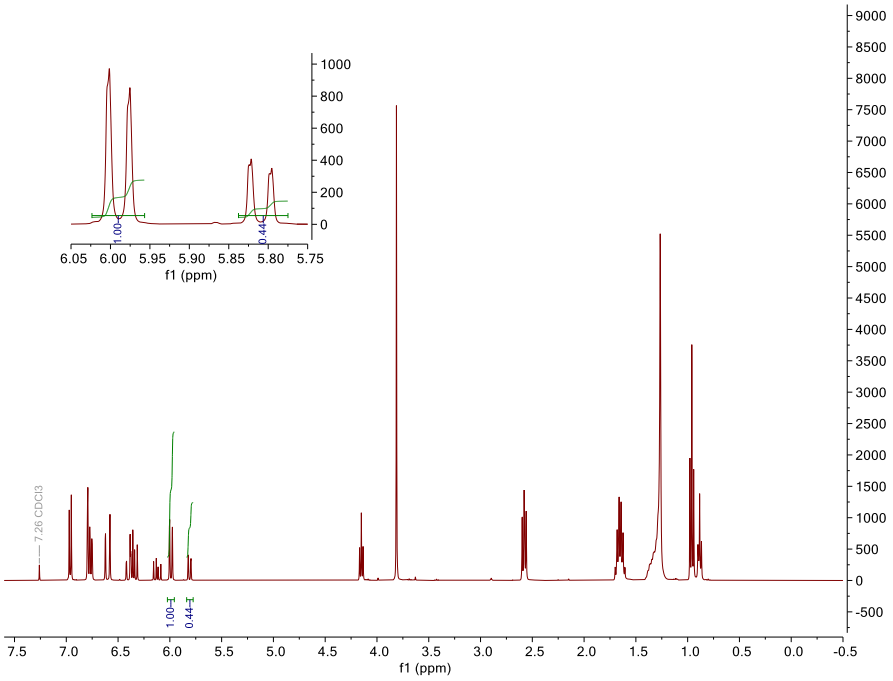

Figure A15F. ^{1}H NMR spectrum of uncured 4-pGA-3 resin after printing illustrating nearly unchanged molar ratio of 4-pGA to LA of 1.00:0.44. Inset shows integration for the peaks used to compare monomer ratios.

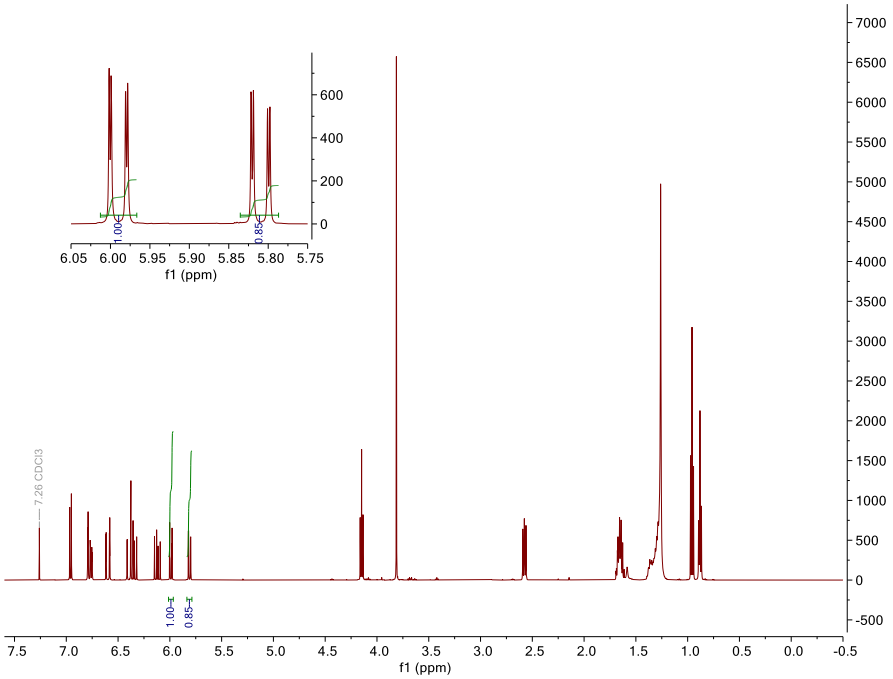

Figure A15G. ^{1}H NMR spectrum of uncured 4-pGA-4 resin before printing illustrating molar ratio of 4-pGA to LA of 1.00:0.85. Inset shows integration for the peaks used to compare monomer ratios.

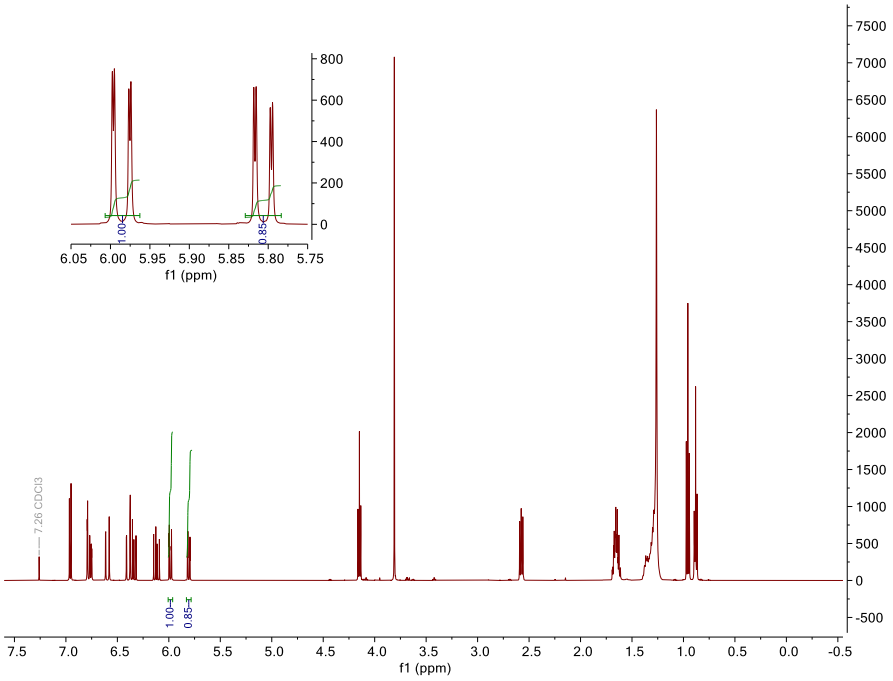

Figure A15H. ^{1}H NMR spectrum of uncured 4-pGA-4 resin after printing illustrating unchanged molar ratio of 4-pGA to LA of 1.00:0.85. Inset shows integration for the peaks used to compare monomer ratios.

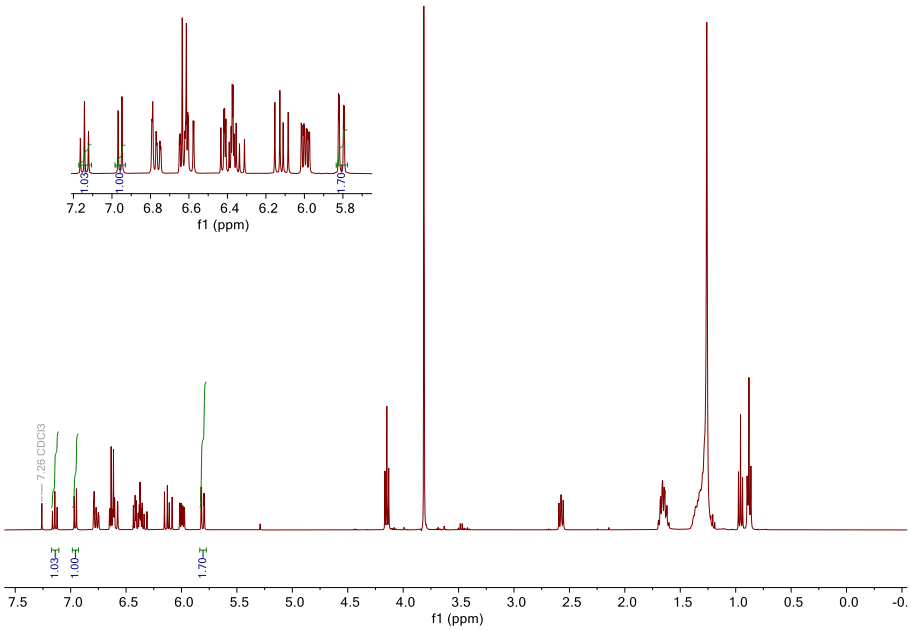

Figure A15I. ^{1}H NMR spectrum of uncured 4-pGA-5 resin before printing illustrating molar ratio of 4-pGA to LA to SA of 1.00:1.70:1.03. Inset shows integration for the peaks used to compare monomer ratios.

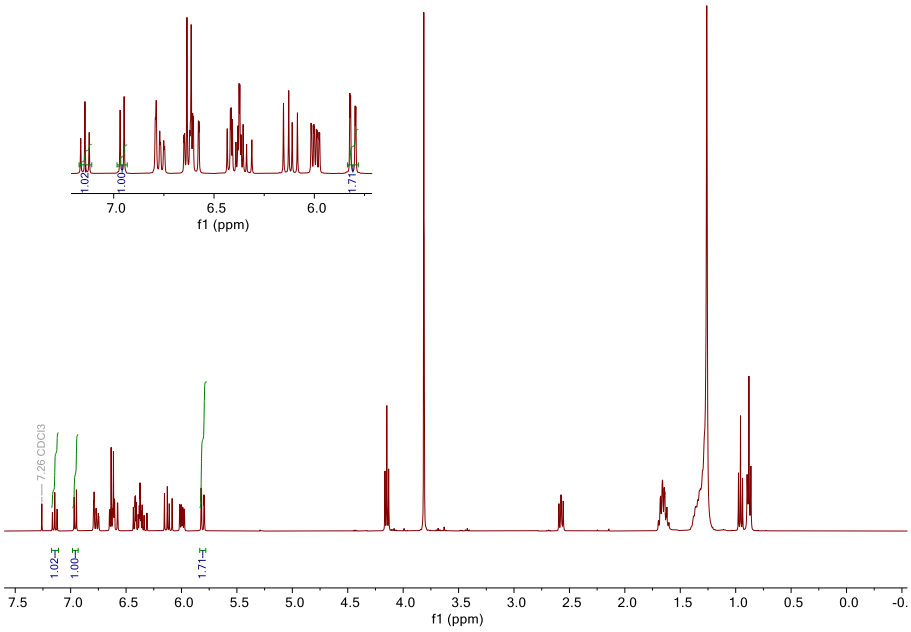

Figure A15J. ^{1}H NMR spectrum of uncured 4-pGA-5 resin after printing illustrating nearly unchanged molar ratio of 4-pGA to LA to SA of 1.00:1.71:1.02. Inset shows integration for the peaks used to compare monomer ratios.

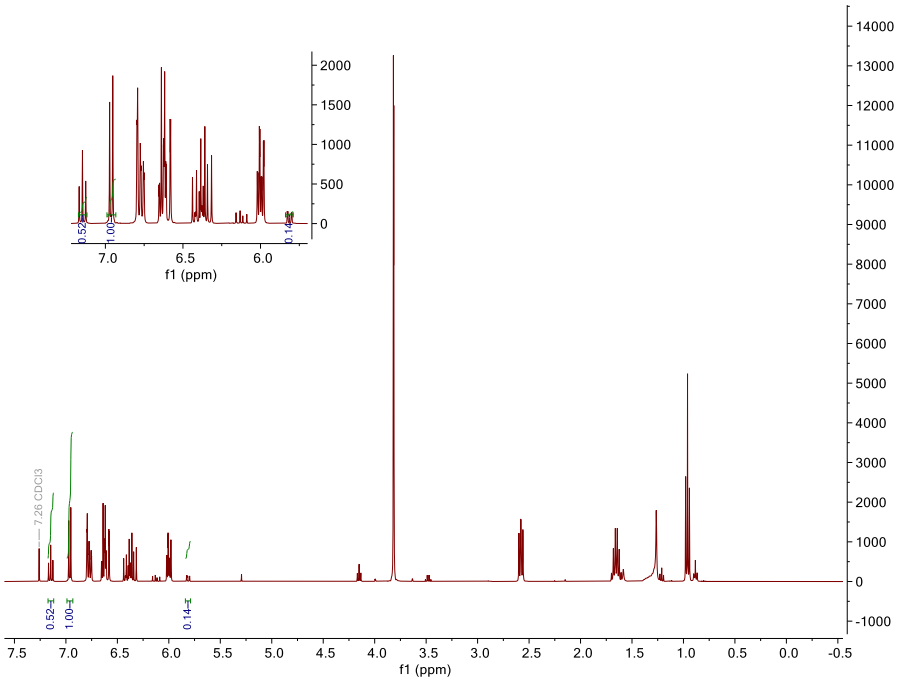

Figure A15K. ^{1}H NMR spectrum of uncured 4-pGA-6 resin before printing illustrating molar ratio of 4-pGA to LA to SA of 1.00:0.14:0.52. Inset shows integration for the peaks used to compare monomer ratios.

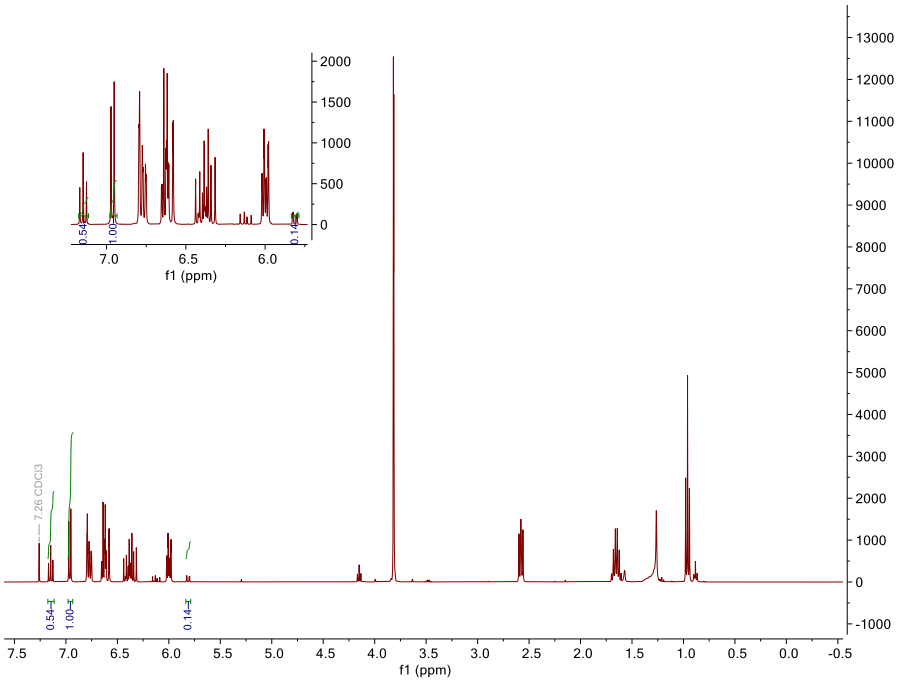

Figure A15L. ^{1}H NMR spectrum of uncured 4-pGA-6 resin after printing illustrating nearly unchanged molar ratio of 4-pGA to LA to SA of 1.00:0.14:0.54. Inset shows integration for the peaks used to compare monomer ratios.

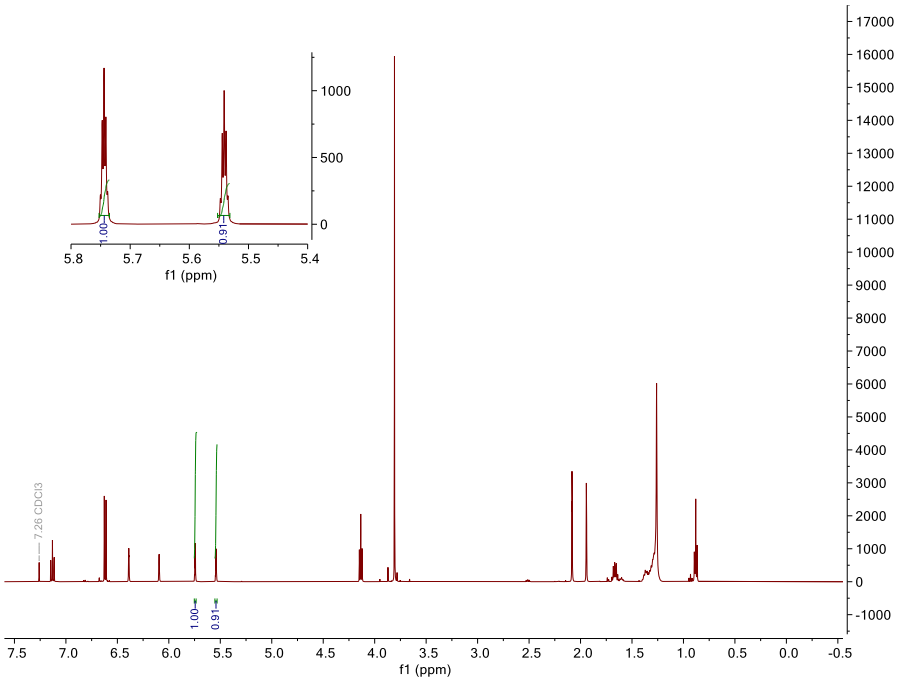

Figure A15M. [1]H NMR spectrum of uncured SMA-2 resin before printing illustrating molar ratio of SMA to LMA of 1.00:0.91. Inset shows integration for the peaks used to compare monomer ratios.

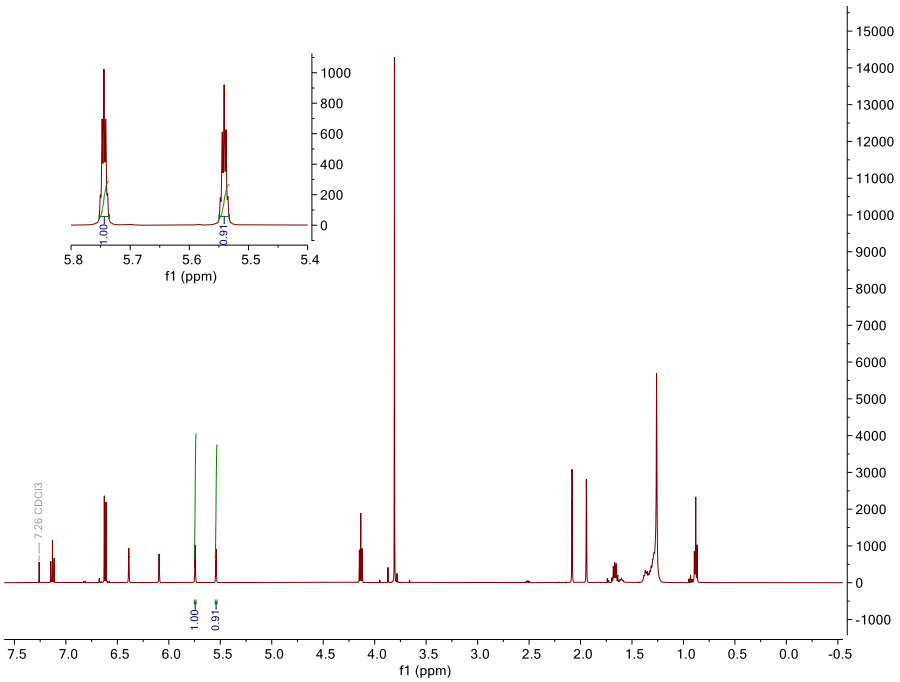

Figure A15N. [1]H NMR spectrum of uncured SMA-2 resin after printing illustrating unchanged molar ratio of SMA to LMA of 1.00:0.91. Inset shows integration for the peaks used to compare monomer ratios.

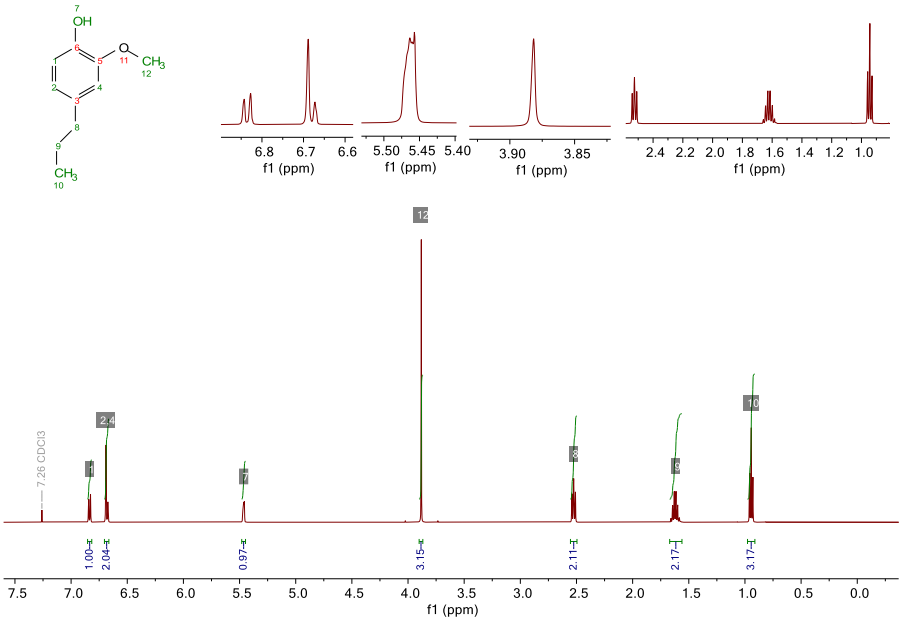

Figure A16A. [1]H NMR spectrum of commercially obtained 4-pG in $CDCl_3$. Chemical shifts and integration match with previous literature reports.[1]

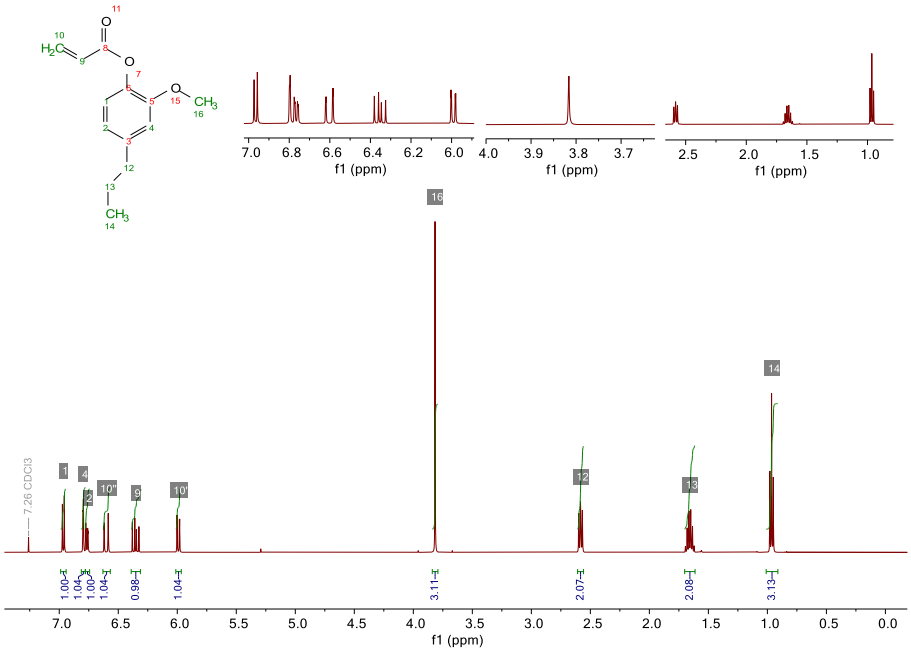

Figure A16B. [1]H NMR spectrum of synthesized 4-pGA in $CDCl_3$. Chemical shifts and integration match with previous literature reports.[2]

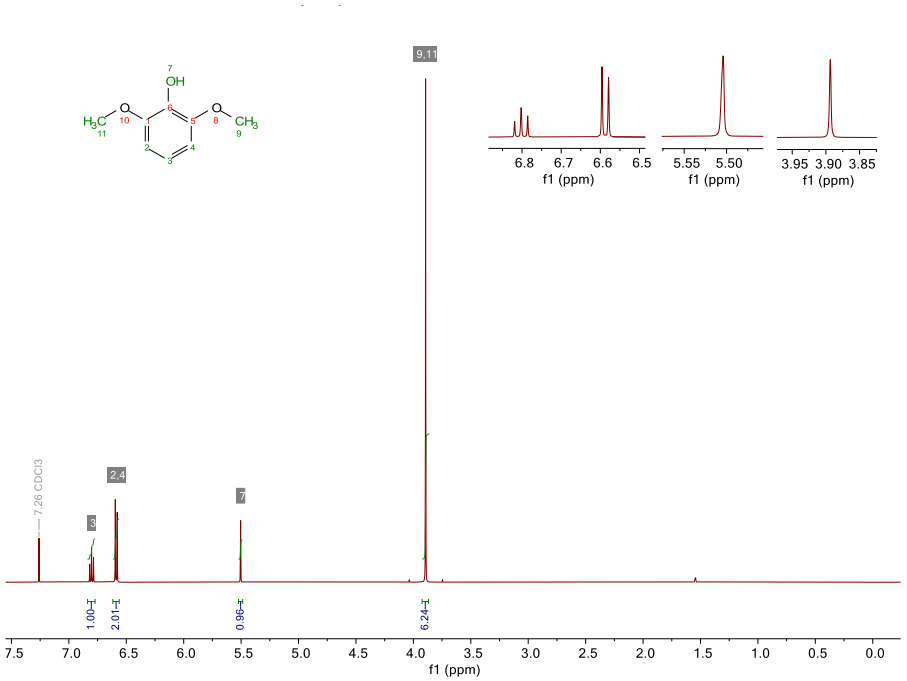

Figure A16C. ^{1}H NMR spectrum of commercially obtained syringol in $CDCl_3$. Chemical shifts and integration match with previous literature reports.[3]

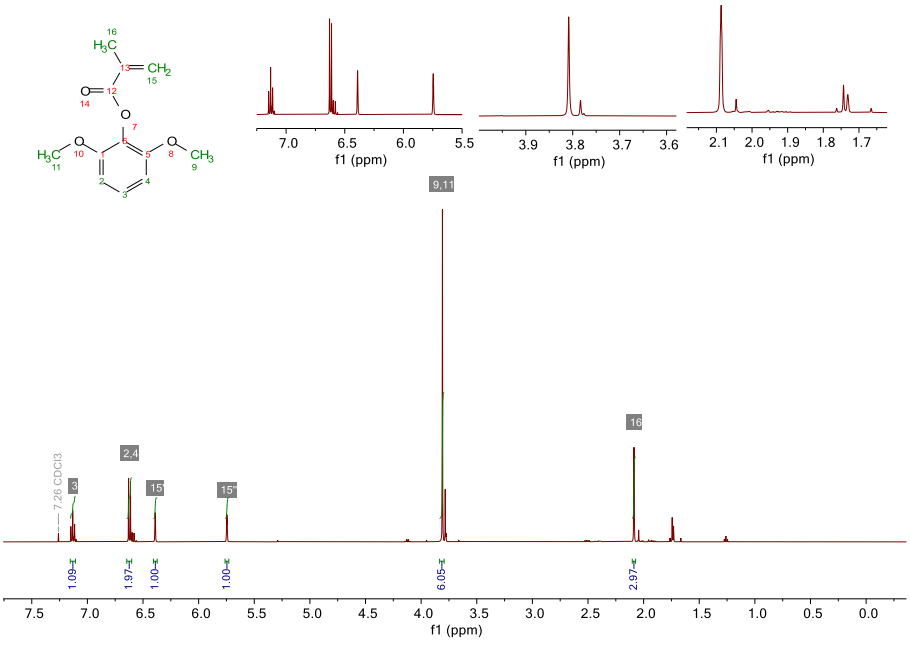

Figure A16D. ^{1}H NMR spectrum of synthesized SMA in $CDCl_3$. Small amounts of ethyl acetate and an unidentified impurity remained in the resin. Chemical shifts and integration match with previous literature reports.[4]

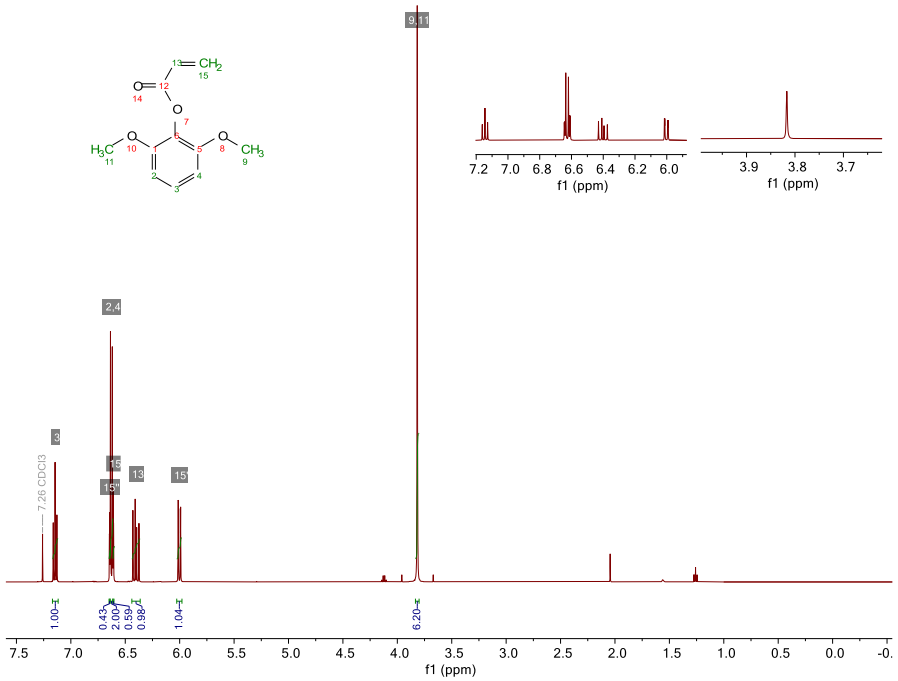

Figure A16E. [1]H NMR spectrum of synthesized SA in $CDCl_3$. A small amount of ethyl acetate remained in the resin. Chemical shifts and integration match with previous literature reports.[5]

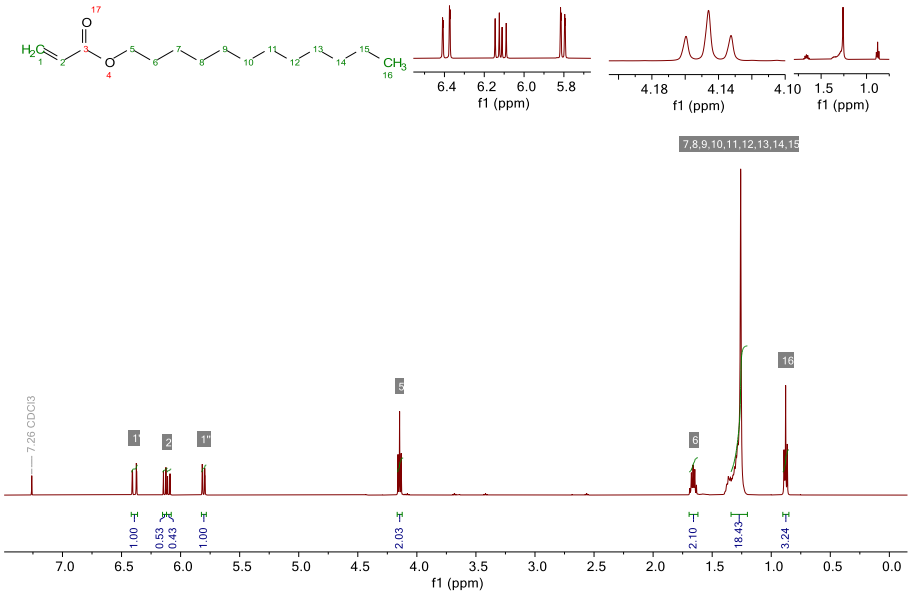

Figure A16F. [1]H NMR spectrum of the lower purity commercially obtained LA in $CDCl_3$. A small amount of an unidentified impurity was present in the commercially-sourced monomer.[6]

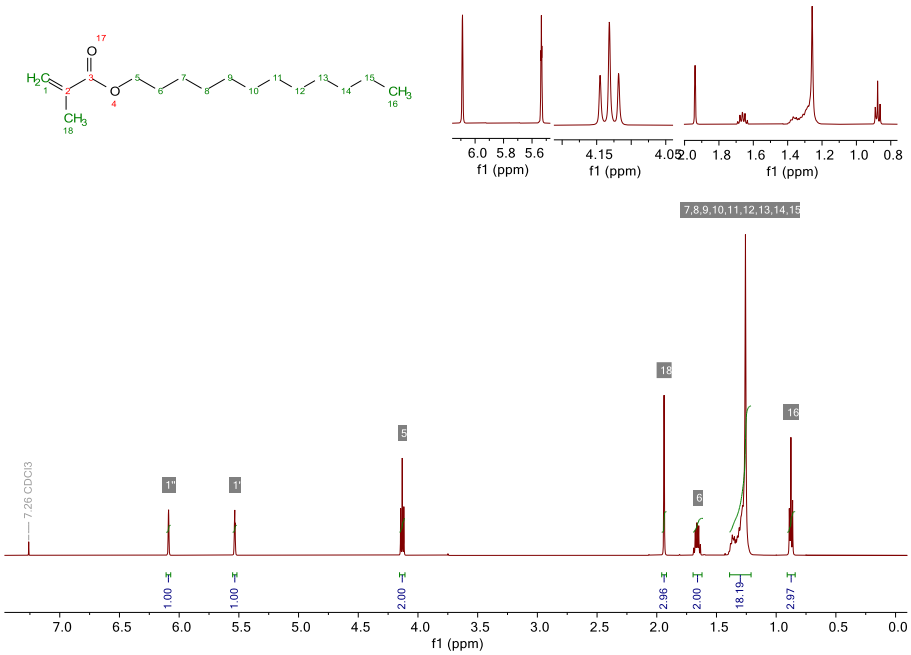

Figure A16G. ^{1}H NMR spectrum of commercially obtained LMA in $CDCl_3$. Chemical shifts and integration match with manufacturing specifications.[7]

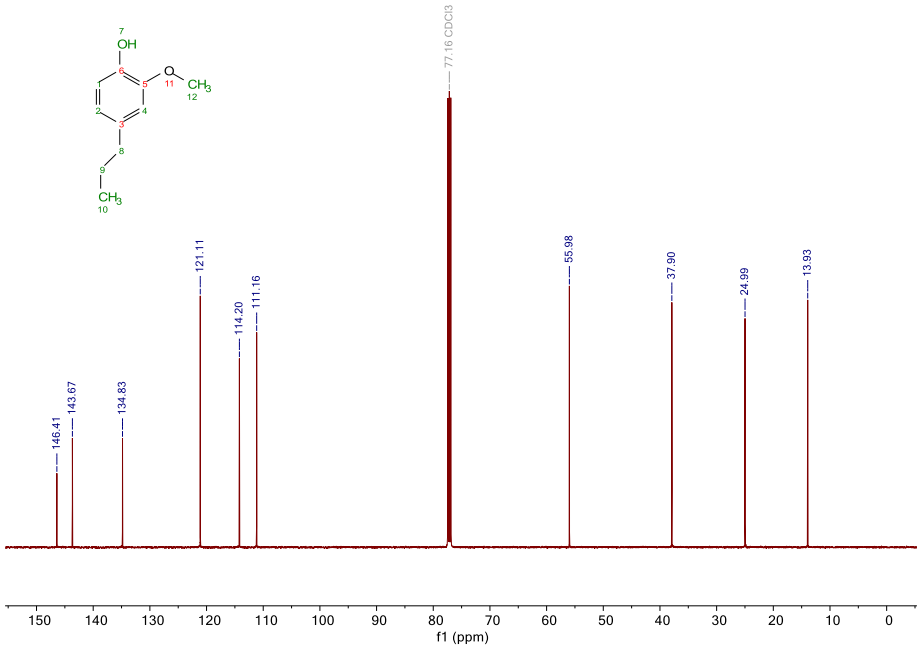

Figure A17A. ^{13}C NMR spectrum of 4-pG in $CDCl_3$. Chemical shifts match with previous literature reports.[1]

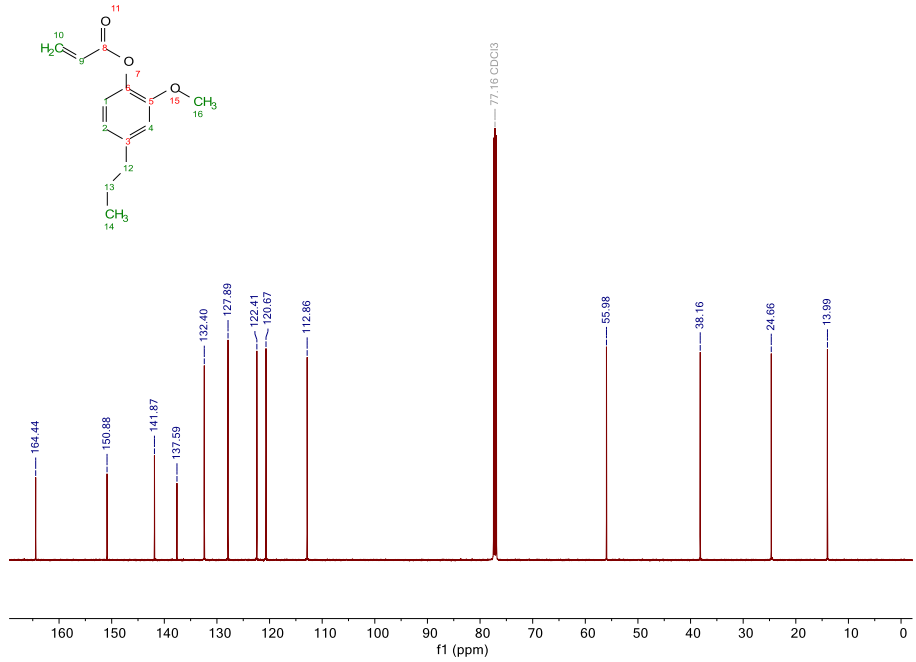

Figure A17B. ^{13}C NMR spectrum of synthesized 4-pGA in $CDCl_3$. Chemical shifts match with previous literature reports.[2]

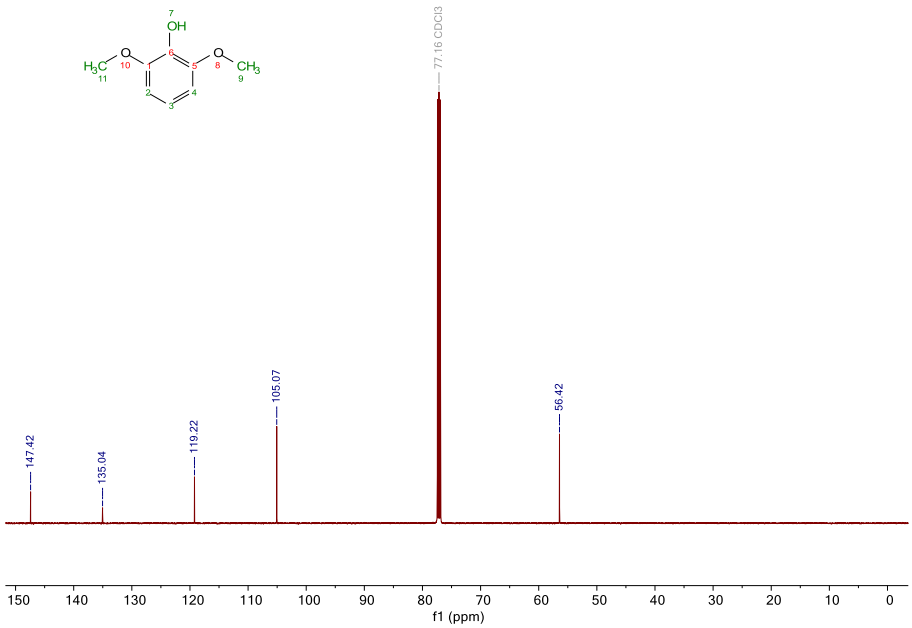

Figure A17C. ^{13}C NMR spectrum of syringol in $CDCl_3$. Chemical shifts match with previous literature reports.[3]

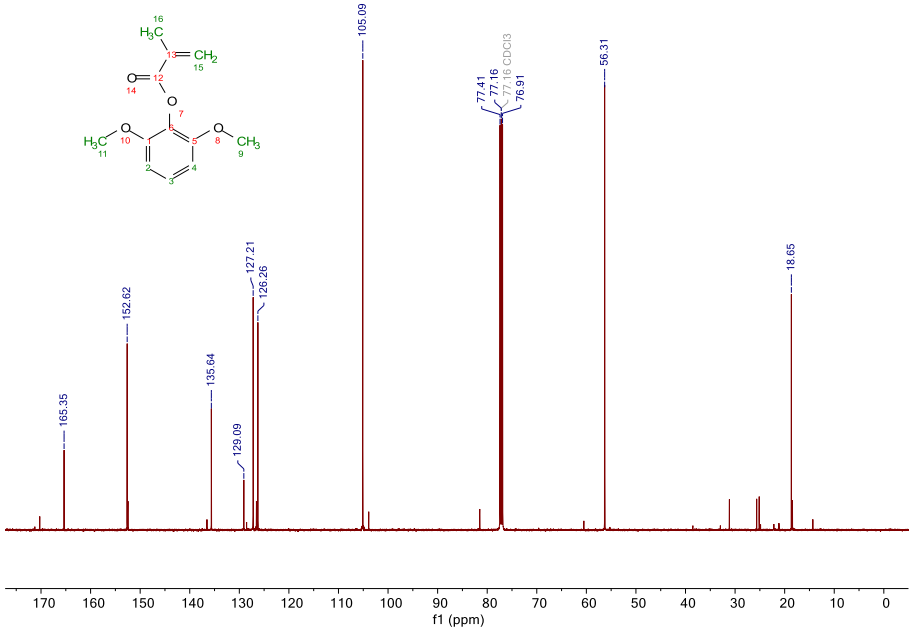

Figure A17D. ^{13}C NMR spectrum of synthesized SMA in $CDCl_3$. A small amount of an unidentified impurity was present. Chemical shifts match with previous literature reports.[4]

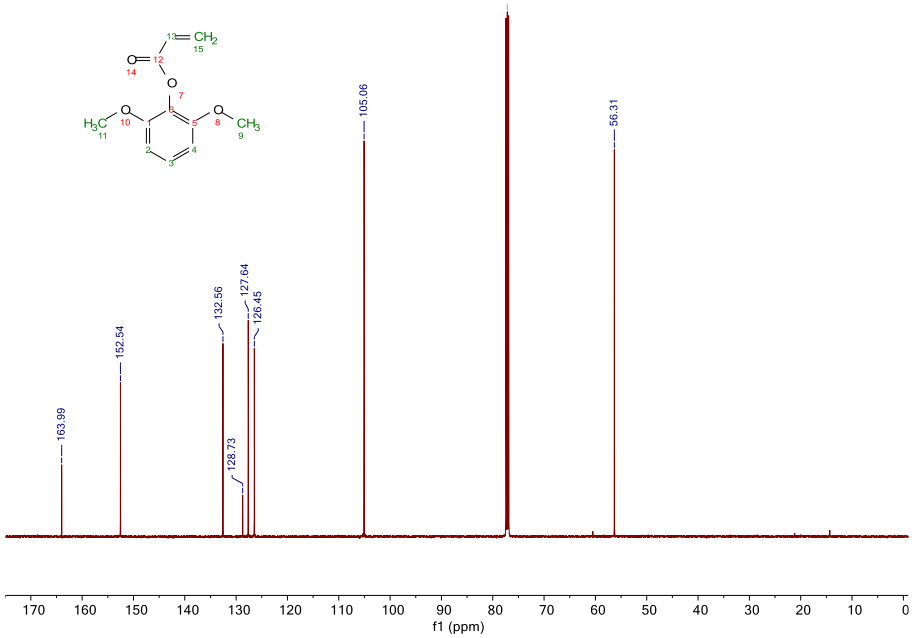

Figure A17E. ^{13}C NMR spectrum of synthesized SA in $CDCl_3$. Chemical shifts match with previous literature reports.[5]

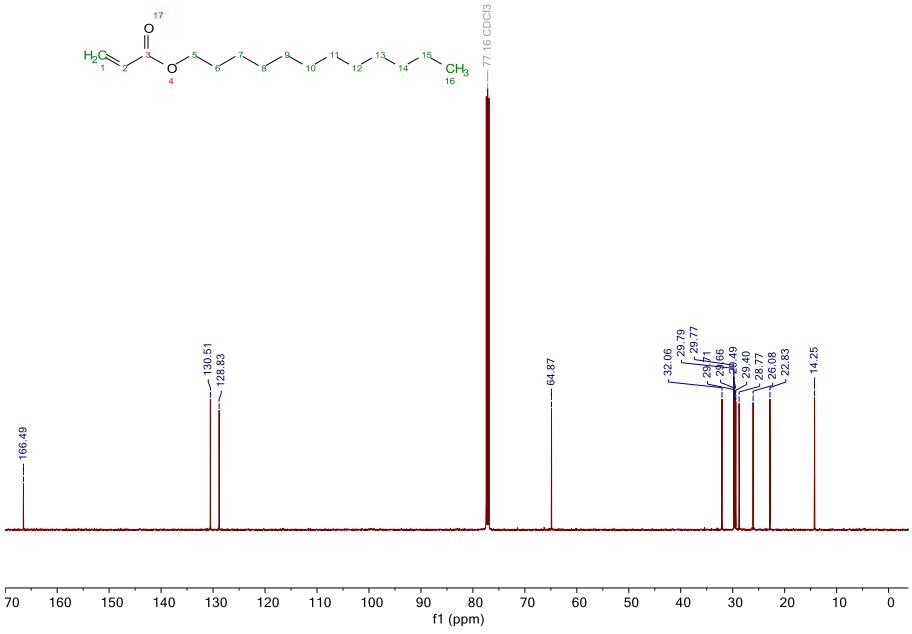

Figure A17F. ^{13}C NMR spectrum of the lower purity LA in $CDCl_3$. Chemical shifts match with previous literature reports. [6]

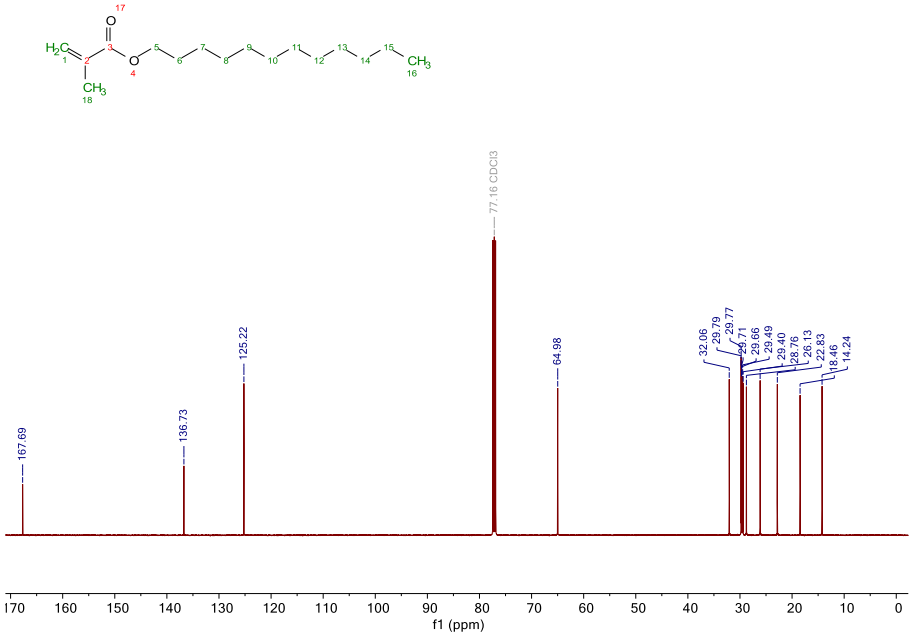

Figure A17G. ^{13}C NMR spectrum of LMA in $CDCl_3$. Chemical shifts match with manufacturing specifications.[7]

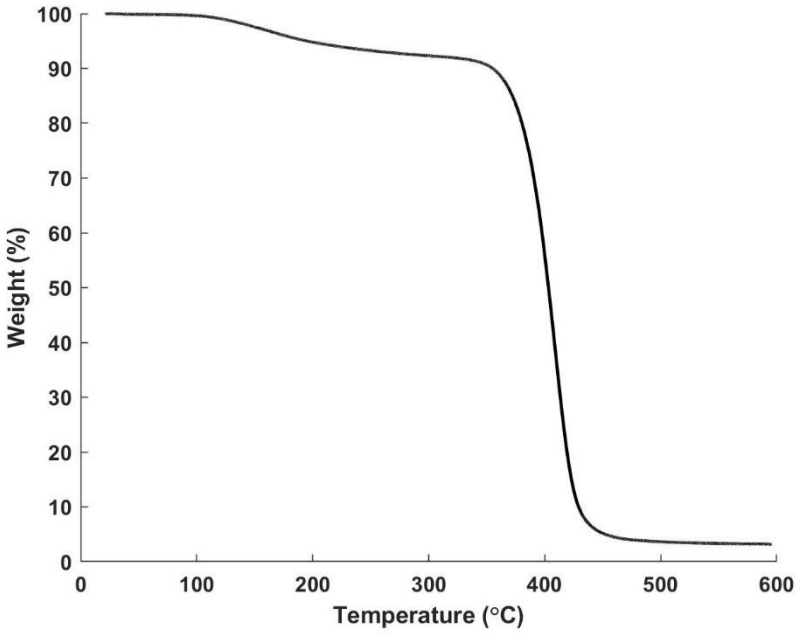

Figure A18A. TGA of parts printed from 4-pGA-1 resin with a 1 h post-cure with 405-nm light at 20 °C. The decomposition temperatures were $T_{d,2\%}$=143 °C and $T_{d,50\%}$=403 °C.

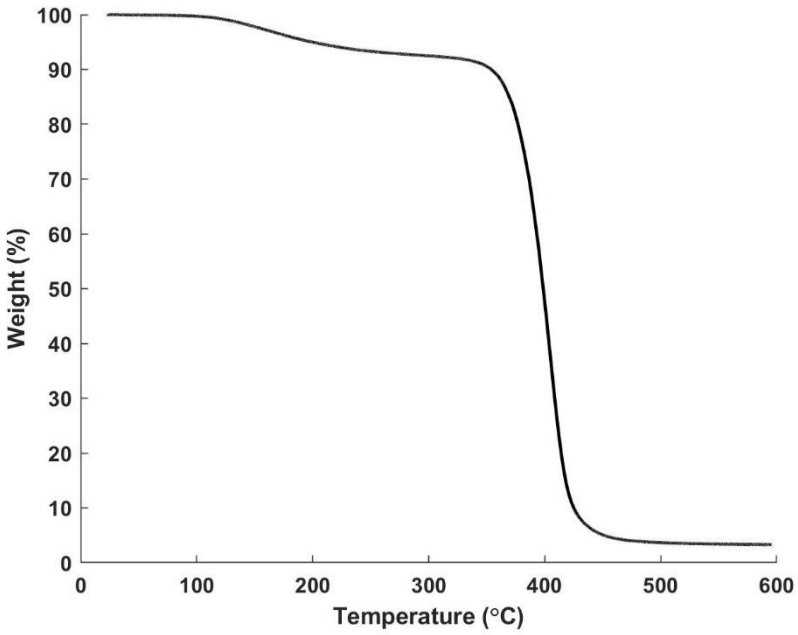

Figure A18B. TGA of parts printed from 4-pGA-2 resin with a 1 h post-cure with 405-nm light at 20 °C. The decomposition temperatures were $T_{d,2\%}$=146 °C and $T_{d,50\%}$=399 °C.

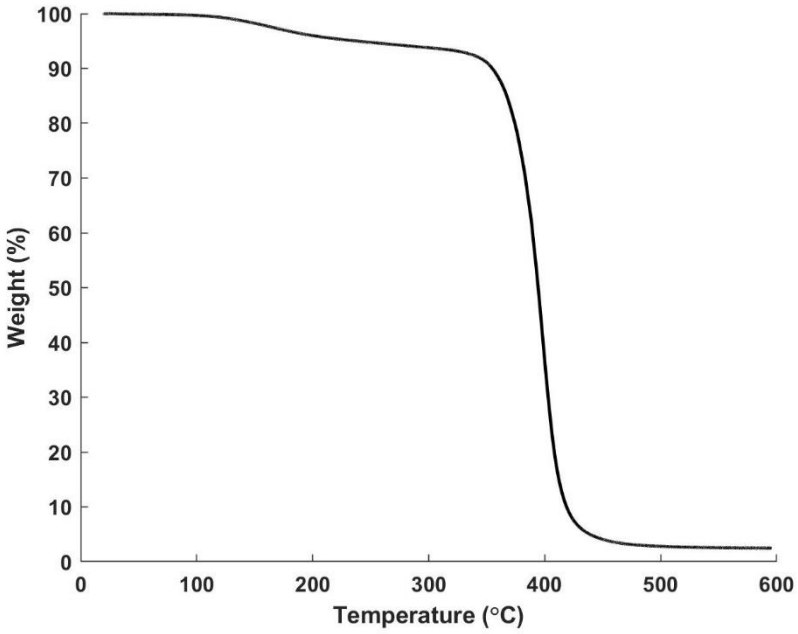

Figure A18C. TGA of parts printed from 4-pGA-3 resin with a 1 h post-cure with 405-nm light at 20 °C. The decomposition temperatures were $T_{d,2\%}$=155 °C and $T_{d,50\%}$=394 °C.

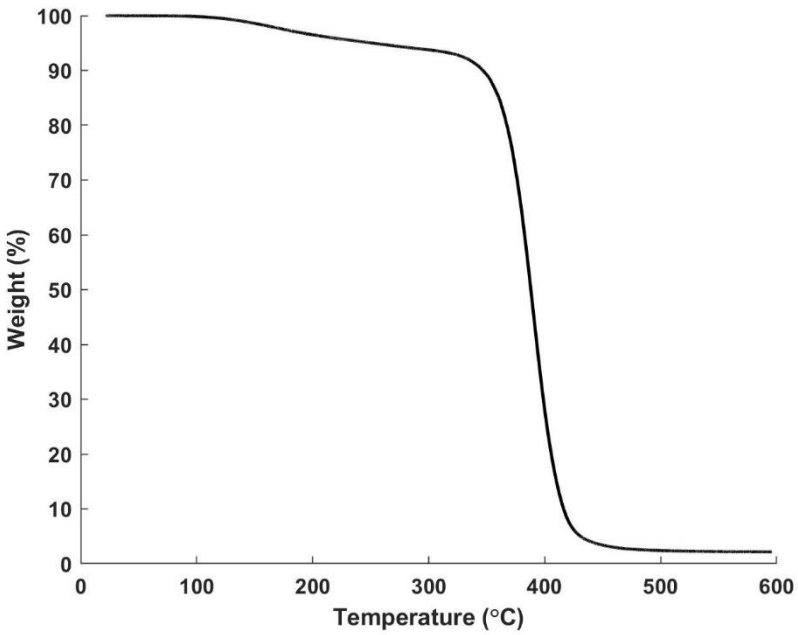

Figure A18D. TGA of parts printed from 4-pGA-4 resin with a 1 h post-cure with 405-nm light at 20 °C. The decomposition temperatures were $T_{d,2\%}$=164 °C and $T_{d,50\%}$=388 °C.

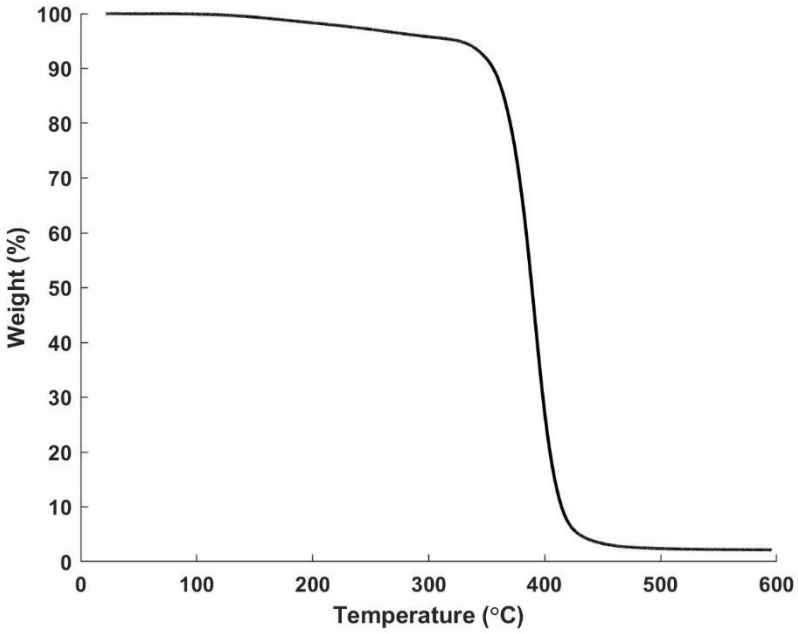

Figure A18E. TGA of parts printed from 4-pGA-5 resin with a 1 h post-cure with 405-nm light at 20 °C. The decomposition temperatures were $T_{d,2\%}$=214 °C and $T_{d,50\%}$=389 °C.

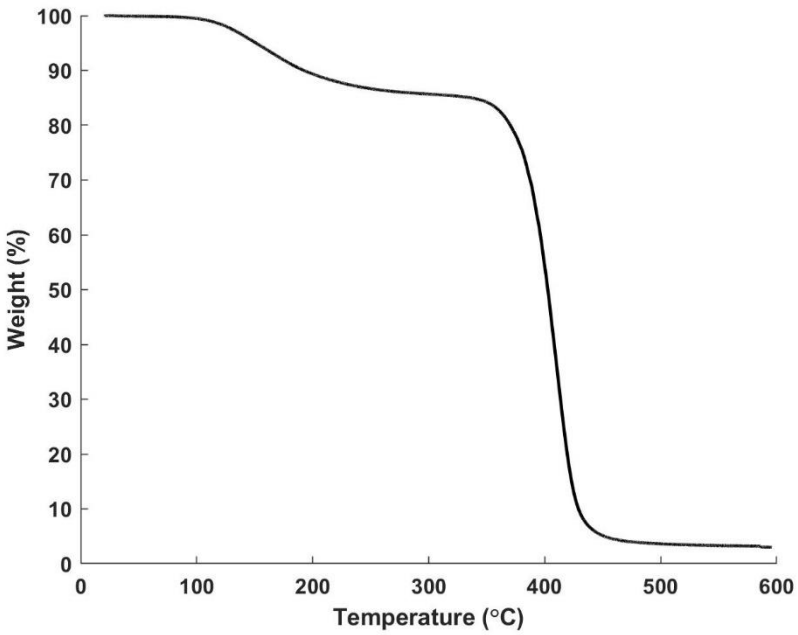

Figure A18F. TGA of parts printed from 4-pGA-6 resin with a 1 h post-cure with 405-nm light at 20 °C. The decomposition temperatures were $T_{d,2\%}$=126 °C and $T_{d,50\%}$=403 °C. The onset of mass loss before 200 °C is likely due to the sample being undercured.

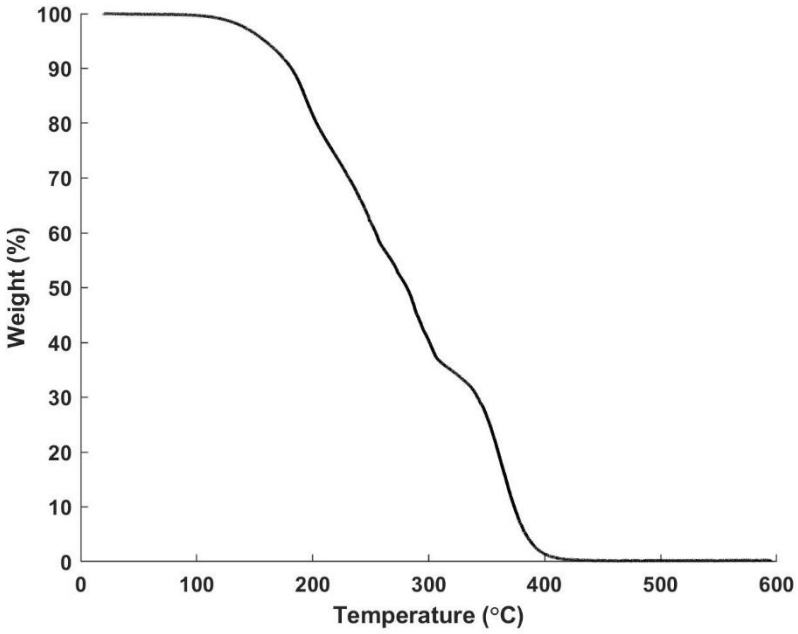

Figure A18G. TGA of parts printed from SMA-1 resin with a 1 h post-cure with 405-nm light and thermal post-cure at 40 °C. The decomposition temperatures were $T_{d,2\%}$=137 °C and $T_{d,50\%}$=281 °C. The onset of mass loss before 200 °C is likely due to the sample being undercured.

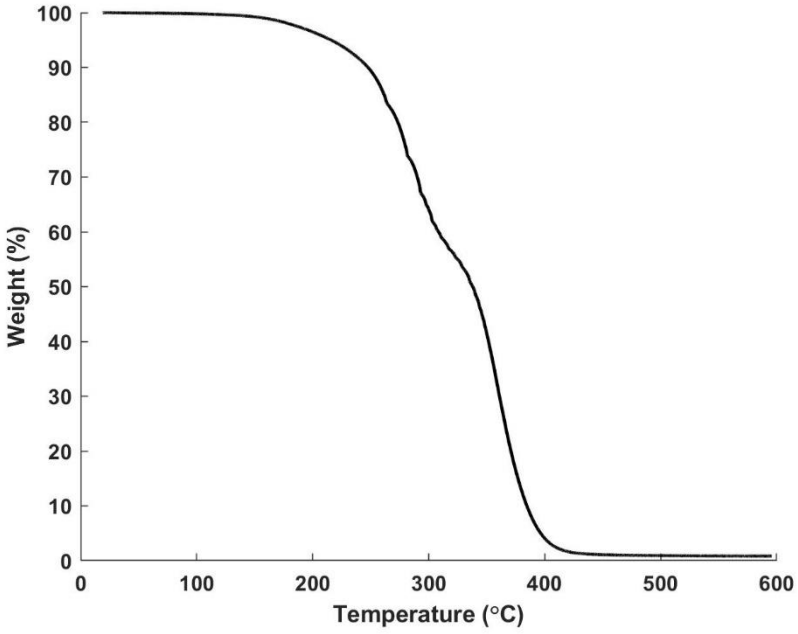

Figure A18H. TGA of parts printed from SMA-1 resin with a 1 h post-cure with 405-nm light and thermal post-cure at 140 °C. The decomposition temperatures were $T_{d,2\%}$=179 °C and $T_{d,50\%}$=338 °C. The onset of mass loss before 300 °C is likely due to the sample being undercured.

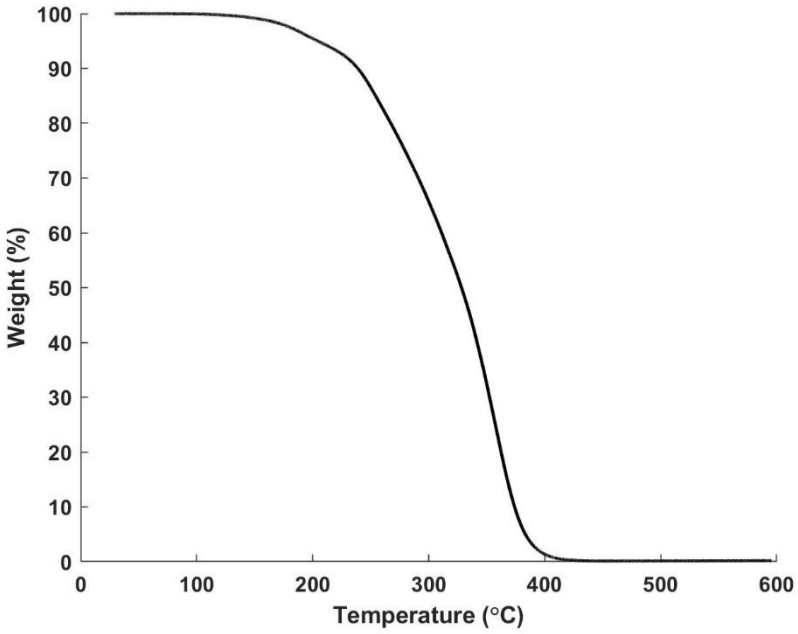

Figure A18I. TGA of parts printed from SMA-2 resin with a 1 h post-cure with 405-nm light and thermal post-cure at 140 °C. The decomposition temperatures were $T_{d,2\%}$=174 °C and $T_{d,50\%}$=328 °C.

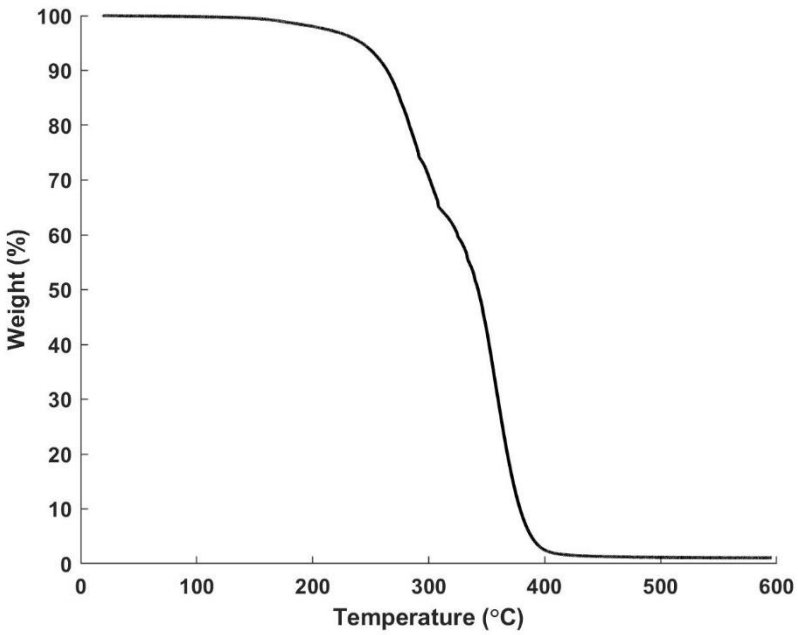

Figure A18J. TGA of parts printed from SMA-3 resin with a 1 h post-cure with 405-nm light and thermal post-cure at 140 °C. The decomposition temperatures were $T_{d,2\%}$=200 °C and $T_{d,50\%}$=343 °C.

Starting materials and [meth]acrylated derivatives were analyzed by GC-MS to identify and quantify impurities. 4-pG, 4-pGA, syringol, SA, SMA, and LMA GC-MS chromatograms are shown below with mass spectra for each synthesized compound and its precursor, respectively. Technical grade and >98% LA chromatograms also are shown stacked for reference. The technical grade LA contains significant amounts of unknown compounds that may interfere with polymerizations.

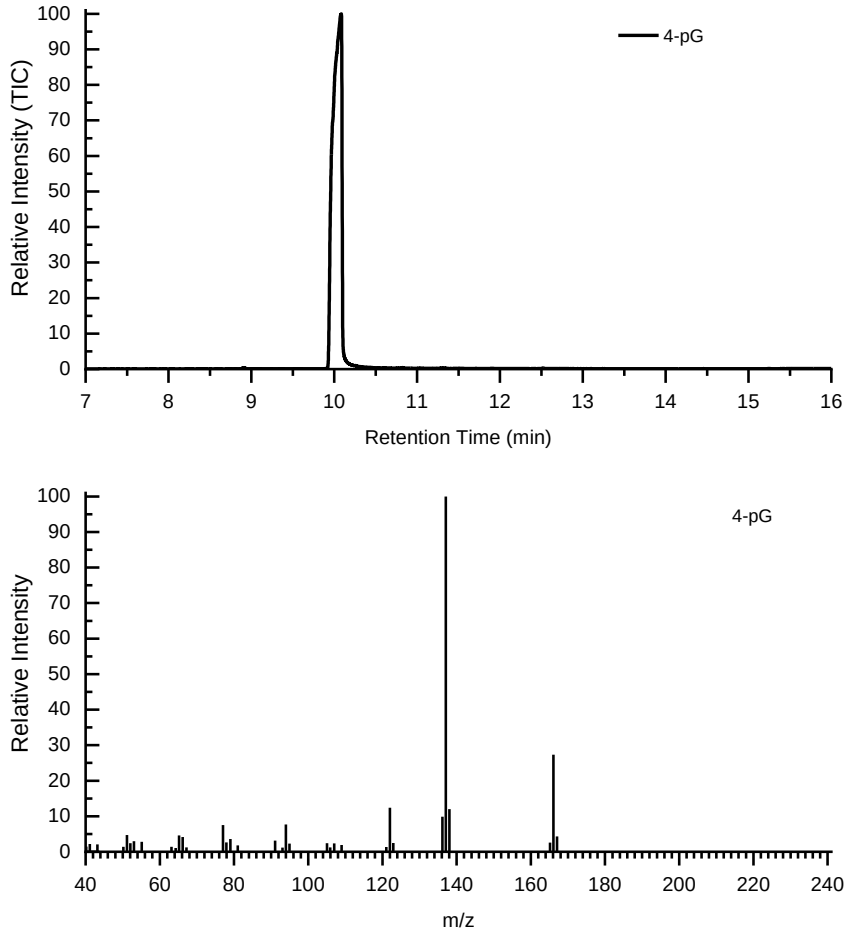

Figure A19A. Top) GC-MS chromatogram of 4-pG. Bottom) Mass spectrum of 4-pG.

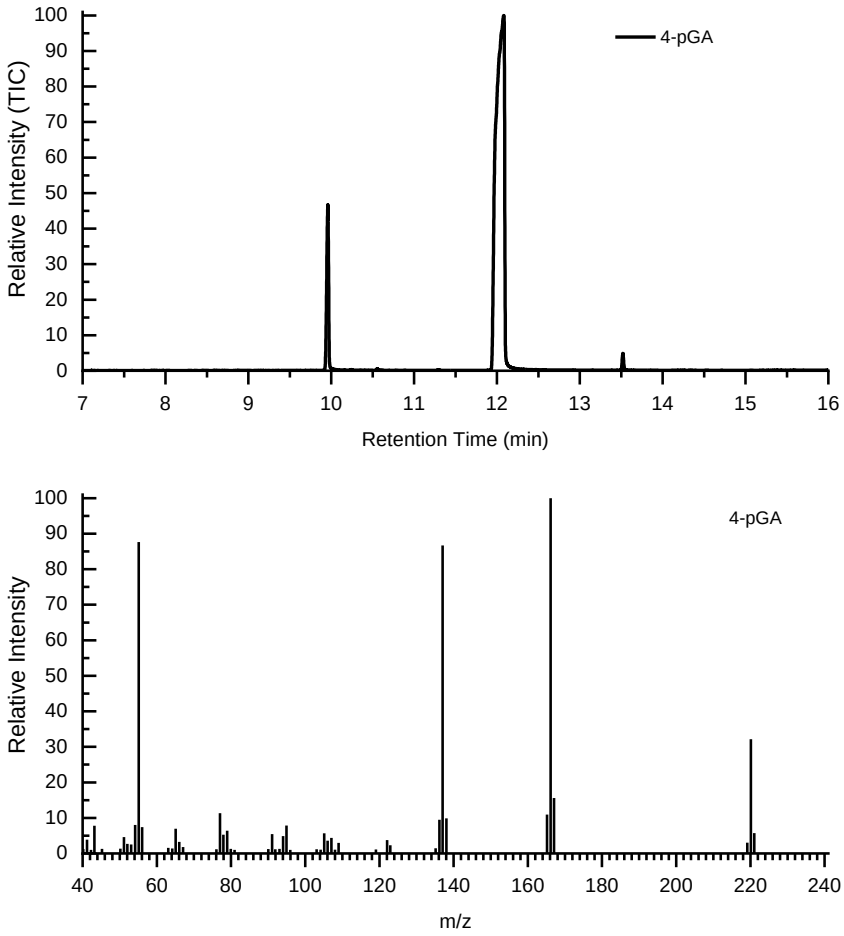

Figure A19B. Top) GC-MS chromatogram of synthesized 4-pGA. The peak at 12 min was identified as 4-pGA by its mass spectrum. Bottom) Mass spectrum of 4-pGA.

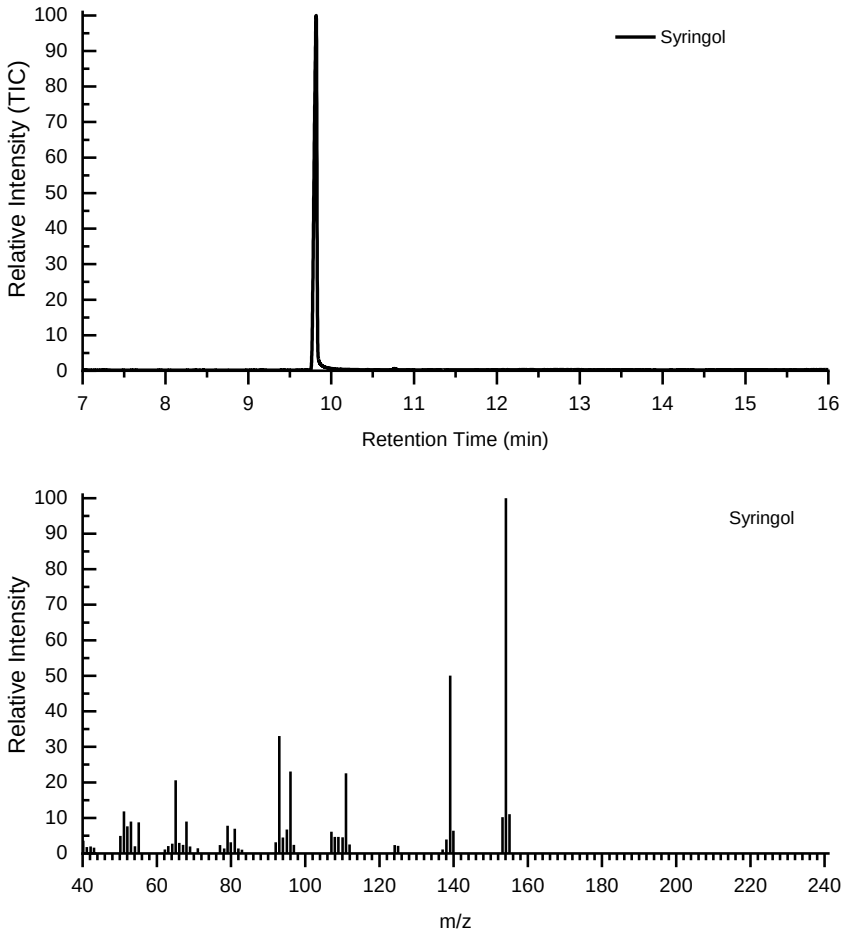

Figure A19C. Top) GC-MS chromatogram of syringol. Bottom) Mass spectrum of syringol.

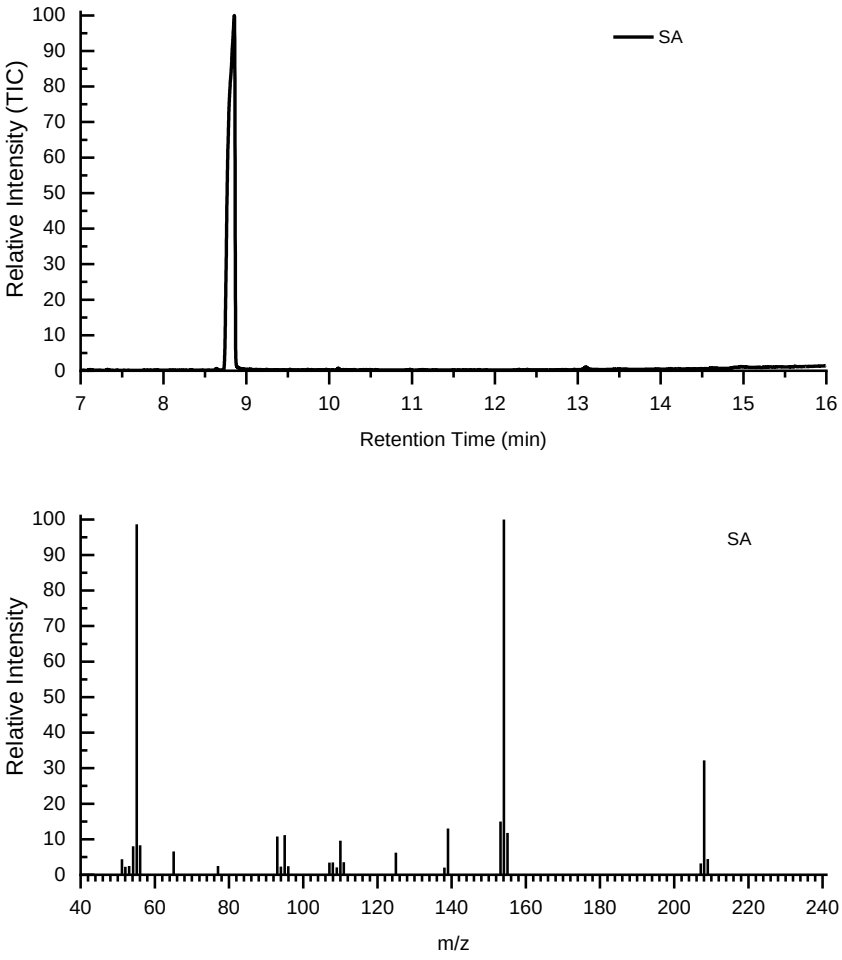

Figure A19D. Top) GC-MS chromatogram of synthesized SA. The peak at 8.8 min was identified as SA by its mass spectrum. Bottom) Mass spectrum of SA.

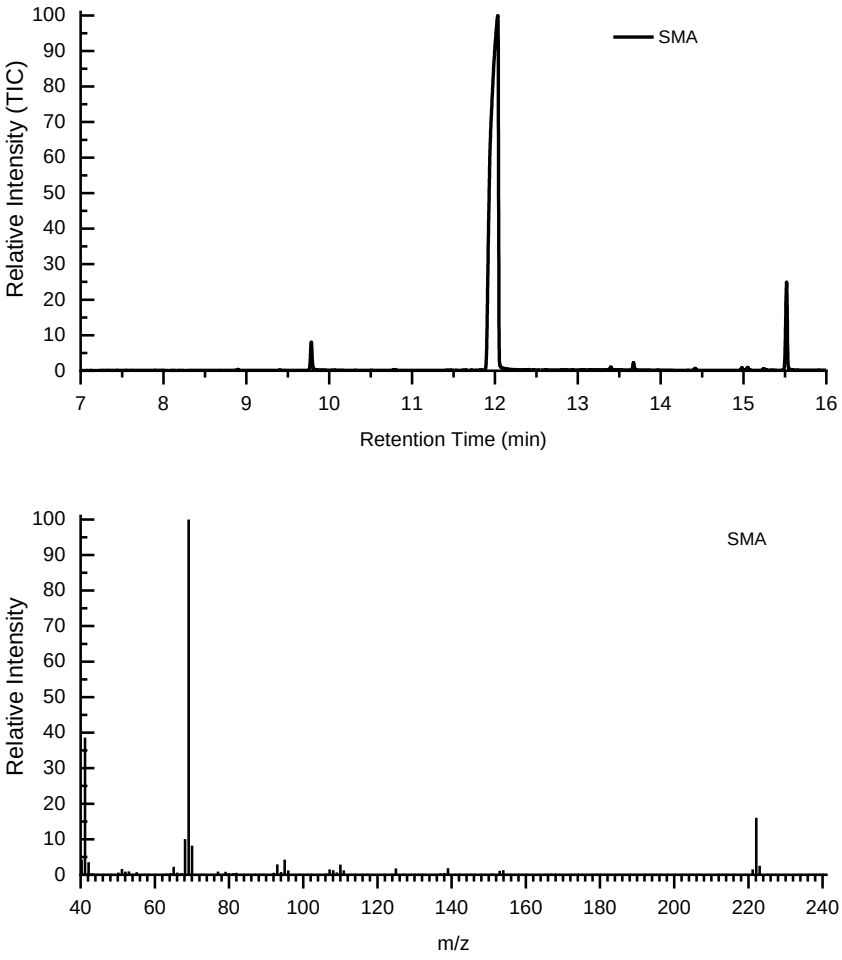

Figure A19E. Top) GC-MS chromatogram of synthesized SMA. The peak at 12 min was identified as SMA by its mass spectrum. Bottom) Mass spectrum of SMA.

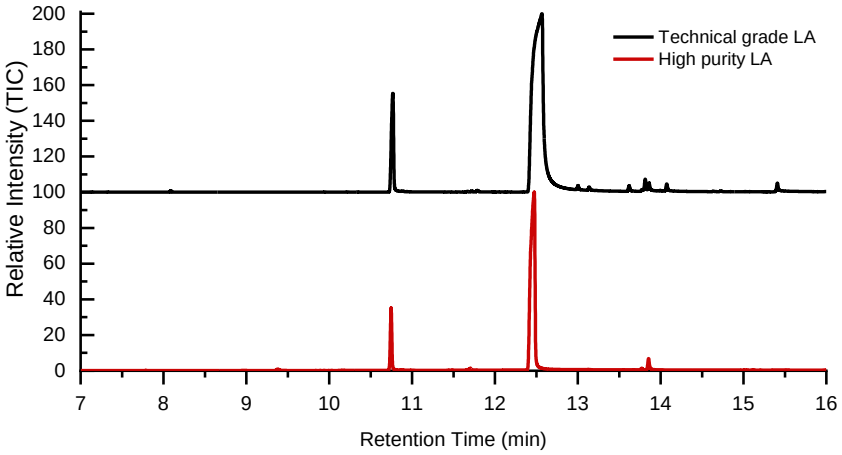

Figure A19F. GC-MS chromatogram of technical grade LA and the higher purity (>98%) LA. The peaks at 12.5 min were identified as n-dodecyl acrylate, and the peaks at approximately 10.7 min were identified as n-dodecanol using the National Institute of Standards and Technology (NIST) mass spectrum library.[8]

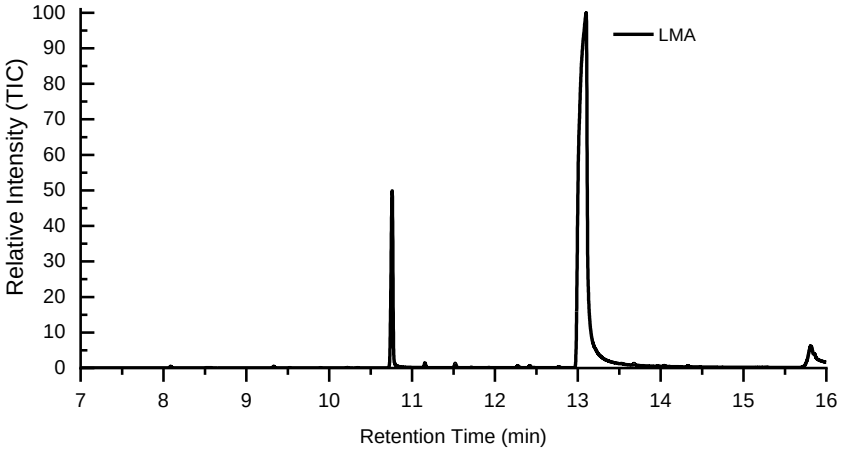

Figure A19G. GC-MS chromatogram of LMA. The peak at 13.1 min was identified as n-dodecyl methacrylate, and the peak at 10.7 min was identified as n-dodecanol using the NIST mass spectrum library.[8]

Print Files:

- https://www.thingiverse.com/thing:1019228/files
- https://www.thingiverse.com/thing:757884
- https://www.thingiverse.com/thing:636415/files
- https://www.thingiverse.com/thing:444267

References:

1. Smit, C.; Fraaije, M. W.; Minnaard, A. J. Reduction of Carbon-Carbon Double Bonds Using Organocatalytically Generated Diimide. *J. Org. Chem.* **2008**, *73* (23), 9482–9485. https://doi.org/10.1021/jo801588d.

2. Wang, S.; Shuai, L.; Saha, B.; Vlachos, D. G.; Epps, III, T. H. From Tree to Tape: Direct Synthesis of Pressure Sensitive Adhesives from Depolymerized Raw Lignocellulosic Biomass. *ACS Cent. Sci.* **2018**, *4* (6), 701–708. https://doi.org/10.1021/acscentsci.8b00140.

3. Ritter, T.; Stanek, K.; Larrosa, I.; Carreira, E. M. Mild Cleavage of Aryl Mesylates: Methanesulfonate as Potent Protecting Group for Phenols. *Org. Lett.* **2004**, *6* (9), 1513–1514. https://doi.org/10.1021/ol049514j.

4. Holmberg, A. L.; Reno, K. H.; Nguyen, N. A.; Wool, R. P.; Epps, III, T. H. Syringyl Methacrylate, a Hardwood Lignin-Based Monomer for High-Tg Polymeric Materials. *ACS Macro Lett.* **2016**, *5* (5), 574–578. https://doi.org/10.1021/acsmacrolett.6b00270.

5. Pham, T. S.; Gönczi, K.; Kardos, G.; Süle, K.; Hegedus, L.; Kállay, M.; Kubinyi, M.; Szabó, P.; Petneházy, I.; Toke, L.; Jászay, Z. Cinchona Based Squaramide Catalysed Enantioselective Michael Addition of α-Nitrophosphonates to Aryl Acrylates: Enantioselective Synthesis of Quaternary α-Aminophosphonates. *Tetrahedron: Asymmetry* **2013**, *24* (24), 1605–1614. https://doi.org/10.1016/J.TETASY.2013.10.008.

6. Porter, N. A.; Chang, V. H. T. Macrolide Formation by Free Radical Cyclization. *J. Am. Chem. Soc.* **1987**, *109* (16), 4976–4981. https://doi.org/10.1021/ja00250a036.

7. Sigma-Aldrich (Spectral data were obtained from Advanced Chemsitry Development, Inc.)

8. NIST Chemistry WebBook, NIST Standard Reference Database Number 69. Linstrom, P. J.; Mallard, W. G., Eds. National Institute of Standards and Technology: Gaithersburg, MD 20899.

Appendix B: Supporting Information Chapter 5

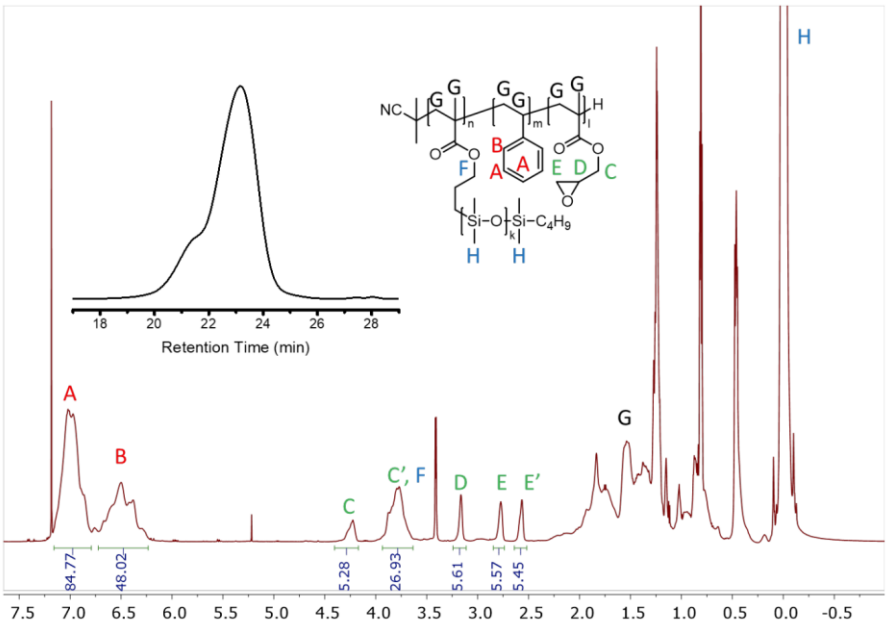

Figure B1. ^{1}H-NMR and GPC of $Si_{11}S_{24}G_{6}$.

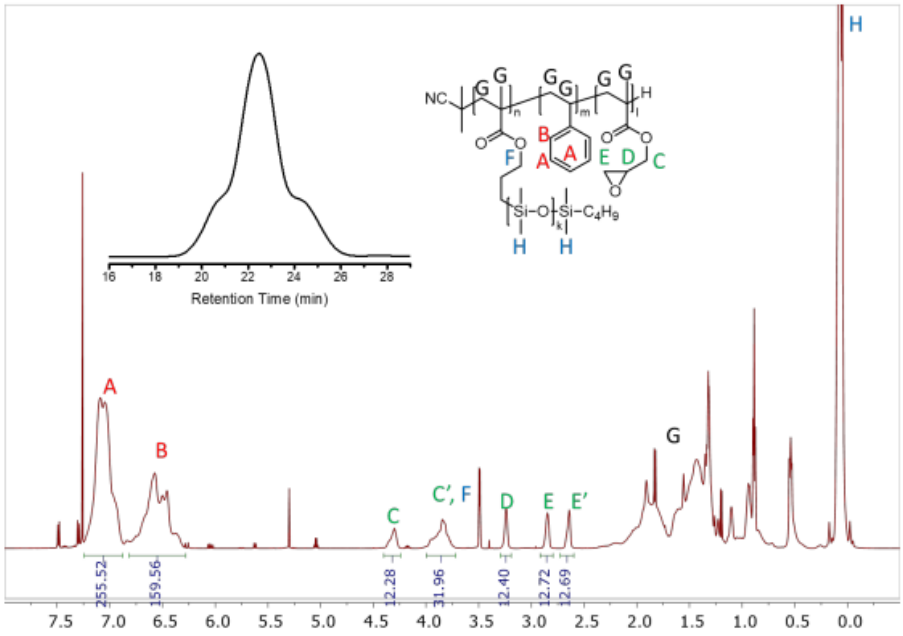

Figure B2. ^{1}H-NMR and GPC of $Si_{11}S_{80}G_{12}$.

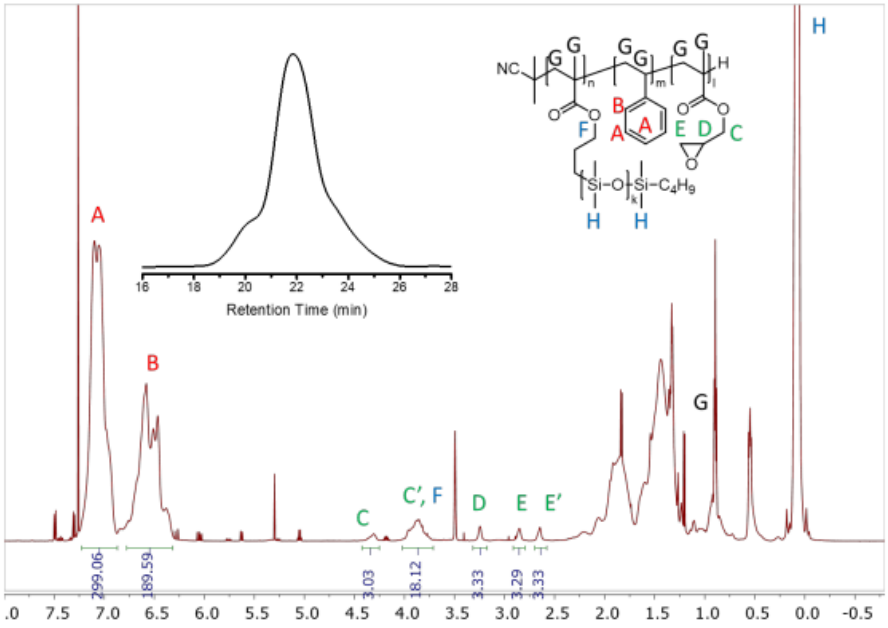

Figure B3. ^{1}H-NMR and GPC of $Si_{11}S_{149}G_{5}$.

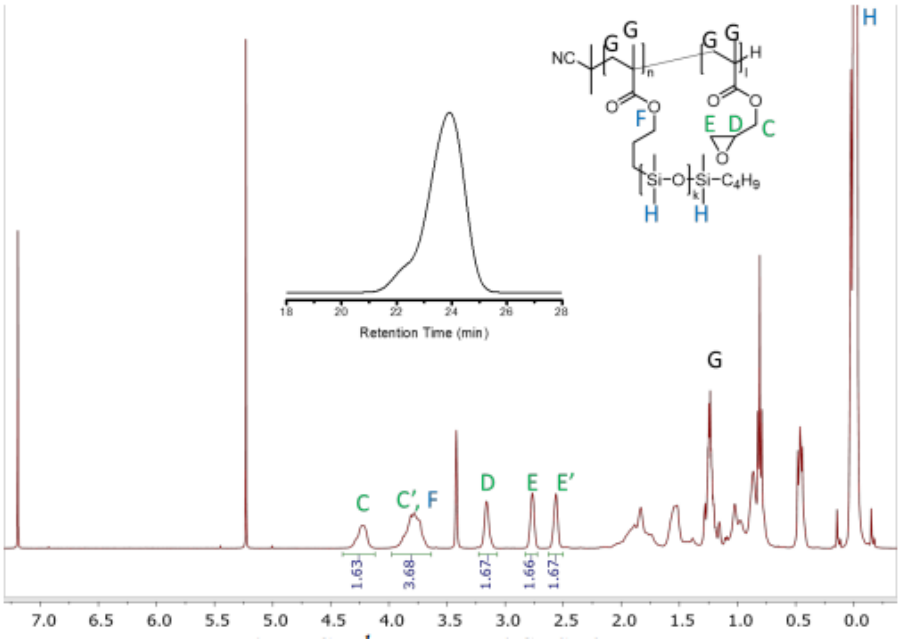

Figure B4. ^{1}H-NMR and GPC of $Si_{16}G_{27}$.

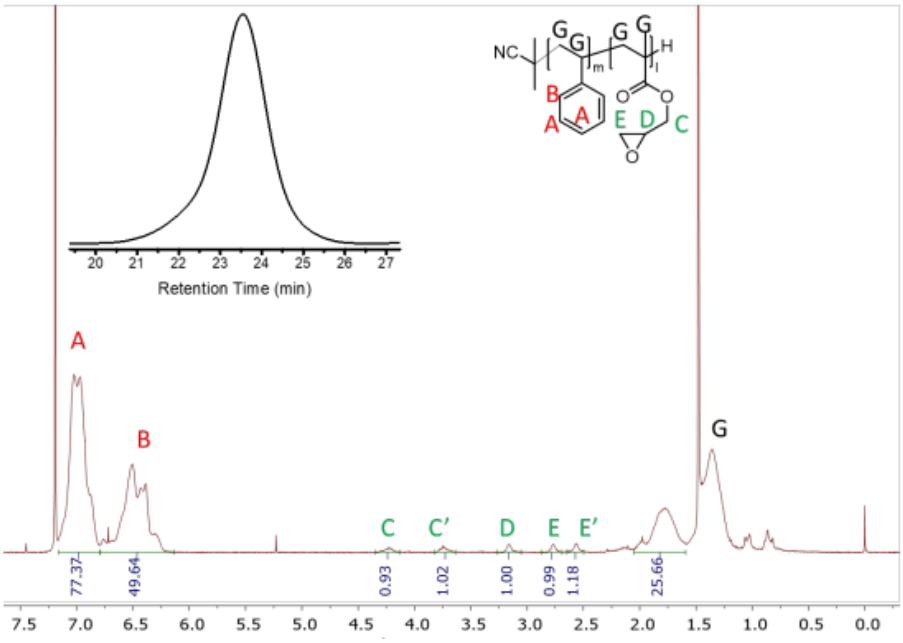

Figure B5. [1]H-NMR and GPC of $S_{25}G_1$.

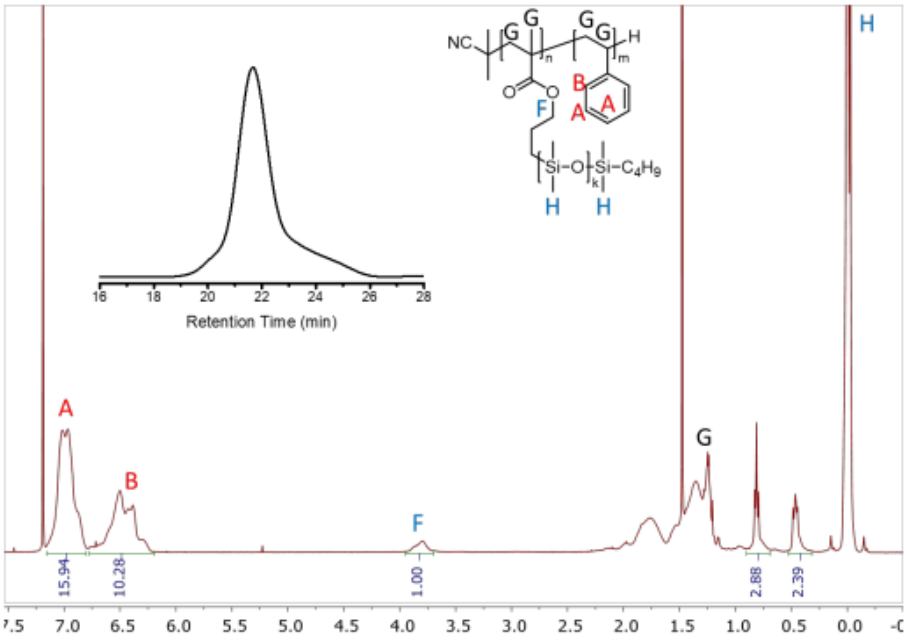

Figure B6. [1]H-NMR and GPC of Si_8S_{61}.

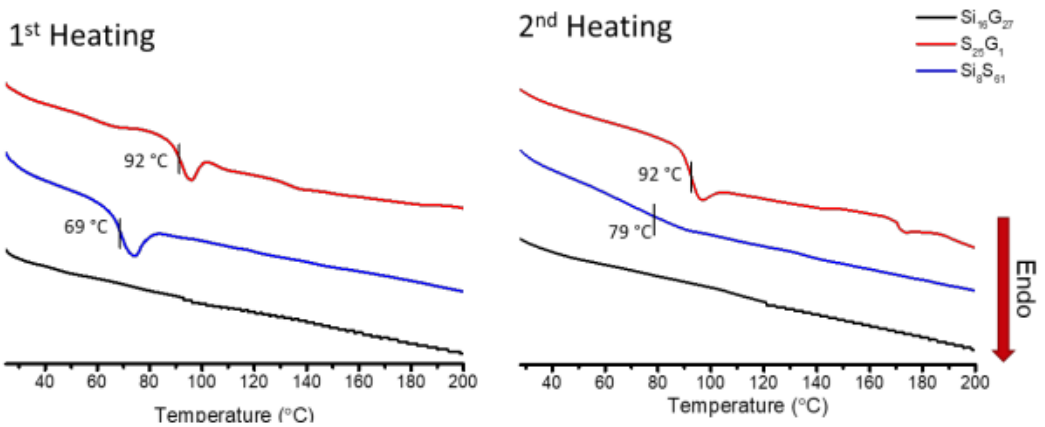

Figure B7. DSC of bulk BCPs. T_g of PS can be observed from Si_8S_{61} and $S_{25}G_1$ polymer. DSC of three control polymers.

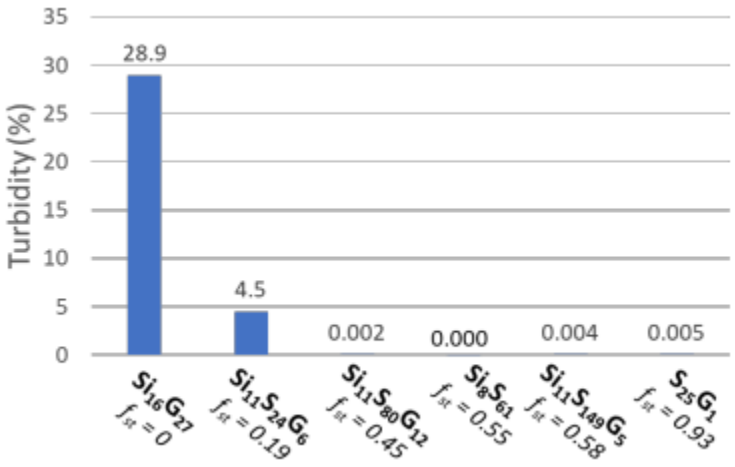

Figure B8. Turbidity of BCP solution in ECC resin at 1 wt.% loading

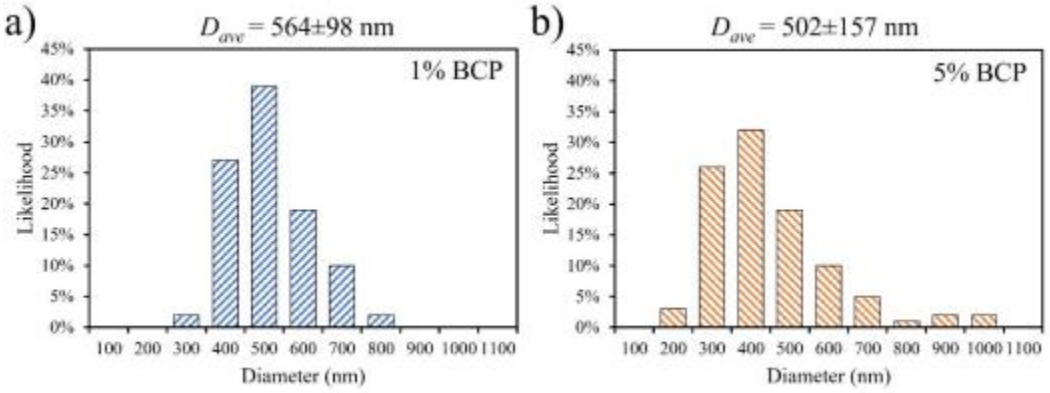

Figure B9. Diameter distributions of the spherical aggregates formed by (a) 1% and (b) 5% BCP in BCP/ECC composite.

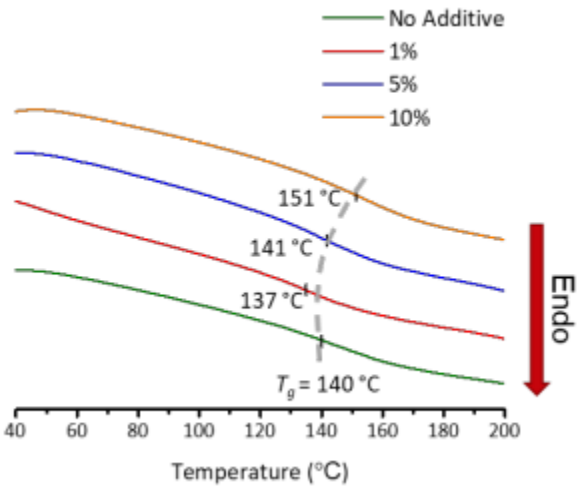

Figure B10. DSC curve of ECC/BCP showing increasing Tg with increasing concentration of BCP.

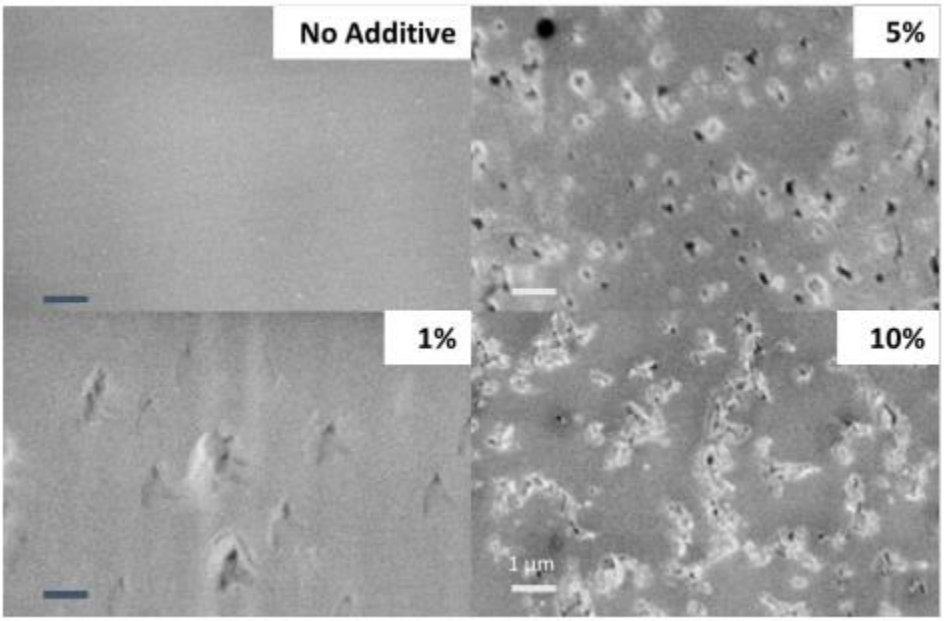

Figure B11. SEM of pristine ECC/BCP blends showing increased formation of aggregates as the concentration of BCP is increased.

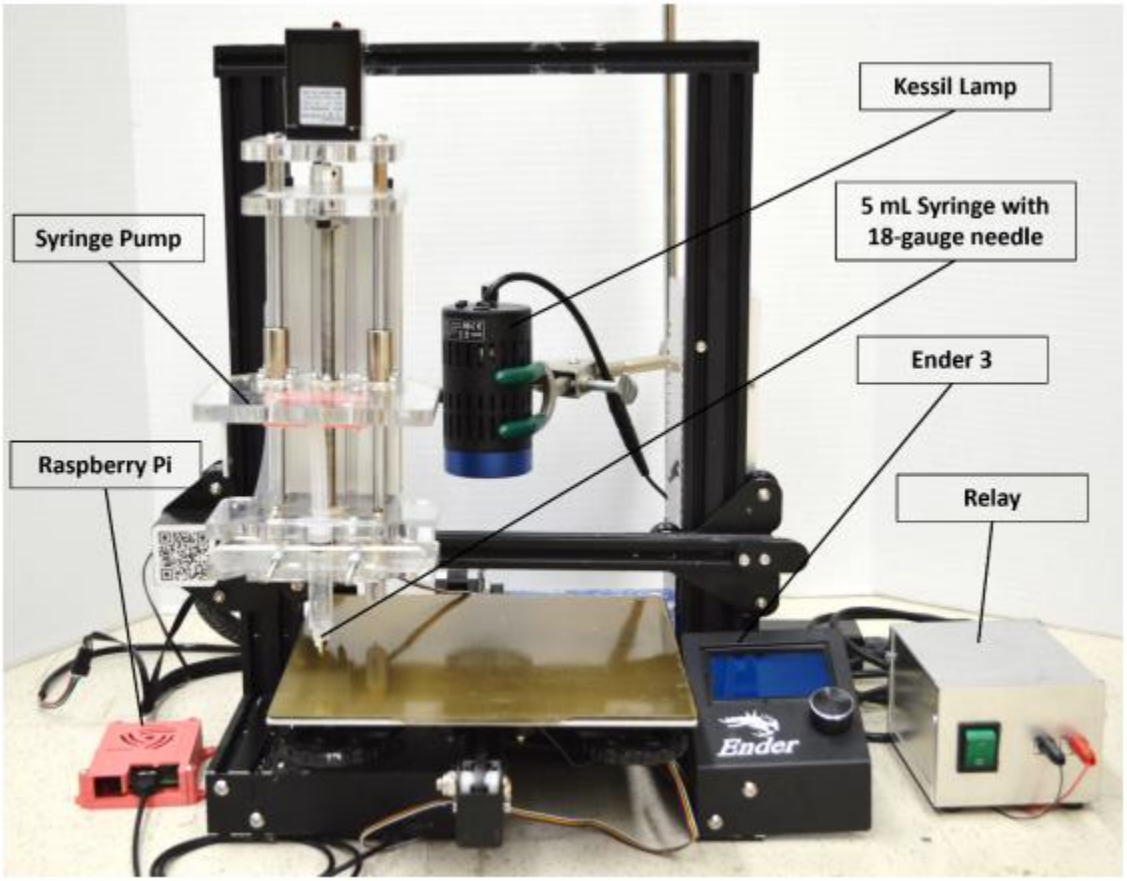

Figure B12. Modified Ender 3 printer with various modified components labeled: Stepper motor driven syringe pump, Raspberry Pi, 370 nm Kessil lamp, 5 mL syringe equipped with 18-gauge needle, the base Ender 3 printer, and a relay. To print, thermally precured resin containing pure resin or resin with polymer additive was added to a plastic syringe outfitted with an 18-gauge stainless steel dispensing needle. The filled syringe was then secured to the syringe pump. Printing files were prepared using Autodesk fusion 360 and sliced using the UltiMaker Cura Slicer program. Object print settings are shown in Table S1.

Table B1. Print Parameters Used for DIW Printing.

Print Parameter	Setting
Layer Line Width	0.83 mm
Layer Height	0.2 mm
Print Speed	3 mm/sec
Retraction	5 mm
Flow	80%
Infill Type	Concentric
Infill %	100%
Cure Time	30 sec

370 nm Kessil Lamp Intensity	50 mW/cm^2

Table B2. Resin formulations used for DLP printing

Resin	IBOA (wt%)[a]	PEGDA-250 (wt%)[a]	ECC (wt%)[a]	TAS (wt%)[b]	BAPO (wt%)[b]	BCP (wt%)[b]
R1	48	2	50	6	0.4	0
R2	48	2	50	6	0.4	1

[a]*Considered monomer component* [b]*Weight percent of total monomer component*

Table B3. Print Parameters Used for DIW Printing.

Print Parameter	Setting
Bottom Layer Time	30 sec
Bottom Layers	6
Regular Layer Time	6 sec
Layer Thickness	50 μm
Lift Distance	1 mm
Lift Speed	60 mm/min
Retract Speed	60 mm/min
Wait Before Print	3 sec
Wait After Lift	3 sec
Wait After Print	0 sec

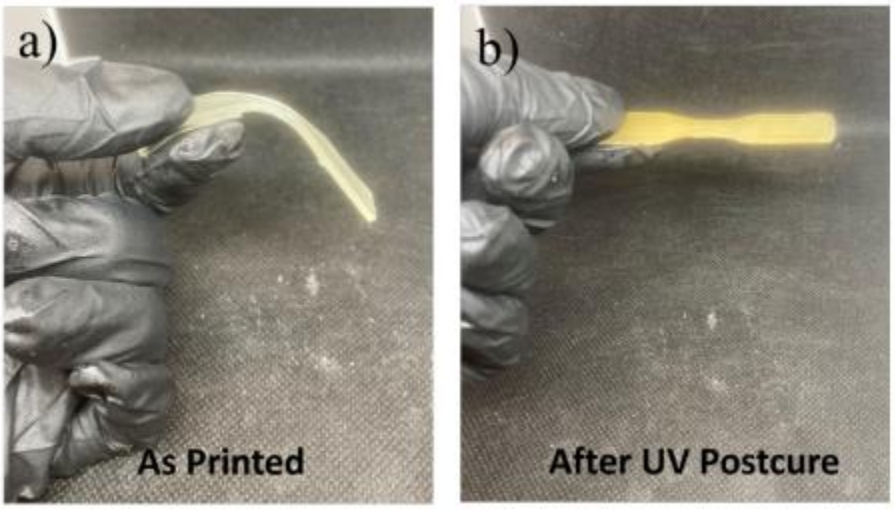

Figure B13. Images of DLP printed samples before and after postcure. Samples before and after postcuring show large changes in stiffness and a slight change in color. a) As printed part showing flexibility due to high degree of swelling from uncured monomers. b) Sample after postcuring and formation of the epoxide network displaying rigidity.

Figure B14. Image showing DLP printed lattice structure with overhanging structures.

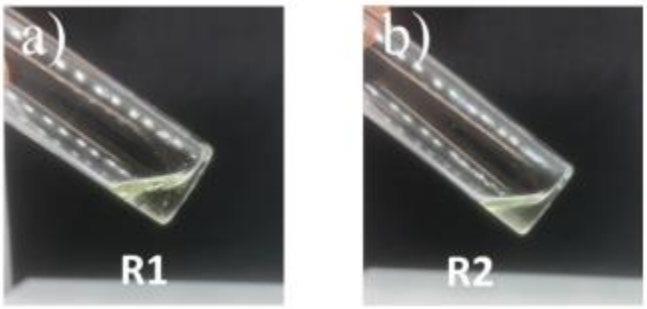

Figure B15. Images showing R1 and R2 resin. a) Clear R1 resin b) Slightly cloudy R2 resin as a result of adding the BCP.

Appendix C: Supporting Information for Chapter 6

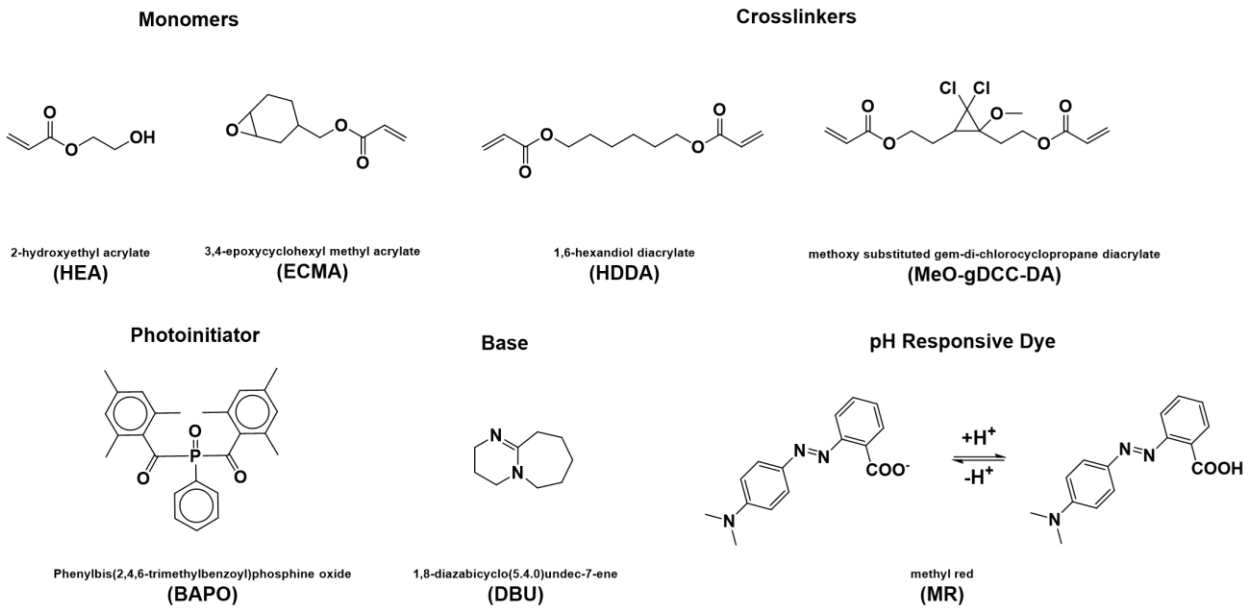

Figure C1. Chemical structures of the compounds used in the resins throughout this investigation.

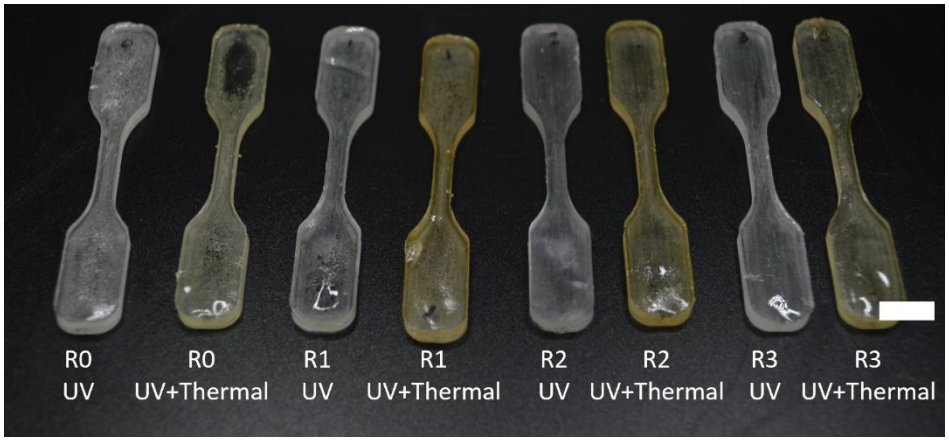

Figure C2. Differences in appearance of UV cured samples compared to UV+ thermally cured samples. Scale bar = 1 cm

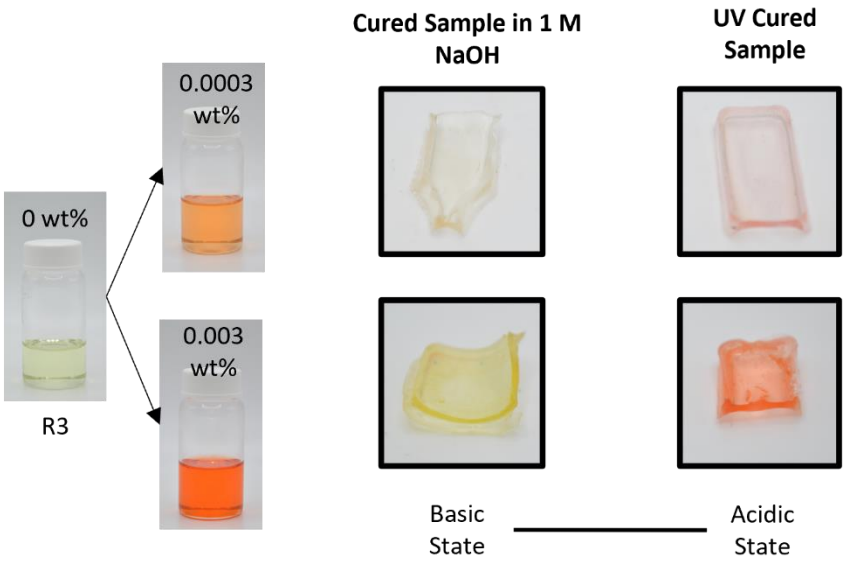

Figure C3. R3 with 0.0003 wt% versus 0.003 wt% of MR added. Additionally, cured samples in the basic and acidic state.

Scheme C1. Synthesis of MeO-gDCC-DA.

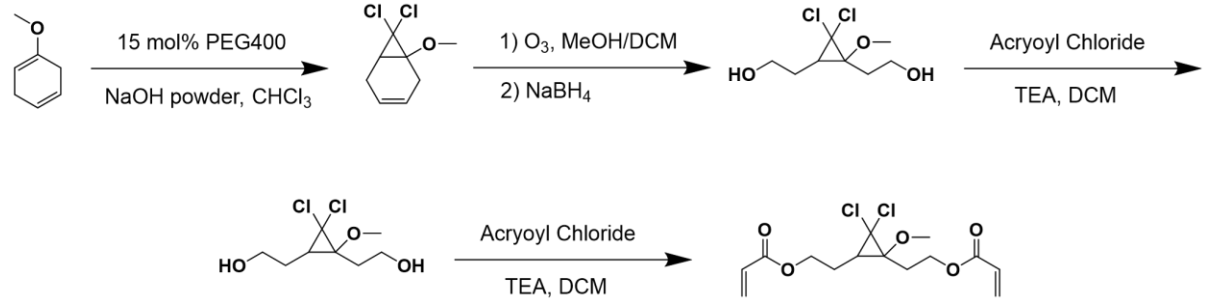

Appendix D: Supporting Information for Chapter 7

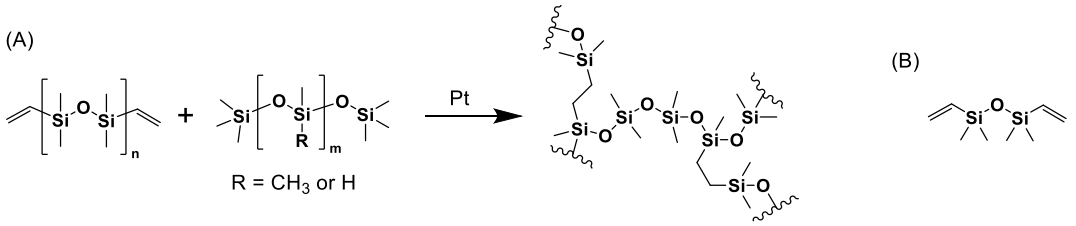

Figure D1. (A) Crosslinking reactions in Sylgard 184 between base and curing agent and (B) 1,3-divinyltetramethyldisiloxane.

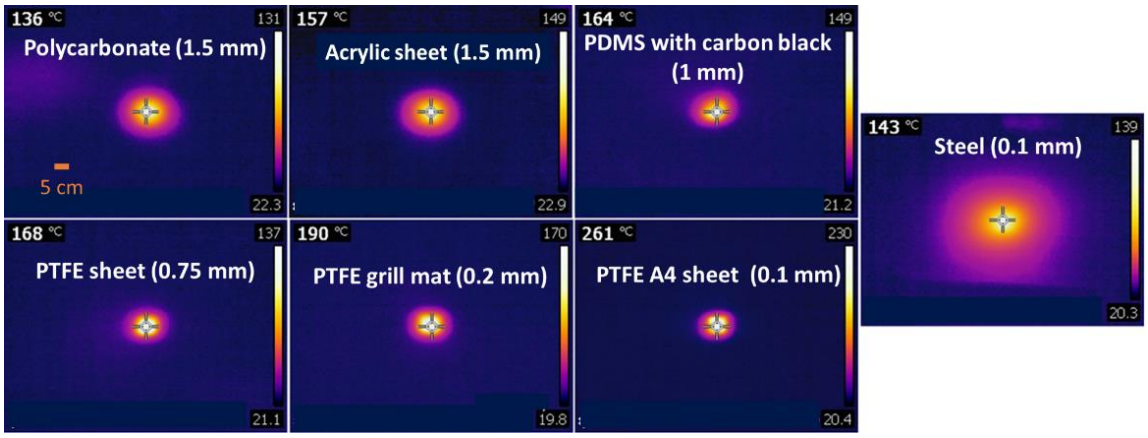

Figure D2. Thermal images during photothermal curing of Sylgard 184 on different photothermal plates with illumination of an 808-nm diode laser. Number in the parenthesis is the thickness of each plate.

(A)

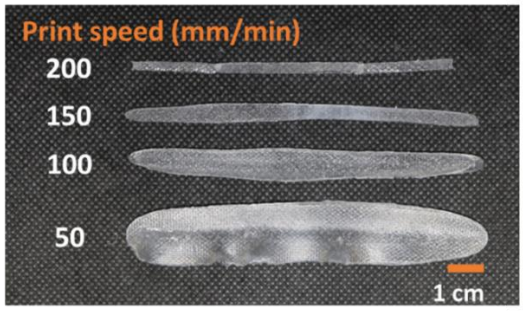

(B)

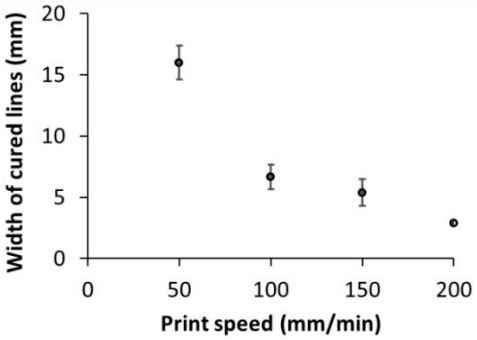

(C)

Print speed (mm/min)	200	150	100	50
Average width of printed lines (mm)[a)]	2.9 ± 0.1	5.4 ± 1.1	6.7 ± 1.0	16 ± 1.4

[a]Values represent average of 3 experiments, errors represent one standard deviation.

Figure D3. (A) Picture of printed, single layer lines of Sylgard 184 at different print speeds, (B) and (C) a plot and table showing the average width of the printed lines.

Table D1. Results of curing Sylgard 184 on photothermal plates using a diode laser

Photothermal plate	Thick-ness of plate [mm]	Thermal conduc-tivity [W/(mK)]	Thermal diffusivity [mm^2/s]	Laser power [W]	Time to Cure [sec.]	Maximum temp.[a] [°C]	Curing of resin	Time to reach < 40 °C after curing [sec.]
Black polycarbonate	1.5	0.2	0.144	4	< 5	> 120	Yes	60 ~ 70
				3	< 5	> 120	Yes	
				2	20 ~ 30	> 120	Yes	
				1	60	50	No	
Black plexiglass (PMMA) plate	1.5	0.2	0.15	4	< 5	> 120	Yes	60 ~ 70
				3	10 ~ 15	> 120	Yes	
				2	20 ~ 25	> 120	Yes	
				1	60	50	No	
Crosslinked PDMS with carbon black (1 wt %)	1	0.27	0.19[b]	4	< 5	> 120	Yes	60 ~ 70
				3	< 5	> 120	Yes	
				2	15 ~ 20	> 120	Yes	
				1	60	60	No	
Black PTFE	0.75	0.25	0.124	4	< 5	> 120	Yes	50 ~ 60
				3	5	> 120	Yes	
				2	10	> 120	Yes	
				1	60	70	No	
Black grill mat (fiberglass coated with black PTFE)	0.2	0.222[c]	0.168[d]	4	< 3	> 150	Yes	30 ~ 40
				3	< 3	> 150	Yes	
				2	< 5	> 120	Yes	
				1.5	5 ~ 10	> 120	Yes	
				1	60	100	Partially yes	
Black PTFE A4 thin sheet	0.1	0.25	0.124	4	< 3	> 150	Yes	15 ~ 20
				3	< 3	> 150	Yes	
				2	5	> 120	Yes	
				1	60	60	No	
Blue-black steel plate	0.1	50	11.72	4	5	> 120	Yes	10
				3	15 ~ 20	> 120	Yes	
				2	60	80	No	

[a] *The maximum temperature recorded at the recorded time to cure and power used.*

[b] *This value was calculated from reported thermal conductivity, density and specific heat capacity of PDMS.*[1]

[c] *This is the measured thermal conductivity at 50 °C of 40% by mass glass fiber:60% by mass PTFE as reported by Price et al.*[2]

[d] *Thermal diffusivity of grill mat was calculated using the following measured and literature values:*

$\rho_{\mathrm{PTFE}} = 2440\,\frac{\mathrm{kg}}{\mathrm{m^3}}$; $\rho_{\mathrm{FiberGlass}} = 1280\,\frac{\mathrm{kg}}{\mathrm{m^3}}$ from the reference;[3]

$\rho_{\mathrm{GrillMat}} = 1617\,\frac{\mathrm{kg}}{\mathrm{m^3}}$ from measurement; $\mathrm{C_{PTFE}} = 970\,\frac{\mathrm{J}}{kg\ \mathrm{K}}$ from reference;[4]

$\mathrm{C_{FiberGlass}} = 750\,\frac{\mathrm{J}}{kg\ \mathrm{K}}$ from reference;[4]

$\mathrm{C_{GrillMat}} = 820\ \frac{\mathrm{J}}{kg\ \mathrm{K}}$ by weight average of $\mathrm{C_{PTFE}}$ and $\mathrm{C_{FiberGlass}}$;

$\mathrm{k_{GrillMat}} = 0.222\,\frac{\mathrm{W}}{\mathrm{m\ K}}$ from the reference.[2]

$$\boldsymbol{\alpha_{\mathrm{GrillMat}} = \frac{k_{GrillMat}}{\rho_{GrillMat} C_{GrillMat}} = 0.168\,\frac{mm^2}{s}}$$

Calculation of volume fraction, f, and weight fraction, w:

$$\mathrm{m}_{\mathrm{GrillMat}} = \mathrm{m}_{\mathrm{PTFE}} + \mathrm{m}_{\mathrm{FiberGlass}}$$

$$V_{\mathrm{Total}}\rho_{\mathrm{GrillMat}} = V_{\mathrm{PTFE}}\rho_{\mathrm{PTFE}} + V_{\mathrm{FiberGlass}}\rho_{\mathrm{FiberGlass}}$$

$$\rho_{\mathrm{GrillMat}} = f_{\mathrm{PTFE}}\rho_{\mathrm{PTFE}} + f_{\mathrm{FiberGlass}}\rho_{\mathrm{FiberGlass}}$$

$$\rho_{\mathrm{GrillMat}} = f_{\mathrm{PTFE}}\rho_{\mathrm{PTFE}} + (1 - f_{\mathrm{PTFE}})\rho_{\mathrm{FiberGlass}} \rightarrow f_{\mathrm{PTFE}} = 29\%; f_{\mathrm{FiberGlass}} = 71\%$$

$$w_{\mathrm{PTFE}} = \frac{\mathrm{m}_{\mathrm{PTFE}}}{\mathrm{m}_{\mathrm{GrillMat}}} = \frac{V_{\mathrm{PTFE}}\rho_{\mathrm{PTFE}}}{V_{\mathrm{Total}}\rho_{\mathrm{GrillMat}}} = \frac{f_{\mathrm{PTFE}}\rho_{\mathrm{PTFE}}}{\rho_{\mathrm{GrillMat}}} = 44\%; w_{\mathrm{FiberGlass}} = 56\%$$

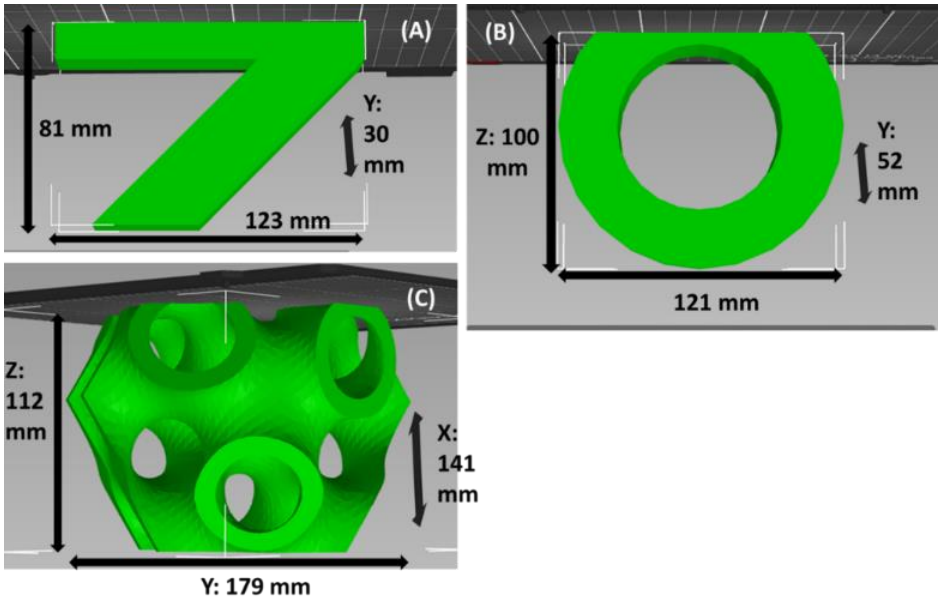

Figure D4. Digital file images of a (A) overhang, (B) open circle and (C) gyroid.

References

1. Liu, G.; Cai, M.; Feng, Y.; Wang, X.; Zhou, F.; Liu, W. *Chem. Commun.* **2016**, *52*, 3681-3683.

2. Price, D. M.; Jarratt, M. *Thermochim. Acta* **2002**, *393*, 231-236.

3. https://www.electronics-cooling.com/2008/02/thermal-properties-of-building-materials/ (accessed 2023-03-03).

4. https://dielectricmfg.com/knowledge-base/teflon/ (accessed 2023-03-03).

Appendix E: Supporting Information for Chapter 8

Table E1. Compiled list of printer components, their cost, and purchasing links divided into the hardware, fasteners, and electronics needed for this project.

Item Number	Part Name	Quantity	Unit Cost ($)	Total Cost ($)	Purchase Link
Hardware					
1	158mm GT2 Timing Belt	1	1.19	1.19	https://a.co/d/cd2YEOL
2	4mm Long Wood Drill	1	4.57	4.57	https://a.co/d/3NBjfsq
3	5mm to 6mm Flexible Couplings	1	1.94	1.94	https://a.co/d/8osQt9w
4	Ender 3 3D Printer	1	168.00	168.00	https://a.co/d/6xaSkjH
5	GT2 5mm Bore 20 Teeth Synchronous Wheel	1	1.68	1.68	https://a.co/d/jahX386
6	GT2 8mm Bore 60 Teeth Synchronous Wheel	1	3.60	3.60	https://a.co/d/83xEKQp
7	M3 Damping Ball	4	0.35	1.40	https://a.co/d/47of7Ap
8	Nema 17 Stepper Motor	2	8.60	17.20	https://a.co/d/4pQLILF
9	Pellet Feeding Screw	1	49.85	49.85	https://a.co/d/gfq5QFk
Fasteners					
10	ISO 10642 M3 x 8 Flat Head Screw	8	0.10	0.80	https://a.co/d/4yJFM9r
11	ISO 10642 M4 x 16 Flat Head Screw	5	0.18	0.92	https://a.co/d/c5u8TNL
12	ISO 10642 M4 x 25 Flat Head Screw	2	0.18	0.36	https://a.co/d/c1Y6I43
13	ISO 4762 M2 x 6 Socket Cap Screw	4	0.26	1.04	https://a.co/d/0KIbFfK
14	ISO 4762 M2 x 6 Socket Cap Screw	4	0.26	1.04	https://a.co/d/1L6gqAO
15	ISO 4762 M3 x 12 Socket Cap Screw	8	0.09	0.72	https://a.co/d/7dwlxFH
16	ISO 4762 M3 x 16 Socket Cap Screw	4	0.17	0.68	https://a.co/d/0Hl8C6d
17	ISO 4762 M5 x 16 Socket Cap Screw	5	0.18	0.92	https://a.co/d/5XnOQmp
Electronics					
18	ATmega328P Arduino UNO R3	1	16.98	16.98	https://a.co/d/azmxl3k
19	1602 LCD Display	1	4.50	4.50	https://a.co/d/9wJBkTb
20	TMC2208 Stepper Motor Driver	1	4.60	4.60	https://a.co/d/d6tVOY6
21	1K ohm Resistor	1	0.06	0.06	https://a.co/d/g0clCk6
22	5V Active Buzzer	1	0.38	0.38	https://a.co/d/3z3KNnJ
23	JST-XH Connector Kit	1	10.88	10.88	https://a.co/d/6ZUM0Rv
24	360 Degree Rotary Encoder	1	1.50	1.50	https://a.co/d/8qIf8FK
			Total Cost ($)	294.8	

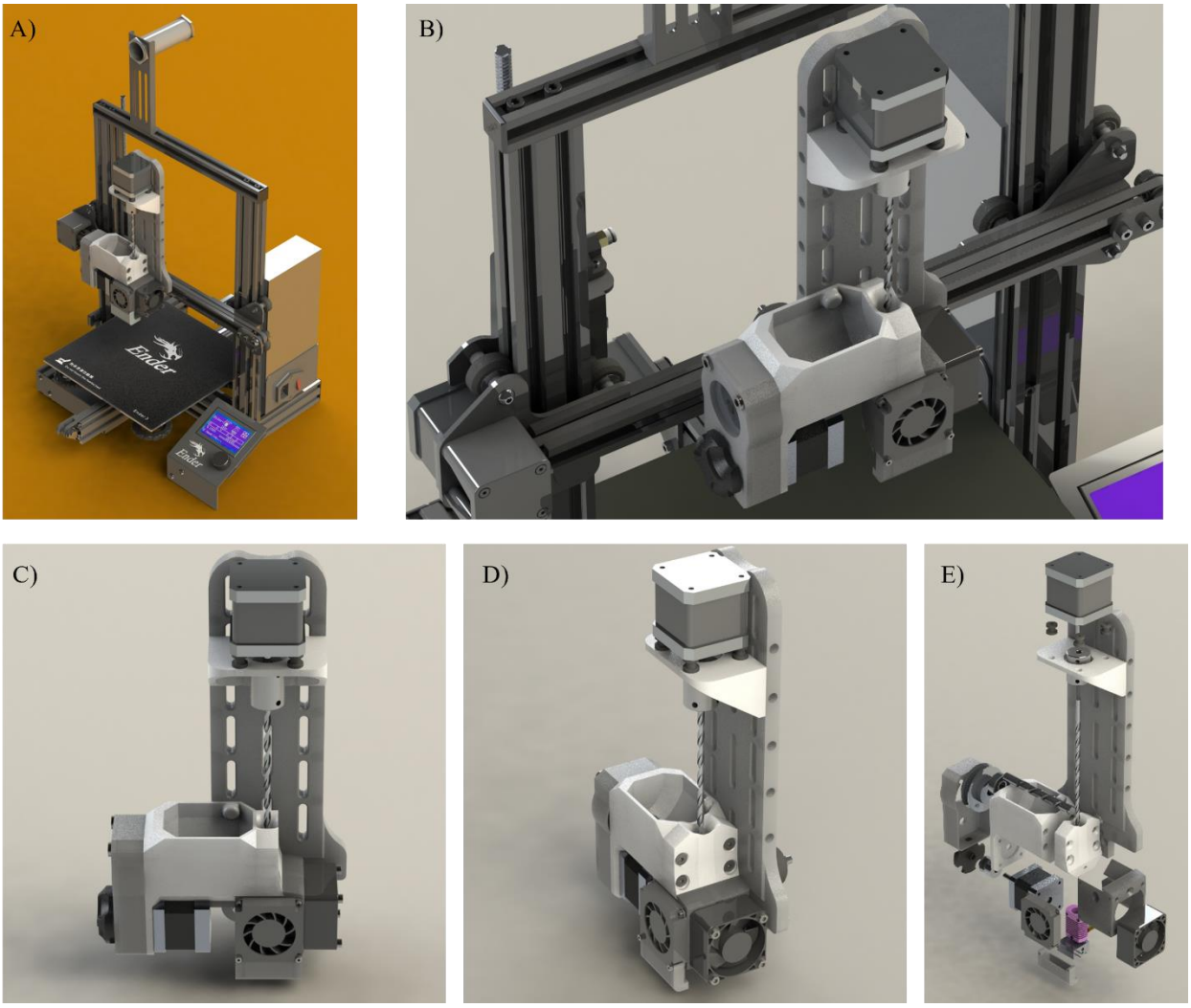

Figure E1. Additional computer aided design images of the modified Ender 3 printer and the custom designed PME print head. A) Computer rendered version of the entire printer. B) Computer rendered image of print head attached to printer. C) Rendered front view of the assembled custom PME print head. D) Rendered side view of the assembled custom PME print head. E) Rendered disassembled custom PME print head showing all the different components.

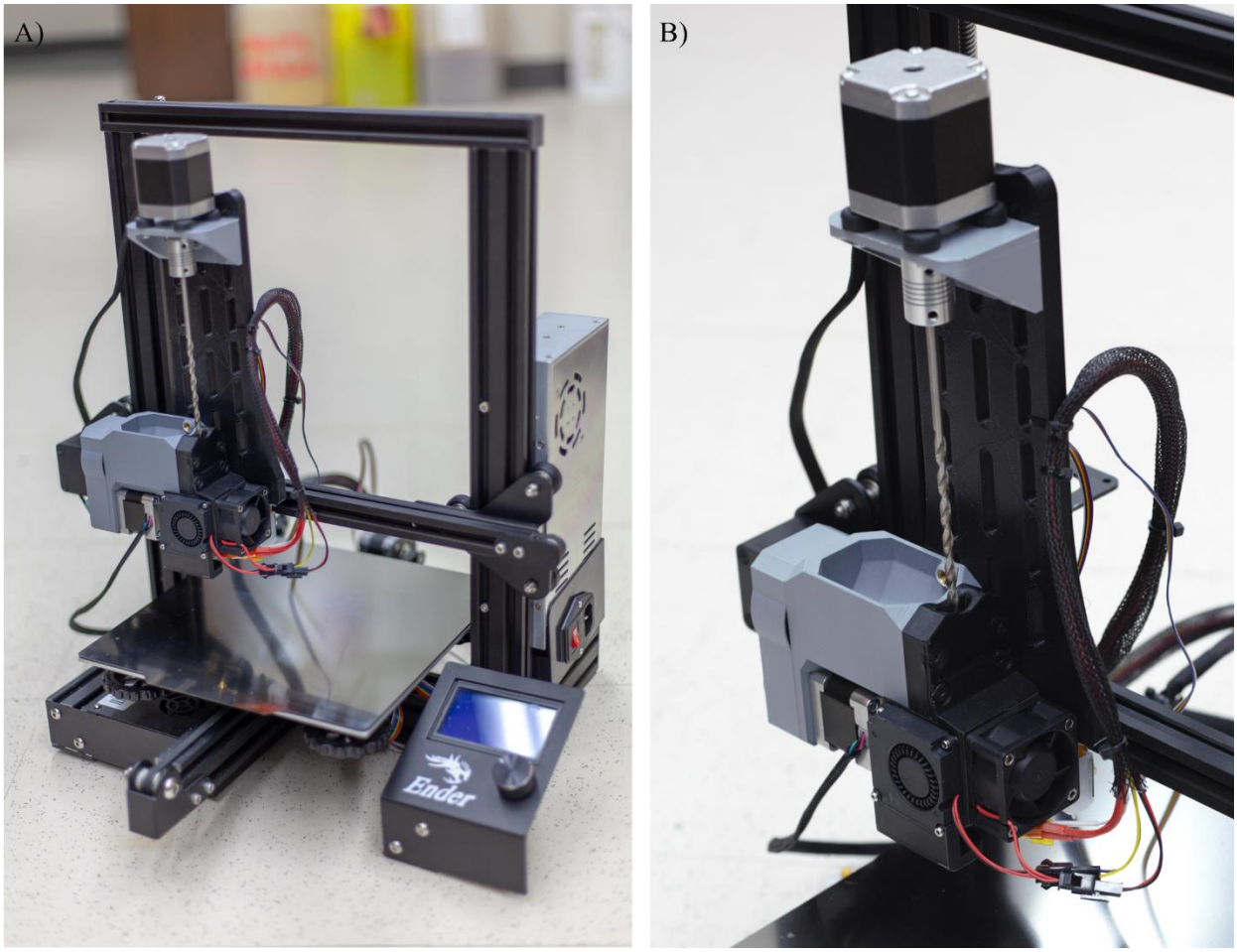

Figure E2. Additional images of the modified Ender 3 printer and the custom designed PME print head. A) Image of the entire printer. B) Image of custom print head attached to printer.

Table E2. Summary of the thermal transitions for the thermoplastic materials used in this study.

Material	**$T_{d,5\%}$ (°C)**	**$T_{d,onset}$ (°C)**	**T_g (°C)**	**$T_{m,1}$ (°C)**	**$T_{m,2}$ (°C)**	**$T_{c,1}$ (°C)**	**$T_{c,2}$ (°C)**
TPU	305	321	-12	166	NA	100	NA
PLA	327	350	63	159	170	102	NA
PCL	328	352	-58	57	68	42	NA
P1 (Mechanophore)	309	328	-59	58	NA	35	NA
HDPE	417	437	nd	130	165	123	120

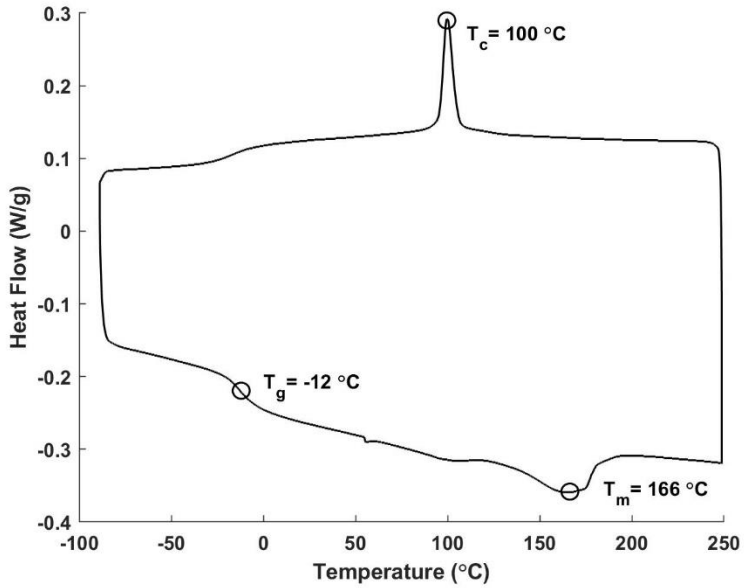

Figure E3A. DSC trace of the first cooling and second heating of TPU. Glass transition, melting, and crystallization temperatures are marked. The experiment was conducted under air with a heating and cooling rate of 10 °C/min.

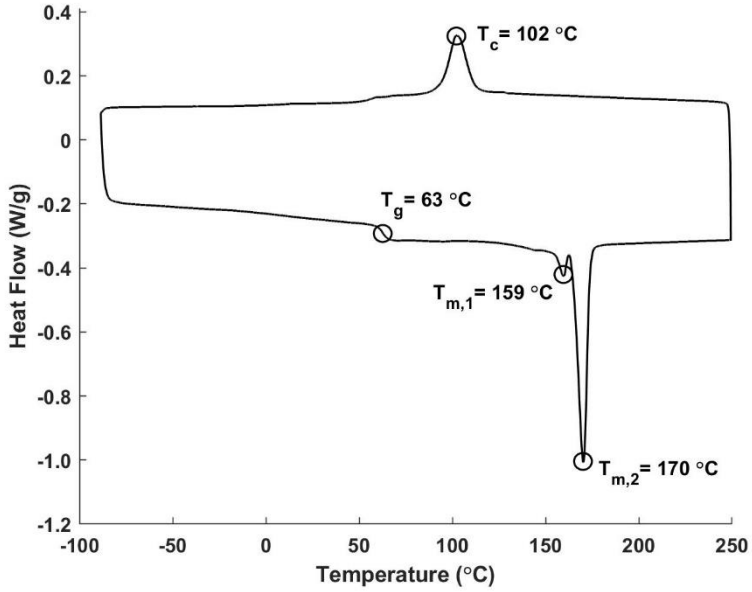

Figure E3B. DSC trace of the first cooling and second heating of PLA. Glass transition, melting, and crystallization temperatures are marked. The experiment was conducted under air with a heating and cooling rate of 10 °C/min.

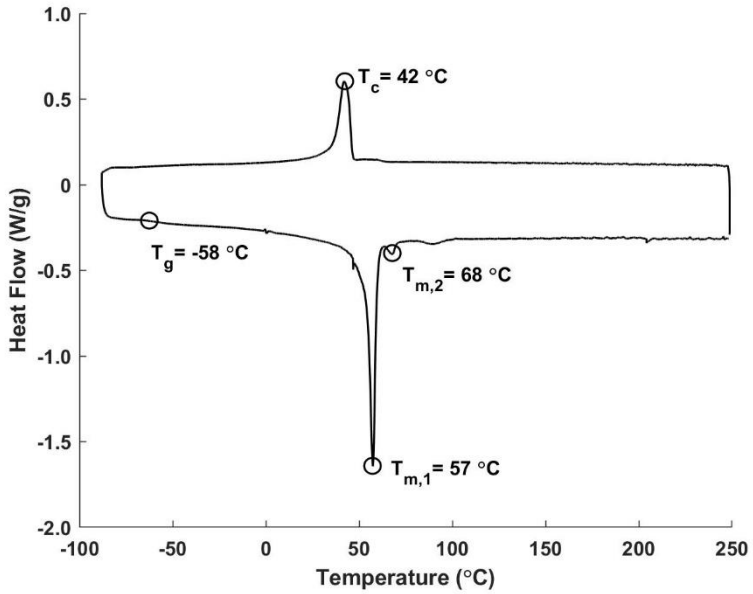

Figure E3C. DSC trace of the first cooling and second heating of PCL. Glass transition, melting, and crystallization temperatures are marked. The experiment was conducted under air with a heating and cooling rate of 10 °C/min.

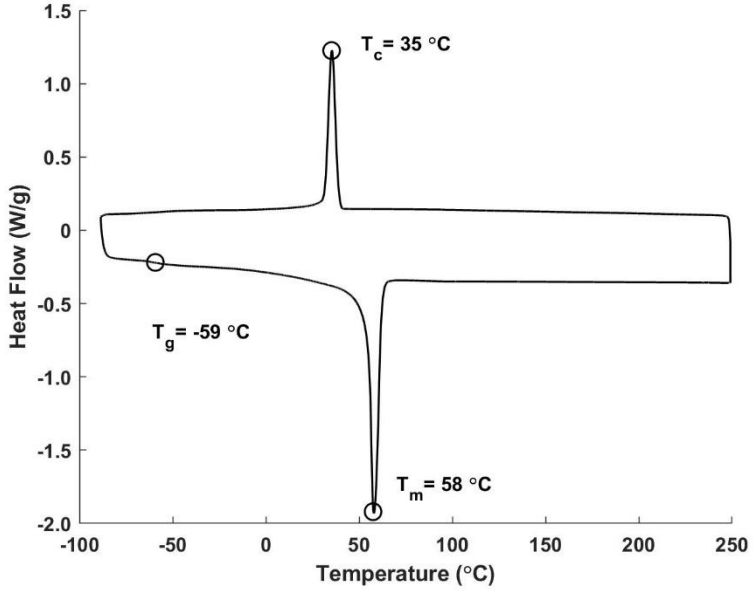

Figure E3D. DSC trace of the first cooling and second heating of P1. Glass transition, melting, and crystallization temperatures are marked. The experiment was conducted under air with a heating and cooling rate of 10 °C/min.

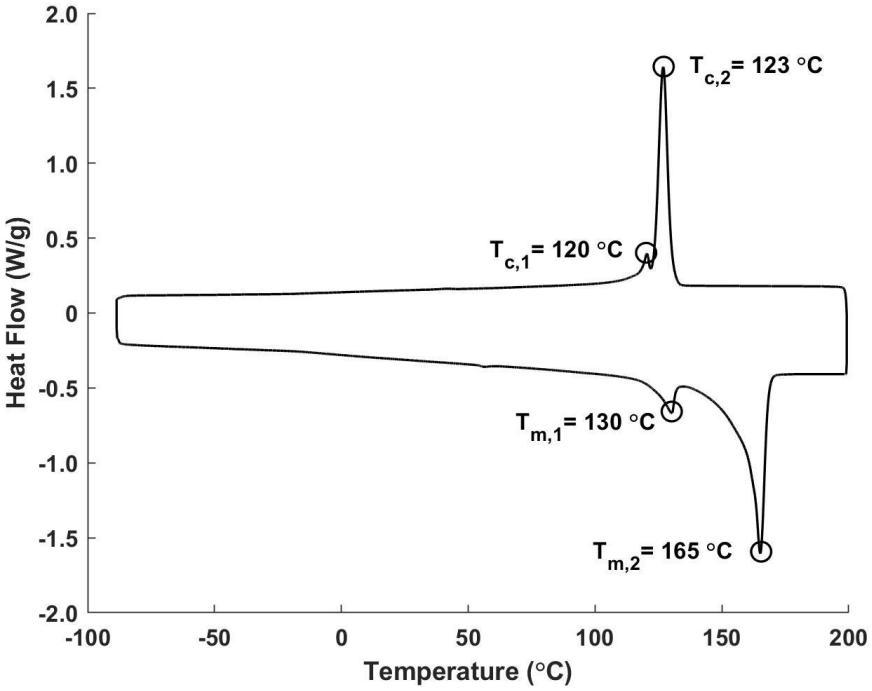

Figure E3E. DSC trace of the first cooling and second heating of mixed HDPE. Glass transition, melting, and crystallization temperatures are marked. The experiment was conducted under air with a heating and cooling rate of 10 °C/min.

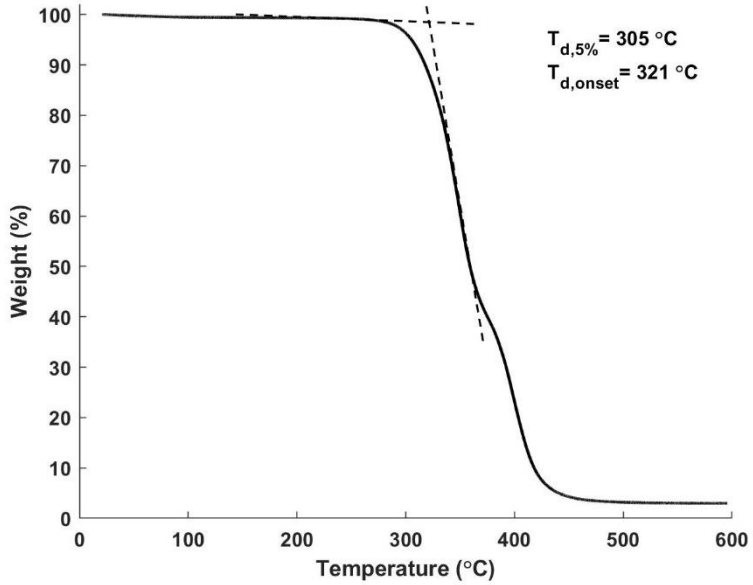

Figure E4A. TGA trace for TPU under nitrogen with a heating rate of 10 °C/min. The 5% degradation temperature and the degradation onset temperature are indicated.

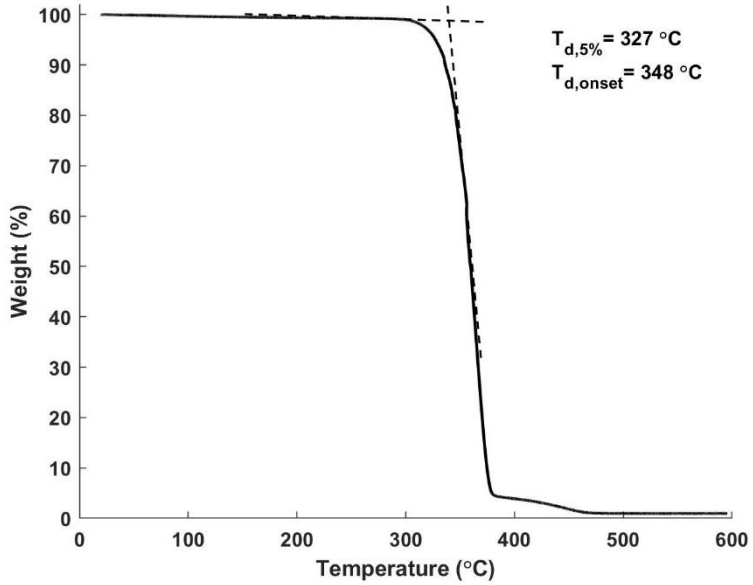

Figure E4B. TGA trace for PLA under nitrogen with a heating rate of 10 °C/min. The 5% degradation temperature and the degradation onset temperature are indicated.

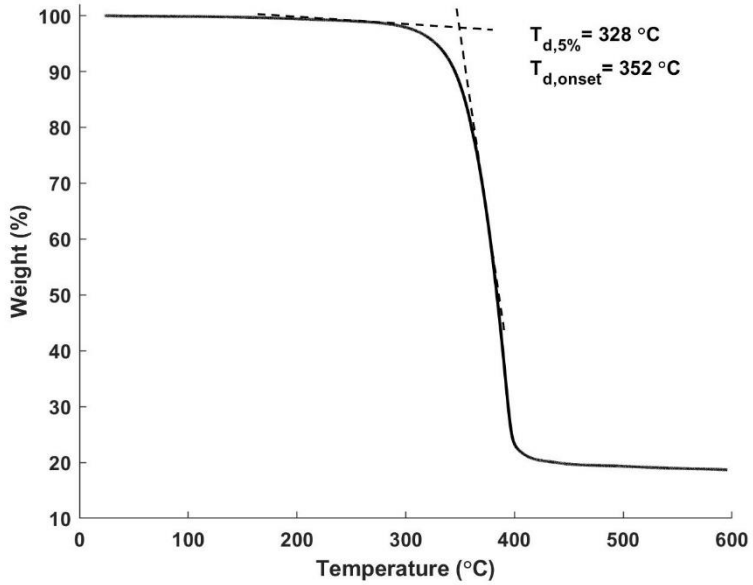

Figure E4C. TGA trace for PCL under nitrogen with a heating rate of 10 °C/min. The 5% degradation temperature and the degradation onset temperature are indicated.

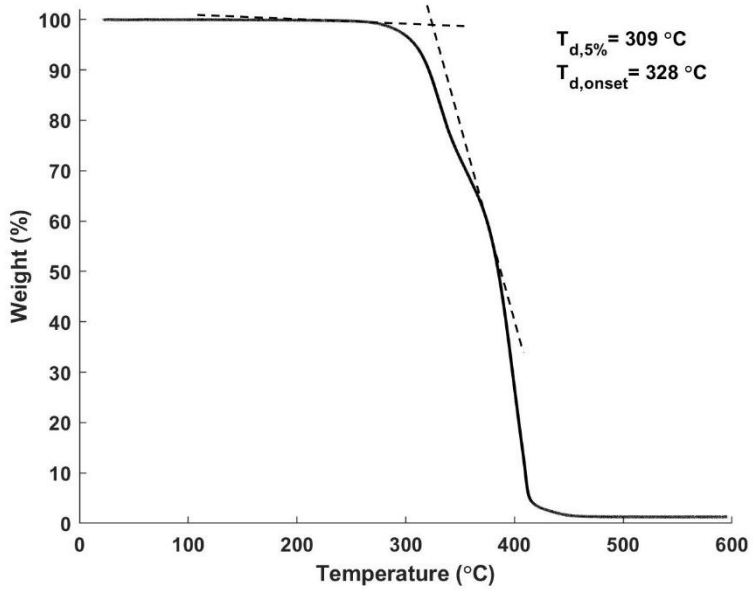

Figure E4D. TGA trace for P1 under nitrogen with a heating rate of 10 °C/min. The 5% degradation temperature and the degradation onset temperature are indicated.

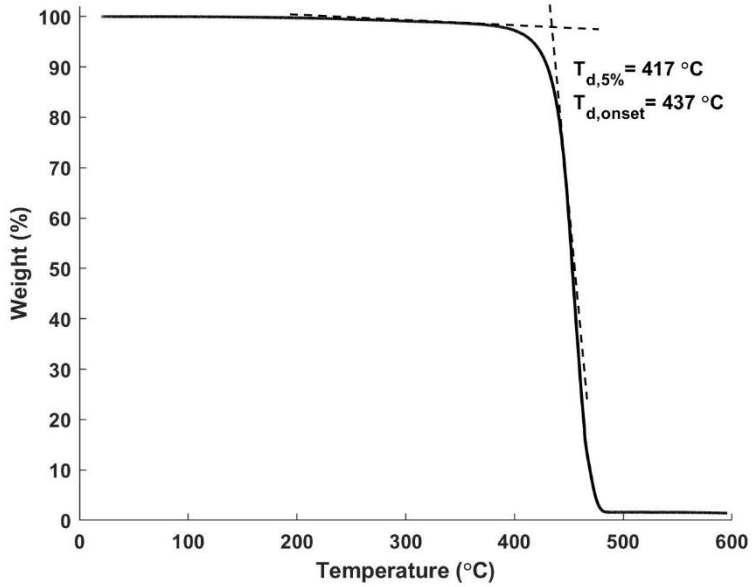

Figure E4E. TGA trace for mixed HDPE under nitrogen with a heating rate of 10 °C/min. The 5% degradation temperature and the degradation onset temperature are indicated.

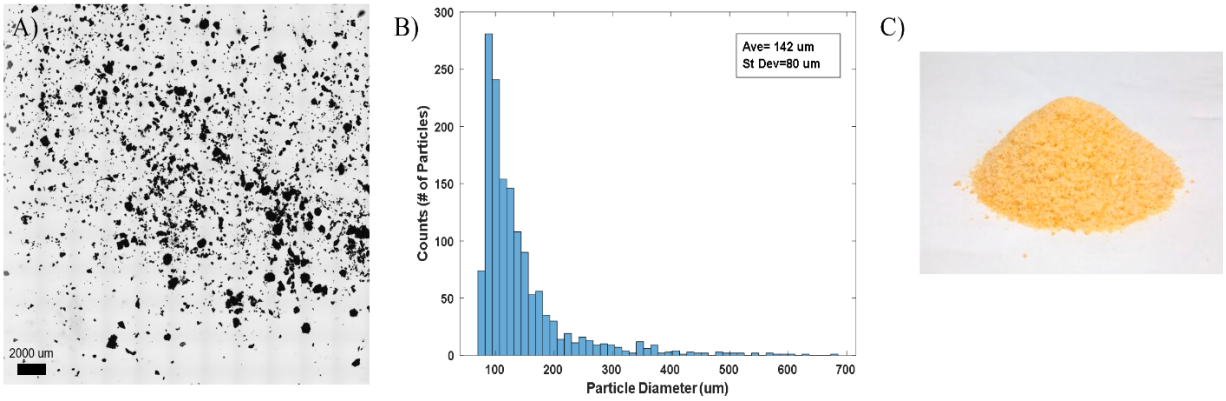

Figure E5. A) Confocal microscopy optical image of particles prepared for PME printing. B) Histogram showing the size distribution of particles prepared for PME printing determined using ImageJ. All particles were less than 700 µm and the average particle size was 142 ± 40 µm. C) Picture of prepared PCL powder

Table E3. Summary of relevant empirically determined print parameters for each material system printed with the PME

Material	Print Temperature (°C)	Print Speed (mm/sec)	Extrusion Multiplier (%)	E steps
TPU	190	10	1500	1000
PLA	200	7	1200	1000
PCL	100	5	1000	1000
PCL-TPU Blend	180	10	1500	1000
P1	180	10	1200	1000
HDPE	150	7	1300	1000
TPU Composite (Glow Powder)	190	10	1500	1000
PCL Composite (Iron Oxide)	100	5	1500	1000

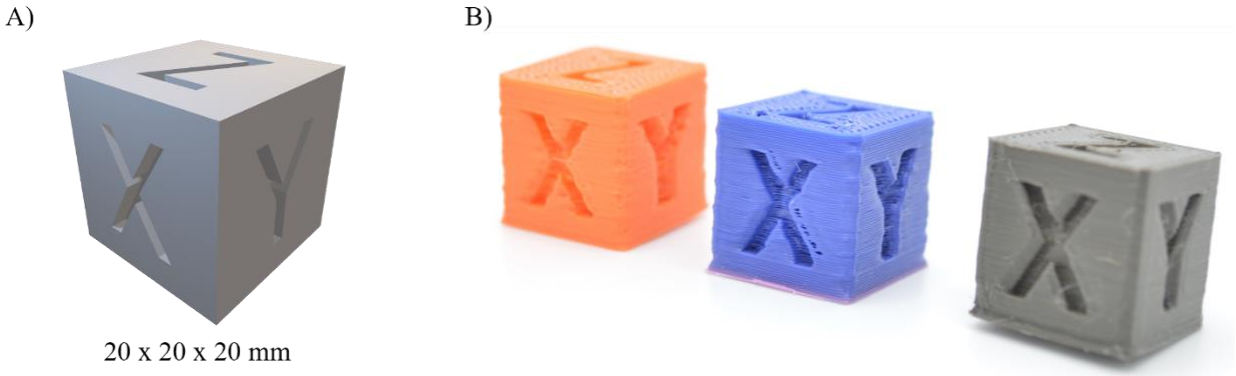

Figure E6. A) STL file of the calibration cube B) PME printed calibration cubes used to determine print accuracy.

Table E4. Summary of the print accuracy along each dimension for the PME and FFF printed calibration cubes.

	X-Axis Accuracy (%)	Y-Axis Accuracy (%)	Z-Axis Accuracy (%)
PME	0.5±0.2	0.5±0.3	1.0±0.7
FFF	0.7±0.1	0.5±0.2	0.7±0.2

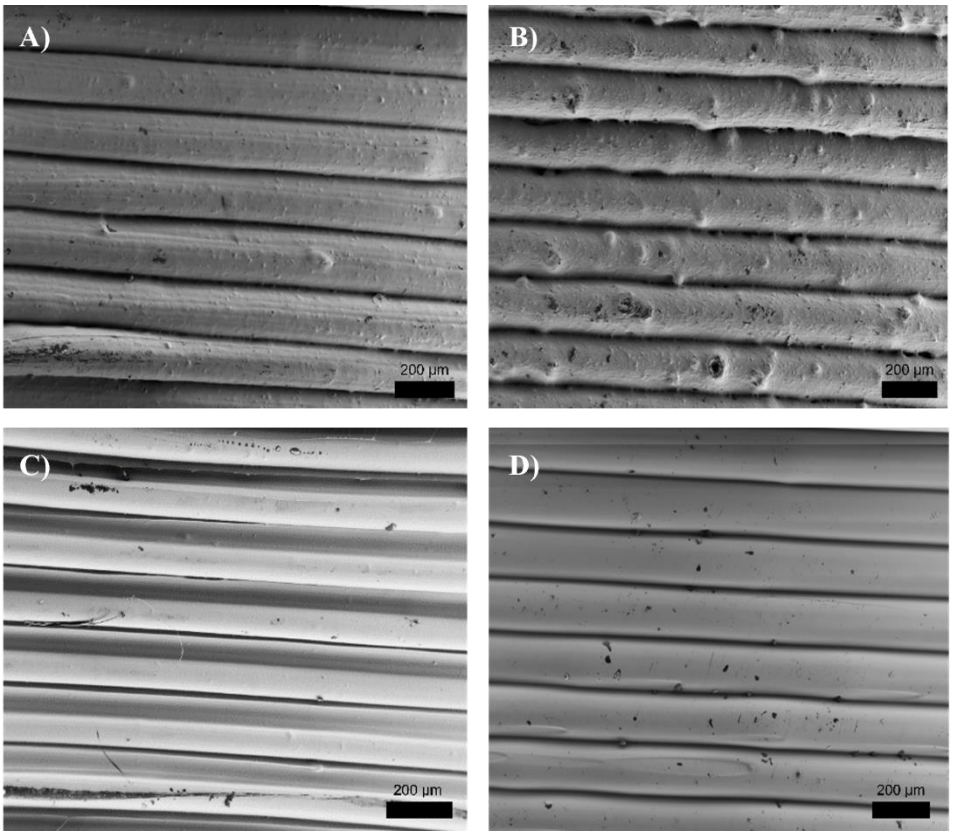

Figure E7. SEM images showing the layer lines of PME and FFF printed PLA and TPU with 200 µm layers. A) PME printed PLA. B) FFF printed PLA. C) PME printed TPU. D) FFF printed TPU.

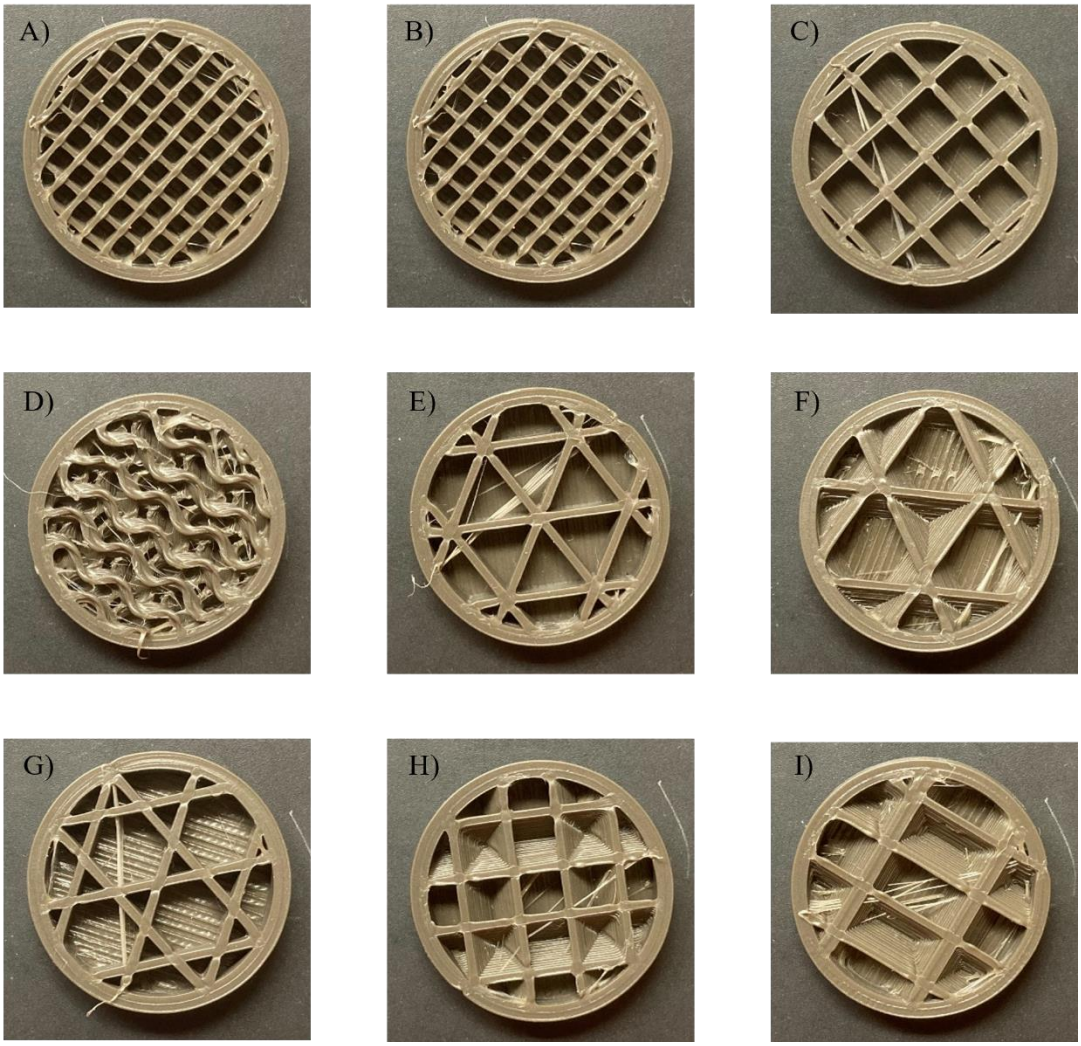

Figure E8. Images showing different infill patterns printed using the PME: A) Grid B) Cubic C) Lines D) Gyroid E) Triangles F) Cubic subdivisions G) Trihexagon H) Octet I) Quarter cubic

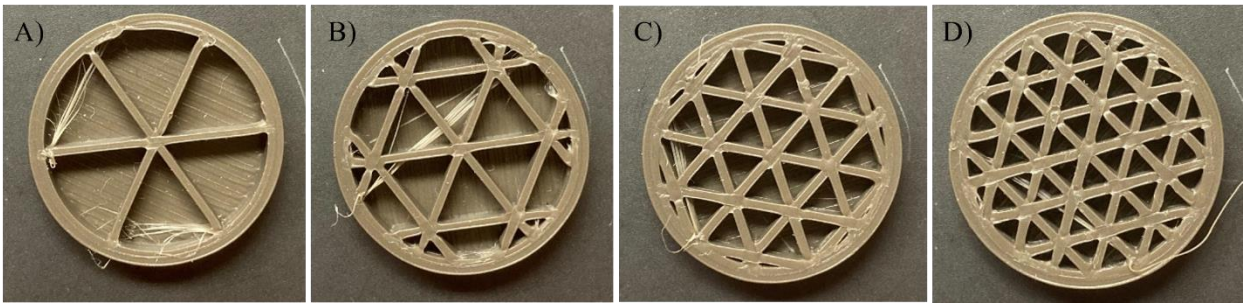

Figure E9. Images showing different infill percentages of trihexagon pattern printed using the PME: A) 15% B) 30% C) 45% D) 60%

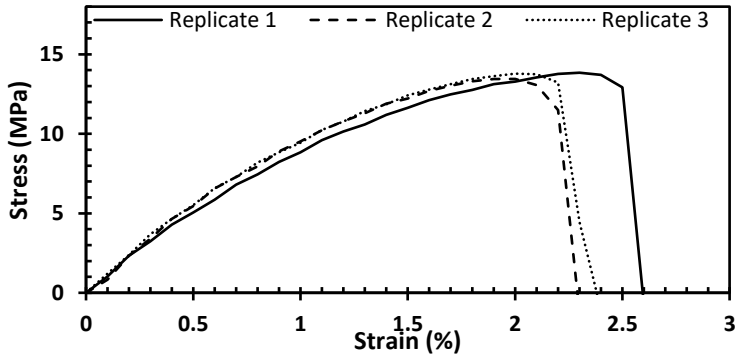

Figure E10A. Stress-strain behavior of ASTM D638 type V samples produced from PCL using a commercial FFF printer. Samples were tested under quasistatic tensile conditions at a strain rate of 10 mm/min.

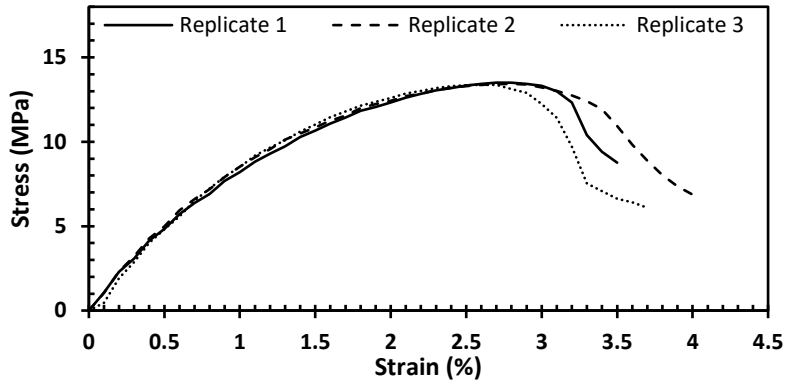

Figure E10B. Stress-strain behavior of ASTM D638 type V samples produced from PCL using a commercial PME printer. Samples were tested under quasistatic tensile conditions at a strain rate of 10 mm/min.

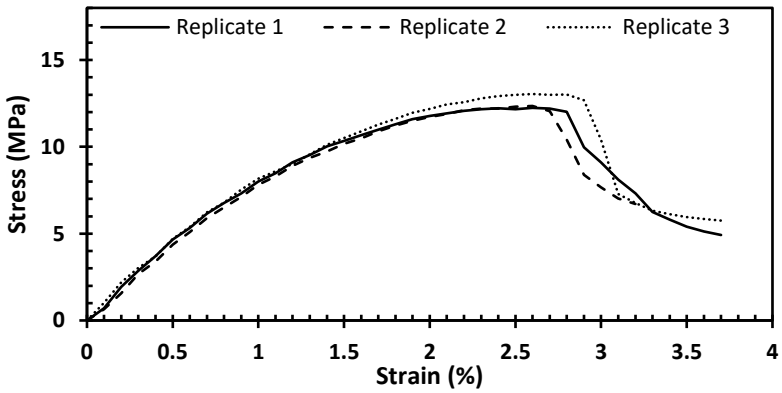

Figure E10C. Stress-strain behavior of ASTM D638 type V samples produced from PCL using a commercial FFF printer at slower speed consistent with PME printed parts. Samples were tested under quasistatic tensile conditions at a strain rate of 10 mm/min.

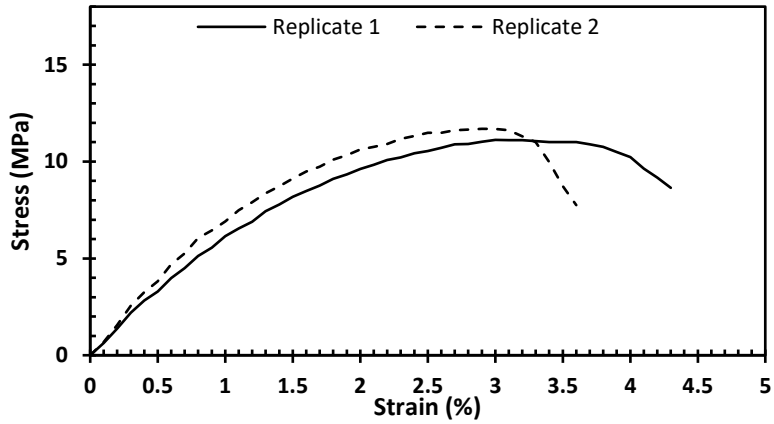

Figure E10D. Stress-strain behavior of ASTM D638 type V samples produced from recycled PCL obtained from reground previously tensile tested samples using a commercial PME printer. Samples were tested under quasistatic tensile conditions at a strain rate of 10 mm/min.

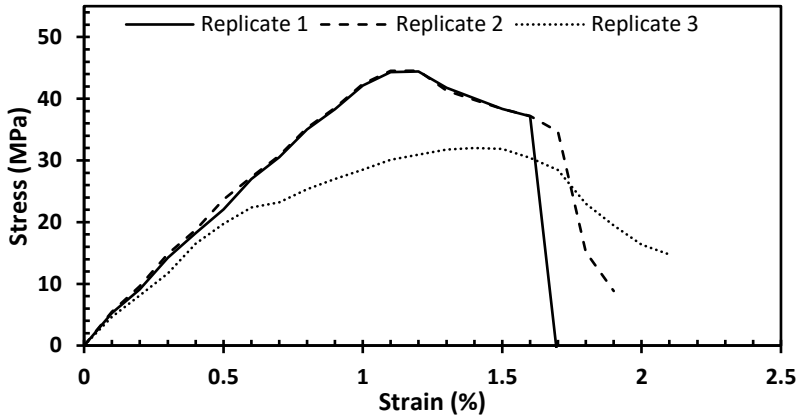

Figure E10E. Stress-strain behavior of ASTM D638 type V samples produced from PLA using a commercial FFF printer. Samples were tested under quasistatic tensile conditions at a strain rate of 10 mm/min.

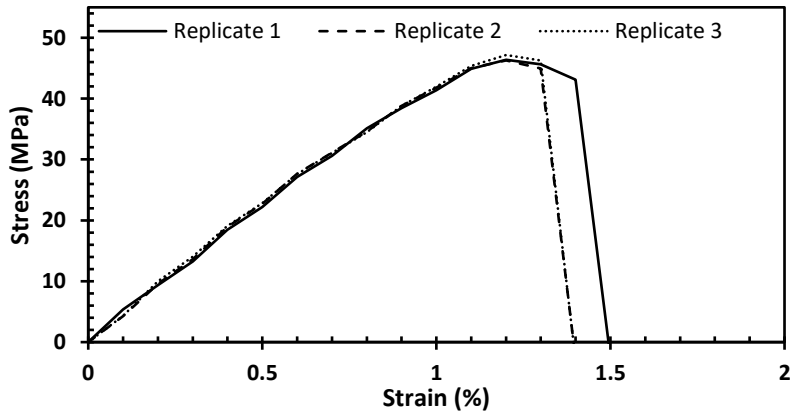

Figure E10F. Stress-strain behavior of ASTM D638 type V samples produced from PLA using a commercial PME printer. Samples were tested under quasistatic tensile conditions at a strain rate of 10 mm/min.

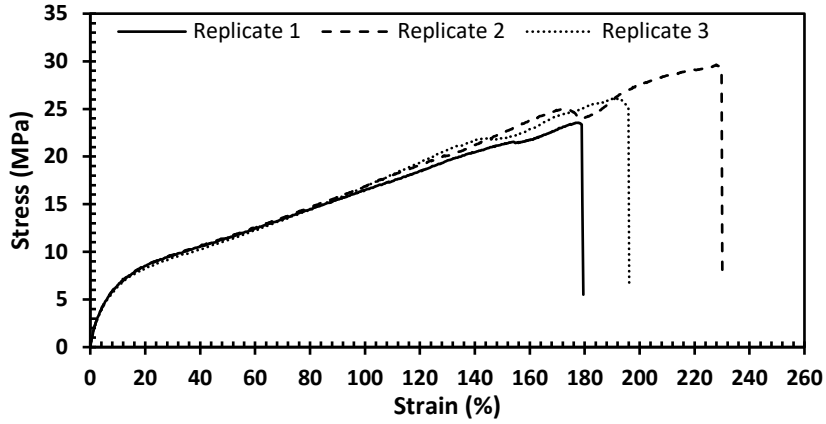

Figure E10G. Stress-strain behavior of ASTM D638 type V samples produced from TPU using a commercial FFF printer. Samples were tested under quasistatic tensile conditions at a strain rate of 100 mm/min.

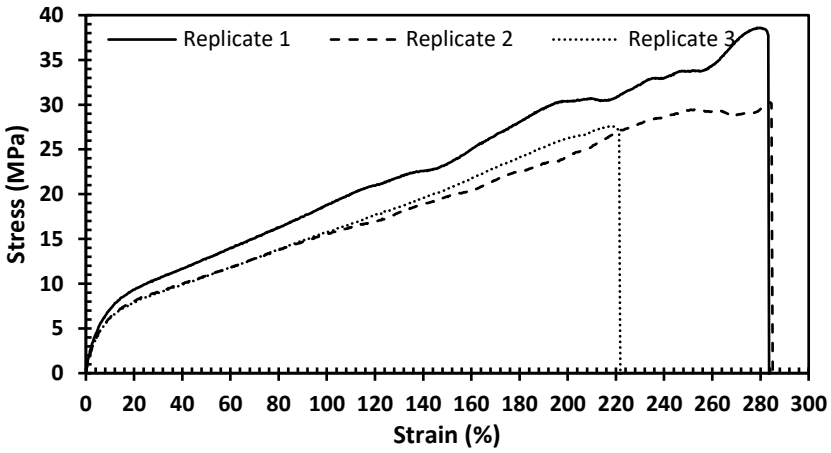

Figure E10H. Stress-strain behavior of ASTM D638 type V samples produced from TPU using a commercial PME printer. Samples were tested under quasistatic tensile conditions at a strain rate of 100 mm/min.

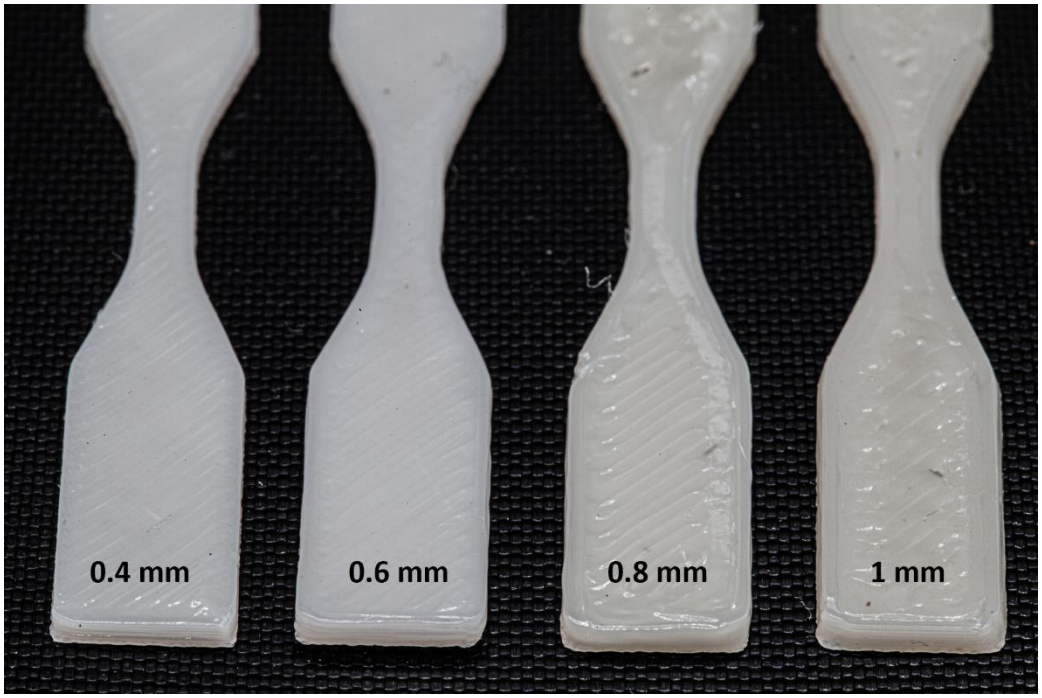

Figure E11. Printed ASTM D638 type V shaped objects using 0.4 to 1 mm nozzle sizes.

Table E5. Empirically determined print parameters for PCL printed with 0.4 to 1 mm nozzle diameters.

Nozzle Diameter (mm)	Print Temperature (°C)	Print Speed (mm/sec)	Extrusion Multiplier (%)	E steps
0.4	100	5	1000	1000
0.6	100	5	1200	1000
0.8	110	5	2000	1000
1	110	5	3500	1000

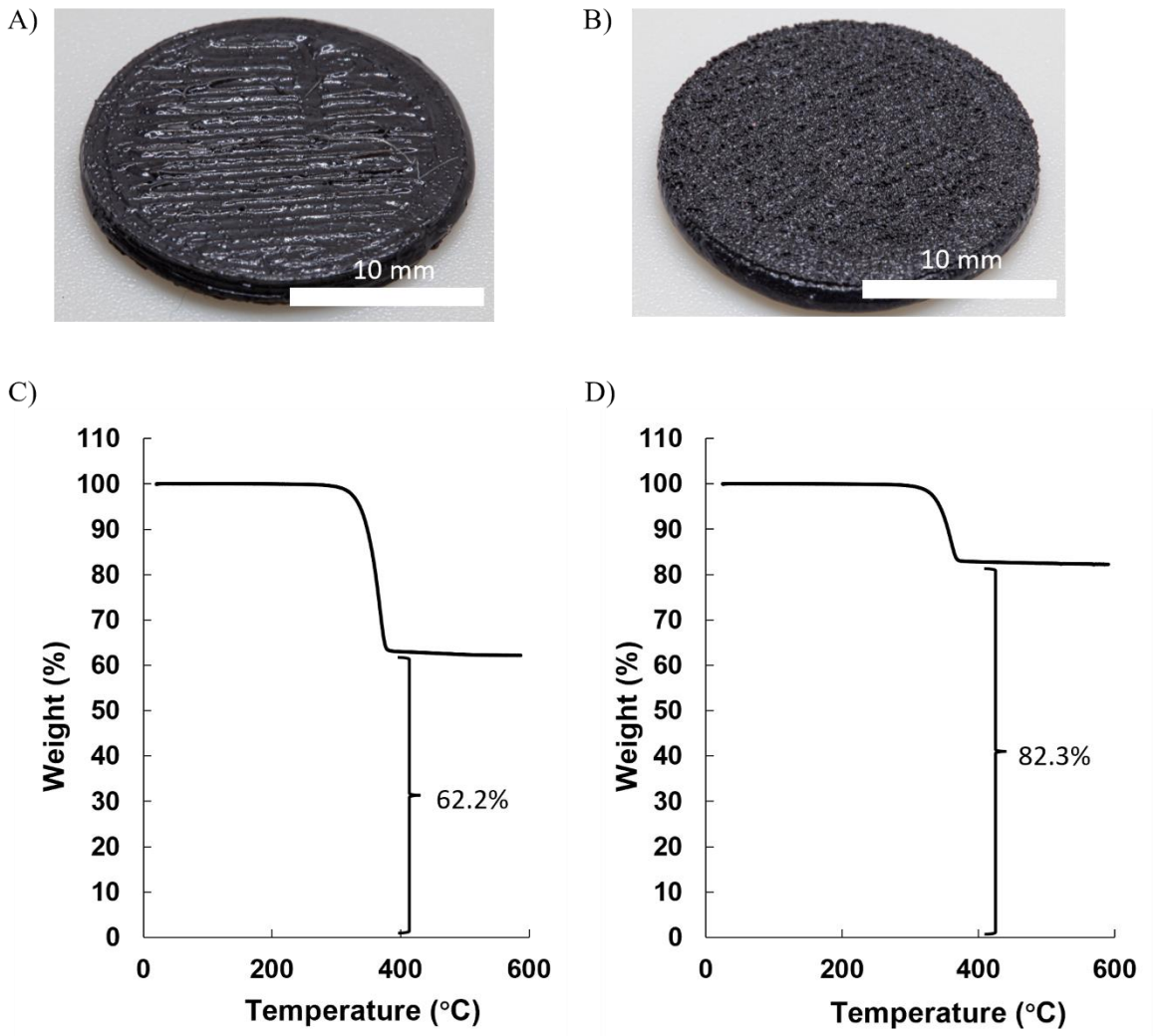

Figure E12. A) PME 3D printed thermoplastic composite containing 60 wt% iron oxide and 40 wt% PCL. B) PME 3D printed thermoplastic composite containing 80 wt% iron oxide and 40 wt% PCL. C) TGA showing the thermal degradation of organic PCL component in the part from figure E12A. Remaining mass is 62.2 % indicating good agreement with loaded mixture. D) TGA showing the thermal degradation of organic PCL component in the part from figure E12B. Remaining mass is 82.3 % indicating good agreement with loaded mixture.

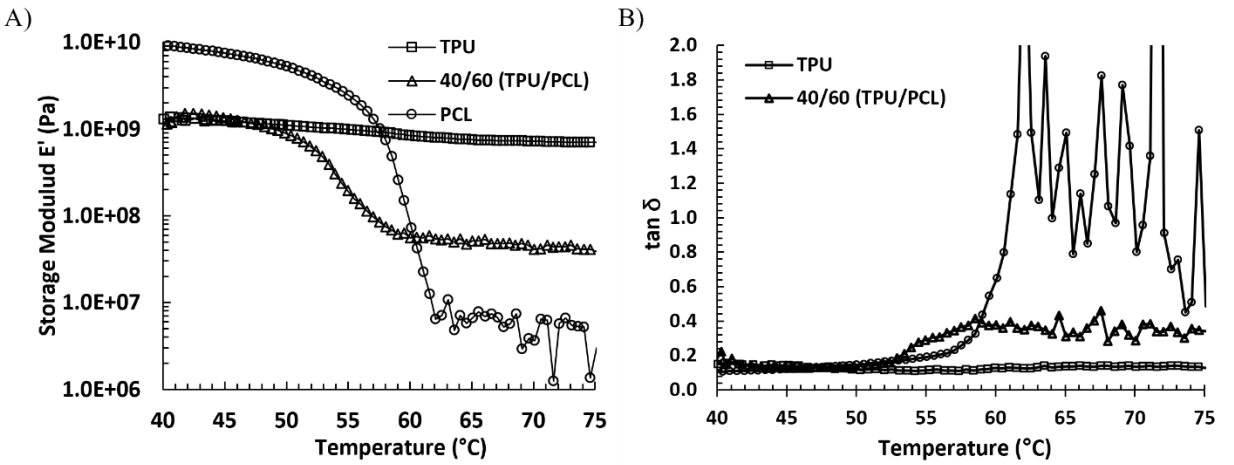

Figure E13. DMA data of the thermomechanical behavior of TPU, 40/60 blend of TPU/PCL by weight, and PCL samples. DMA was performed under a 3-point bend configuration at 0.01 % strain and 1 Hz. A) Temperature dependent storage modulus of TPU, 40/60 blend of TPU/PCL by weight, and PCL samples. B) Temperature dependent tan δ of TPU, 40/60 blend of TPU/PCL by weight, and PCL samples.

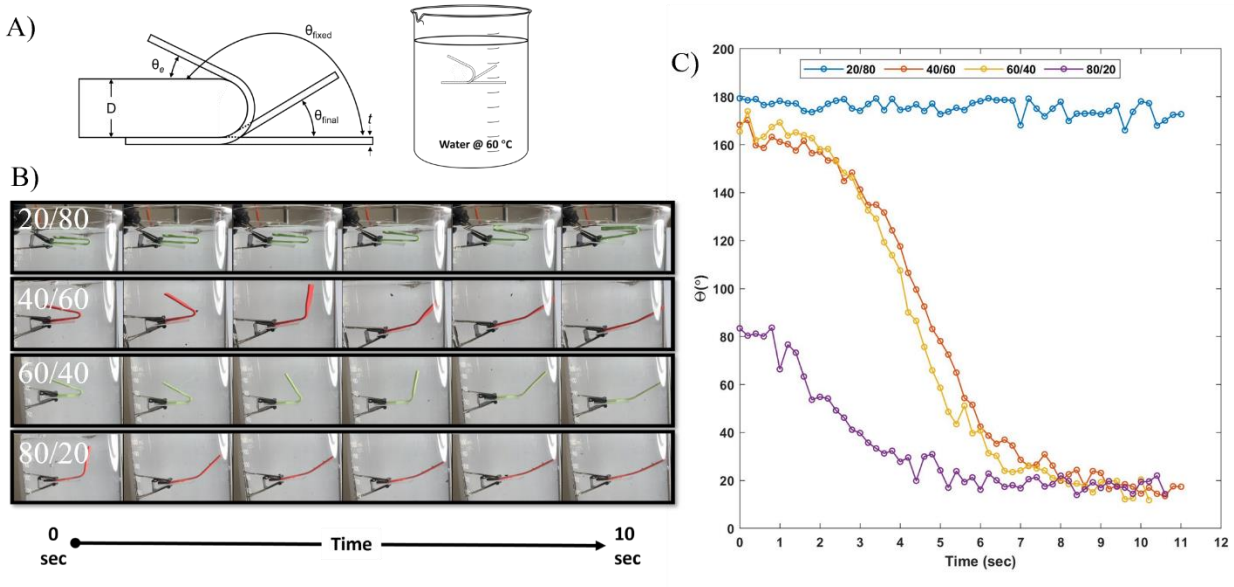

Figure E14. A) Illustration of the bending test and definition of the extracted experimental parameters B) Visualization of the relaxation of representative samples from three replicate experieemtns for different composition TPU/PCL polymer blends. C) Plot showing the change in angle (θ) with time for different polymer blend compositions.

Table E6. Summary of the shape memory properties of various compositions of PCL/TPU blends determined via bending tests and image analysis. Angle were determined using image analysis and tests were done in triplicate. Angle definitions can be seen in Figure E12A.

Sample (TPU/PCL by wt)	θ_e (°)	θ_{final} (°)	η^a (%)
20/80	8 ± 6	169 ± 1	2 ± 3
40/60	13 ± 2	27 ± 12	84 ± 7
60/40	17 ± 4	24 ± 8	85 ± 5
80/20	104 ± 5	21 ± 5	72 ± 8

[a] *Recovery percent (η) determined from the equation:* $\eta = \frac{(\theta_{fixed} - \theta_{final})}{\theta_{fixed}} * 100$

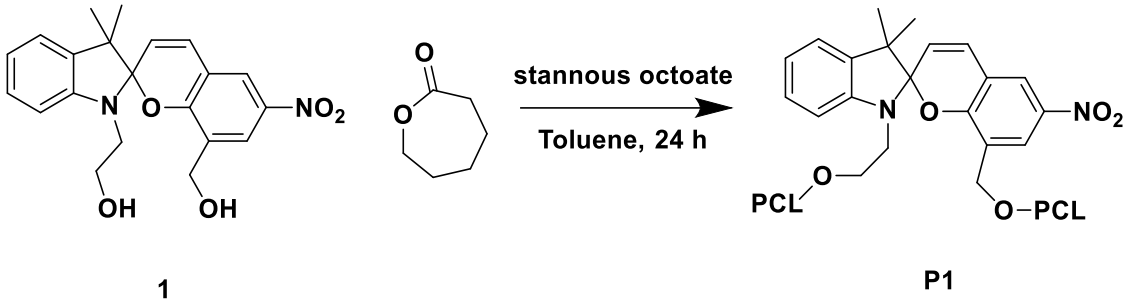

1 P1

Figure E15. Synthetic scheme for synthesis of Spiropyran centered PCL polymer, P1.

Explanation of Additional Supplementary Materials

- Movie 1: PME Printer Operating
- Movie 2: Timelapse of Benchy Printing
- Movie 3: Thermal Responsive Polymer Blend Elastic Energy Storage
- Movie 4: Rapid Shape Recovery of Thermal Responsive Panel
- Open-Source PME Assembly and Operation Guide

Appendix F: Supporting Information for Chapter 9

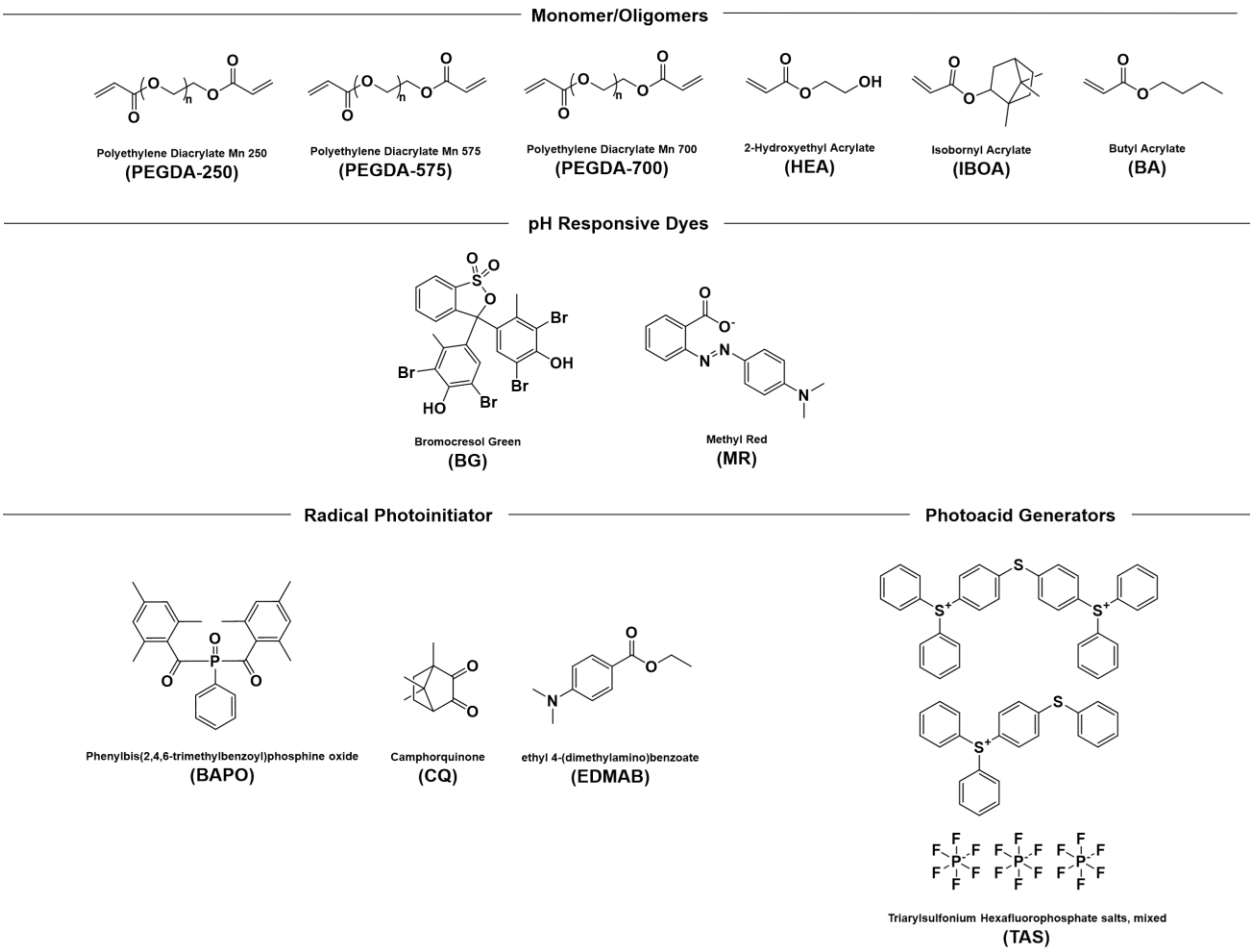

Figure F1. Compounds included in resin formulations along with their structures, names, and abbreviations.

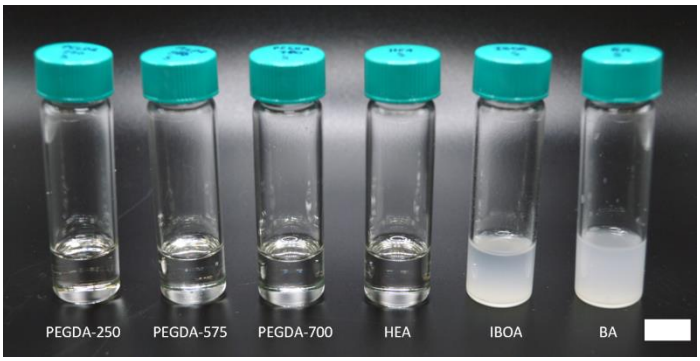

Figure F2) A) Solubility of TAS in PEGDA-250, PEGDA-575, PEGDA-700, HEA, IBOA, and BA at a concentration of 3 wt% compared to monomer. Scale bar= 10 mm

Table F1. Print parameters for each resin printed on a Elegoo Mars 3 printer.

Resin	Normal Layer Time (sec)	Bottom Layer Time (sec)	# Bottom Layers	Layer Thickness (µm)	Lift Distance (mm)	Lift Speed (mm/sec)	Retract Speed (mm/sec)
F1	12	30	6	50	6	60	150
F2	--	--	--	--	--	--	--
F3	12	30	6	50	6	60	150
F4	12	120	8	50	6	60	150
F5	--	--	--	--	--	--	--

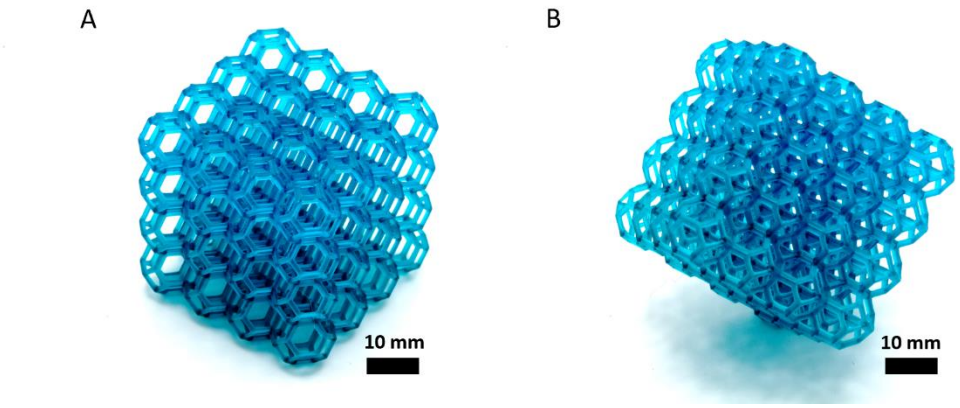

Figure F3. Additional images of complex lattice printed from F1 resin. A) Image taken from above a lattice 3D printed from F1 resin. B) Image taken from the side of a lattice 3D printed from F1 resin.

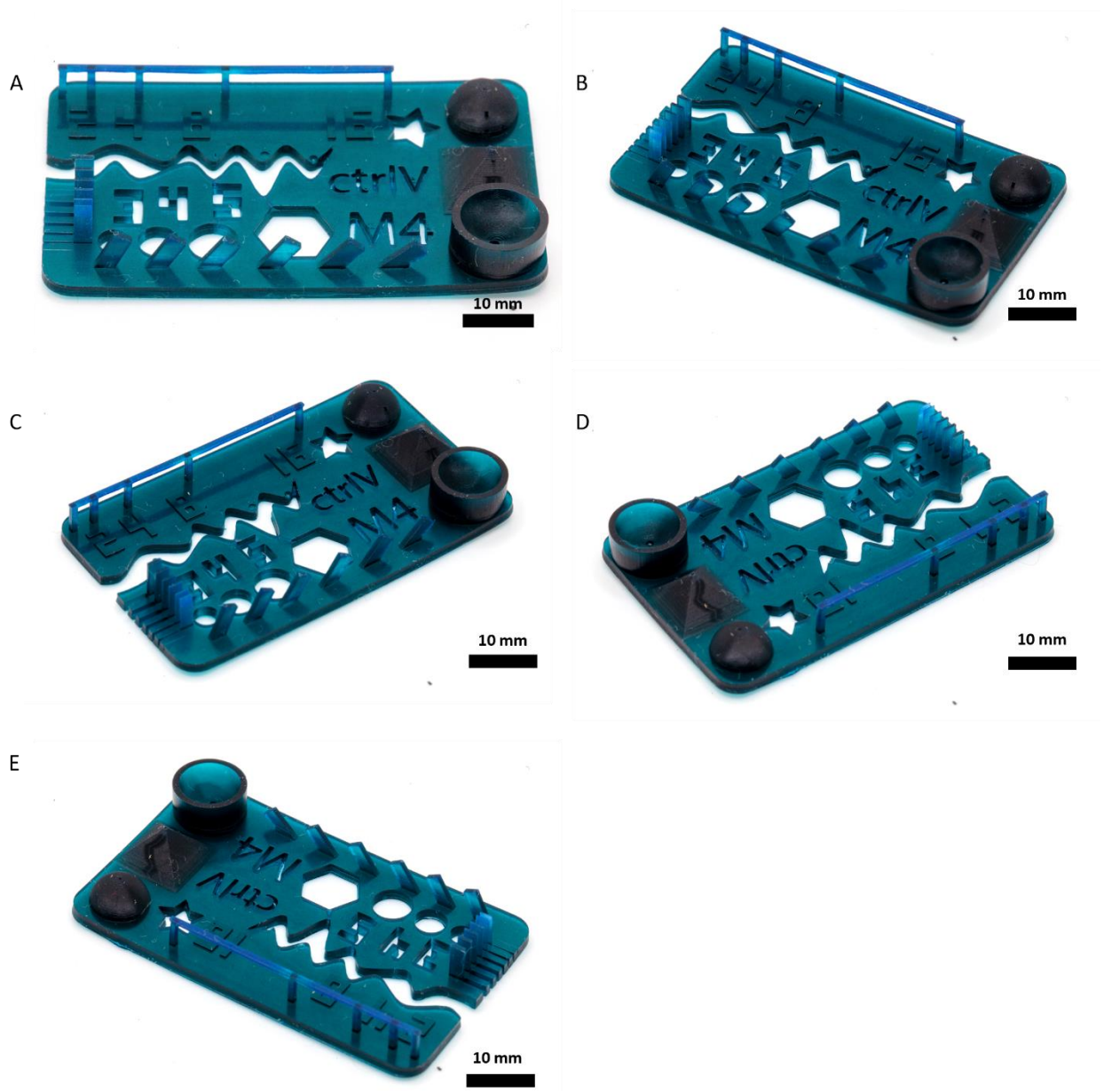

Figure F4. Image of a resolution test object 3D printed from F1 resin taken from different angles. A) front B) tilted right C) tilted left D) back tiled left E) back titled right

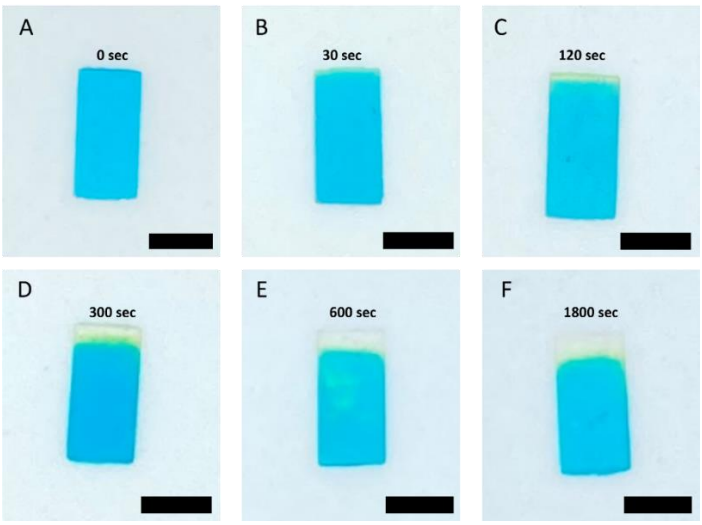

Figure F5. Images of the resulting samples for determining depth of color change with increasing exposures of light. Scale bar= 10 mm A) 0 sec B) 30 sec C) 120 sec D) 300 sec E) 600 sec F) 1800 sec

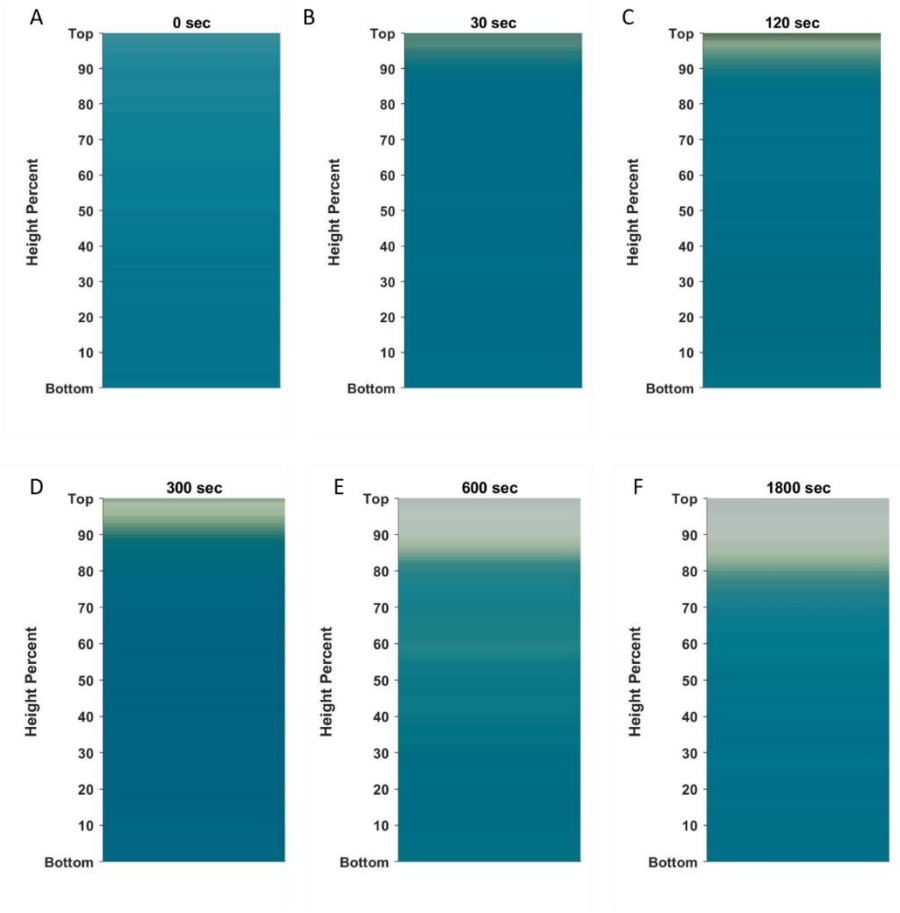

Figure F6. MATLAB extracted images for samples in figure S4 for determining depth of color change with increasing exposures of light. A) 0 sec B) 30 sec C) 120 sec D) 300 sec E) 600 sec F) 1800 sec

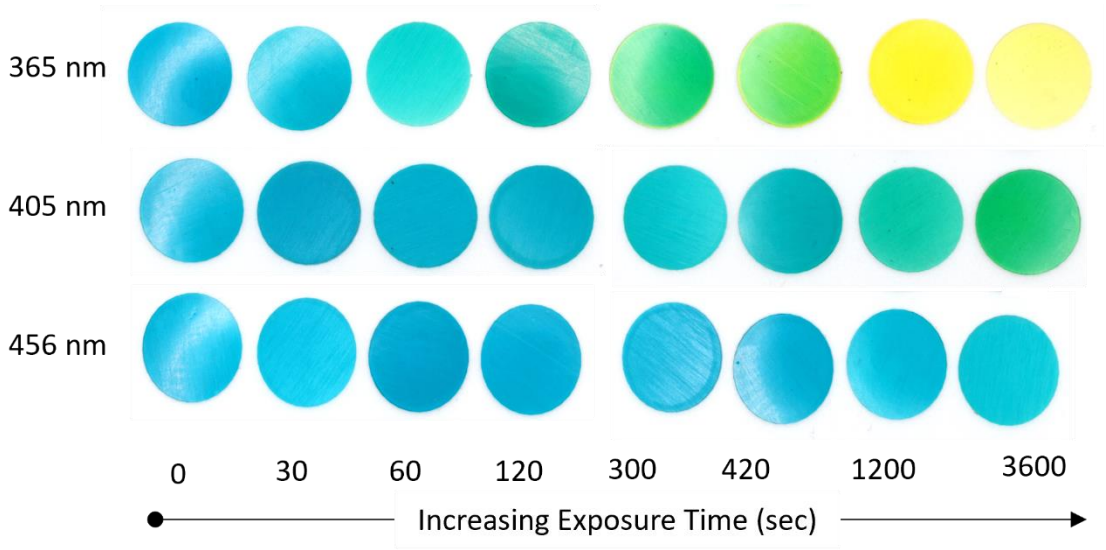

Figure F7. Image of 3D printed samples exposed to various exposures of 10 mW/cm^2 light at either 365 nm (top) 405 nm (middle) or 456 nm (bottom) light.

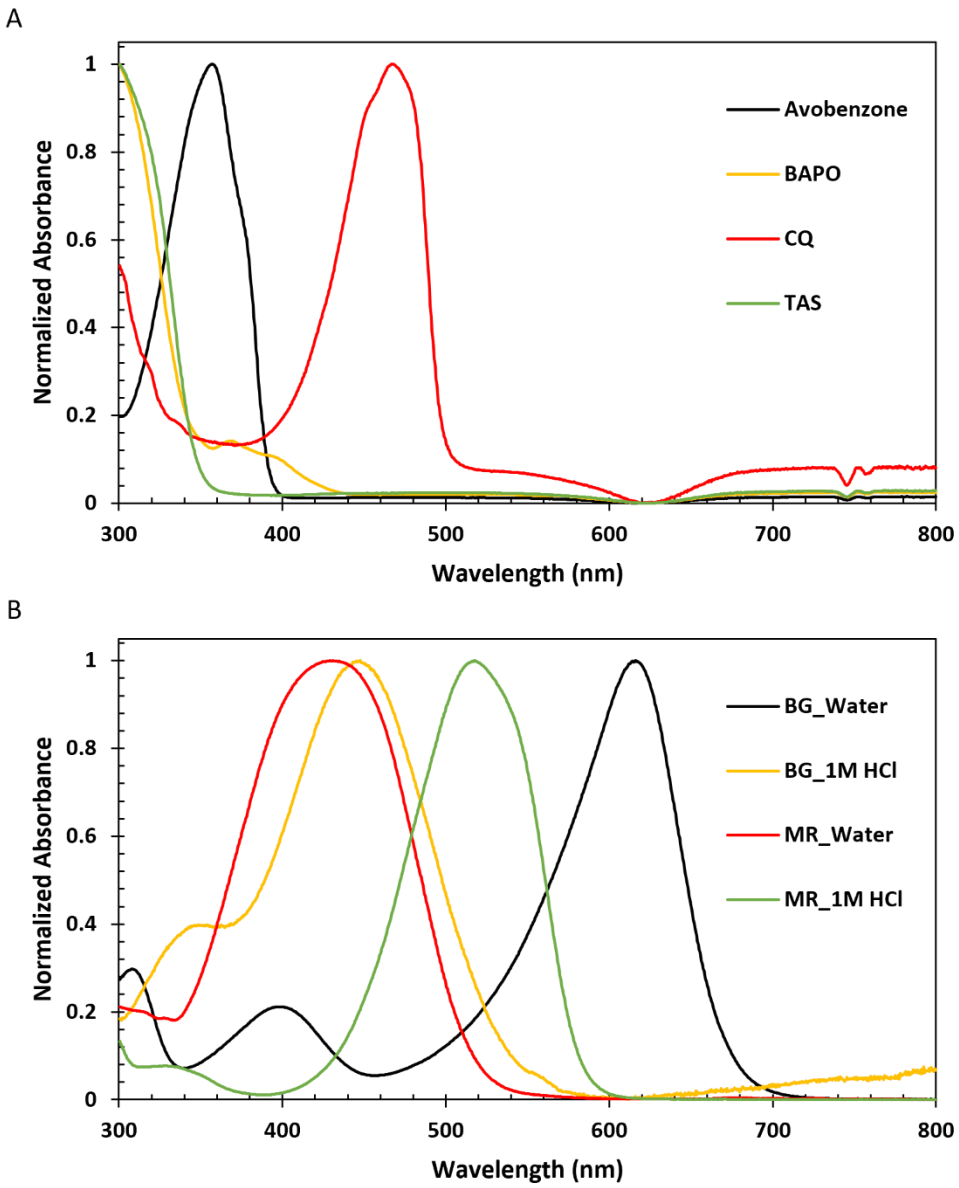

Figure F8. UV-Vis spectroscopy results showing the normalized absorbance v wavelength for A) Avobenzone, BAPO, CQ, and TAS with acetonitrile as solvent B) BG in deionized water, BG in an aqueous 1M HCl solution, MR in deionized water, and MR in an aqueous 1M HCl solution.

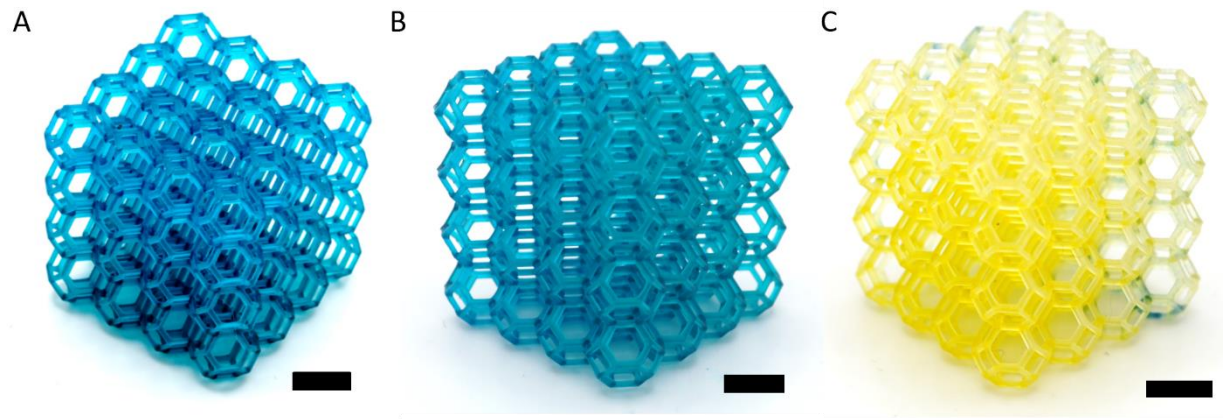

Figure F9. 3D printed lattice from F1 resin. A) As printed B) After 6 weeks stored in the dark C) After 6 weeks stored under ambient lighting

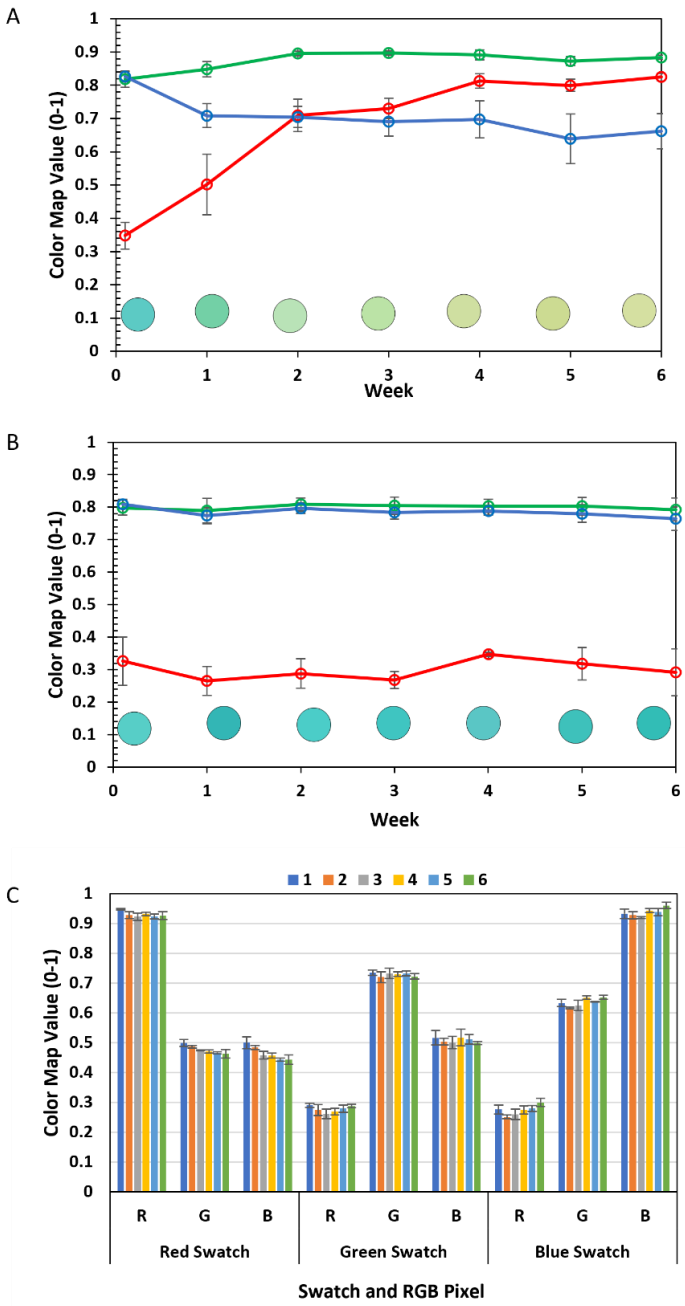

Figure F10. A) RGB value tracking of color change of 3D printed samples from F1 resin over the course of six weeks stored under ambient lighting. Colored circles show the MATLAB extracted value for the color of each sample taken from 10 averaged pixel values across three separate samples. B) RGB value tracking of color change of 3D printed samples from F1 resin over the course of six weeks stored in the dark. Colored circles show the MATLAB extracted value for the color of each sample taken from 10 averaged pixel values across three separate samples. C) RGB values for the color swatches used to over the course of six weeks.

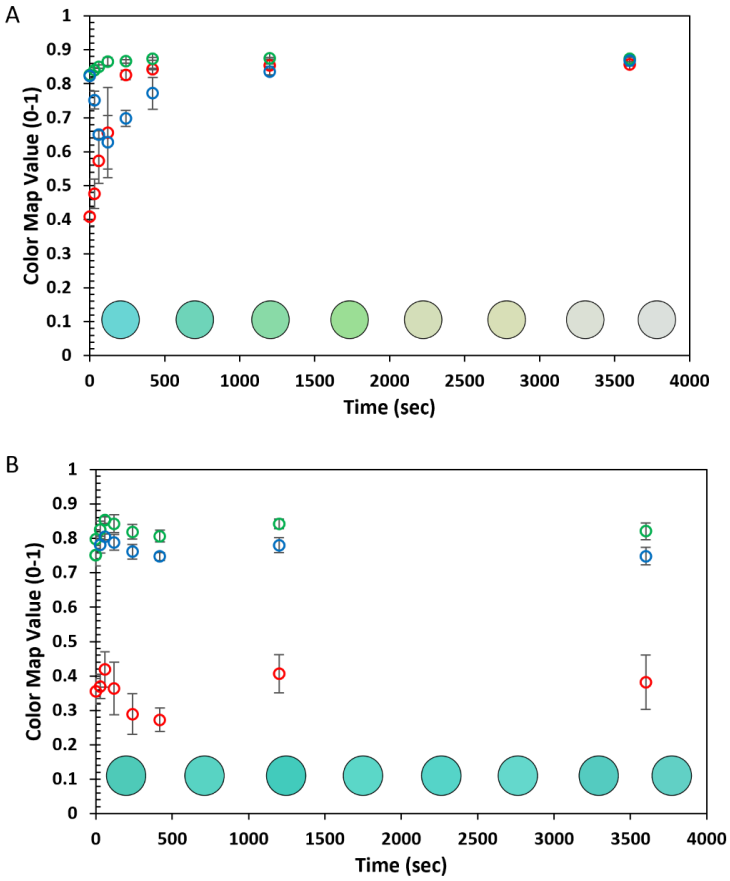

Figure F11. Color stability of samples printed with and without 0.2 wt% avobenzone. A) RGB value tracking of color change of 3D printed samples from F1 resin with increasing exposure to 10 mW/cm2 365 nm light. Colored circles show the MATLAB extracted value for the color of each sample taken from 10 averaged pixel values across three separate samples. B) RGB value tracking of color change of 3D printed samples from F1 resin with 0.2 wt% avobenzone added with increasing exposure to 10 mW/cm2 365 nm light. Colored circles show the MATLAB extracted value for the color of each sample taken from 10 averaged pixel values across three separate samples.

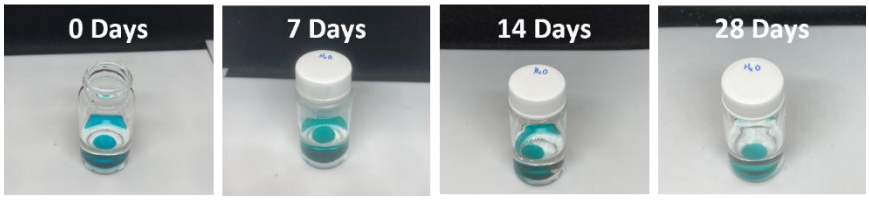

Figure F12) Images of F1 printed samples submerged into water for 0, 7, 14, and 28 days.

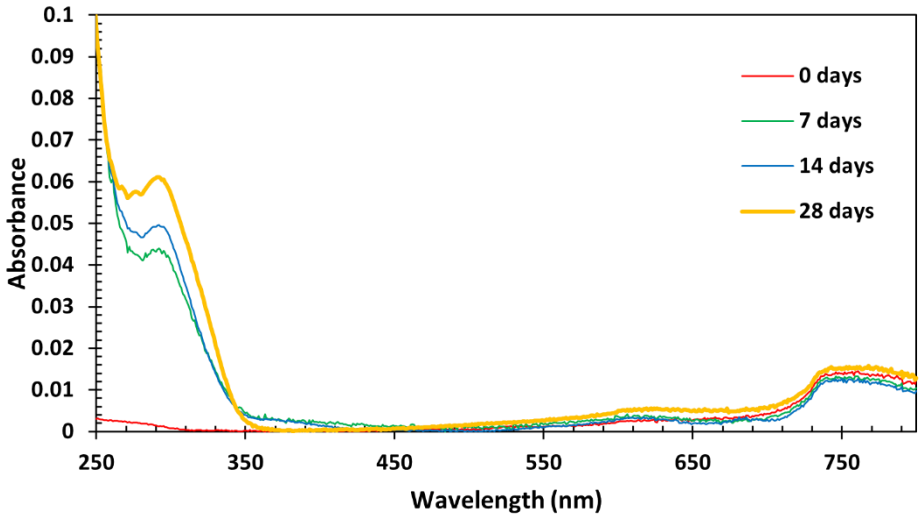

Figure F13) UV-Vis spectra of solution with printed F1 samples submerged at 0, 7, 14, and 28 days. A small peak begins to appear between 550 and 650 nm indicating almost negligible leaching of BG dye into the water.

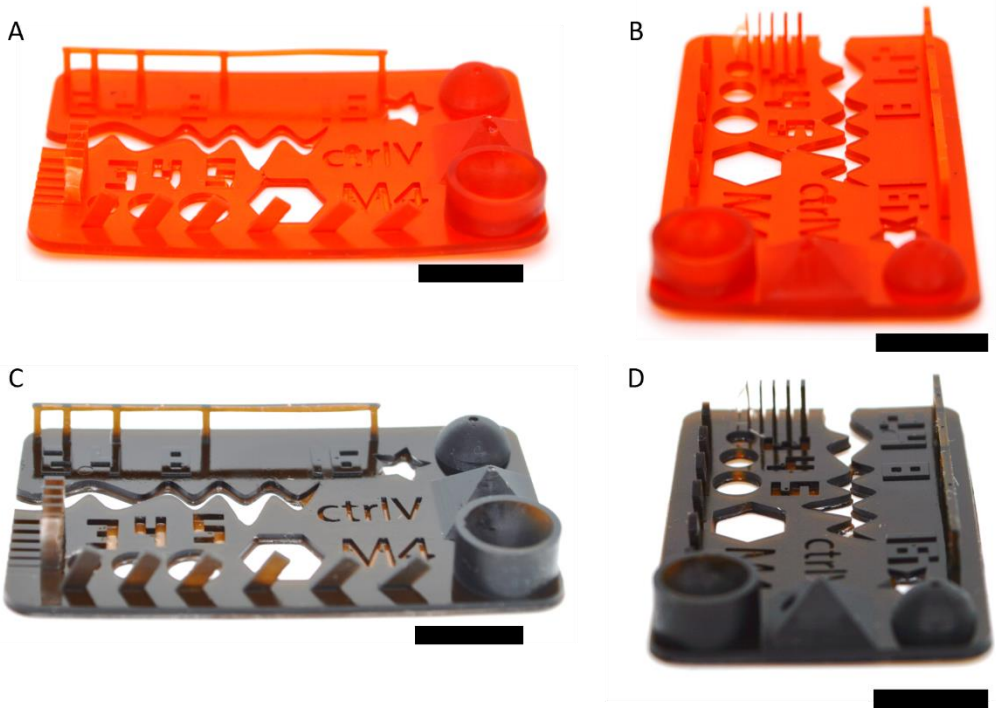

Figure F14) Resolution test prints of F3 and F4 resin printed with a commercial 3D printer. A) F3 front view of test print. B) F3 side view of test print. C) F4 front view of test print. D) F4 side view of test print.

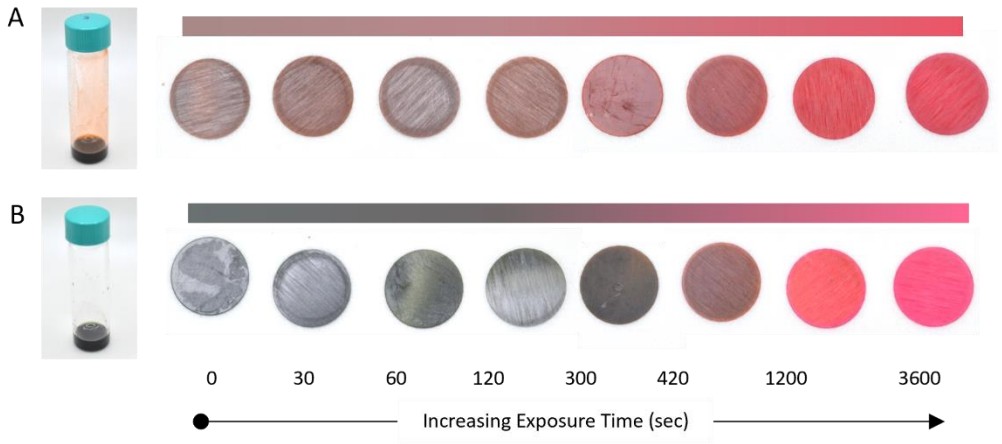

Figure F15) A) Resin formulation for F4 made with a 1:3 ratio of BG and MR. To the right of the resin are printed disks exposed to increasing dosages of UV 365-nm light. B) Resin formulation for F4 made with a 3:1 ratio of BG and MR. To the right of the resin are printed disks exposed to increasing dosages of UV 365-nm light.

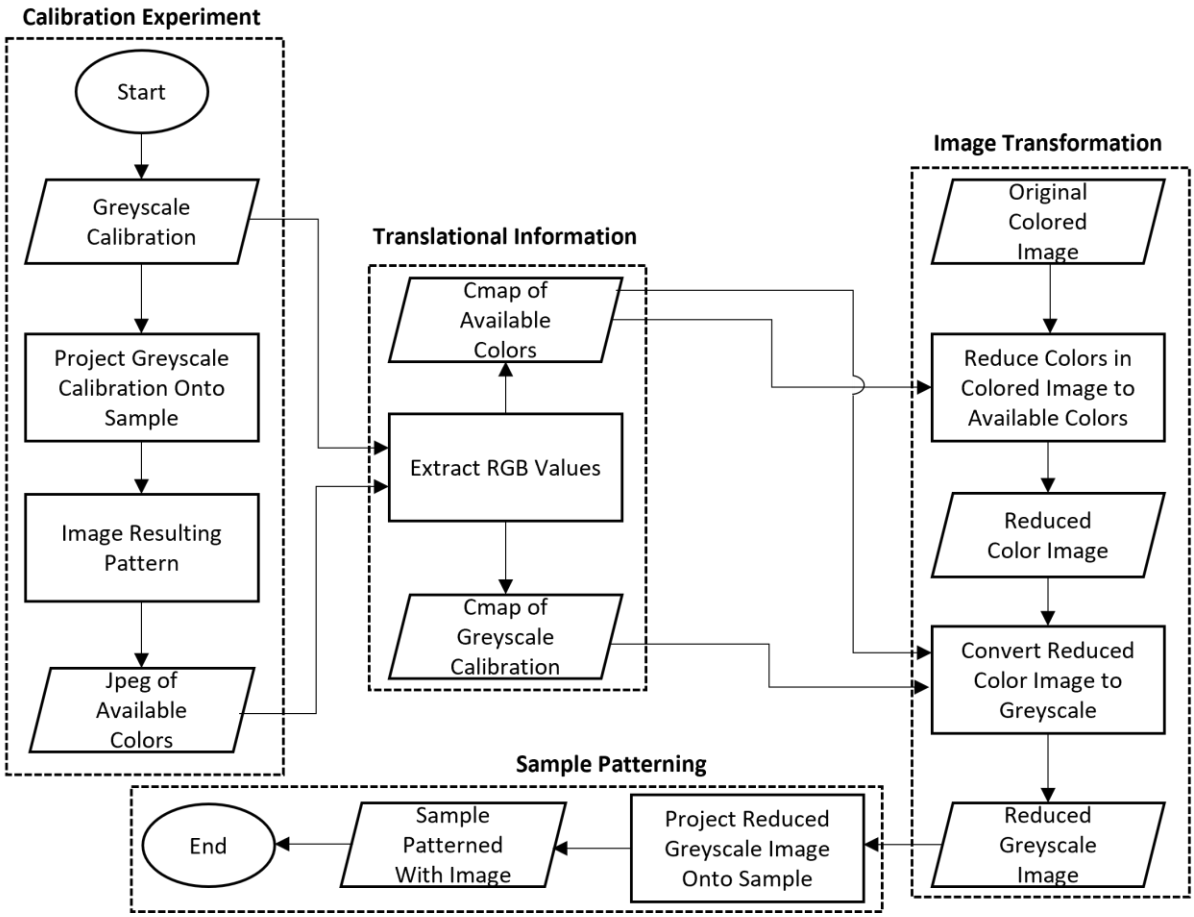

Figure F16) Flowchart of the workflow for photopatterning object printed from multicolor resins using MATLAB.

A

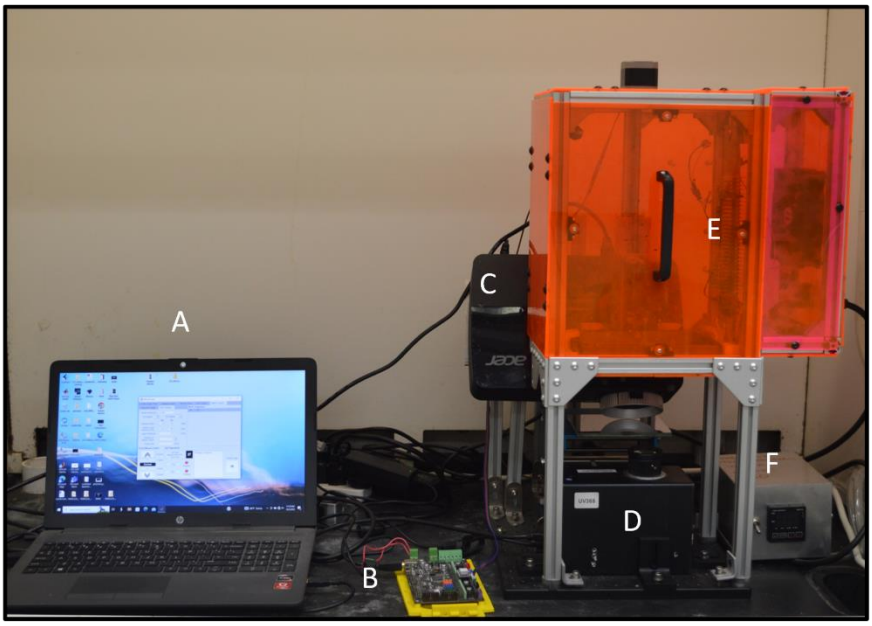

A. Computer displaying MATLAB app for printer operation

B. Controller board

C. White light projector

D. UV light projector with 365 nm LED

E. Printer body

F. Temperature controller

B

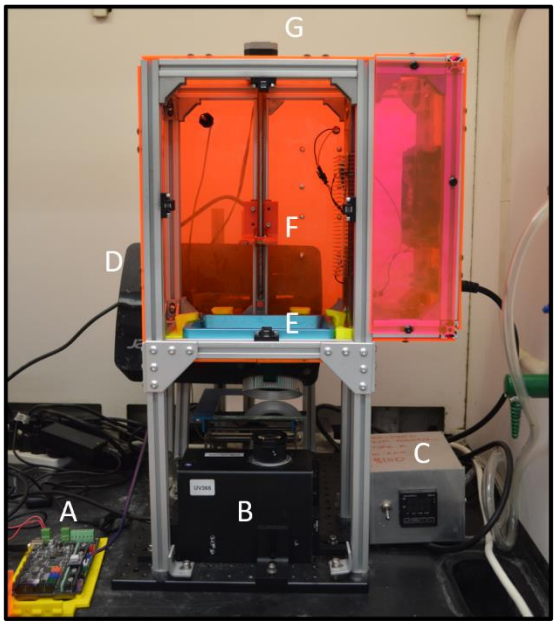

A. Controller board

B. UV light projector with 365 nm LED

C. Temperature controller

D. White light projector

E. Resin vat

F. Build plate attachment point

G. Z-axis stepper motor

Figure F17) Images of the custom dual-wavelength printer with key components labeled. A) Entire 3D printer including the computer with MATLAB app used to operate printer. Key components are labeled to the right of the image. B) Zoomed in image of printer hardware with key components labeled to the right of the image.

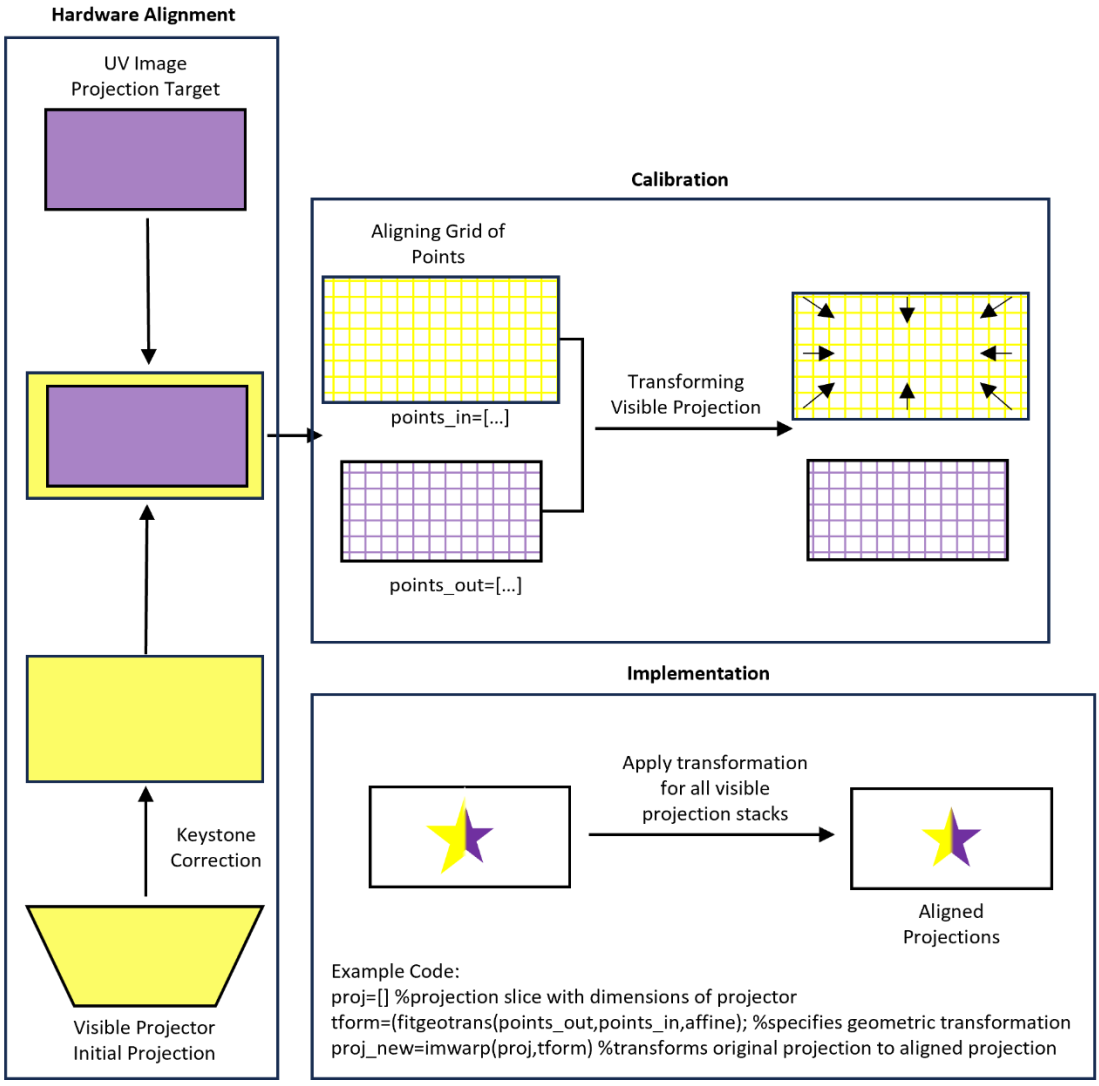

Figure F18. Flowchart showing the process used to align the visible and UV projector images. Both hardware and software were used to align images. The hardware alignment involved keystone correction to account for image distortion from projector angle. Then image transformation of each layer slice of the visible image is performed using a calibration by mapping a grid for each projector area.

Calibration Step (only needs to be performed once for a given printer setup):

1. Both projectors show a grid of 493 evenly spaced points across the entire projection area
2. The pixel coordinates for the intersection of the grid lines were selected from top left to bottom right in sequential order.
3. The same was done for the UV projection grid.
4. Each point was saved in an array.
5. Point coordinated of visible projector were stored in points_in array, while corresponding points on UV projector were stored in points_out array.
6. output_dim (resolution of UV projector), points_in (coordinates of clicked points on Visible projected image), and points_out (coordinates of of clicked points on uv projected image) were exported as 493_points.mat file, which is recovered during implementation step.

Implementation (align the larger projection, in our case the visible projector, to the smaller projection, in our case the uv projector)

1. The imwarp function was used to shrink the visible projection down to the UV projection using the point mapping previously identified in the calibration step (493_points.mat).
2. Pad the resized image on all sides using padarray, replicating edge values to fill new pixels. Since the edge values typically correspond to black color, it practically means we are assigning a ‘black’ color to fill the newly added borders, integrating them seamlessly with the original content of the image.
3. Repeat for all of the projections for a given sliced 3D model.

Table F2) Print parameters used for dual-wavelength printing of multicolor resins from a single resin vat.

Resin	Visible Layer Time (sec)	UV Layer Time (sec)	Layer Thickness (μm)	Lift/Retract Distance (mm)
F1	4	180+	100	5
F5	25	160	100	5

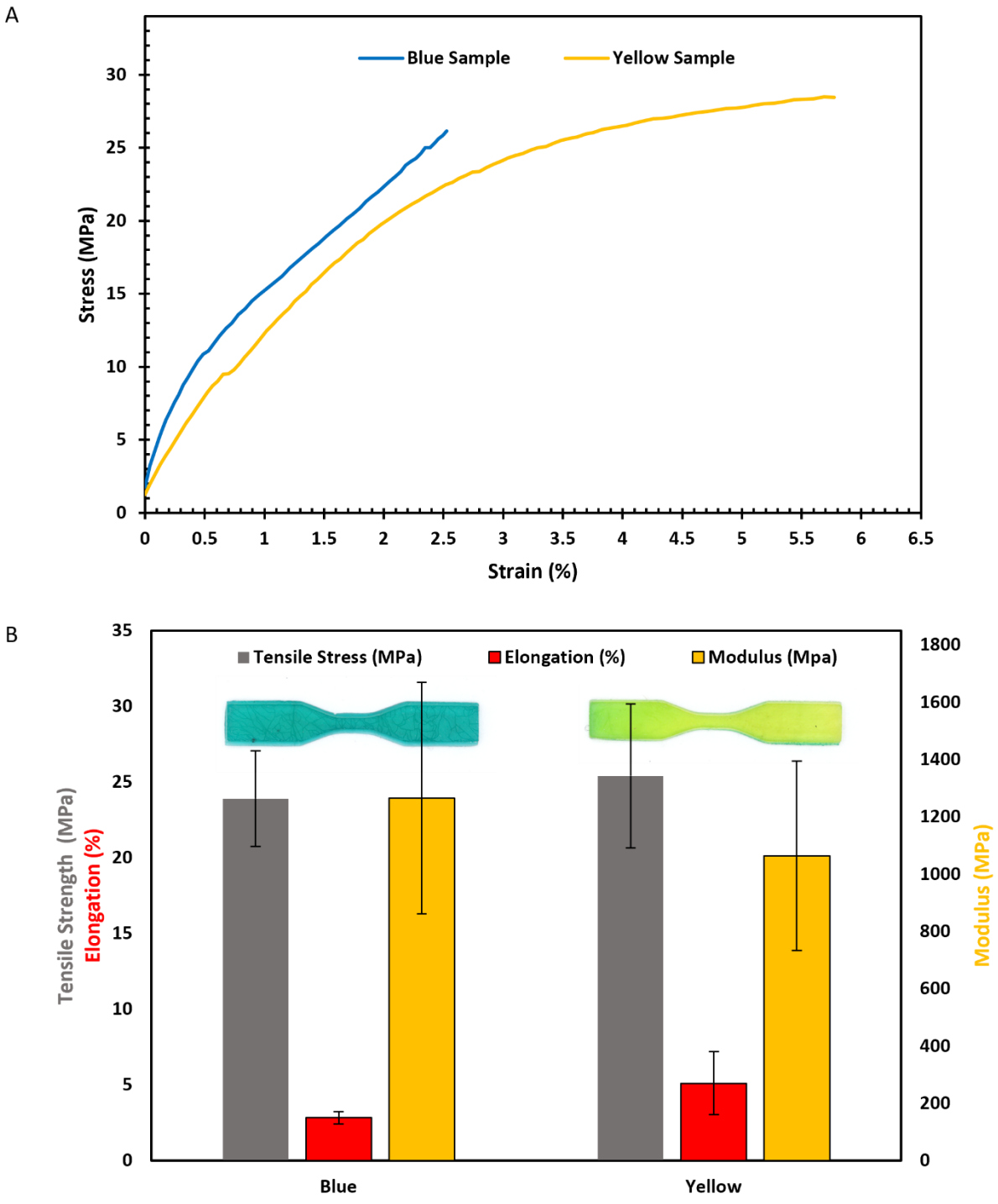

Figure F19) A) Representative tensile plot for blue and yellow samples under quasistatic tensile testing. B) Summary of tensile strength, elongation, and modulus results for quasistatic tensile testing with three replicates of blue and yellow samples.

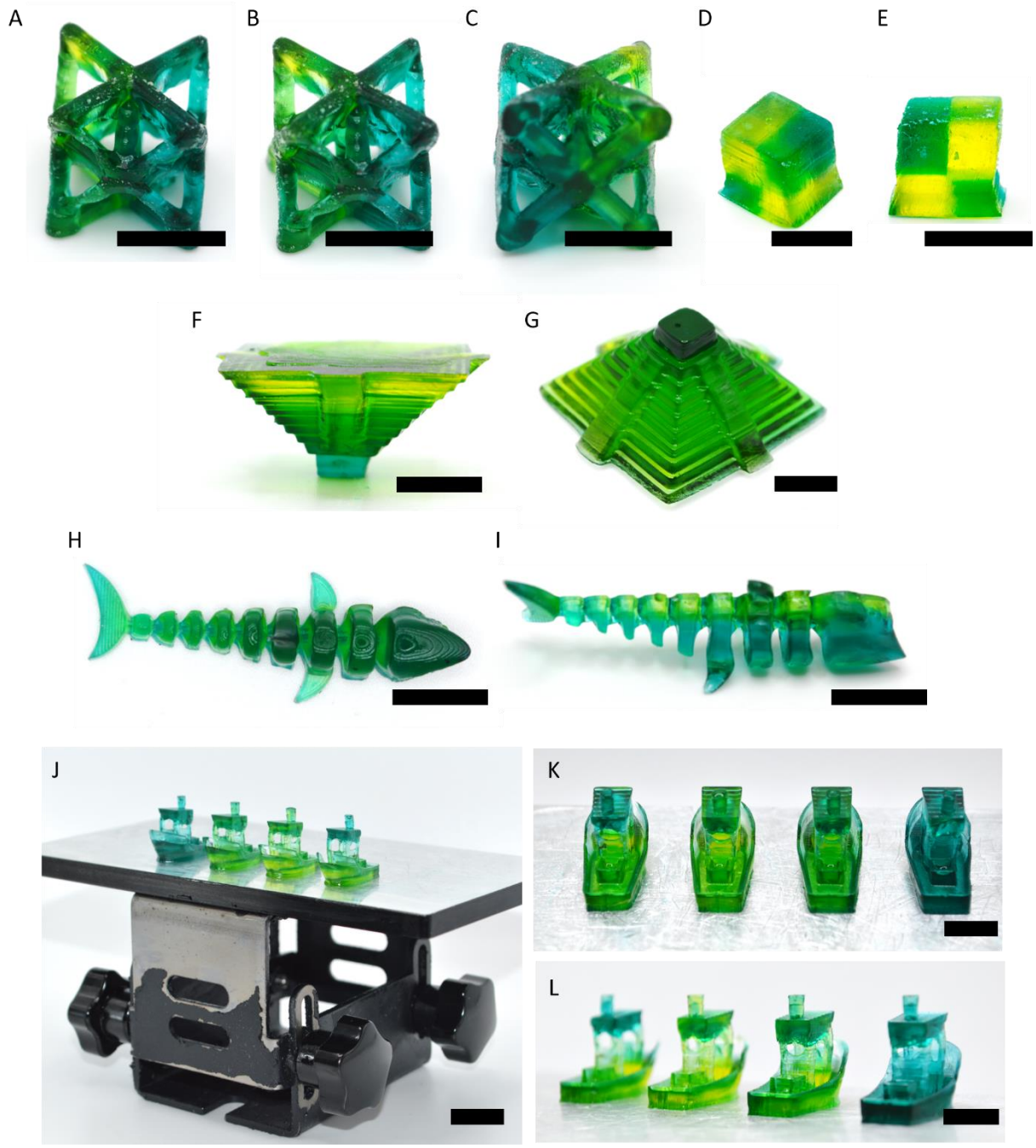

Figure F20) Additional images of dual-wavelength 3D printed objects. Scale bar=10 mm (A) Octet truss (B) Octet truss (C) Octet truss (D) Cube (E) Cube (F) Pyramid (G) Pyramid (H) Shark (I) Shark (J) Benchys (K) Benchys (L) Benchys

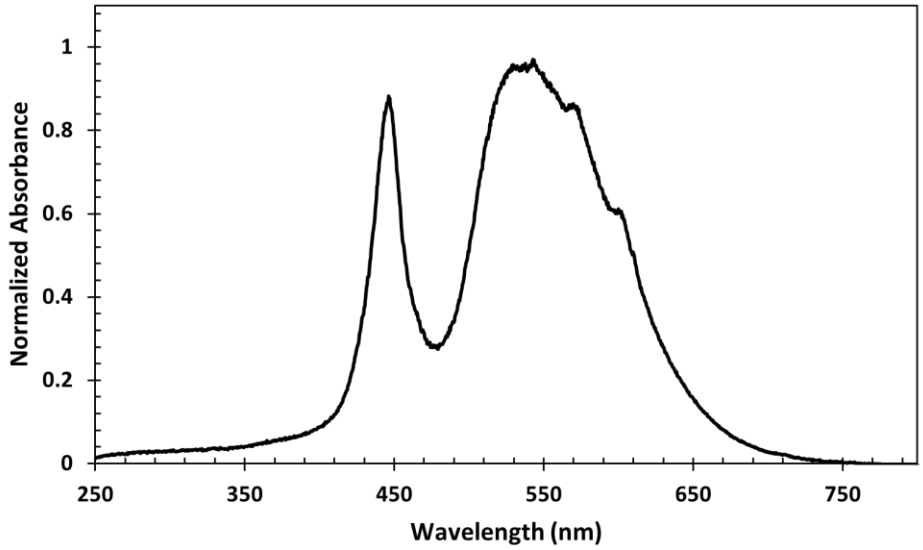

Figure F21A) Normalized emission spectra for the white light lamp used to cure objects in Teflon mold.

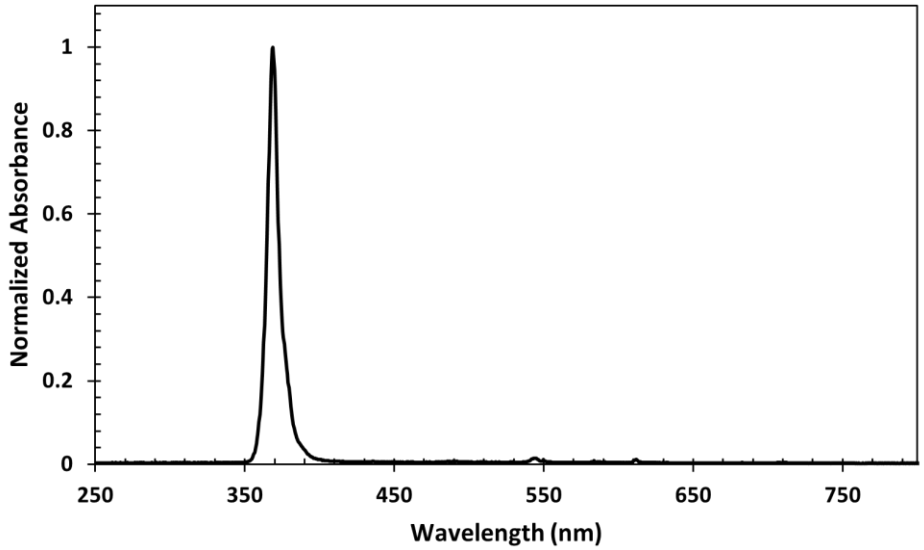

Figure F21B) Normalized emission spectra for 365 nm Kessil lamp. The wavelength with max absorption was found to be 369 nm.

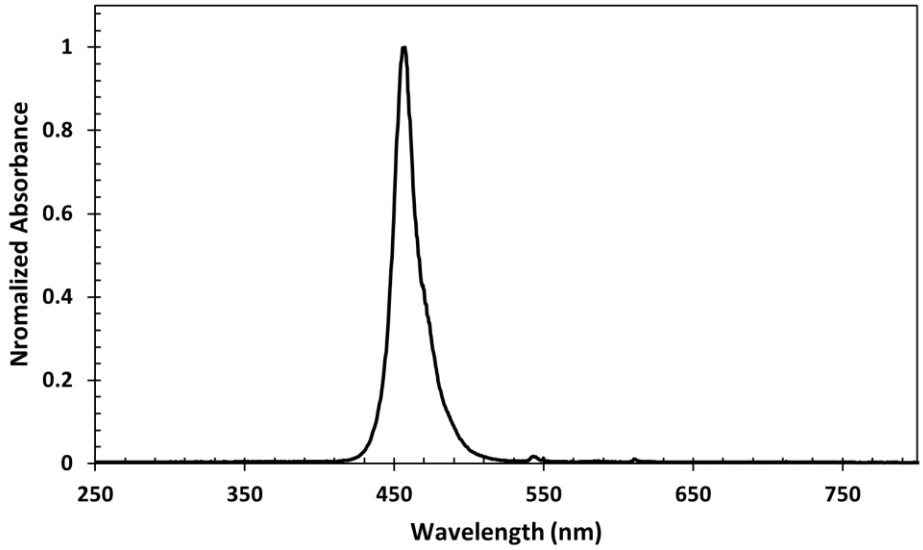

Figure F21C) Normalized emission spectra for 456 nm Kessil lamp. The wavelength with max absorption was found to be 457 nm.

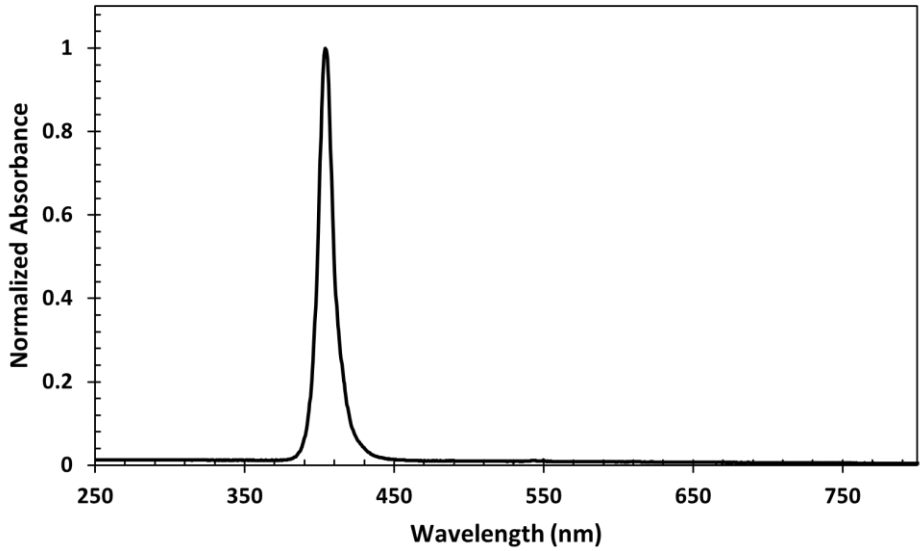

Figure F21D) Normalized emission spectra for 405 nm light source. The wavelength with max absorption was found to be 404 nm.

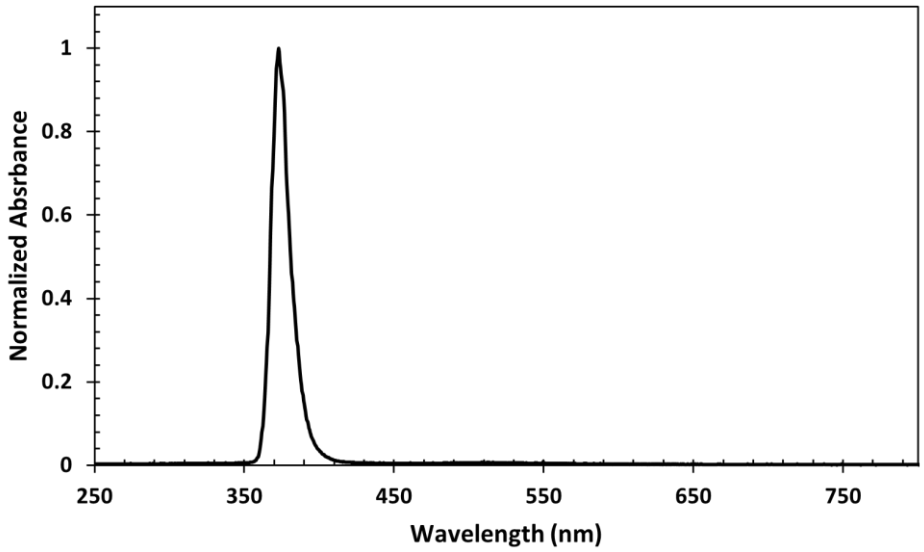

Figure F21E) Normalized emission spectra for 365 nm projector. The wavelength with max absorption was found to be 373 nm.

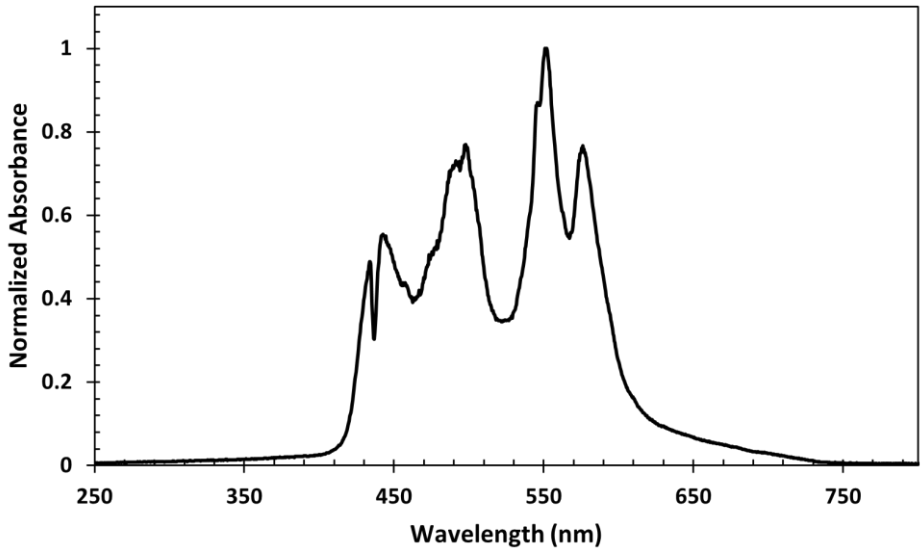

Figure F21F) Normalized emission spectra for the white light projector.

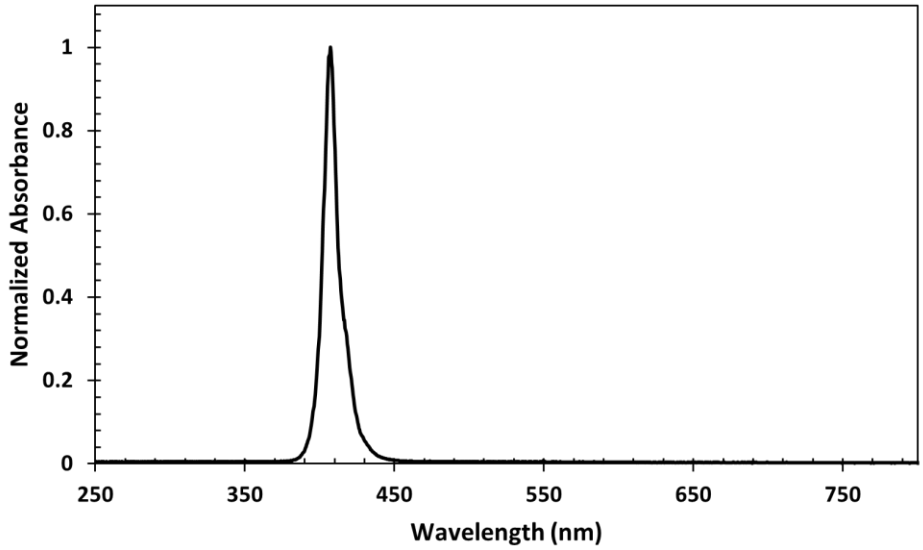

Figure F21G) Normalized emission spectra for Elegoo Mars 3 LCD 3D printer.

Design Files:

Shark: https://www.thingiverse.com/thing:3845304/files
Benchy: https://www.thingiverse.com/thing:5293974
Octet Truss: https://www.thingiverse.com/thing:5250099
Pyramid: https://www.thingiverse.com/thing:4155

Movie S1 (See online version of article for movie):

Colored CAD model of design files next to GIF of the projected layer slices used for dual wavelength 3D printing.